Cavitation Inception In Separated Flows

Thesis by

Joseph Katz

In Partial Fulfillment of the Requirements

for the Degree of

Doctor of Philosophy

California Institute of Technology

Pasadena, California

1982

(Submitted December 1, 1981)

Acknowledgment

I would like to express my deepest gratitude and appreciation to my advisor Dr.A.J.Acosta for his guidance and support during the course of the present research, and for his friendship, encouragement and assistance in the times that they were extremely needed.

Special thanks go also to Elton Daly and Joe Fontana for their help in the design and the machining of the present experimental equipment, and for their tireless efforts to make the life in the laboratory as easy as possible. I would also like to thank Dr.H.Shapiro for the design of the electronic equipment; G.Lundgren for the machining of some of the test bodies; and R.Eastvedt, L.Montenegro and R.Relles for their help with the experiments. My thanks go also to B.Hawk, S.Berkley and R.Dudek for their help with the administrative details and for the preparation of the thesis manuscript.

I would like to acknowledge the financial support of the Naval Sea System Command General Hydrodynamic Research Program administered by David W.Taylor Naval Ship Research and Development Center.

Finally, I would like to express my love and gratitude to my family who stood by me and brought me to where I am today and to Vickie Mitchell for her care and understanding that lightened some of the difficulties I had to face.

ABSTRACT

The phenomenon of cavitation was studied on four axisymmetric bodies whose boundary layers underwent a laminar separation and subsequent turbulent reattachment. The non-cavitating flow was studied by holography and the Schlieren flow visualization technique. Surface distributions of the mean and the fluctuating pressures were also measured. The conditions for cavitation inception and desinence were determined and several holograms were recorded just prior to and at the onset of cavitation. The population of microbubbles and the nature of the subsequent development of visible cavitation was determined from the reconstructed image.

High rms and peak values of the fluctuating pressure were measured (up to 90 percent of the dynamic head), the negative peaks being larger than the positive ones except for the reattachment zone where large positive peaks existed. The power spectra contained peaks thought to originate within the large eddies of the mixing layer and in one case there were also peaks due to the laminar boundary layer instability waves.

Cavitation inception occurred in the turbulent shear layer downstream of the transition region. When the separation zone was large the inception region was located within the most developed section of the mixing layer but upstream of the reattachment zone. When the separation region was small inception occurred close to the reattachment zone but still detached from the body surface. A comparison

between the surface minimum pressure and the cavitation inception indices also indicated that inception could not occur near the surface of the bodies having a large separation region.

The appearance of visible cavities was preceded by the appearance of a cluster of microbubbles only in the cavitation inception region. The nuclei population in the other sections of the flow field remained fairly uniform. This observation supports the assumption that cavitation is initiated from microscopic free stream nuclei. The rate of cavitation events was estimated from the nuclei population and from the dimensions of the separation region. It was shown for one of the bodies that at least one bubble larger than 10 micrometers radius was exposed every second to a pressure peak which was sufficiently large to cause a cavitation event.

Chapter I - Figure Captions

1.1 Nuclei distribution from various sources. The data of the HSWT and Beers et al (1973) are superimposed on a graph presented by Gates and Acosta (1978).

1.2 A schematic description of the L.T.W.T.

1.3 A schematic description of the holocamera.

1.4 A photograph of the holocamera.

1.5 A schematic description of the laser cooling system.

1.6 A schematic description of the conventional reconstruction system.

1.7 A schematic description of the schlieren reconstruction system.

1.8 A photograph of the schlieren reconstruction system.

Chapter II - Figure Captions

Chapter III - Figure Captions

Chapter IV - Figure Captions

4.1 A photograph of an early stage of cavitation on the two inch blunt body $Re_D = 3.6x10^5$, $\sigma = 1.70$.

4.2 A photograph of cavitation on the two inch blunt body. $Re_D = 3.6x10^5$, $\sigma = 1.60$.

4.3 Holograms of the first microscopic signs of cavitation near the surface of the two inch blunt body. $Re_D = 2.3x10^5$, $\sigma = 1.21$. The "large" sheared bubbles are located at a) $x/D = 0.89$, $y/D = 0.13$; b) $x/D = 0.96$, $y/D = 0.22$.

4.4 A hologram that displays the population of bubbles below and above the shear layer of the blunt body during cavitation inception. $Re_D = 2.3x10^5$, $\sigma = 1.15$. The hologram covers the region between $x/D = 0.23$ and 0.45 and $y/D = 0.11$ and 0.27.

4.5 Maps of bubble population near the surface of the two inch blunt body. a) $Re_D = 2.83x10^5$, $\sigma = 3.55$; b) $Re_D = 2.94x10^5$, $\sigma = 3.00$; c) $Re_D = 3.06x10^5$, $\sigma = 2.56$.

4.6 The number density distribution function of bubbles that were counted near the surface of the two inch blunt body. The counted sections are defined by the dashed lines in Figure 4.5.

a) $Re_D = 2.85x10^5$, $\sigma = 4.74$; b) $Re_D = 2.83x10^5$, $\sigma = 3.55$;
c) $Re_D = 2.83x10^5$, $\sigma = 2.99$; d) $Re_D = 2.84x10^5$, $\sigma = 2.67$;
e) $Re_D = 2.99x10^5$, $\sigma = 3.05$; f) $Re_D = 3.00x10^5$, $\sigma = 3.04$;
g) $Re_D = 2.94x10^5$, $\sigma = 3.00$; h) $Re_D = 3.02x10^5$, $\sigma = 2.86$;
i) $Re_D = 2.99x10^5$, $\sigma = 2.76$; j) $Re_D = 3.06x10^5$, $\sigma = 2.56$.

LIST OF SYMBOLS

a	acceleration
C_p	the average pressure coefficient defined by $(P-P_\infty)/(0.5\ \rho u_\infty^2)$
C_{ps} or C_{PB}	the average pressure coefficient inside the separation zone
C_p'	the rms pressure fluctuations coefficient defined by $\sqrt{\overline{P'^2}}/(0.5\ \rho u_\infty^2)$
D	body diameter
f	frequency of fluctuations
f_{max}	maximum range of pressure fluctuations spectrum
$f_1; f_2$	a calculated frequency defined by $0.56\ \frac{u_\infty}{L_1}$; $0.56\ \frac{u_\infty}{L_2}$
h	the height of the separated bubble (separation stream line)
h'	the height of the separated bubble upstream of the step
H	the height of the step on the step body
L	length of separation zone
L_1	the distance between separation and reattachment defined by $x_r - x_{sep}$
L_2	the distance between transition and reattachment defined by $x_r - x_{tr}$
ℓ	the distance between two neighboring vortices in a shear layer
ℓ'	the length of the pressure transducer calibrating tank
$N(R)$	the number of density distribution functions of nuclei
$n(R)$	the density of nuclei
P	static pressure
P'	fluctuating pressure
$\sqrt{\overline{P'^2}}$	rms values of pressure fluctuations

P_{atm}	atmospheric pressure
P_∞	the tunnel free stream static pressure
P_v	vapor pressure in room temperature
P_c	the pressure in the core of the vortex
$Q(R)$	the flow rate of bubbles in the shear layer
$Q_c(R)$	the flow rate of bubbles that are exposed to pressure peaks
R	bubble radius
$\dot{R}$	dR/dt
r	the radius of the pressure transducer
r_c	the radius of a vortex core
Re_D	body Reynolds number defined by $\frac{u_\infty D}{\nu}$
Re_θ	momentum thickness Reynolds number defined by $\frac{u_\infty \theta}{\nu}$
Re_{δ^*}	displacement thickness Reynolds number defined by $\frac{u_\infty \delta^*}{\nu}$
S	distance along the surface of the body
St	Strouhal number defined by fD/u_∞ or $\frac{fL}{u_\infty}$
T	surface tension
t_B	characteristic response time of a bubble
u	local velocity
u_∞	free stream velocity
u_{Av}	average velocity
Δu	velocity difference across a shear layer
u_c	convection velocity
x	axial distance from the stagnation point
x'	axial distance from the step
x_{sep}	axial location of separation

x_{tr}	axial location of transition
x_r	axial location of reattachment
x_i	axial location of cavitation inception
y	a dimension normal to the body surface
δ^*	boundary layer displacement thickness
δ_ω	shear layer slope thickness defined by $\Delta u/(\frac{\partial u}{\partial y})_{max}$
θ	momentum thickness
θ_s	momentum thickness at separation
ρ	water density
ω	frequency in rad/sec
Γ	circulation
λ	wavelength of eddies in the shear layer
σ	cavitation index defined by $(P_\infty - P_v)/(0.5\ \rho u_\infty^2)$
σ_i	cavitation inception index
σ_d	cavitation desinence index

TABLE OF CONTENTS

TABLE OF CONTENTS (continued)

TABLE OF CONTENTS (continued)

I. INTRODUCTION

I.1 Background

I.1.1 Scale Effects in Cavitation

Vapor and gas cavities are formed in a liquid either when there is sufficiently high temperature or when the pressure is reduced below a critical value. The former process is usually described as boiling, thermal effects being the main contributor, and the latter is defined as cavitation and is controlled by inertial or dynamic phenomena. A comparison between these processes is made by Plesset (1949, 1956) and is reviewed also by Knapp et al. (1970).

The present work focuses on cavitation whose physical appearance can be either in the form of bubbles of various sizes and shapes, or in the form of large vapor (and gas) cavities that are attached to the surface of a body. Cavitation appears on ship propellers and on the components of pumps, turbines, valves, and hydrofoils. It may become a major design problem due to its effect on the performance of hydraulic machinery and to its contribution to erosion and noise.

One of the major differences between the gas and the liquid phases is the ability of the latter to withstand tensile forces. According to Plesset (1969) a pure homogeneous liquid can sustain, theoretically, a tension of thousands of atmospheres, but the most careful experiments lead only to a few hundred atmospheres. The discrepancy is explained by the postulation of imperfections or "weak spots" within the liquid that become the sites for the onset or the inception of cavitation. The nature and the origin of these nuclei is one of the major subjects in

cavitation research and part of the existing literature enclosed with this topic will be discussed in the following sections.

One of the major problems in fluid mechanics is to predict the characteristics of a prototype from the results of tests on a model. The common technique is to use similarity parameters thought to be appropriate which, together with known scaling laws, assist in extrapolating the model results to the full scale design. Insofar as cavitation is concerned, the scaling laws are not fully understood, as has been recently discussed by Acosta and Parkin (1975).

The basic parameter for cavitation experimentation is the cavitation index (or number), σ, defined as

$$\sigma = \frac{P_\infty - P_v}{\frac{1}{2} \rho u_\infty^2}$$

P_∞ and u_∞ being the characteristic pressure and velocity, respectively, ρ the density, and P_v the vapor pressure of the bulk liquid. In the present experiments P_∞ and u_∞ are the conditions in the tunnel test section measured far from the body. There are two critical values of σ; the first one, σ_i, is the cavitation inception index determined by reducing the tunnel pressure keeping the velocity constant until the first signs of cavitation appear. The second critical value is the desinent cavitation index, σ_d, that is determined by increasing the pressure from an established cavitating condition until the last signs of cavitation just disappear. These parameters are not necessarily equal, a discrepancy that is usually described as cavitation hysteresis. If

σ were the only significant parameter to use in such testing, we should not have any difficulty in predicting the prototype behavior from a model behavior. This is not the case, however, for most applications of fluid mechanics that involve cavitation, as will be shown by the following examples. Parkin and Holl (1953) and Kermeen (1952) report that the cavitation inception index for hemispherical headform bodies depends on the body diameter and on the free stream velocity, and not necessarily on the Reynolds number. Kermeen and Parkin (1957) later found a strong Reynolds number effect on the inception index for the separated flow behind sharp edge disks. The most famous example is the comparative test program on a similar body of revolution organized by the International Towing Tank committee (ITTC) in various test facilities (see Lindgren and Johnsson (1966) and Johnsson (1969)). The findings showed a poor agreement both in the physical appearance of cavitation and in the measured values of σ_i. It was suggested that the discrepancy was due to the different environment (the amount and the type of cavitation nuclei in the free stream) and to the existence of a laminar separated bubble on the body at low test velocities. This dependence of σ_i on additional parameters (scale effects) became the major problem in cavitation research (see Arndt (1981)). The contributing factors can be divided into two categories: the first includes the effects of the flow field (velocity, pressure distribution, body size and shape, turbulent phenomena, etc.), and the second includes the parameters that affect the susceptibility of water to cavitation such as the amount, type, and size of cavitation nuclei.

I.1.2 Cavitation Nuclei

The weak spots or the cavitation nuclei that are essential to the onset of cavitation can originate either from the free stream or the surface of a body. The presence of the surface nuclei may be due to the material itself and the finish of the body surface. Holl and Treaster (1966), Holl (1968), Reed (1969), Gupta (1969), and Van der Meulen (1972a,b) have all studied this aspect of nuclei. These investigators tested stainless steel bodies with different surface finishes, Teflon, nylon, and glass bodies, and found significant differences between their inception indices and the appearance of cavitation. Acosta and Hamaguchi (1967) found that a thin silicon oil coating (this oil dissolves a large amount of air) on a body surface altered the inception indices first by increasing them when the layer was fresh and then by decreasing them (beyond the pure water results) after the coated body was submerged for a long time. Peterson (1968) measured the cavitation inception indices for the very same body, first after exposing it to air and then by taking measures to remove the gas pockets from the surface. He found significant differences between the results, 0.78 for the former and 0.63 for the latter.

The effects of the surface quality and material and the significance of the pressure time history experienced by the body led some investigators (see Holl (1969)) to suggest that cavitation is initiated from air pockets that were trapped in microscopic cracks and crevices that exist on the surface.

The second and most commonly suggested source of cavitation nuclei is the free stream itself. These nuclei are thought to be vapor or

gas bubbles, or solid particles that contain gas pockets. The mathematical behavior of a spherical bubble that contains vapor and a noncondensable gas is described by the Rayleigh-Plesset equation (see Plesset and Prosperetti (1977)) from which the conditions for equilibrium and instability can be developed (the latter will be discussed in Chapter 4). Epstein and Plesset (1950) showed that gas bubbles will disappear by mass diffusion in an undersaturated liquid, and this conclusion led several investigators to propose various explanations for the presumed existence of gas bubbles or nuclei in liquids. Some of these are discussed by Plesset (1969), but Harvey et al. (1944, 1947) appear to provide the most tenable suggestion, namely, that gas is contained within cracks on the surface of microscopic solid particles. This physical mechanism has attracted much attention (see, for example, Keller (1972, 1973)) but a direct observation has not yet been possible.

The importance of these nuclei as a source of nucleation has led to the development of several detection or observation techniques. These include the microscopic observations of water samples, the "Coulter counter," "single particle light scattering," the "acoustic" techniques for detection of gas bubbles, holography with microscopic observation of the reconstructed image, and finally, the liquid quality meter (Oldenziel (1979)). These different detection techniques are discussed by Godefroy et al. (1981), Gates (1977), and Morgan (1972).

Several investigators made an attempt to combine their measured data with a theory that explains the rate of cavitation events (bubble cavitation) near the surface of a streamlined body. Ripken and Killen

(1962, 1964) and Schiebe (1969) applied an acoustic method to measure the undissolved gas content in test water and thereby obtained an estimate of the concentration of microbubbles. For other reasons the predicted rate of cavitation events compared poorly with measured data. Keller (1972, 1973) determined the nuclei population by using a single particle light scattering device (the sample volume was illuminated by a He-Ne laser). This technique could not distinguish between solid particles and bubbles, but Keller came to the conclusion that most of the detected nuclei were solid by comparing his results for various types of prepared test water (filtering and degassing). He then pursued the Harvey nucleus model to show that this concept would explain a part of his experimental findings.

Only a few investigators have applied holography to cavitation nuclei detection, namely, Peterson et al. (1975), Feldberg and Shlemenson (1973), Gates and Acosta (1978), and Billet and Gates (1979). This method, however, has been extensively used in aerosol measurements (Thompson et al. (1967)) and even for identification of plankton (Beers et al. (1973)). The holographic technique is widely used in the present study and the system used for this purpose will be described later.

Gates and Acosta (1978) have recently summarized the nuclei number density distributions from a variety of sources and their results are presented in Figure 1.1. These distributions include acoustically determined population of bubbles in the ocean (Medwin (1977)), and photographic observations of plankton by Beers et al. (1973). Note the several orders of magnitude difference in the populations shown; it

would seem plain that this difference could create significant "scaling" errors while applying laboratory results to field cavitation phenomena. Also note that the nuclei in the Caltech HSWT are found to be mostly solid particles, while the Caltech LTWT contains mainly free stream bubbles. This difference may explain why it is easier to cavitate the same body in the LTWT (provided that the flow is nonseparating) while the liquid in the HSWT can support a certain tension (Gates and Acosta (1978)).

I.1.3 Cavitation Inception-Physical Models

There have been several attempts to develop a detailed theory that will explain the occurrence of cavitation near the surface of a streamlined body. One of the earliest models was that of Parkin (1952) who used the Rayleigh-Plesset equation and the known pressure field around a test body to determine the behavior of air and vapor nuclei that were stabilized on small solid particles in the liquid. Later Parkin and Kermeen (1953) carried out a series of experiments on a hemispherical headform body. They came to the conclusion that cavitation is sustained by small bubbles that grow at a fixed point in the body boundary layer until they are large enough to be entrained by the flow, travel downstream, and appear as macroscopic cavitation.

Parkin's theory was extended by Holl and Kornhauser (1969) to include the effects of initial conditions, stream and surface nuclei, thermodynamic effects of bubble growth, and the existence of a boundary layer. Van der Walle (1962) was motivated by Parkin and Kermeen's observations to describe the conditions for the stabilization of bubbles

in the boundary layer under the action of the body pressure gradient, adhesion forces to the surface, and viscous drag. Oshima (1961) made an attempt to develop scaling laws with the help of assumed similarity laws and by claiming that cavitation inception took place when the bubble diameter grew to one-half the size of the boundary layer displacement thickness. These theories were based on Parkin and Kermeen's (1953) interpretation of their own experiments on the hemispherical body, and as will be discussed later, they ignored the most important phenomenon, namely, the existence of a laminar separation bubble on this body. A theory in which viscous effects were neglected was developed by Johnson and Hsieh (1966). They calculated the trajectories and the stability of bubbles near the minimum pressure region on a body surface from which they developed the conditions for cavitation inception. This theory was used by Schiebe (1969), whose work was mentioned earlier, while trying to estimate the rate of cavitation events with the acoustically-measured bubble population. Schiebe's results showed only qualitative agreement with experimentally measured values. Keller's (1972, 1973) model that was also mentioned earlier is based on the potential pressure field. He attributed the disagreement between his theory and the experimental results to viscous effects inside the pore of Harvey's solid nucleus.

The effect of diffusion of dissolved gas into a bubble during its motion in the supersaturated sections of the flow field (where the pressure is low) is neglected in the above theories. According to Holl (1969), however, cavitation can also occur due to gas diffusion (a

process defined as gaseous cavitation) but the rate of such bubble growth is on the order of seconds (see Epstein and Plesset (1950)) unlike the dynamic bubble growth (vaporous cavitation) that occurs in milliseconds (see Knapp et al. (1970)). Oldenziel (1979) subsequently made additional calculations of gas diffusion during vaporous cavitation growth and showed that a significant amount of gas is actually released into the bubble and thus his results suggest that these processes, that is, the gaseous and the vaporous cavitation, cannot be totally separated.

All the above theories deal with the behavior of a nucleus near the surface of a streamlined body exposed to the pressure field there. These models do not bring into full consideration several real-fluid flow phenomena such as the laminar boundary layer separation and the subsequent development of an unstable shear layer and turbulent reattachment. These phenomena are known to take place on many surfaces of interest.

I.1.4 Viscous Effects on Cavitation Inception

It was not until recently that the effect of viscous phenomena on cavitation was demonstrated by Arakeri and Acosta (1973, 1974, 1976) and Arakeri (1973) who applied the schlieren technique to observe the flow and the inception of cavitation on submerged axisymmetric bodies. They found that the laminar boundary layer on the surface of the hemispherical nose body separated, and that cavitation inception occurred in the turbulent reattachment zone. Some small cavitating bubbles were observed to be carried upstream by the reverse flow inside the separation zone until they reached the separation point where they were swept

away by the main external flow. Other bubbles were observed to grow at a fixed point inside the separation zone until they were large enough to be carried downstream. This form of cavitation disappeared when the pressure was lowered slightly to be replaced by a clear attached "band" type cavity. This sequence of events is also demonstrated by Gates (1977) with a series of schlieren photographs and by Van der Meulen (1976) with a series of reconstructed holograms.

Arakeri and Acosta (1976) proceeded with their experiments and removed the separation bubble either by tripping the boundary layer in order to enforce early transition, or by increasing the free stream velocity. They found that as the laminar separated zone disappeared the clear band type cavity became unstable, patchy, and intermittent until no form of attached cavity could be maintained on several test bodies. These observations demonstrate clearly that for those bodies that possess a separated bubble, cavitation phenomena are closely related to the characteristics of this separation zone. Arakeri et al. (1978) demonstrated this relation also on a 1/8 caliber ogive body. They showed that a sudden change in the dimensions of the separation zone (when the separated bubble bursts) causes also a large change in the cavitation inception index.

These results led Arakeri and Acosta (1979) to classify the axisymmetric bodies according to their viscous flow characteristics and their cavitation inception scaling trends. The first group includes the bodies that possess a large separation bubble where the free shear layer can develop without being disturbed by the body surface and contains a large eddy structure. An example of a body belonging to this

group is the sharp edge disk tested by Kermeen and Parkin (1957). They observed that the first cavities appear within the shear layer, and further suggested that cavitation inception occurs in the core of the vortices in the mixing zone. This group is characterized by a strong dependence of the inception index on the Reynolds number.

The second group includes the bodies with a smaller separated zone where the neighboring surface affects the development of the mixing layer. Cavitation inception occurs near the reattachment zone due to the large pressure fluctuations there. This last statement is supported by Arakeri (1975a) and by Huang (1979) who measured the fluctuating pressure on the surface of the hemispherical nose body and found pressure peaks of 25 and 45 percent of the dynamic head, respectively. The cavitation inception index shows a weak dependence on the Reynolds number and its value is close to the absolute value of the pressure coefficient in the separated zone.

The third group includes the bodies with a very small separated bubble such as the ITTC headform (Arakeri (1973)) and is characterized by a cavitation index that is independent of the Reynolds number, and his upper bound is the absolute value of the pressure coefficient in the separation zone. The fourth group includes those cases where the laminar boundary layer undergoes natural transition to turbulence without separation. This group is characterized by a relatively low cavitation inception index whose upper bound is the minimum pressure coefficient on the body,and the cavities usually appear either as traveling bubbles or in attached patches downstream of the minimum pressure point. Some typical examples are the Schiebe body (Van der

Meulen (1976)) and a series of headforms that were tested by Huang (1979).

Being motivated by his suspicion that the height of the separated zone plays a dominant role in cavitation phenomena, Arakeri (1979) proceeded by artificially changing this height by means of a small downstream-facing step at the tangency point of the hemispherical body. His results show that the dependence of the inception index on the step height (remarkably large changes in σ) is limited to small steps ($H/D \leq 0.01$) beyond which the cavitation number reaches an asymptotic value that depends only on the Reynolds number. Another example of the effect of the dimensions of the separation zone is that of Van der Meulen (1980) on two hydrofoils at various angles of attack. His holographic study of the flow displays the transition from a small separated zone at small angles of attack (similar to the second group in Arakeri and Acosta's (1979) classification) to the large scale eddies in the shear layer at large angles (similar to the first group). As a result, the cavitation inception indices display a growing dependence on the Reynolds number, and the physical appearance of the cavities changes from traveling bubbles to band type and then to the intermittent shear layer cavities as the dimensions of the separation zone are increased.

I.1.5 Remarks

The preceding short introduction forms the background to the present work whose scope will be described in the following section. More extensive, older material can be found in the book by Knapp et al. (1970), bubble dynamics is reviewed by Plesset and Prosperetti (1977),

a recent state of the art review on cavitation is provided by Arndt (1981) and two earlier reviews by Acosta and Parkin (1975, 1980).

I.1.6 Scope of the Present Work

The present work focuses on cavitation in separated flows, that is, those cavitation phenomena that occur near the surface of a body whose boundary layer undergoes laminar separation followed by transition in the shear layer and turbulent reattachment.

The first step will be to study the flow around the test bodies selected. This will be accomplished with holography and schlieren photography that will help in visualizing the flow patterns under fully wetted and cavitation inception conditions. Then the average pressure coefficients and the surface pressure fluctuations will be carefully measured (including the rms, peak values, and spectral distributions). The results will assist us in relating the location and the physical appearance of cavitation to flow phenomena such as the location and the dimensions of the separated bubble, the position of transition and reattachment, the eddy structure in the shear layer, and the location of high pressure fluctuations. The pressure field may also help explain the relatively high cavitation inception indices that characterize these separated flows.

The second step or interest is to identify the type, the location and the role of the nuclei in the cavitation process. The population of these nuclei will be studied in the neighborhood and inside the separation zone with the help of holography that enables us to record details down to 10 micrometers in diameter. An attempt will be made to

follow the development of cavitation from the micro to the macro (visible) scale in order to provide direct evidence that the detected nuclei are the source of the large cavities. Some of the major parameters that affect the nuclei population will also be studied, in particular the effect of the pressure-time history of the water in the test facility and various experimental procedures.

The discussion that follows the presentation of the results includes an attempt to estimate the rate of cavitation events around the present bodies by combining some of the major contributing factors. These factors include the nuclei population and size distribution, the negative pressure fluctuation peaks, their probability of occurrence, their frequency, and the location and dimensions of the observed cavitation inception region.

I.2 Experimental Equipment

The following section contains a description of the water tunnel, the test bodies, and the holographic system. The rest of the experimental equipment and test procedures that apply only to a certain experiment will be described in each chapter separately.

I.2.1 Water Tunnel

All the experiments were carried out in the Low Turbulence Water Tunnel (LTWT) whose schematic description is displayed in Figure 1.2. This facility is described in detail by Gates (1977) and only some of its main features are presented here.

The rectangular test section is 8.33 feet long and its cross section expands from 12 by 12 inches at the entrance to 14 inches high

and 12 inches wide at the exit. The square settling (stagnation) chamber has a cross section of 48 by 48 inches, resulting in a contraction ratio of 16:1. This chamber is equipped with two honeycombs and three damping screens that contribute in reducing the test section turbulence level to about 0.04 percent.

The water in the tunnel is pumped by a mixed-flow type pump that is driven by a 30 HP d.c. electric motor through a belt drive. The resulting maximum velocity in the test section is fairly low ,about 24 ft/sec.

The pressure is controlled with a Nash 5 HP vacuum pump that is connected to a tank located above the settling chamber and a bypass valve to the atmosphere that is connected to the vacuum line.

I.2.2 Test Bodies

Four stainless steel axisymmetric bodies were tested in the present experiments. The first two bodies had a flat blunt nose but a different size. The first one was two inches in diameter and the second was one-half inch in diameter. The other two bodies had a hemispherical headform, both two inches in diameter, the first with a smooth tangency, and the second with a one-millimeter downstream facing step at the tangency point. (This last model will be referred to as the step body.) The bodies were mounted on a two-blade sting support and were 13 inches long and thus the nose was located 6.5 diameters upstream of the sting.

Each headform was built several times for the different experiments. The first body had a series of pressure taps on its surface as described in Figures 2.1 and 2.2; the second body was designed for the pressure

fluctuation measurements (see Chapter 3) and the third one had a smooth, polished surface for the cavitation tests. A detailed description of each of these headforms is provided in the following chapters.

I.2.3 The Nuclei Counter - The Holography System

Holography is the only existing technique that allows direct observations of microparticles and bubbles in a moving liquid, and thus to know their exact shape and size. In this method, a three-dimensional image of a sample volume is reconstructed and all the observations are made in this image. The measurements can be made in any part of the sample volume and in almost any desired magnification.

A common photographic record contains information about the intensity of the light scattered from a certain object. The hologram, however, contains also information about the phase difference between the radiation from the object and a reference wave. This information is stored on a film in the form of an interference pattern, and a proper technique can be used to relocate any object to its original position in space.

Recording and Reconstruction. The hologram is recorded in the experimental facility. A desired sample volume is illuminated by a beam of collimated, coherent, and semimonochromatic light. The light diffracted from any object in this volume interferes with another coherent reference beam, and the resulting pattern is recorded on film. The technique used in the present study is the lensless Fraunhofer holography that is limited to holograms recorded in the "far field" of small objects. Instead of using two beams, a subject wave and a reference wave, only one light source is used for both purposes. The undisturbed part of the illuminating beam

becomes the reference wave that interferes with the light diffracted from the objects. The resulting pattern is recorded on a high resolution film that is located on the other side of the sample volume.

The developed holographic record is illuminated by another collimated coherent light source. While passing through the hologram whose transmittance is proportional to the recorded interference pattern, the reconstruction light is diffracted to create a three-dimensional image of the original volume. Actually, two images are created, a real and a virtual one. They are formed symmetrically on both sides of the hologram plane and have the same axis. The far field requirement in Fraunhofer holography insures that the virtual image will produce only a weak and almost uniform background illumination in the real image plane. A detailed analysis of this technique is described in chapters two and eight of Collier et al (1971).

The recording light source in the present system is a pulsed ruby laser. The use of such a laser is essential while recording a hologram of a moving object due to the high intensity required for a very short exposure time. The reconstruction light source is a five mw CW He-Ne laser. The difference between the wavelength of the lasers, 0.6943 μm of the ruby and 0.6328 μm of the He-Ne laser does not change the dimensions in the plane normal to the illumination axis but does affect the axial dimension.

I.2.4 The Holocamera

A schematic description of the holocamera is presented in Figure 1.3 and a photograph of the system in Figure 1.4. As shown, the setup consists of a pulsed laser generator, collimating and beam expanding components, a

recording film, and an alignment system.

Laser Cavity. A three-inch long, quarter-inch diameter cylindrical ruby rod is "excited" by a helical xenon flashlamp. The ruby is located in a 22-inch long optical cavity created by two flat mirrors. The back mirror is a 100 percent reflecting dielectric surface, and the front one is a sapphire etalon ($\simeq$ 60 percent reflectivity). The front mirror also plays a role in longitudinal mode control of the laser. Two iris apertures located inside the cavity keep the light beam sufficiently narrow to avoid generation of multiple transverse modes.

The ruby rod and the flashlamp are located inside a sealed box whose interior is filled with filtered and deionized cooling water. The flashlamp is covered with a highly reflecting cylindrical surface made of aluminum sheeting. This reflector insures that most of the flashlamp's light will be directed toward the center where the ruby is located.

When the laser is triggered, approximately 1000 joules that are stored in loaded capacitors discharge through the flashlamp. The flash is initiated by a high voltage pulse generated from a different capacitor and magnified by a series injection trigger transformer. This high voltage, more than 20,000 volts, is needed for ionizing the xenon in the flashlamp, and thus activate the discharge of the main power whose voltage is only 3500 volts. The duration of the flash is more than one millisecond.

"Q Switching." The amount of energy that is supplied to the system and the duration of the flash are sufficient for generating several laser pulses. In order to control the number of these pulses, the laser has to be "Q switched". A KD*P cylindrical ring electrode Pockel's cell and a

calcite glan laser polarizer are used for this purpose. The switching system is located inside the cavity between the ruby and the front mirror.

The KD*P crystal introduces a retardation between the two mutually orthogonal components of the input field that is proportional to the voltage applied to it. In the present system the Pockels cell is loaded with 1.8 KV, a potential that is sufficient to cause a retardation of a quarter wavelength. After being emitted from the ruby the light is polarized by the glan polarizer and enters the crystal. While passing through the Pockels cell, a retardation of quarter wavelength is introduced and after reflection from the back mirror the light is retarded again by the same amount. As a result, the plane of polarization is rotated by 90°, and this light will be deflected by the glan polarizer. This Q switch prevents the oscillations of light in the cavity and the system cannot lase.

In a prescribed time the voltage on the Pockel's cell is dropped to zero for a very short duration. Since the crystal does not alter the polarization in this period, the light can oscillate in the cavity. This light and the continuously added energy from the flashlamp bring the ruby to a critically excited state that results in the emission of a large laser pulse. The duration of this pulse is between 20 and 50 nanoseconds. If the cavity is switched more than once, two (or more) laser pulses will be emitted, thus the sytem can be applied for interferometry.

The control and power supply unit of the Pockel's cell is connected to the main power source. The time delay between the flashlamp triggering and the switching can be adjusted in order to activate the laser in an optimum period during the flash.

Cooling. Efficient cooling of the laser head is required due to the sensitivity of the ruby and the flashlamp to small temperature changes. The cooling water is injected from six orifices that are located between the rod and the flashlamp at the rate of one gpm. As illustrated in Figure 1.5, the cooling system consists of a five-gallon storage tank, a pump, two filters (for 5.0 and 0.22 micron particles) and a deionizer. A conductivity meter located before the entrance to the laser head indicates the quality of the water before use. To prevent any scale deposit on the ruby rod and the flashlamp, the water is recirculated through the deionizer several times, bypassing the laser to provide a resistivity of at least 18 M cm (much less than 0.1 ppm of any contamination). The deionizer also cleans the water continuously during the operation. Brass coils in which tap water flows are located inside the storage tank. This heat exchanger removes the heat from the cooling water.

The electronic power supply and control system were built by Shapiro Scientific Instruments. The mechanical components, the mounts, and the laser head assembly were designed and manufactured at Caltech.

Recording a Hologram. The laser output is split just after exiting from the cavity, and four percent of the light is directed toward a PIN diode whose output is observed on an oscilloscope screen. The rest of the beam is expanded by a microscope objective, spatially filtered by a ten-micron pinhole, and collimated by a 2.5-inch diameter lens. This beam illuminates the sample volume and the resulting image is recorded on a 70 mm wide Agfa Bevaert 10E75 photographic film. The resolution of this film is 2800 lines/mm and its optimum sensitivity is 1-3 microjoules/cm^2.

Since the intensity of the laser is much higher, the cavity output is attenuated by a neutral density filter.

Alignment. The alignment system consists of an autocollimator and a 0.5 milliwatt CW He-Ne laser. The autocollimator assists in aligning the laser cavity components which are mounted on carriers that can be carefully adjusted. The He-Ne laser helps in bringing all the components to a common axis and in positioning the pinhole in the focal plane of the objective.

I.2.5 Reconstruction System

After developing the film, the hologram is mounted on the reconstruction system. The light source is a 5 milliwatt CW He-Ne laser whose output is expanded by an objective, spatially filtered by a pinhole, and collimated by a lens. The resulting beam illuminates the hologram, and the diffraction pattern caused by the film transmittance creates a three-dimensional image of the original volume. A magnifying system, positioned inside the image field, focuses any desired cross section on a TV vidicon and the image can be seen on the screen of a monitor. The hologram is mounted on an x-y-z vernier carriage so that any point in the reconstruction field can be focused on the vidicon.

The magnifying and focusing lenses consist of either a microscope objective as described in Figure 1.6, or a lens and a knife edge as sketched in Figure 1.7 and shown in a photograph in Figure 1.8. The microscope objective is used when a large magnification is needed for nuclei counting, and the lens and knife edge are used for a smaller magnification and for schlieren reconstruction. This last technique combines

the principles of holography with the schlieren effect. Instead of simply magnifying the image it is first focused to a point by the lens on the knife edge located in the focal plane. Most of the backward illuminating light source is thereby cut off and only the diffracted light can propagate downstream. The resulting schlieren effect is recorded by the vidicon and displayed on the TV screen. This modification in the reconstruction procedure eliminates most of the background noise and a major part of the laser speckle. A few examples of the difference between the "filtered" and "non-filtered" reconstructed image are displayed in Figures 2.20 to 2.22.

The main advantage of this technique over the conventional schlieren system comes from the coherent recording light source that makes the diffraction pattern a first-order phenomenon unlike the common schlieren photograph recorded with a white light source. This difference allows one to record a hologram in the usual manner and to adjust the position of the knife edge only while reconstructing the image. As a result one can concentrate on any part or characteristic of the flow-field without losing the rest of the information.

Calibration. The magnification of the reconstruction system was determined by observing the image of a microscope reticule that was positioned in the reconstruction system. A few holograms of a sample volume that contained particles of known sizes. 10, 19, and 50 micrometers verified the results of the theoretical analysis, (see Collier et al. (1971), chapter two) that the same magnification applied also to the original volume. The details of the calibration process and some examples of the particle images are provided by Katz (1979).

Most of the nuclei were counted with a magnification of 220. The flow visualization and cavitation observations were made with different magnifications and a proper scale is provided in each illustration.

The present description is brief and incomplete. A detailed description and design instructions of solid state lasers are provided by Koechner (1976) and the theoretical background in holography is explained by Collier et al. (1971) and by Born and Wolf (1975). Similar nuclei counters are also described by Thompson and Ward (1966), Thompson et al. (1967), Parrent and Thompson (1964), Feldberg and Shlemenson (1973), Peterson et al. (1975), and Gates (1977).

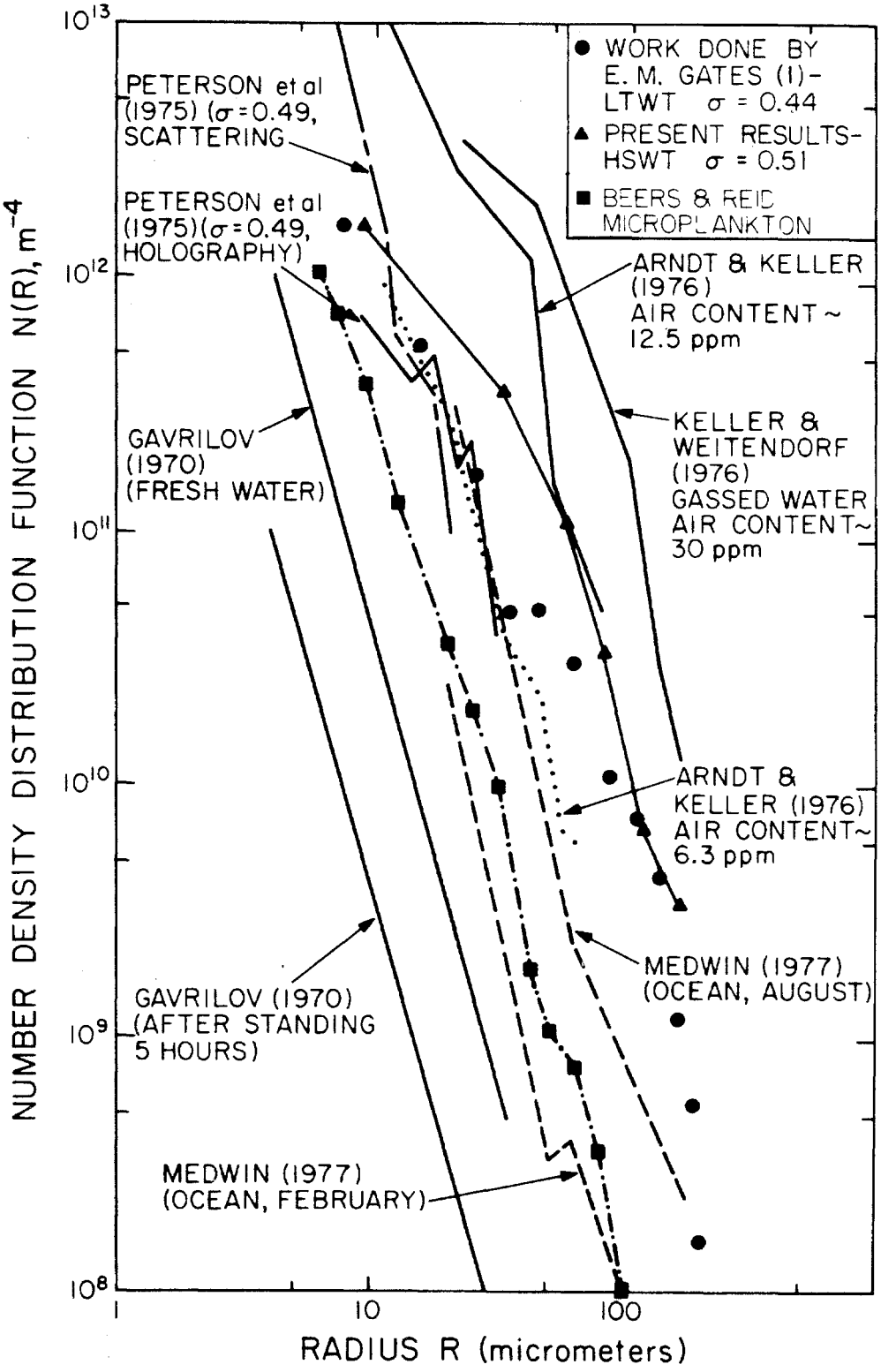

Figure 1.1. Nuclei distribution from various sources. The data of the HSWT and Beers et al (1973) are superimposed on a graph presented by Gates and Acosta (1978).

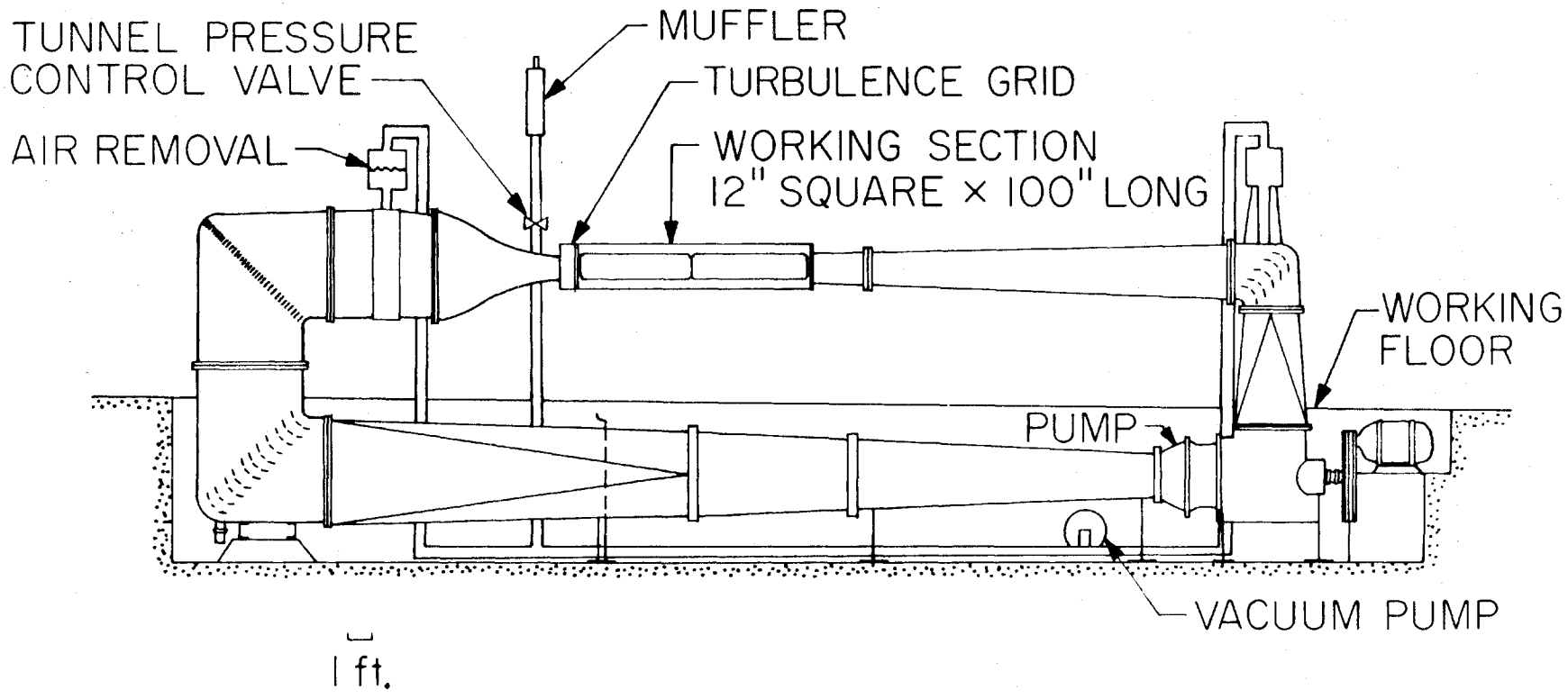

Figure 1.2. A schematic description of the L.T.W.T.

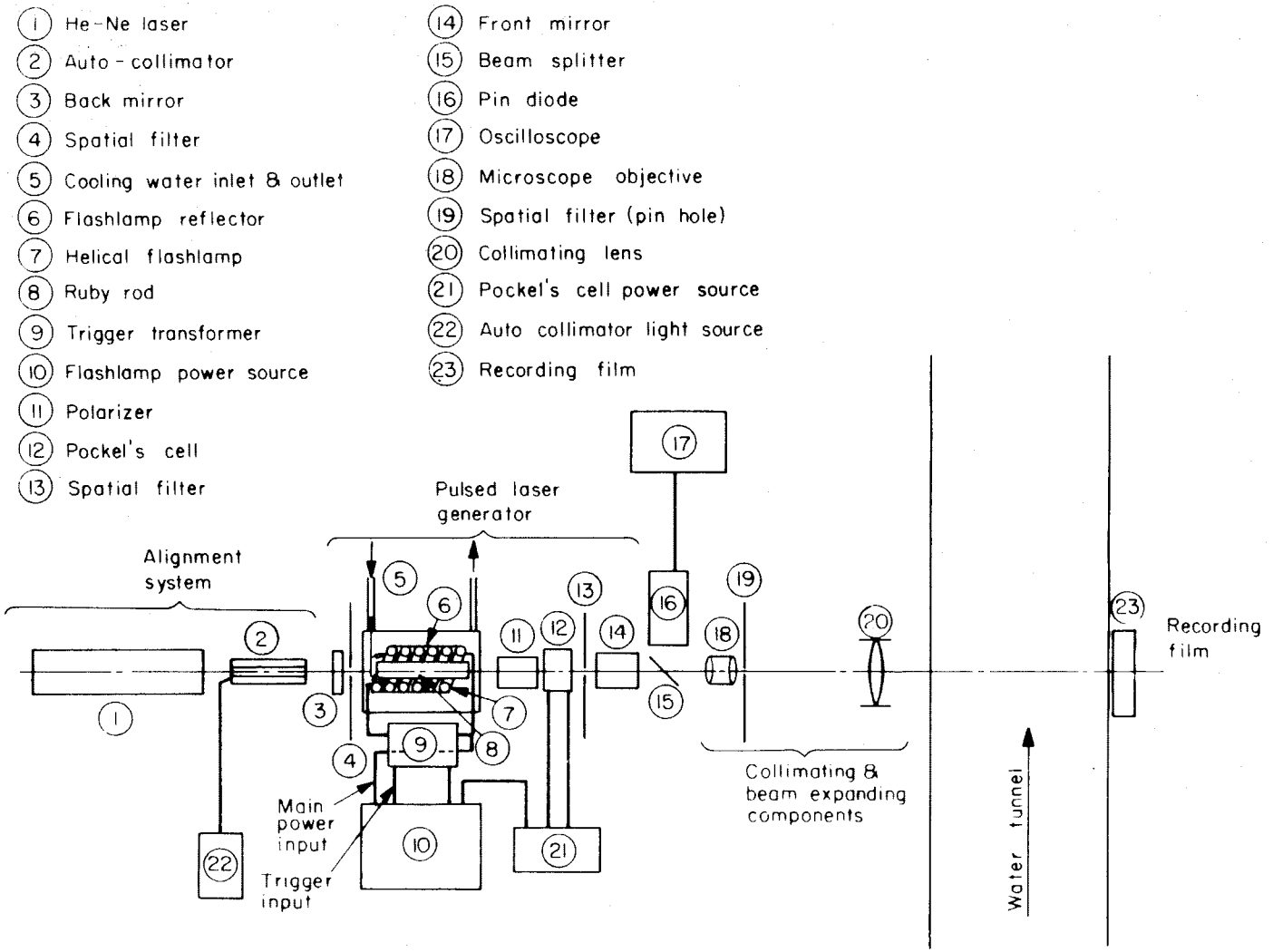

Figure 1.3. A schematic description of the holocamera.

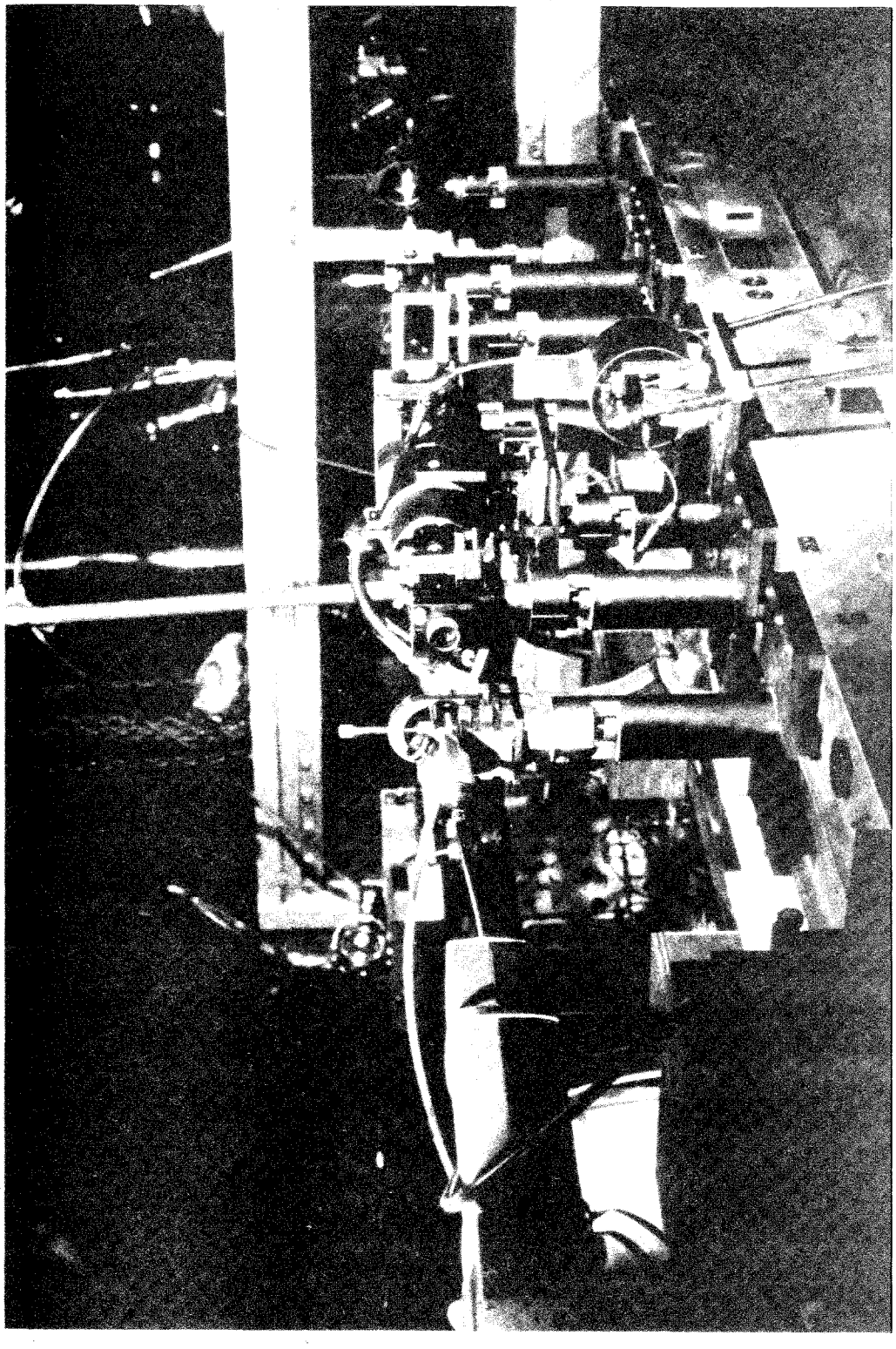

Figure 1.4. A photograph of the holocamera.

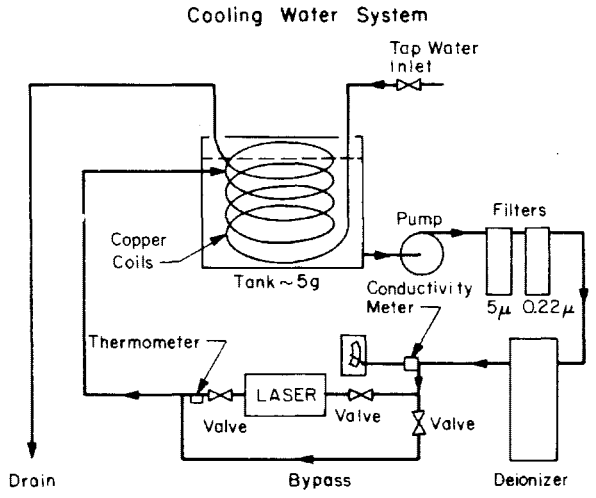

Fig. 1.5. A schematic description of the laser cooling system.

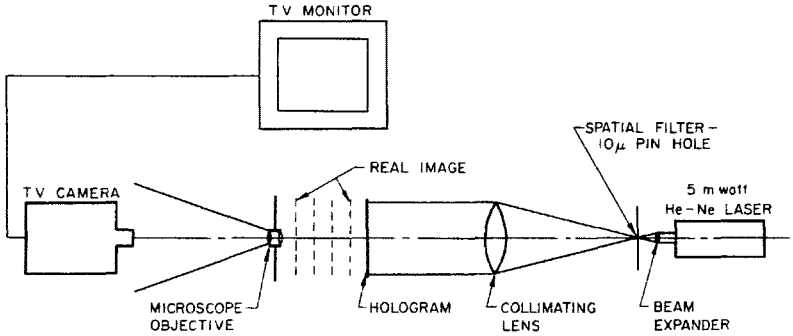

Fig. 1.6. A schematic description of the conventional reconstruction system.

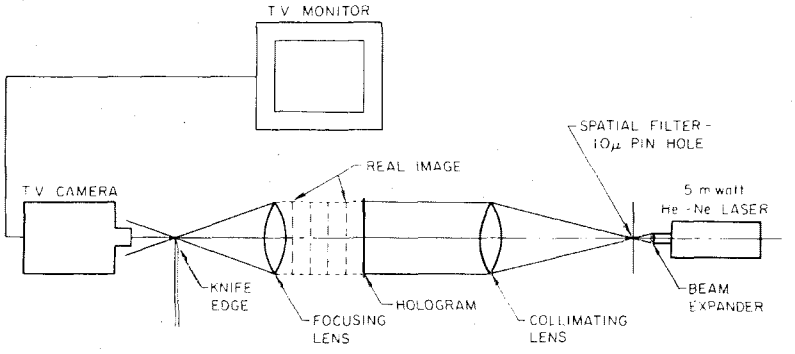

Fig. 1.7. A schematic description of the schlieren reconstruction system.

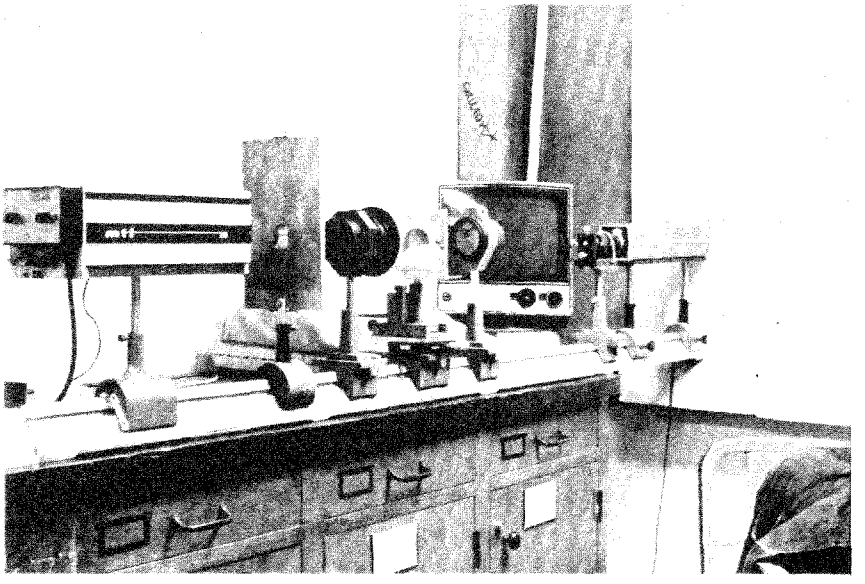

Fig. 1.8. A photograph of the schlieren reconstruction system.

II. A STUDY OF THE NONCAVITATING FLOW AROUND THE TEST BODIES

Introduction

As noted before, the focus of the present study is on the cavitation phenomena associated with axisymmetric bodies whose boundary layers undergo laminar separation and turbulent reattachment. The first step will be to study some of the characteristics of the flow around the test bodies, especially those that are associated with their separated zone. This chapter is divided into three sections. The first will present the pressure distribution measurements, and the second will describe the observations of the flow inside and around the separated regions by using several flow visualization techniques. The third section is a short discussion wherein some of the results that are of special interest will be emphasized, and needed information from other sources will be presented. These results will provide part of the background that will be needed later during the description of the cavitation experiments.

II.1 Average Pressure Measurements

The average or mean pressure field provides basic reference for the understanding of the viscous flow on surfaces and the local pressures which contribute to the onset of cavitation. The section to follow describes the measurements of the average pressure distribution along the bodies of interest in the present work. First, the experimental set-up will be described and then the results will be presented and discussed.

II.1.1 Apparatus and Procedure

The pressure was measured at twelve different points along the

surface of the two-inch bodies by drilling small pressure taps 0.032 inches in diameter at selected locations. The position of these taps is shown in Figures 2.1 and 2.2. The first figure shows the measuring points on the surface of the blunt nose. As one can see from Figure 2.1, it is possible to replace the forebody with any of the three forms shown in Figure 2.2. The hemispherical and step noses have six pressure taps. The first five are located at 0, 30, 45, 60, and 75 degrees, and the sixth tap is located just downstream of the tangent point on the surface of the hemisphere and behind the step on the step nose. Each pressure tap was connected by a flexible polyethylene tube to a valve mounted on a central panel. The valves led to a manifold connected to a Statham pressure transducer. The control panel also had a bleed system essential for removal of air and vapor bubbles. The same transducer was used for measuring the pressure at the entrance of the water tunnel test section, and a mercury manometer was used for measuring the velocity at the same point. The transducer was calibrated during the experiments by comparing its output to the reading on another mercury manometer while measuring the water tunnel pressure.

The experiments were carried out for various free stream velocities and pressures. By opening each of the valves on the control panel, one at a time, the transducer was exposed to a different pressure tap. A series of at least ten measurements was recorded and averaged when the transducer output fluctuated.

The tunnel pressure and velocity were recorded before and after each series of measurements along the surface of the body, and the experiment was repeated when the results changed by more than one percent. Since the

water tunnel has a diverging test section (its height is 12 inches at the entrance and 13 inches where the body is mounted); the "free stream" conditions that were measured at the entrance had to be corrected, taking into account also the developing boundary layer along the walls. The proper correction factors were measured by Gates (1977) in the same water tunnel. By applying his factors to the present experiments the resulting calculated pressure coefficient at the stagnation point was always equal to unity. Hence, Gates's correction factors proved to be satisfactory. The cross section of the body was only about two percent of the test section area, so blockage effects were not taken into account.

II.1.2 Results

Figure 2.3 displays the static pressure coefficient distribution along the surface of the blunt nose. As one can see, the pressure reaches a minimum at x/D = 0.75 and recovers back to free steam values at x/D = 1.75. From Figure 2.4 it is evident that the minimum pressure coefficient shows some dependence on Reynolds number, its value being around -0.6. The present results match the distribution obtained by Ota (1975) who, in addition to conducting his own measurements, provides a collection of other results of pressure measurements along the surfaces of bodies with sharp edges (such as blunt noses and sharp-edged disks). Keller and Prasad (1978) obtained a pressure distribution that reached a minimum of -0.9 in certain conditions, a result that contradicts both the present measurements and the various sources mentioned by Ota. The free stream pressure did not affect the results as long as it was kept high enough to prevent cavitation. But when the body started cavitating, significant changes occurred in the

pressure distribution and an example of this phenomenon is shown in Figure 2.5. The biggest changes occurred when the cavitation number was between 1.7 and 1.9; as the free stream pressure was lowered beyond these values the results converged toward that for a noncavitating body. This effect of the cavitation index is especially clear at x/D=1.0, 1.25 and 1.5. The same phenomenon occurred in all the measurements and only a single example of this effect is shown.

The pressure distribution along the surface of the hemispherical nose is presented in Figure 2.6. The minimum pressure obtained at S/D = 0.65 (75 degrees) is around -0.7 and shows very little dependence on velocity. Just downstream of the tangent point, at S/D = 0.82, the pressure coefficient is around -0.56. These results agree fairly well with those of Kermeen (1952) and are slightly higher than those of Holl and Carroll (1979) who measured -0.78 at the minimum pressure region and -0.6 just downstream of the tangent point. This pressure distribution will be used later to estimate the dimensions of the boundary layer along the hemispherical nose body and to predict the point of laminar separation.

Figure 2.7 displays the pressure distribution along the surface of the step nose. As one can see, there is some difference between the hemispherical and the step nose results. Upstream of the minimum pressure point the hemispherical nose results are slightly lower but the lowest pressure coefficient on the surface of the step nose is around -0.76. Behind the step the values vary from -0.59 to -0.65.

Unlike the two-inch bodies, the pressure was measured at only one point, x/D = 0.5 on the surface of the one-half inch blunt nose. According to Figure 2.8, the pressure coefficient is equal to -0.5 and does not show

any dependence on velocity. These results are similar to those obtained on the surface of the two-inch blunt nose at the same point.

II.2 Flow Visualization

Before dealing with cavitation phenomena we need to discuss the real fluid flows about these bodies, and in particular the properties of the laminar separated regions associated with these flows. We study the size of the separated zone, its height and length, and the position of transition to a turbulent flow in the free shear layer of this separated flow. Of particular interest here are some of the characteristics of the turbulent part of the separated zone with special reference to the large coherent structure found in the free shear layer of jets and wakes. Such a coherent structure will clearly affect the pressure field. Finally, the effect of the free-stream velocity, the size of the body and its shape on the characteristics of separated zones are of special interest while trying to understand the scale effects on these flows. The present section will contain first a description of the apparatus and the experimental procedure and then a presentation of the results.

II.2.1 Apparatus and Procedure

The methods of flow visualization used in the present work were schlieren and schlieren holography. The first technique as applied to water was described in detail by Arakeri (1973), Gates (1977), and Gates et al. (1979). The second method which combined the principles of holography with the schlieren effect, was described earlier in Chapter 1.

The hemispherical, step, and two-inch blunt noses were heated by a

1 kw heater inserted inside the bodies. The heater was adjusted to create a 3°F temperature difference (approximately) between the surface of the body and the free stream water. Whenever separation occurred, the fluid that was originally in the boundary layer departed from the surface and created a hotter layer in the flow above the immediate neighborhood of the body. This hot layer had a different density and thus a different refractive index which caused the refraction of the illuminating light source. The resulting image was recorded either as a hologram or as a schlieren photograph.

The dimensions of the separated zone on the surface of the blunt nose were quite large and for most of the velocity range the simple heating proved to be unsatisfactory for flow visualization. Hence the flow around this body was observed by using the pressure taps themselves to inject fluid from the surface into the flow above. The injected water contained one percent (by weight) $MgSO_4$ that provided the proper density contrast needed for the experiments. On the two-inch blunt body, the resultant jets served two purposes. The first one was to help in defining the boundaries of the separated zone and the second was to allow us to observe the direction of the flow in the vicinity of the jet exit. We expected to find some evidence of the reverse flow inside the separated zone and to locate the region of reattachment where the recirculation should change direction. The schlieren method was used for these observations mainly because of convenience at the time when these experiments took place. In order to determine the effect of the jets on the flow and on the dimensions of the separated zone, some of the experiments were repeated by closing part of the jets or by observing the image when the water was injected from the

downstream part of the separated zone. These last observations had to be made by using the holocamera for recording laser shadowgraphs, since the intensity of the schlieren effect was too low. The dimensions of the separated zone on the half-inch blunt body were determined in a similar way by injecting salt water from two jets and observing the patterns with the holocamera.

II.2.2 Results--Blunt Noses

Figure 2.9 shows a combined picture of the jets injected from the surface of the two-inch blunt body. For clarification, a plot of the same images is shown in Figure 2.10. As one can see, the jets located between x/D = 0.05 and 1.25 are directed upstream, indicating that the flow is reversed in these points. Between x/D = 1.5 and 1.75 the jets change their direction toward the free stream flow direction, suggesting that reattachment occurs somewhere between these points. The same jets are shown in a series of photographs presented in Figures 2.11a-e. Since the salt water was injected from the same source, we can learn more about the flow in the separated zone by comparing the shape of the jets. For example, the first one maintains its shape for a longer distance than the jet located at x/D = 1, where the reverse flow pushes the injected water back to the surface just after the exit. Near reattachment, that is, near x/D = 1.75 the jets rise again, suggesting that the flow in this region is slow again. Above the zone of reverse flow the injected water changes its direction toward the free stream flow, suggesting that the jets crossed the line of zero average velocity. Traces of salt water can be seen up to y/D = 0.43. We should keep in mind that these traces do not indicate the separating

stream line, since the salt water can cross this line due to velocity fluctuations. These traces do show the upper boundary of the turbulent mixing zone.

The photographs that are presented in Figure 2.11 overlap each other. We can verify by them that the general trend of the jets is not due to an instantaneous velocity field but to a more stationary behavior. As noted before, the recording process was carried out while keeping part of the injection points either closed or opened. The negligible effect of these jets on the characteristics of the separated zone can be seen by comparing Figure 2.11d to 2.12. They both display the region between $x/D = 1.5$ and 2.0, the first with injection from the upstream points, and the second with the upstream jets closed. The small effect of these jets can be also seen in Figure 2.13 which shows a laser shadowgram of the flow pattern in the upstream part of the separated zone by injecting the water from downstream.

Figure 2.14 shows a graph of the height of the upper boundary of the mixing zone and the length of the separated zone plotted against the Reynolds number. These dimensions do not show a significant dependence on velocity, at least in the range of the present experiments.

The final stage of flow visualization on the surface of the two-inch blunt body was to try to observe the structure of the free shear layer at the upper boundary of the separated zone. Unfortunately, detailed observation of this structure was possible only in a very low velocity--around 1.5 ff/sec and less. Figure 2.15a,b shows to laser shadowgraphs of a heated body corresponding to free stream velocity of 0.5 and 1.5 ft/sec. A large coherent eddy structure in the free shear layer is evident from

both records. When the tunnel velocity was increased above 2 ft/sec, the image of the vortices was destroyed by the mixing in the separated zone. However, the reconstructed hologram of Figure 2.16 provides evidence that the laminar shear layer still rolls up to form a series of eddies at higher velocities. Some traces of this coherent structure can be seen in Figures 2.11b and 2.13 by following the shape of the upper boundary of the mixing zone. The implication of the development of these eddies will be discussed later.

All the pictures that cover the edge of the blunt body, i.e., Figures 2.11a, 2.13, 2.15, and 2.16, show clearly that the separation is laminar and that the transition to turbulence in the free shear layer occurs a short distance downstream. This observation is true for all the present range of free stream velocities.

Two illustrations of the shape of the separated zone on the surface of the half-inch blunt body are shown in Figure 2.17. A copy of the first image is plotted in Figure 2.18, indicating the points of salt water injections and the suggested point of reattachment. Figure 2.19 displays the dependence of the height and the length of the separated zone on the Reynolds number. As one can see, the height of the upper boundary of the mixing layer and the length of the separated zone are one-half and twice the body diameter, respectively, and do not show a significant dependence on velocity. These dimensions are slightly higher than those of the two-inch blunt body as shown in Figure 2.14. The upper boundary of the separated zone presented in Figure 2.17b is wavy, possibly indicating again that the mixing layer contains large scale eddies.

II.2.3 Results--Hemispherical Nose

The advantage of schlieren reconstruction can be clearly seen in Figures 2.20, 2.21, and 2.22, which display the separated zone on the surface of the hemispherical nose body at different velocities. Each figure shows both the unfiltered image and the schlieren reconstructed hologram. These pictures show the points of laminar separation, the stable part of the separated bubble, and the transition to turbulence (the point where the separation line becomes wavy is assumed to be the transition point). The mixing of the hotter water with the free stream flow downstream of the transition point that reduces the density contrast needed for the present experiments prevents further observations of the turbulent part of the separated zone. As a result, these photographs do not indicate the reattachment region which, according to pressure fluctuation measurements, exists far downstream of the point where the present image disappears. As previously found by Arakeri (1973), Gates (1977), Van der Meulen (1976), and Holl and Carroll (1979), these figures show the strong effect of the Reynolds number on the dimensions of the separated bubble. Figure 2.23 shows the position of separation and transition taken from the holograms plotted against the Reynolds number. The present results suggest that the point of separation moves downstream from 84° to 87° and the point of transition moves upstream from $x/D = 0.55$ to $x/D = 0.52$ as the Reynolds number is changed from 1×10^5 to 3.7×10^5. This figure also shows the points where the trace of the free shear layer disappears. The dependence of the maximum height of the laminar part of the separating stream line on velocity is shown in Figure 2.24. This height changes from

$h/D = 9.5 \times 10^{-3}$ to 2.5×10^{-3} as the Reynolds number is increased from 1.5×10^{5} to 3.7×10^{5}. The reattachment points shown in Figure 2.23 are taken from Table 3-1 and were determined from pressure fluctuation measurements. A comparison between the present results and those of the previously mentioned investigators is made in the discussion that follows.

II.2.4 Results--Step Nose

Figures 2.25a to d are four examples of schlieren reconstructed holograms of the separated zone on the surface of the step body corresponding to velocities of 8.6, 10.9, 13.8, and 16.1 ft/sec, respectively. The photographs show clearly that the flow separates upstream of the step to form a free shear layer whose traces can be seen far downstream. All these figures indicate that transition occurs downstream of the step. In Figure 2.25a the separation line becomes wavy; in Figures 2.25b and c the initially laminar free shear layers roll up to form large coherent eddies and in Figure 2.25d, the image remains laminar until it disappears. The points where the separation line either becomes wavy or disappears and the points where the first eddy appears are assumed to be the transition region. The dependence on velocity of the separation, transition, and the maximum height of the separated zone upstream and downstream of the step are shown in Figures 2.26 and 2.27. The separation point that is located at 85.5° and the height of the separated bubble upstream of the step ($h/D = 0.0056$) seem to be independent of the Reynolds number. The location of transition, however, changes from $x/D = 0.60$ to $x/D = 0.52$ and the maximum height of the stable part of the separation stream line changes from 2.0 to 1.35 times the step height when the Reynolds number is increased from

1.1×10^5 to 3.75×10^5. The location of the reattachment zone cannot be determined from the present schlieren holograms, since the traces of the free shear layer disappear due to mixing when the flow becomes turbulent. The position of reattachment will be estimated later from pressure fluctuation measurements.

II.3 Discussion

As is evident from the present results, a separation zone exists on the surface of all the test bodies all over the present range of velocities. The separation is always laminar, followed by transition in the shear layer and turbulent reattachment (the exact location of reattachment is not detected by flow visualization on the hemispherical and step bodies and will be estimated from pressure fluctuation measurements).

There is a small difference in the values of the pressure coefficient inside the separation zone of the present test bodies, being -0.6, -0.56, and -0.65 for the blunt, hemispherical and step noses, respectively. These bodies, however, display a variety of separated flows, a variety in the dimensions and the shape of the separated bubbles, and a variety in the characteristics of the shear layer downstream of separation.

As expected, the flow separates on the edge of the blunt bodies and the laminar shear layer becomes unstable after a short distance, rolls up and forms a series of growing vortices. The dimensions of their separation zones are quite large; their scaled maximum heights of the mixing regions extends to 0.43 and 0.52 and the flow reattaches only after 1.7 and more than two times the body diameter for the two and the half-inch bodies, respectively. This reattachment length is in good agreement with the measurements of

Ota (1975) who determined this length by measuring the surface skin friction. There is also a good agreement between the location of the presently measured pressure recovery region and the observed reattachment length. Ota's (1975, 1980) measurements indicate that the separating stream line maximum height is $y/D \simeq 0.2$, much lower than the presently observed upper boundary of the mixing layer. The turbulence intensity, however, in Ota's experiments reaches a maximum at $y/d \simeq 0.3$ and drops back to free stream conditions when y/D exceeds 0.5. These results may explain the extent of the region that contains traces of the salt water ($y/D \simeq 0.45$) in the present experiments.

The measurements on the surface of the hemispherical headform, which is one of the most studied bodies in cavitation research, confirm the presence of a small separation zone first reported by Arakeri (1973) and then by Van der Meulen (1976), Gates (1977), Keller (1979), and Holl and Carroll (1979). Unlike the others, the present results show that the separation point moves slightly downstream when the velocity is increased, but the location of this point agrees with Arakeri and Van der Meulen. The length and the height of the separated bubble and their dependence on the Reynolds number agree with the results reported by Gates and by Van der Meulen, but do not agree with Arakeri's results which are considerably larger. The sensitivity of the separated bubble on this headform to small imperfections or slight changes in the nose shape, a sensitivity that became evident during the pressure fluctuation measurements, may be the reason for this discrepancy.

An estimate of the location of the separation point using the measured pressure distribution and Thwaites method is described in the next chapter and presented in Figure 3.63. The calculated separation point S/D = 0.77 agrees well with the measurements considering the rough pressure distribution used. According to these estimates the relation between the momentum thickness at separation, θ_S, and the body Reynolds number is:

$$\frac{\theta_S}{D} = \frac{0.34}{\sqrt{Re_D}}$$

then

$$\frac{h}{\theta_S} = \frac{h/D}{0.34}\sqrt{Re_D} = 8.7\left(\frac{h}{D}\right)\left(\frac{\theta_S u_\infty}{\nu}\right)$$

h being the height of the separation bubble. By using the present results for h/D we obtain that the ratio h/θ_S drops from around eight to six when the Reynolds number is increased from 1.5×10^5 to 3.5×10^5 ($\theta_S u_\infty / \nu$ changes from 130 to 200, respectively). These results are in good agreement with the correlation between H/θ_S and $\theta_S u_\infty / \nu$ that is reported by Arakeri (1979) for various separated flows (including the classical studies of Gaster (1966)). The equations above, however, indicate that as long as h/D depends on Re_D (or $\theta_S u_\infty / \nu$) there cannot be the linear relation between h/θ_S and $\theta_S u_\infty / \nu$ that is suggested by Arakeri.

Since the adverse pressure gradient that leads to separation on the step nose is slightly steeper than this gradient on the hemispherical body, one would expect that the flow will separate earlier on the step body. This conclusion is confirmed by the observations for most of the present velocity range. As will be shown later (Table 3-3) the pressure fluctuation measurements suggest that the reattachment point on the step body changes

from $x/D = 0.72$ to 0.68 as the Reynolds number is increased from 1.4×10^5 to 3.6×10^5 far downstream of the transition point. Eaton and Johnson (1980) summarize the available literature about the flow downstream of a backward facing step. Their collection shows that the length of the separated bubble varies from five to eight times the height of the step, and their own experiments suggest that the reattachment length depends on the Reynolds number when the flow approaching the step is laminar and becomes constant when this flow is turbulent. The present results suggest that the flow reattaches at $x'/H \simeq 10$, a significantly larger number. Keeping in mind, however, that the flow is already separated at the step, the ratio between the reattachment length and the height of the separation stream line is less than eight. This result agrees with the observations by Eaton and Johnson for either turbulent or transitional approaching boundary layer.

The most important result of the present flow visualization experiments is the evidence of a large eddy structure in the shear layer of the step and the blunt bodies. Moreover, the observed sections of the mixing layer that contain these eddies do not touch the body surface. Unlike these headforms, the mixing region that develops near the surface of the hemisphere is in constant contact with the body, and thus one would expect that the neighboring surface would affect the characteristics of the flow there. As is already suspected by Arakeri and Acosta (1979), these observations put the hemispherical body in a different category of separated flows. The present experiments do not provide clear evidence that a coherent eddy structure exists also near the surface of the hemispherical

body. As will be shown in the following chapter, however, the spectra of pressure fluctuations imply that such a structure exists also in the shear layer of this body. The presence of these vortices is reported also by Keller (1979) for a very low velocity (1 ft/sec) and can be deduced from the shape of the mixing layer traces in Arakeri (1973), Gates (1977), and the present observations. The relation between the cavitation phenomena and the characteristics of the separation zone, especially those that are related to surface effects and the shear layer eddies, will become evident in Chapter IV, where they will be demonstrated and discussed. Further discussion about the turbulent shear layer is postponed to the next chapter, which focuses on the pressure fluctuation measurements.

To recapitulate, four bodies have been tested: two flat, blunt noses and two hemispherical bodies, one of them with a small downstream facing step. The two blunt noses have a large separation zone whose dimensions scale with the body diameter and do not display a significant dependence on the Reynolds number. The two hemispherical bodies have a smaller separation bubble whose dimensions are sensitive to free stream velocity and change considerably due to the introduction of the step. The separation on all bodies is laminar and the free shear layer becomes unstable after a short distance and rolls up to form a series of large scale vortices. This turbulent region appears to be in constant contact with the hemispherical body surface and partially detached from the surface on the rest of the headforms.

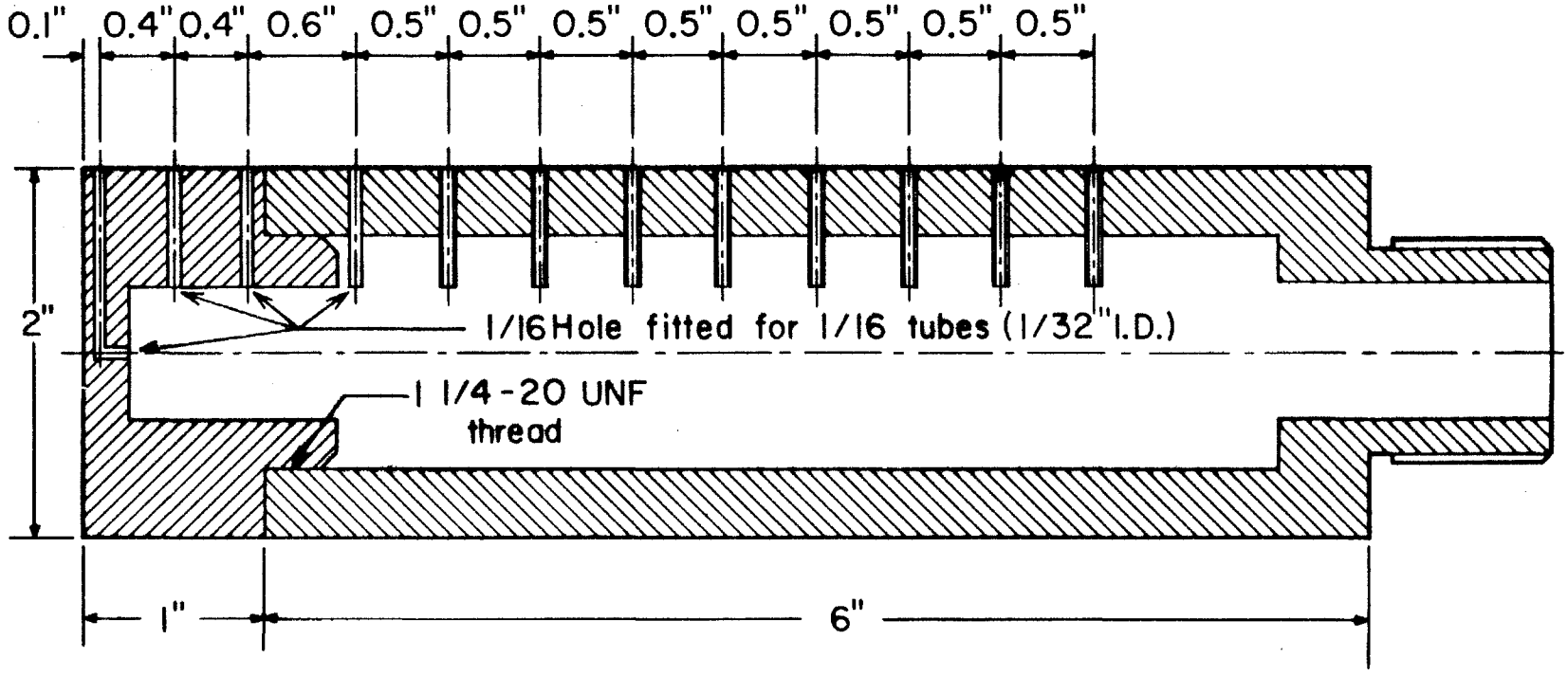

Figure 2.1. A schematic description of the blunt body with the pressure taps on its surface.

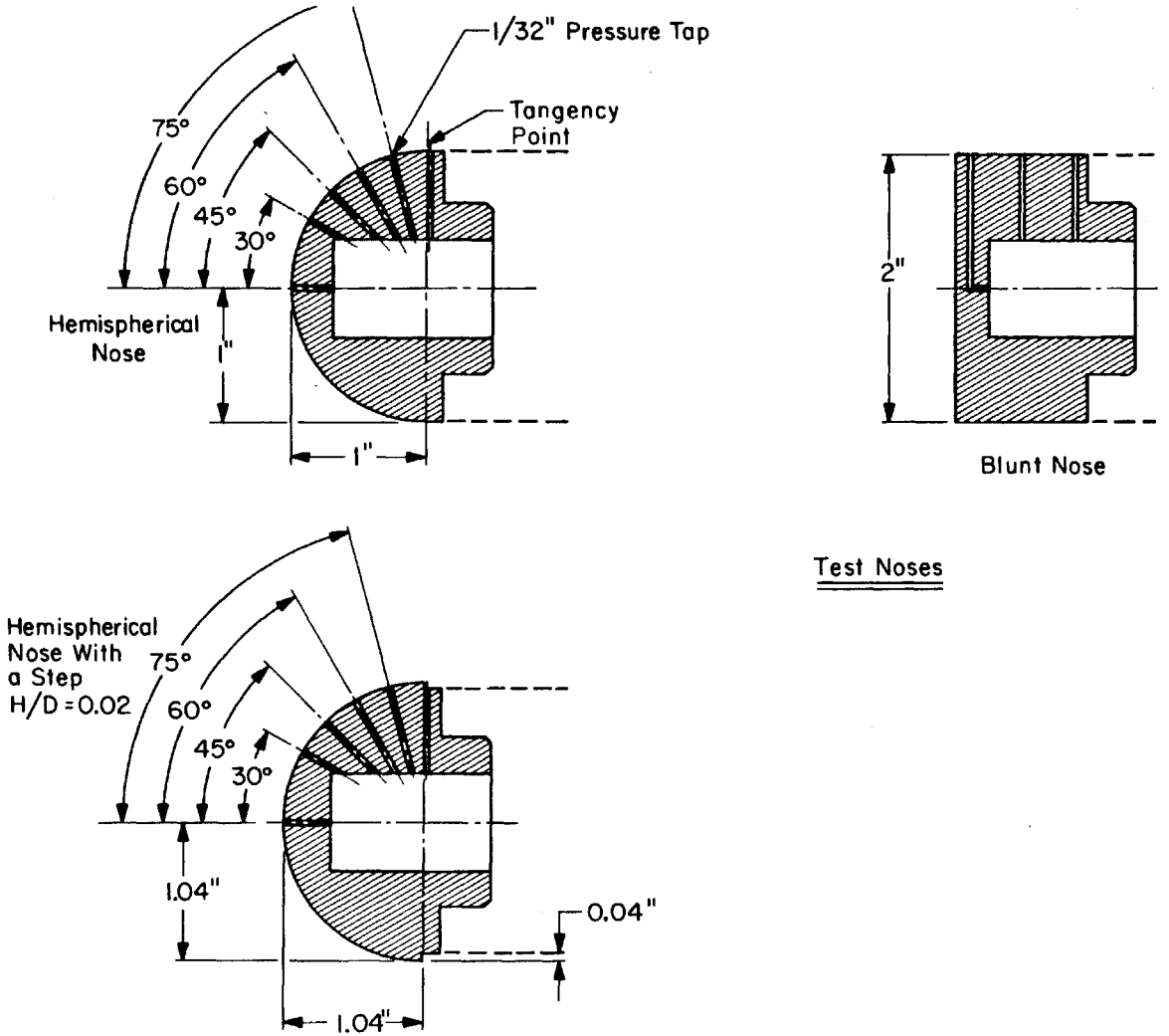

Test Noses

Figure 2.2. A schematic description of the different headforms with the pressure taps on their surface.

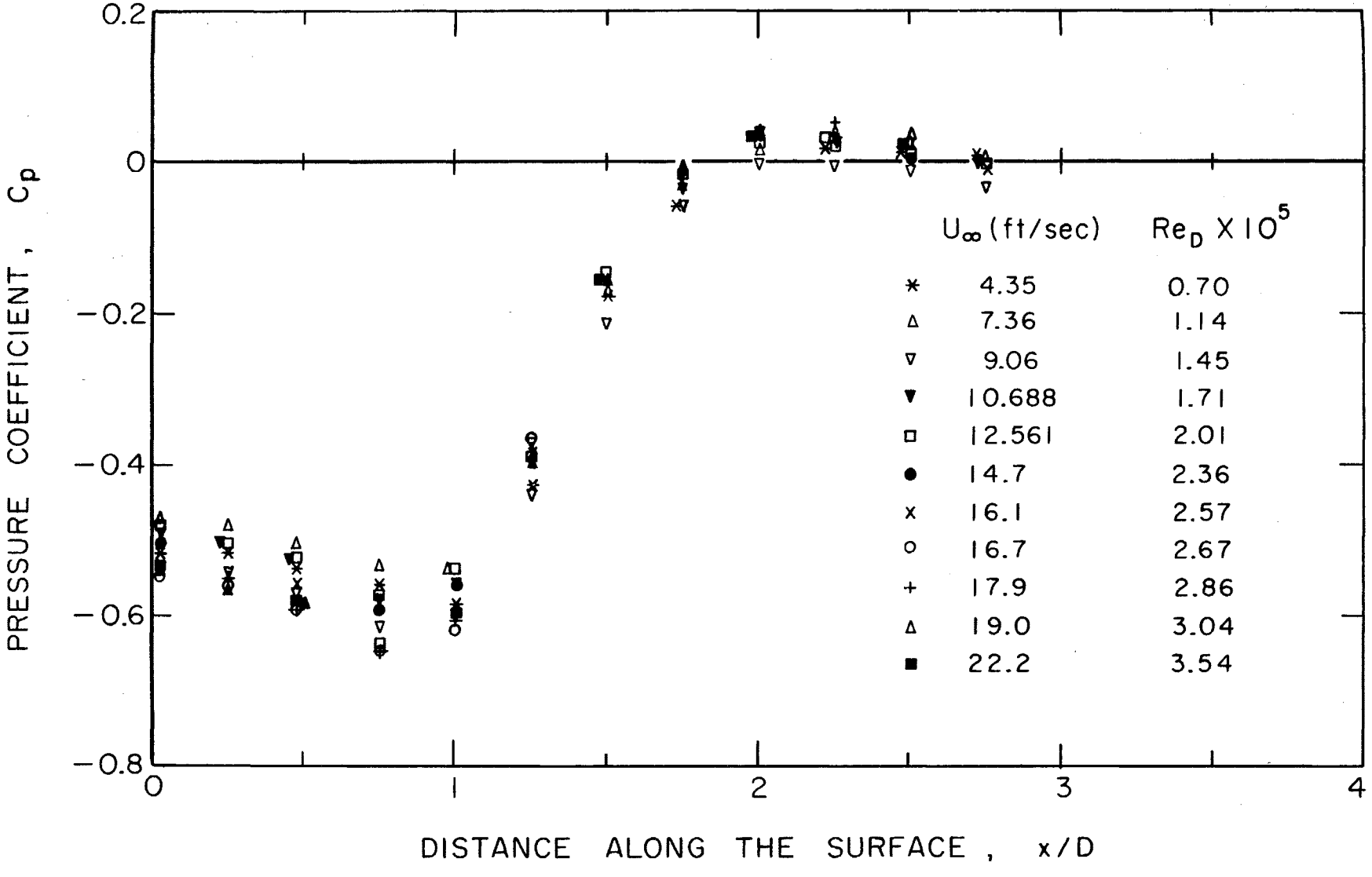

Figure 2.3. The pressure coefficient distribution on the surface of the two inch blunt body.

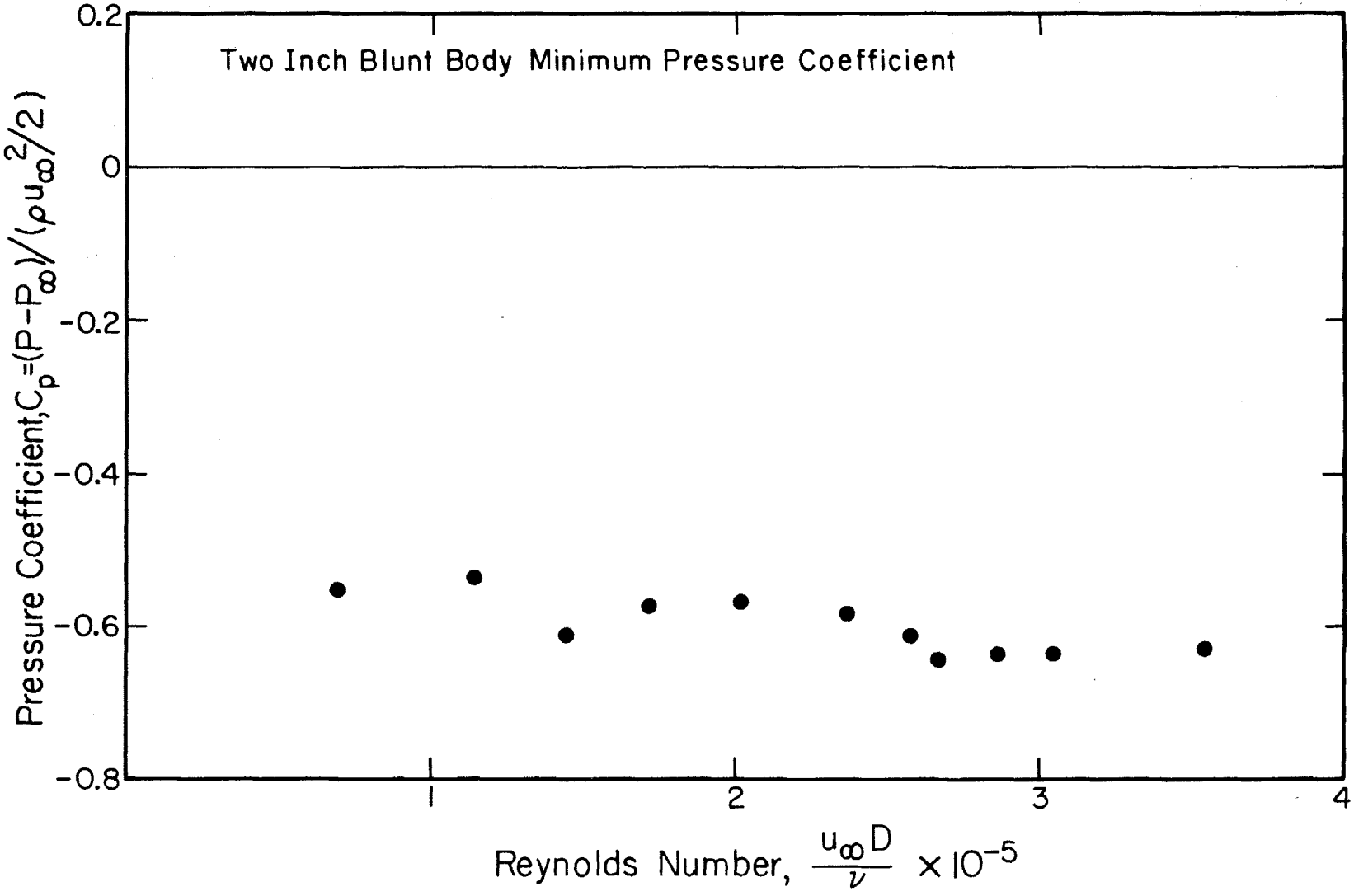

Figure 2.4 The separation zone minimum pressure coefficient on the two inch blunt body.

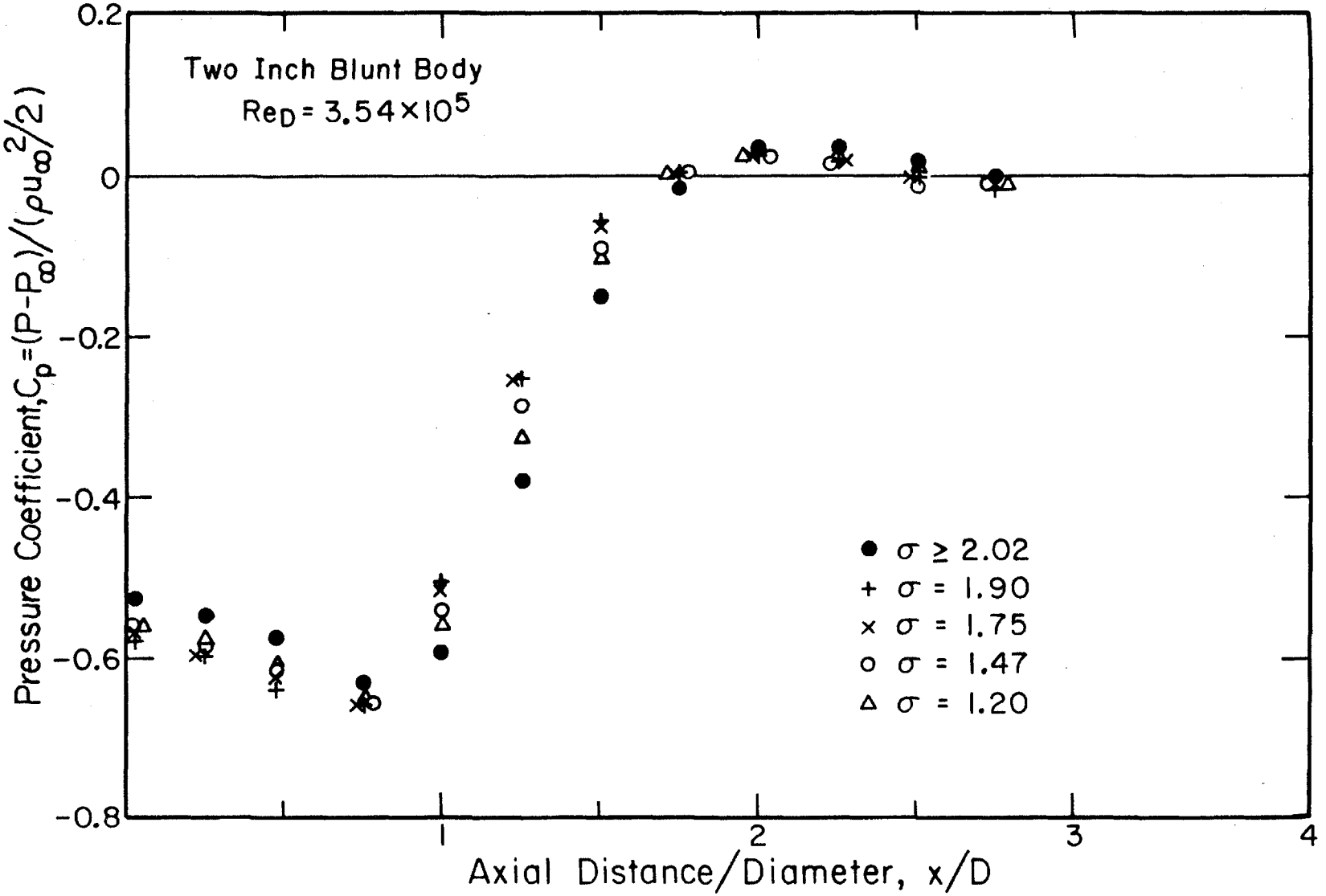

Figure 2.5. The pressure distribution on the surface of the blunt body in various cavitation indices and in the same velocity.

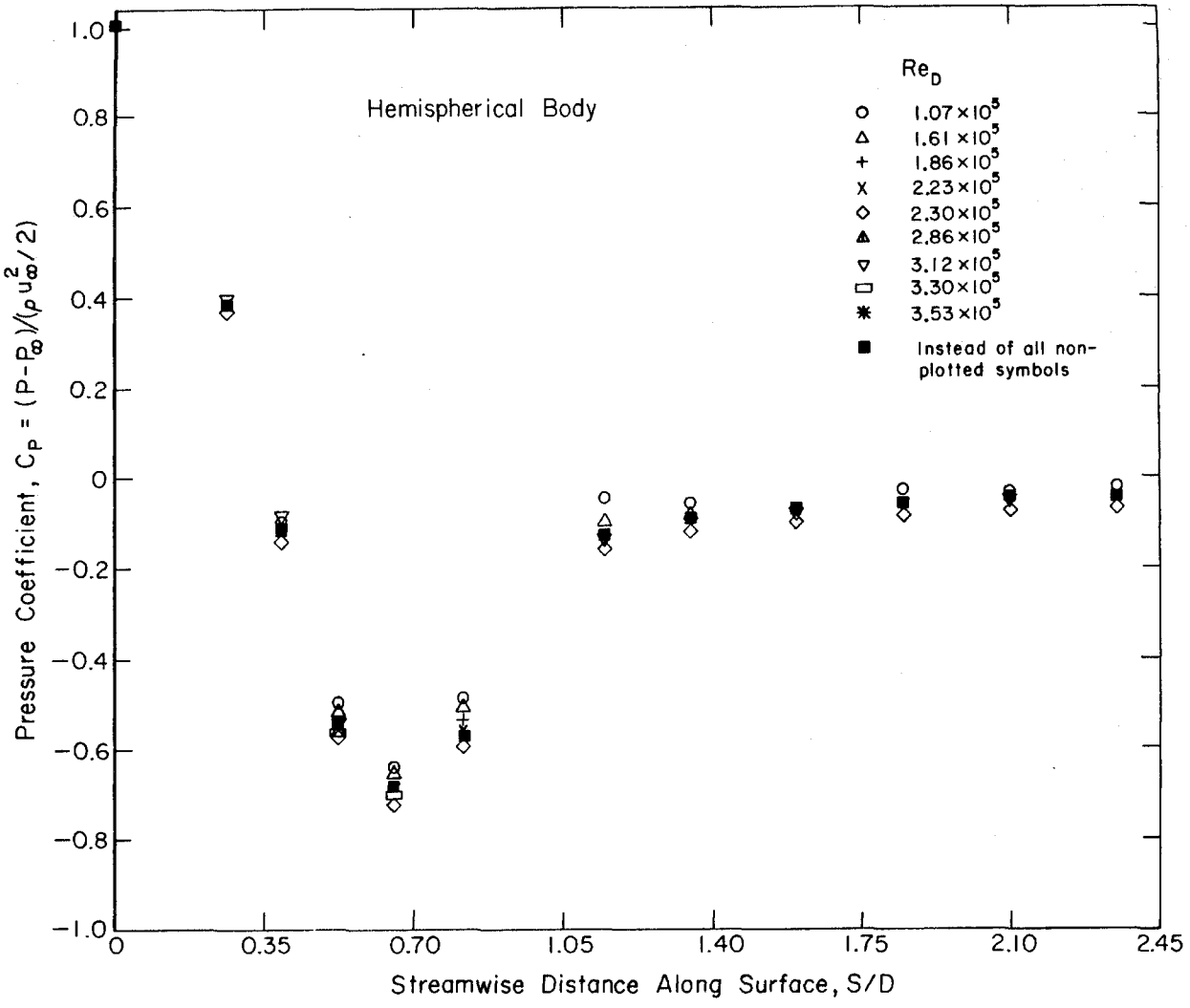

Figure 2.6. The pressure coefficient distribution on the surface of the hemispherical body.

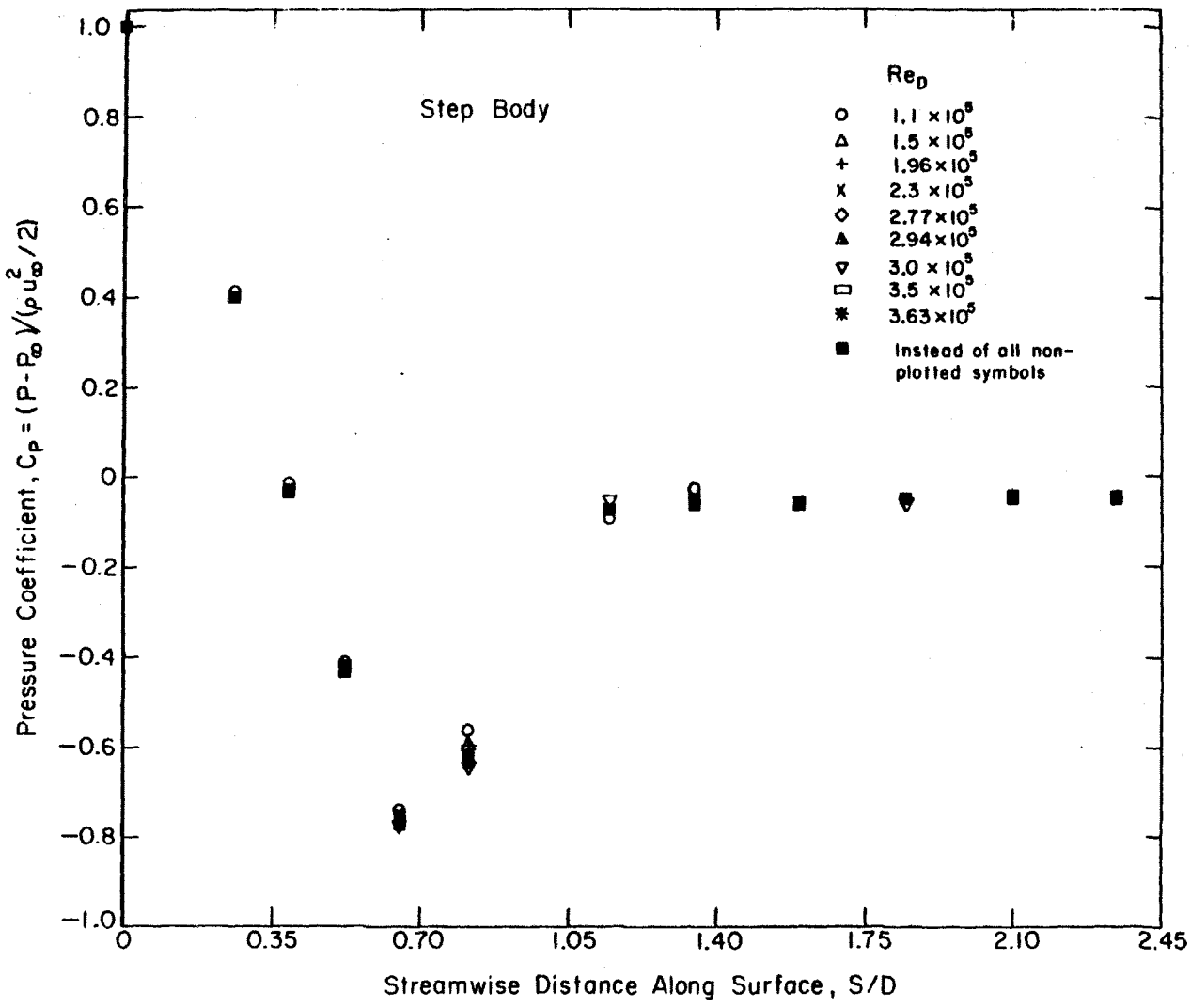

Figure 2.7. The pressure coefficient distribution on the surface of the step body.

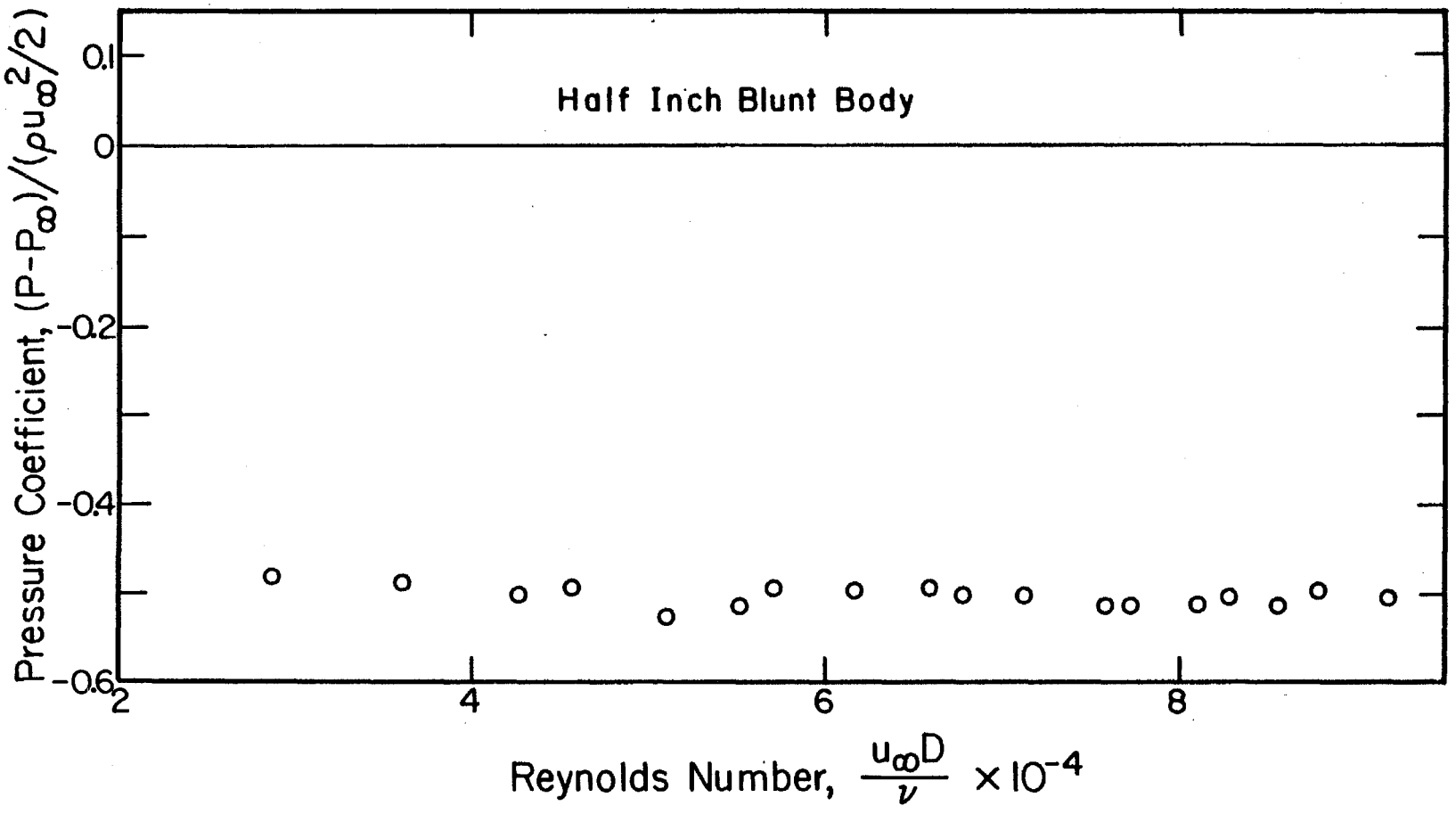

Figure 2.8. The pressure coefficient at x/D = 0.5 on the one-half inch blunt body plotted against the Reynolds number.

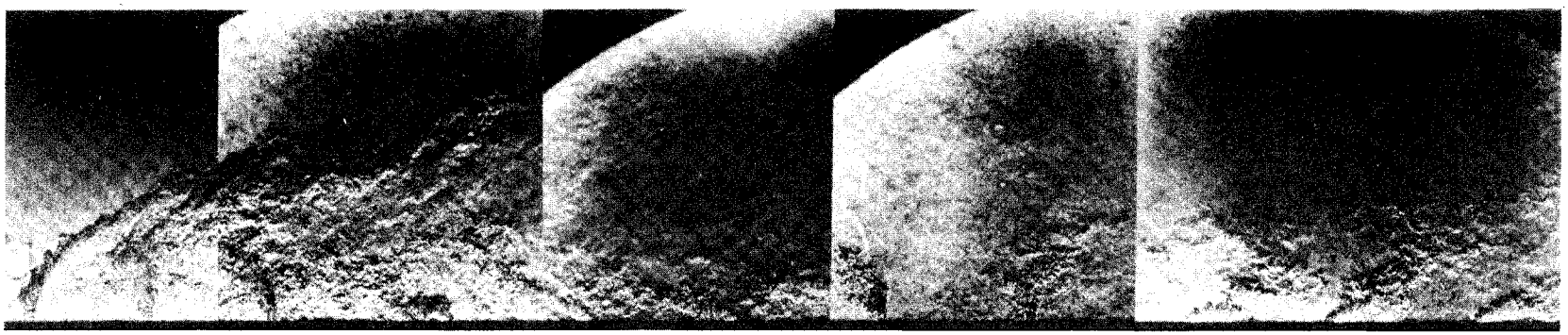

Figure 2.9. A combined series of schlieren photographs displaying the entire separation and reattachment zones on the surface of the two inches blunt body.

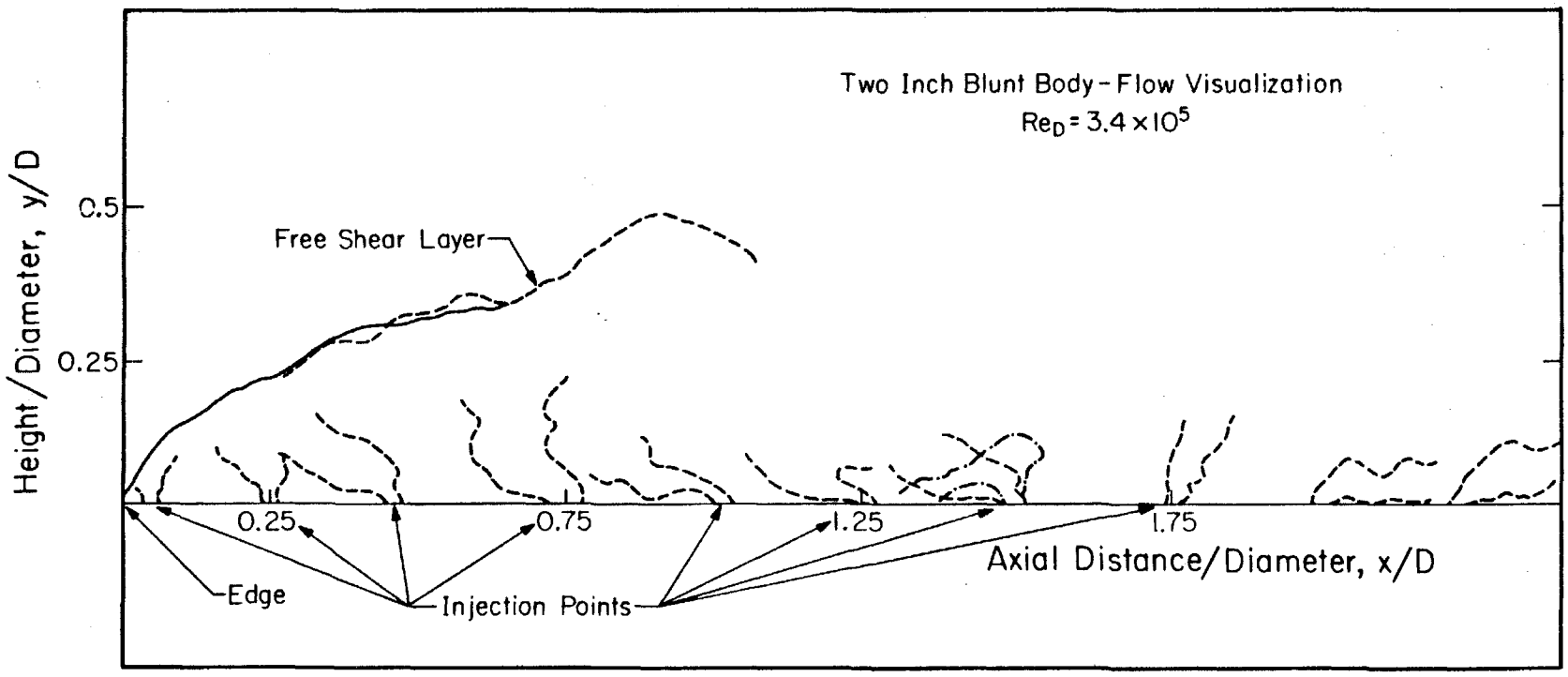

Figure 2.10. A schematic illustration of the injection points, the jets, and the separation zone on the two inch blunt body that is shown in Figure 2.9.

(a)

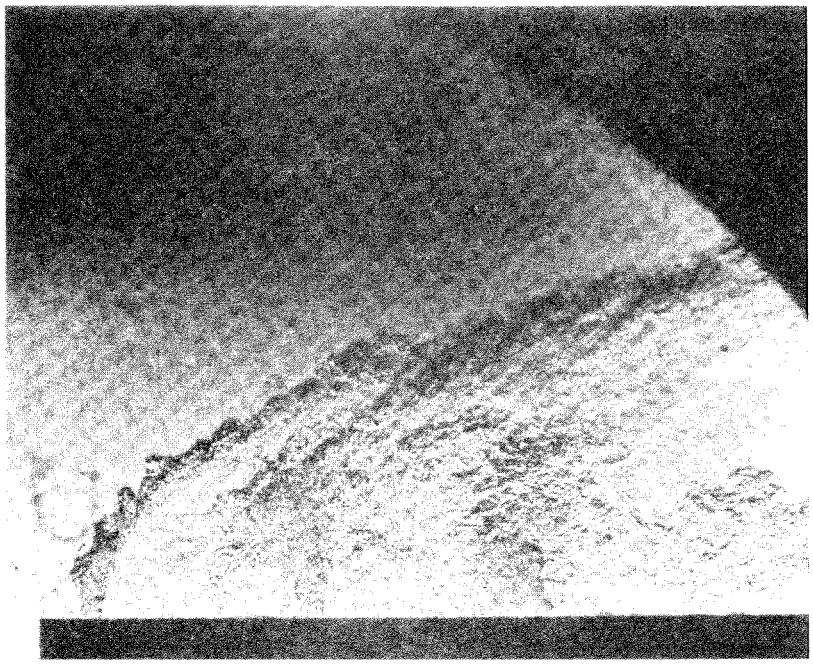

(b)

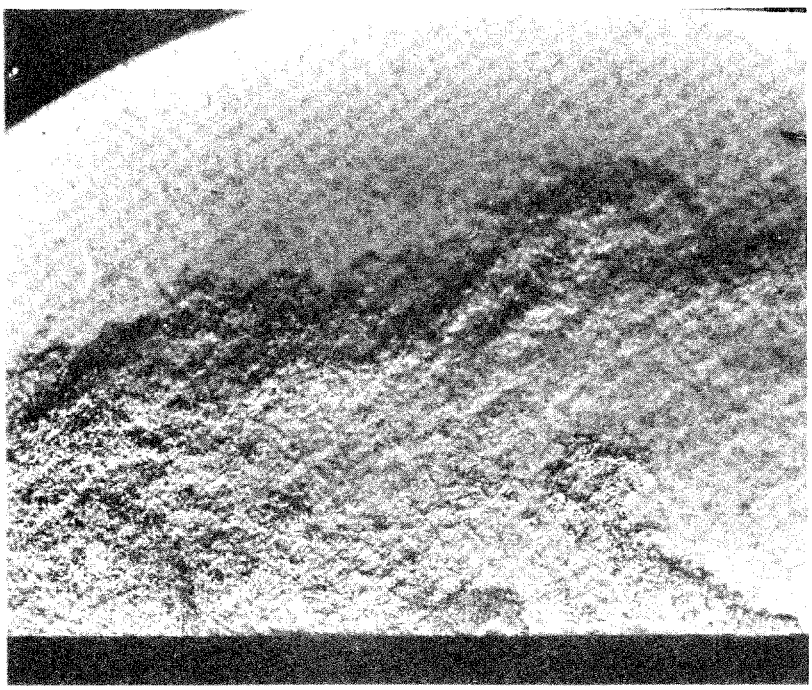

Fig. 2.11. Schlieren photographs of different sections of the flow field around the blunt body showing the injection points at: a) x/D=0.1, 0.25 and 0.45, b) x/D=0.45, 0.75 and 1.0 c) x/D=1.0, 1.25 and 1.5 d) x/D=1.5, 1.75 and 2.0 e) x/D=2.0, 2.25 and 2.5.

(c)

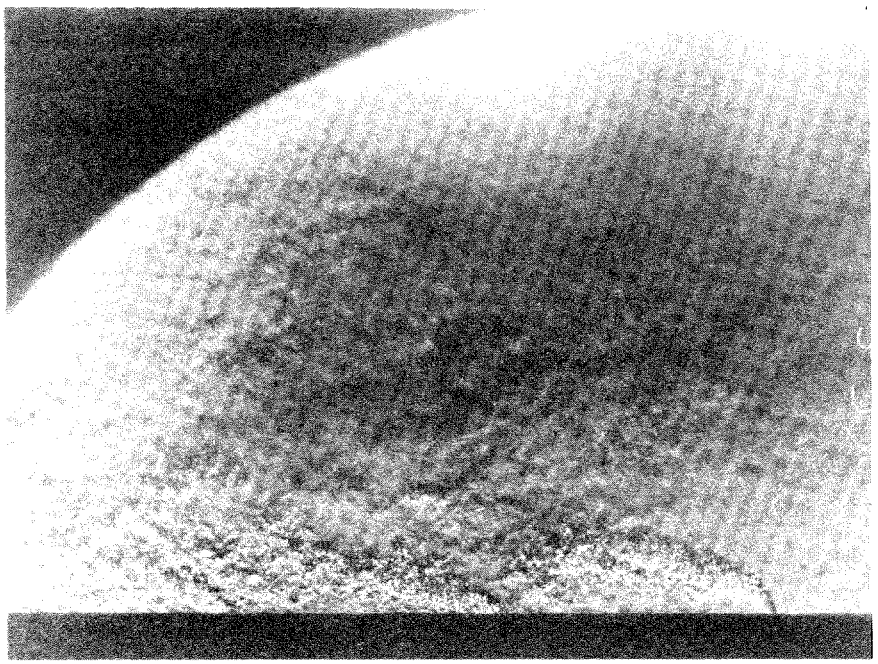

(d)

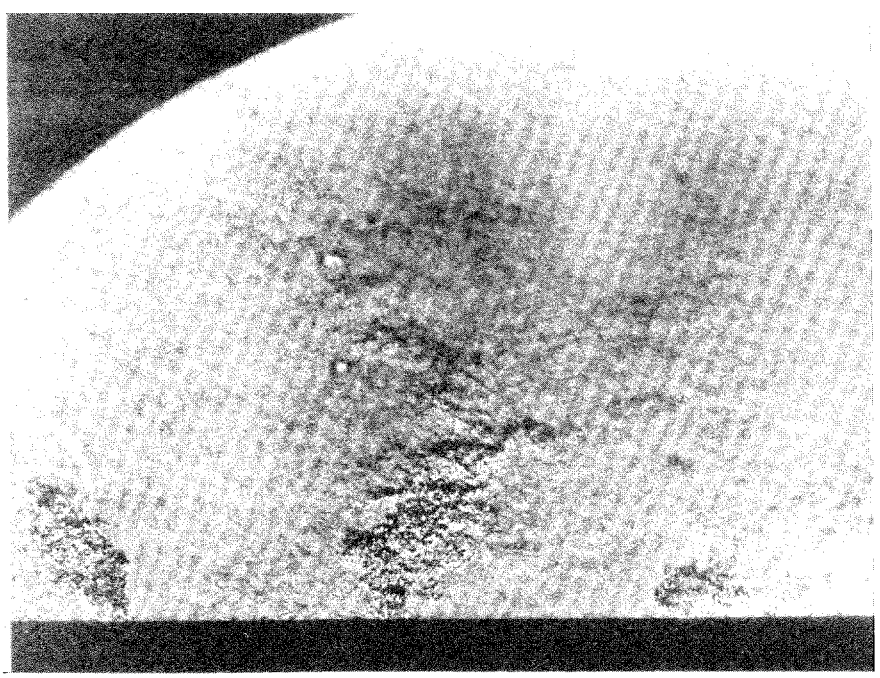

Fig. 2.11

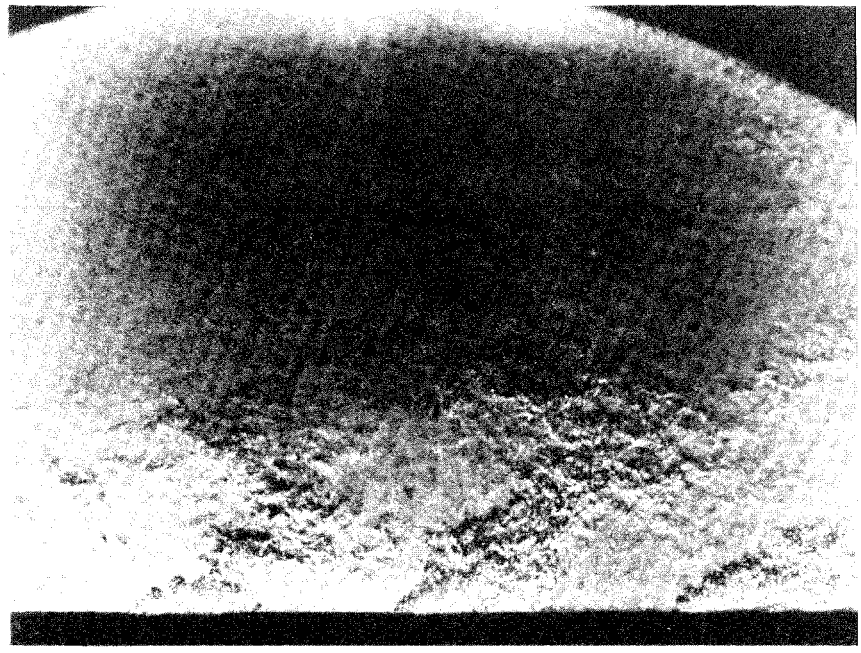

(e)

Fig. 2.11

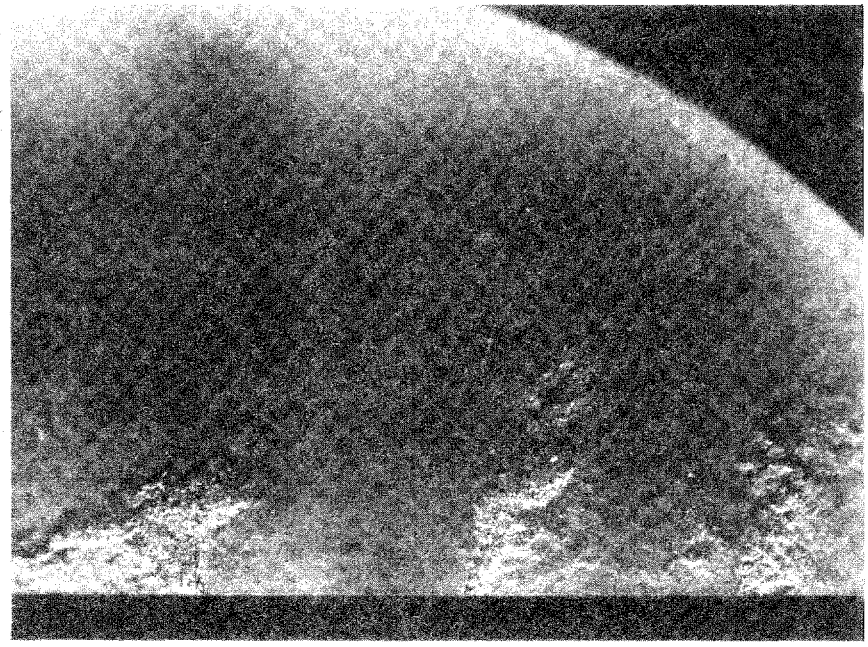

Fig. 2.12. A schlieren photograph of the injections points at x/D=1.5, 1.75 and 2.0 when the upstream jets are closed.

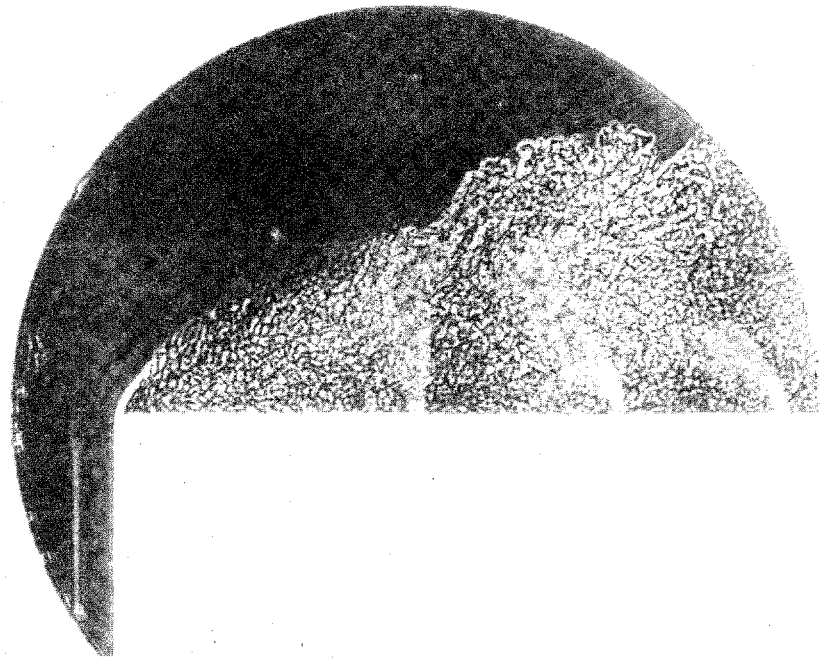

Fig. 2.13. A laser shadowgraph of the flow around the two inches blunt body. $Re_D = 1.1 \times 10^5$

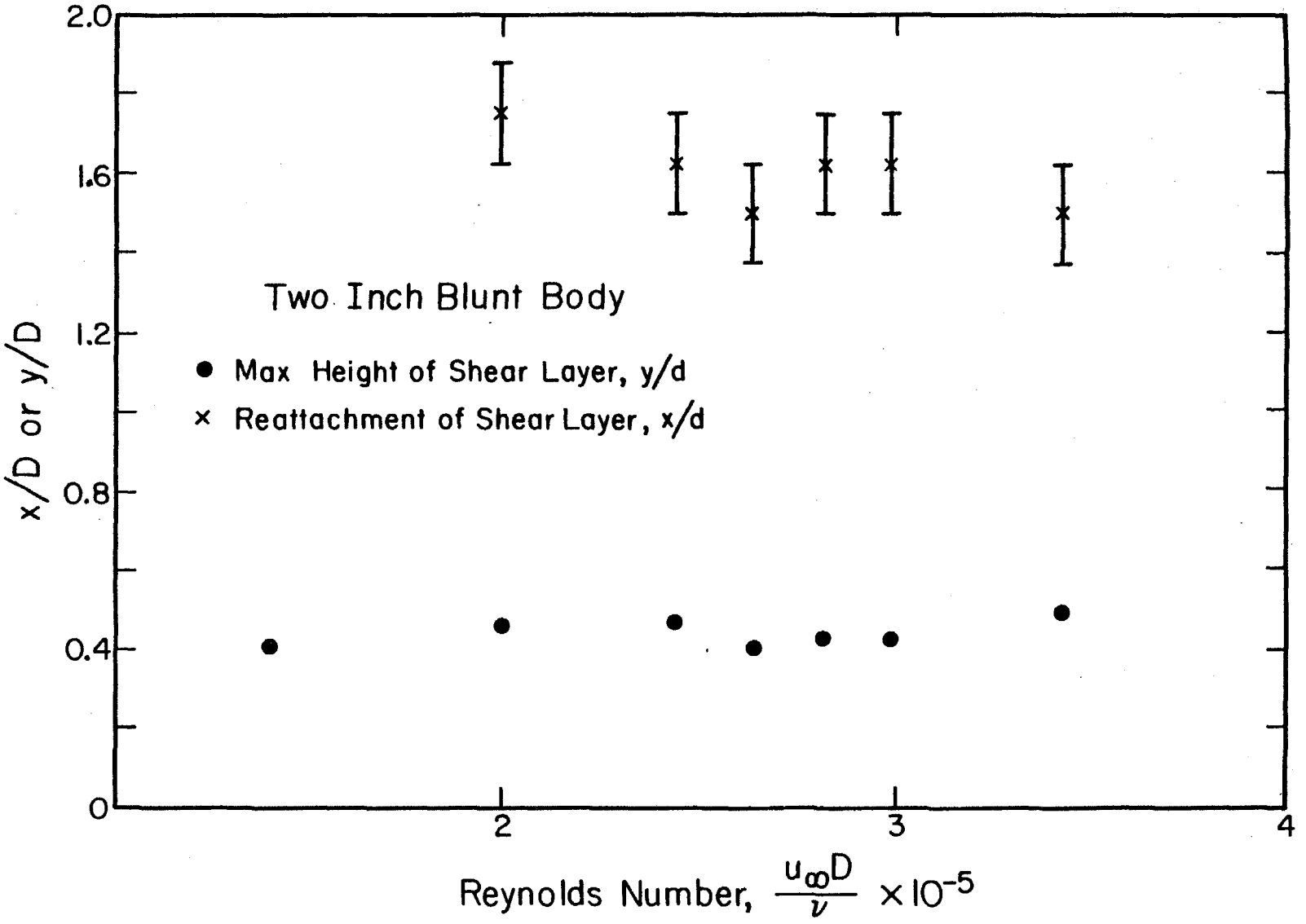

2.14 The height of the mixing layer boundary and the reattachment length on the two inch blunt body.

(a)

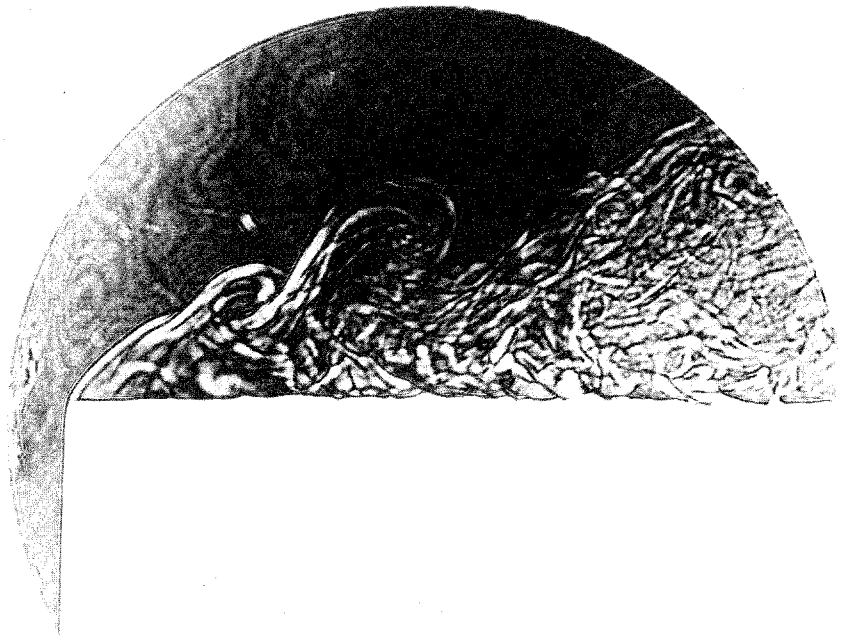

(b)

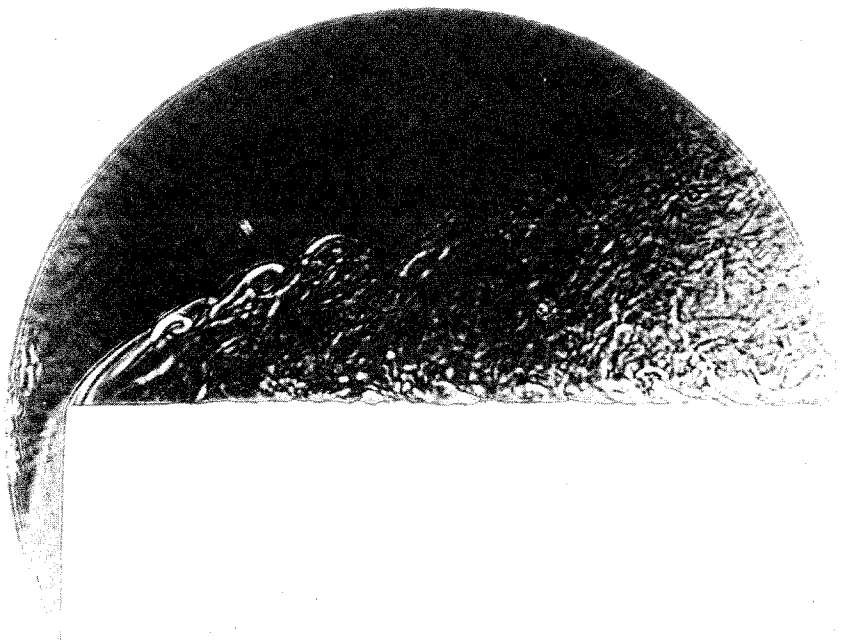

Fig. 2.15. Laser shadowgraphs of the flow around the blunt body in a very low velocity; a) $u_\infty = 0.5$ ft/sec , b) $u_\infty = 1.5$ ft/sec .

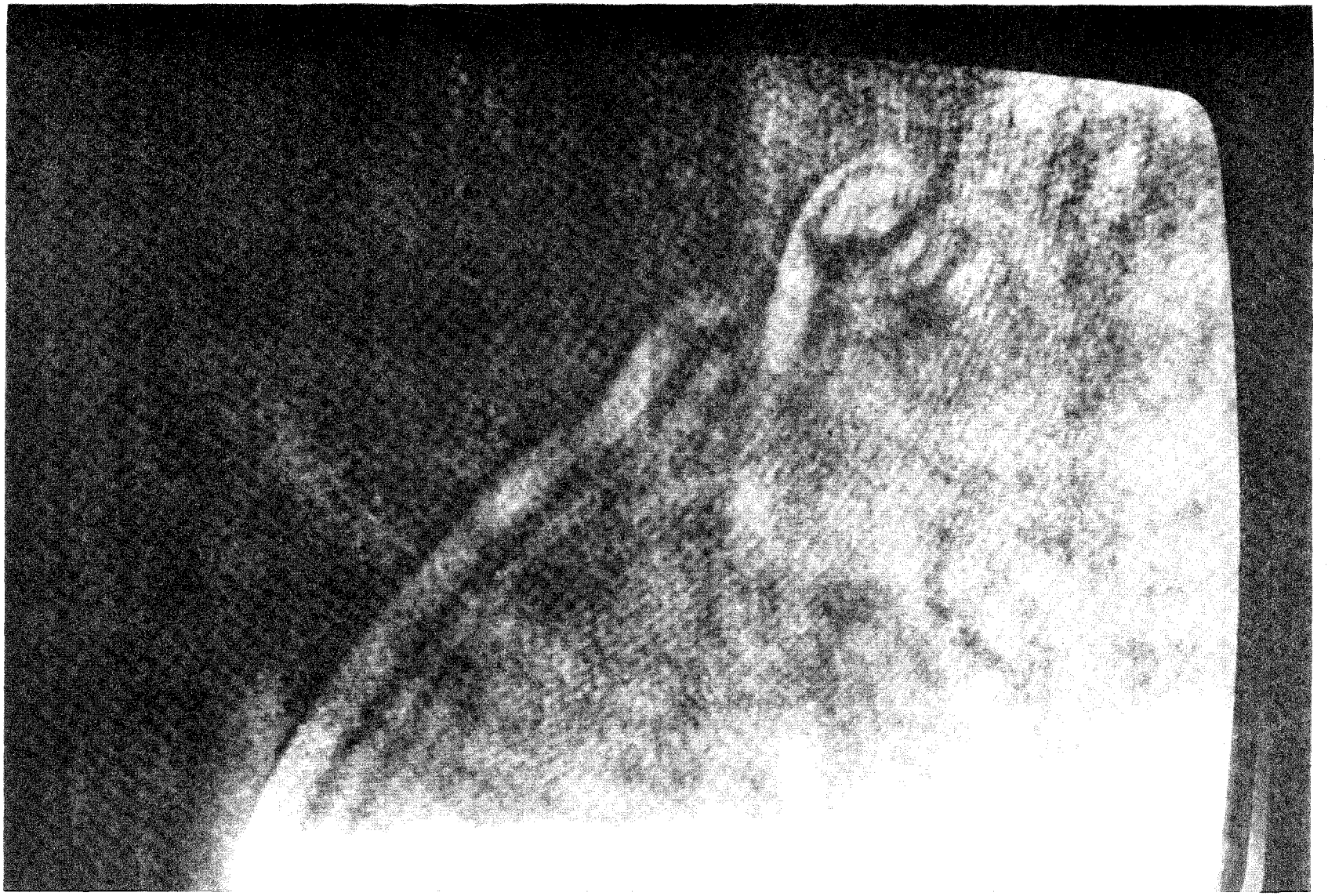

Figure 2.16 A reconstructed hologram of the separation and transition regions on a heated two inch blunt body; u_∞=4.7 ft/sec.

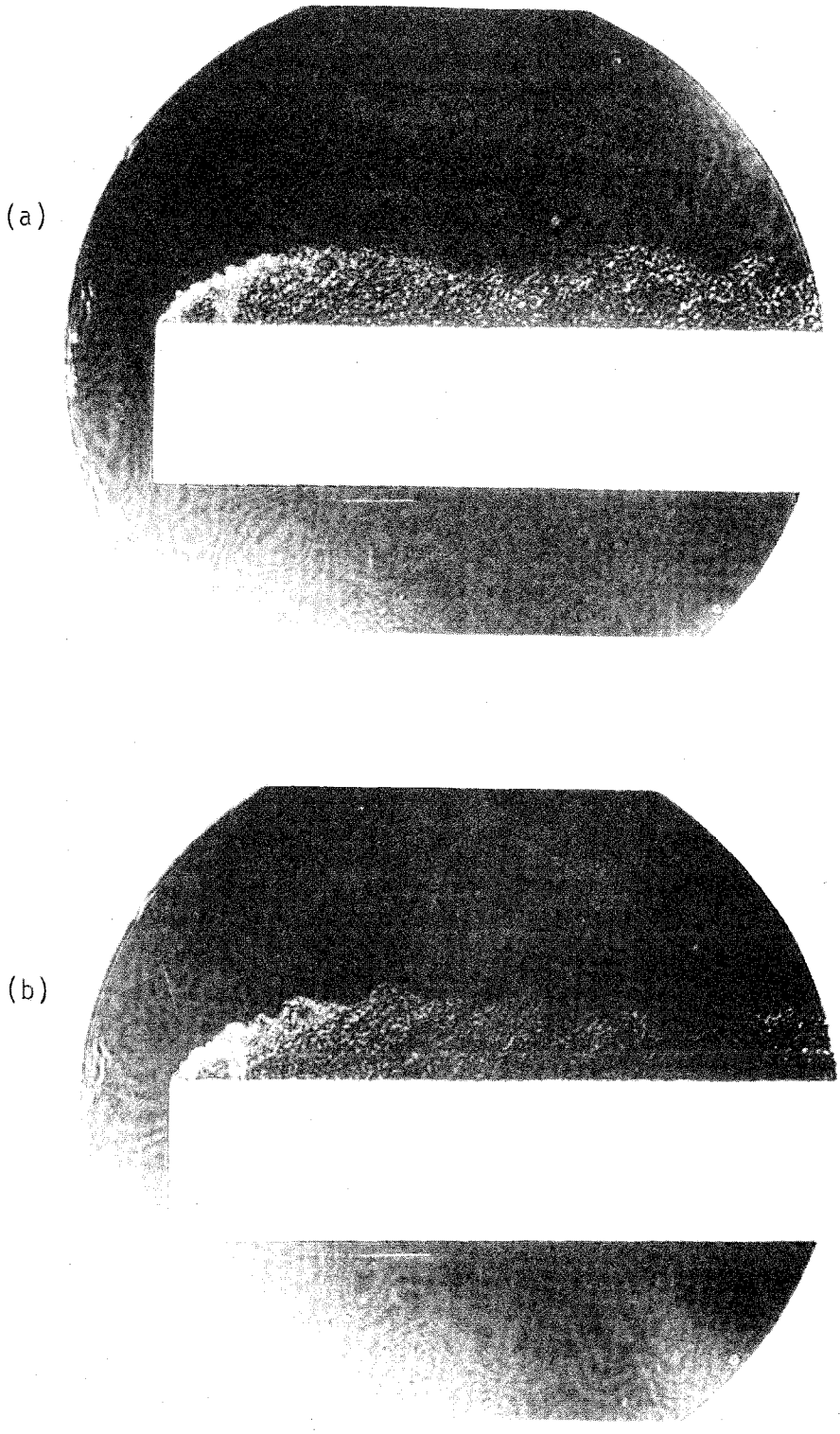

Fig. 2.17. Laser shadowgraphs of the flow around the one-half inch blunt body a) u_∞ = 18.5 ft/sec , b) u_∞ = 14.3 ft/sec.

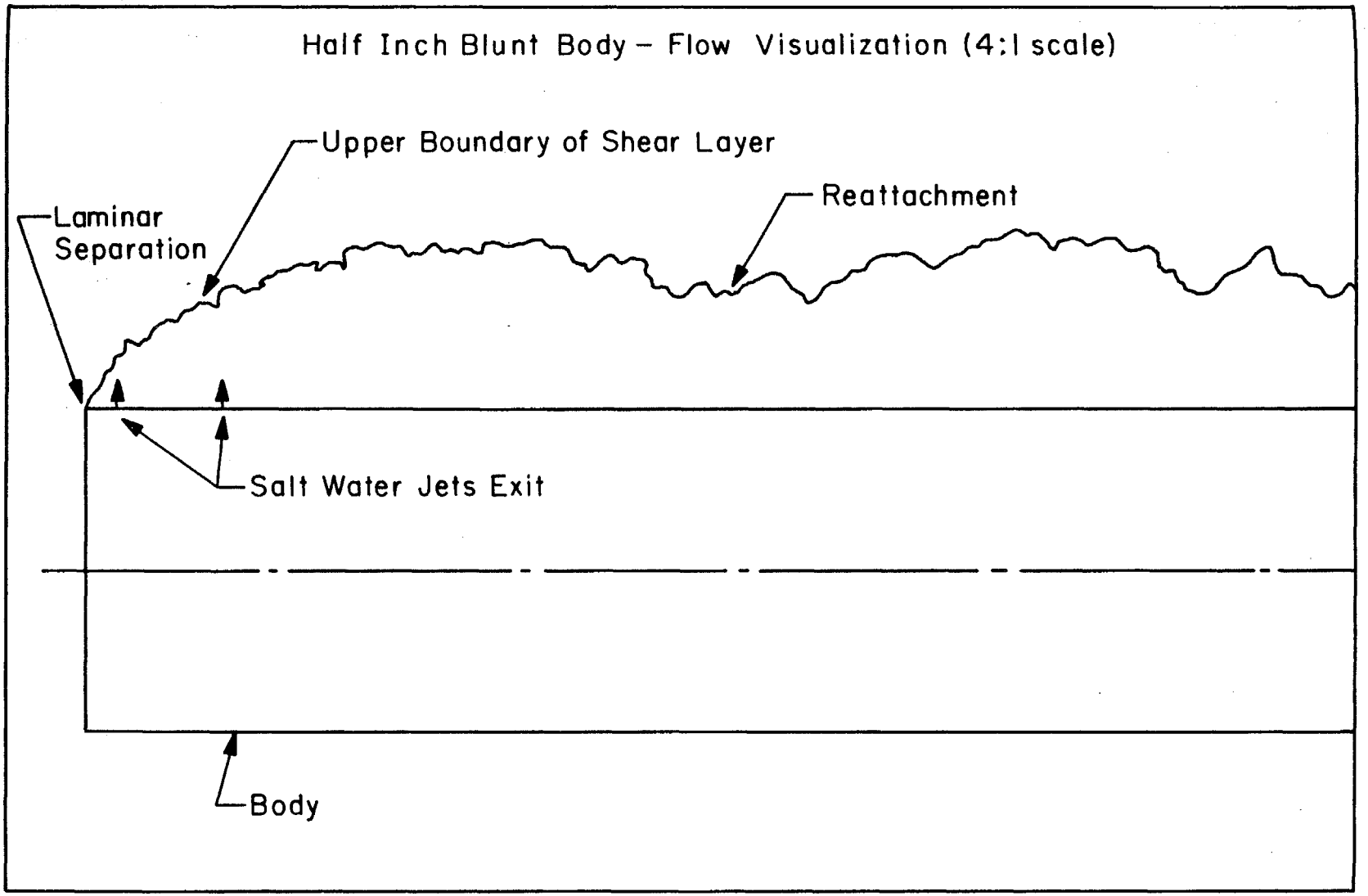

2.18. A sketch of the shadowgraph that is displayed in Figure 2.17a.

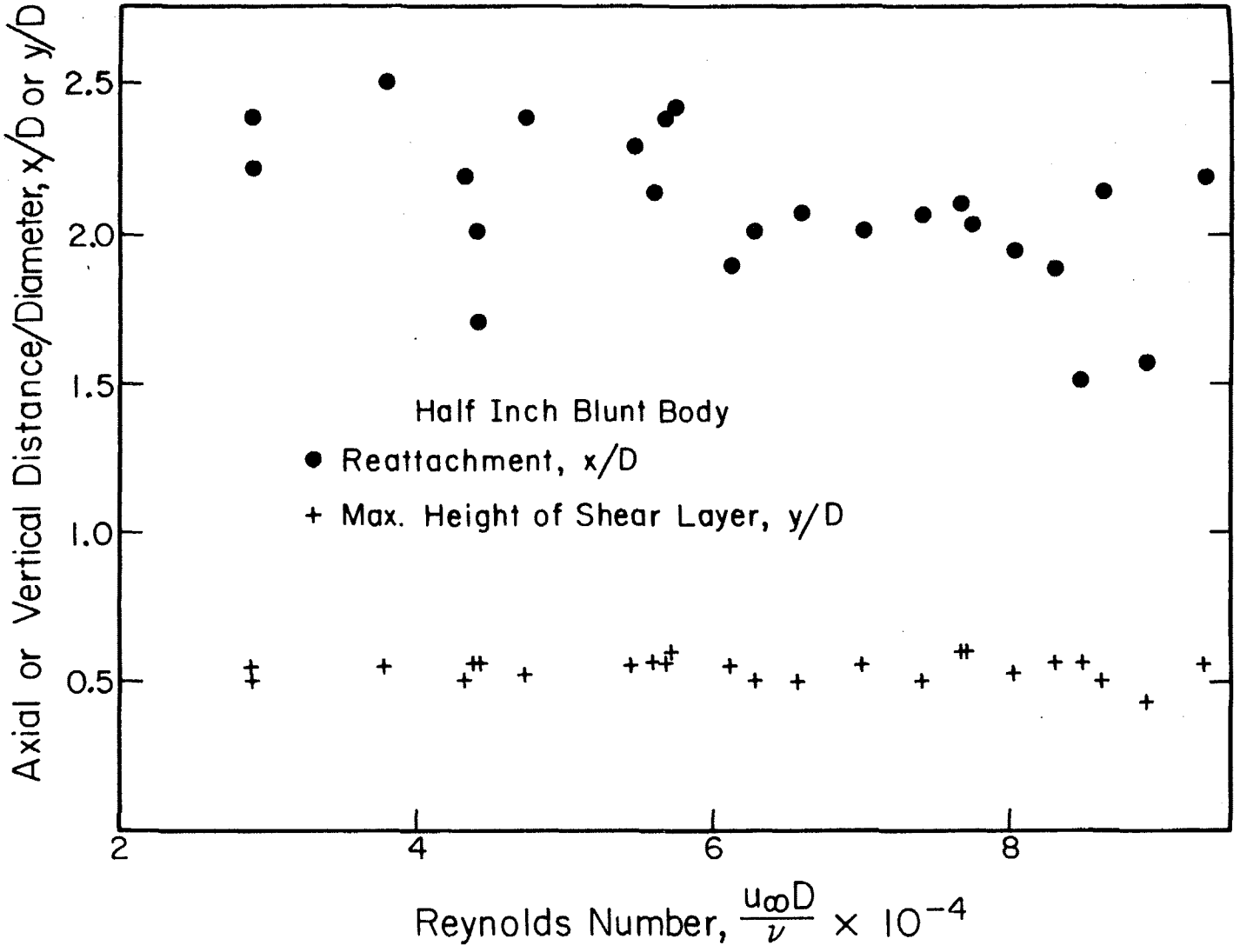

Figure 2.19. The height of the mixing layer boundary and the reattachment length on the one-half inch blunt body.

(a)

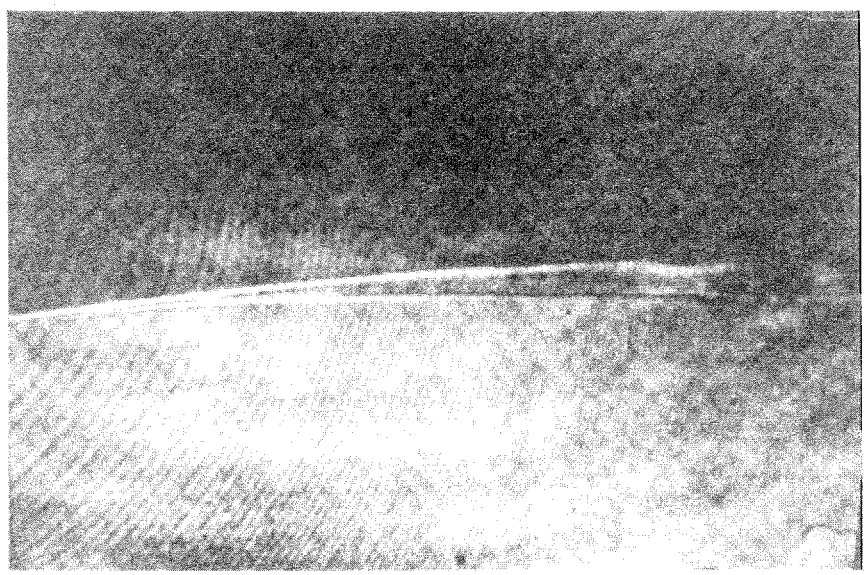

(b)

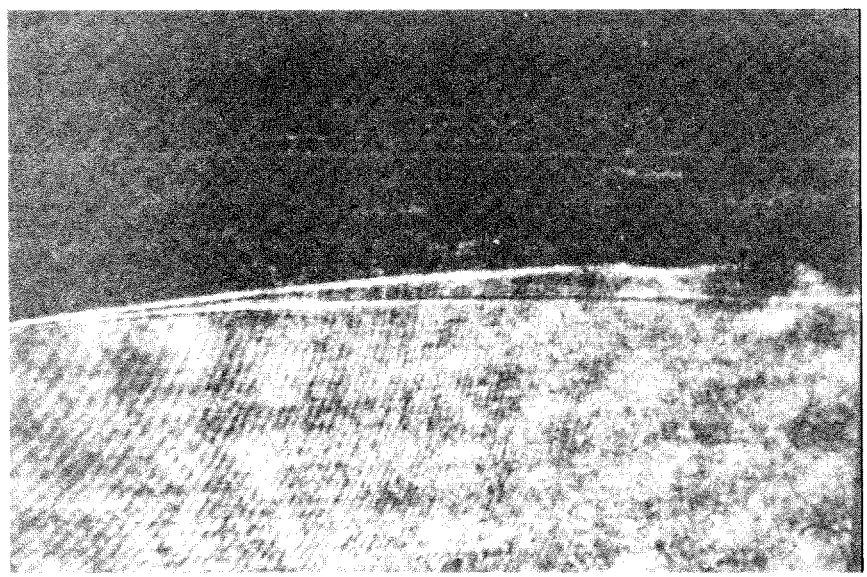

Fig. 2.20. Two images of the same hologram displaying the separation zone on the hemispherical body (u_∞ = 11.2 ft/sec, Re_D = 1.8 x 10^5); a) schlieren reconstruction, b) non filtered image.

(a)

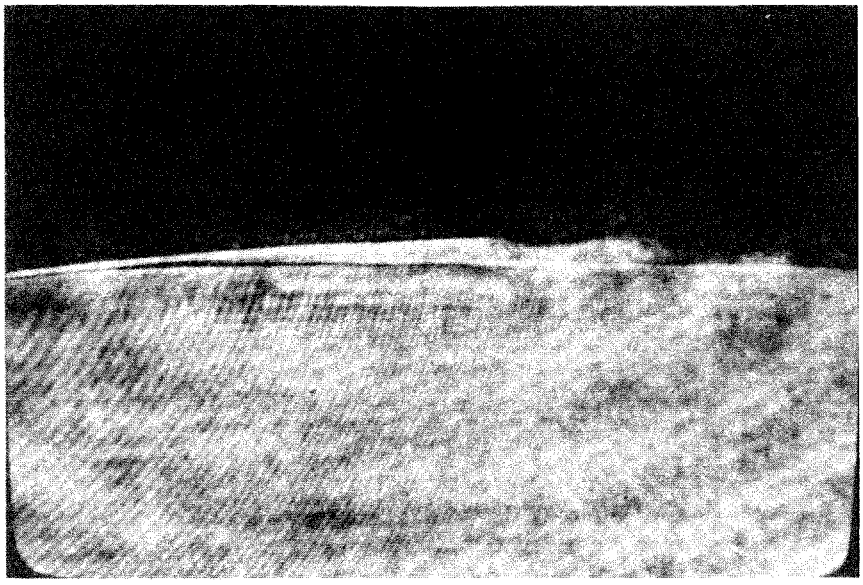

(b)

Fig. 2.21. Two images of the same hologram displaying the separation zone on the hemispherical body (u_∞ = 15.9 ft/sec , $Re_D = 2.5 \times 10^5$); a) schlieren reconstruction; b) non filtered image.

(a)

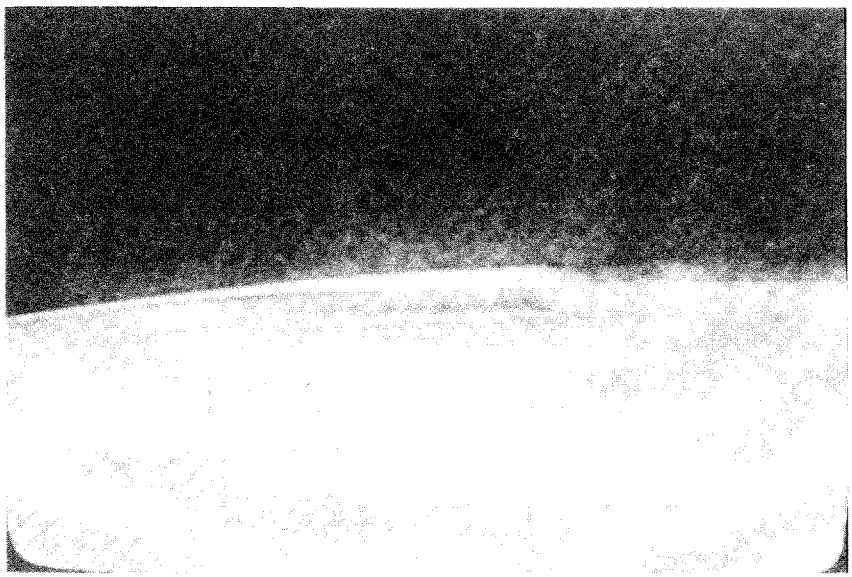

(b)

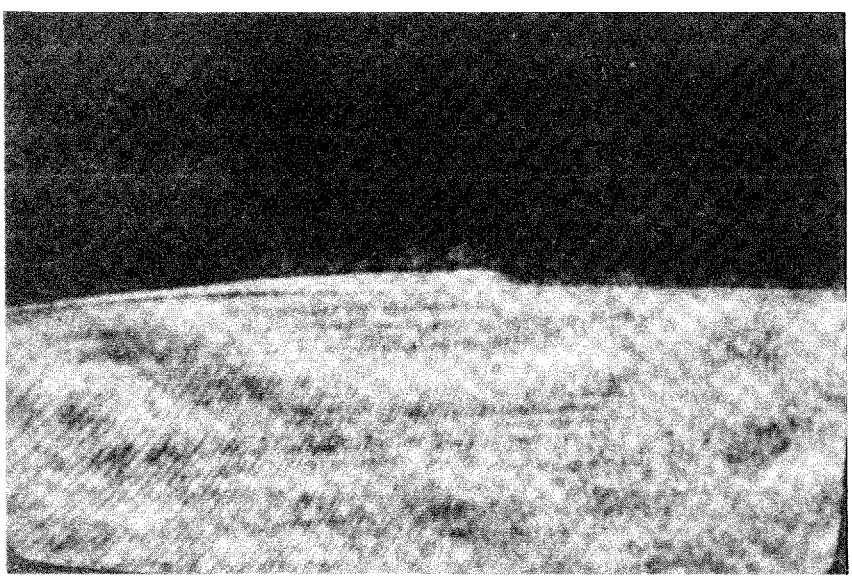

Fig. 2.22. Two images of the same hologram displaying the separation zone on the hemispherical body ($u_\infty = 23.1$ ft/sec , $Re_D = 3.7 \times 10^5$); a) schlieren reconstruction; b) non filtered image.

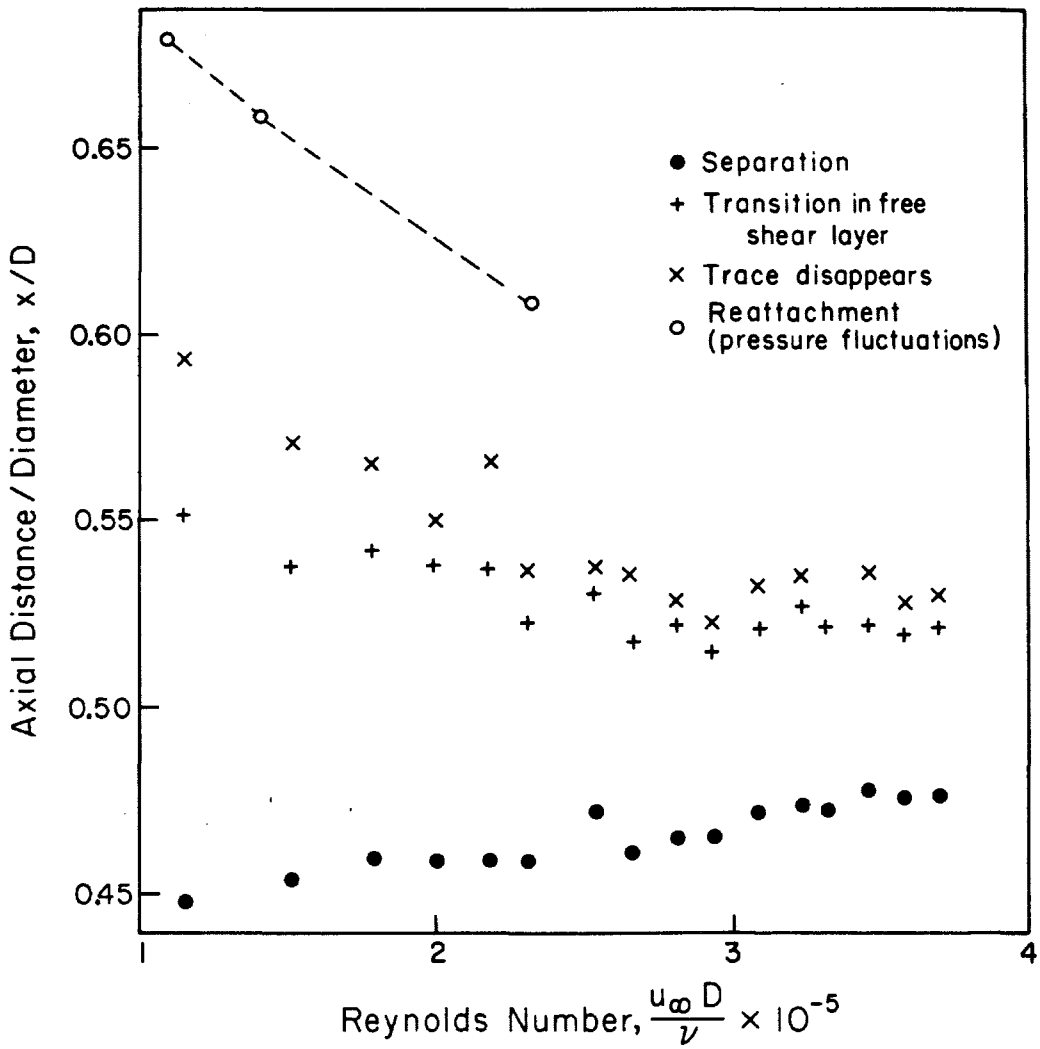

Figure 2.23. The location of separation and transition on the hemispherical body.

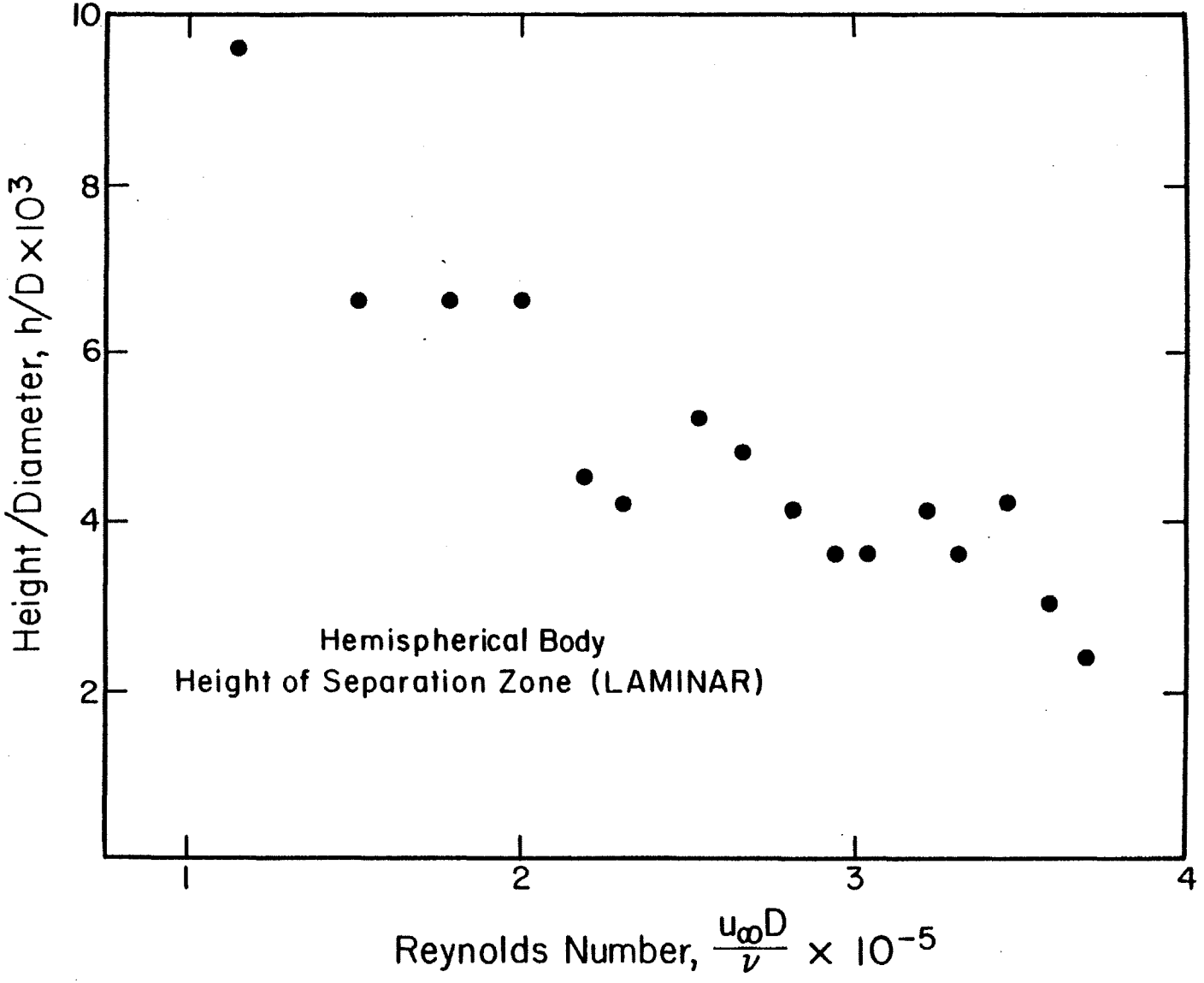

Figure 2.24. The height of the separation bubble on the surface of the hemispherical body.

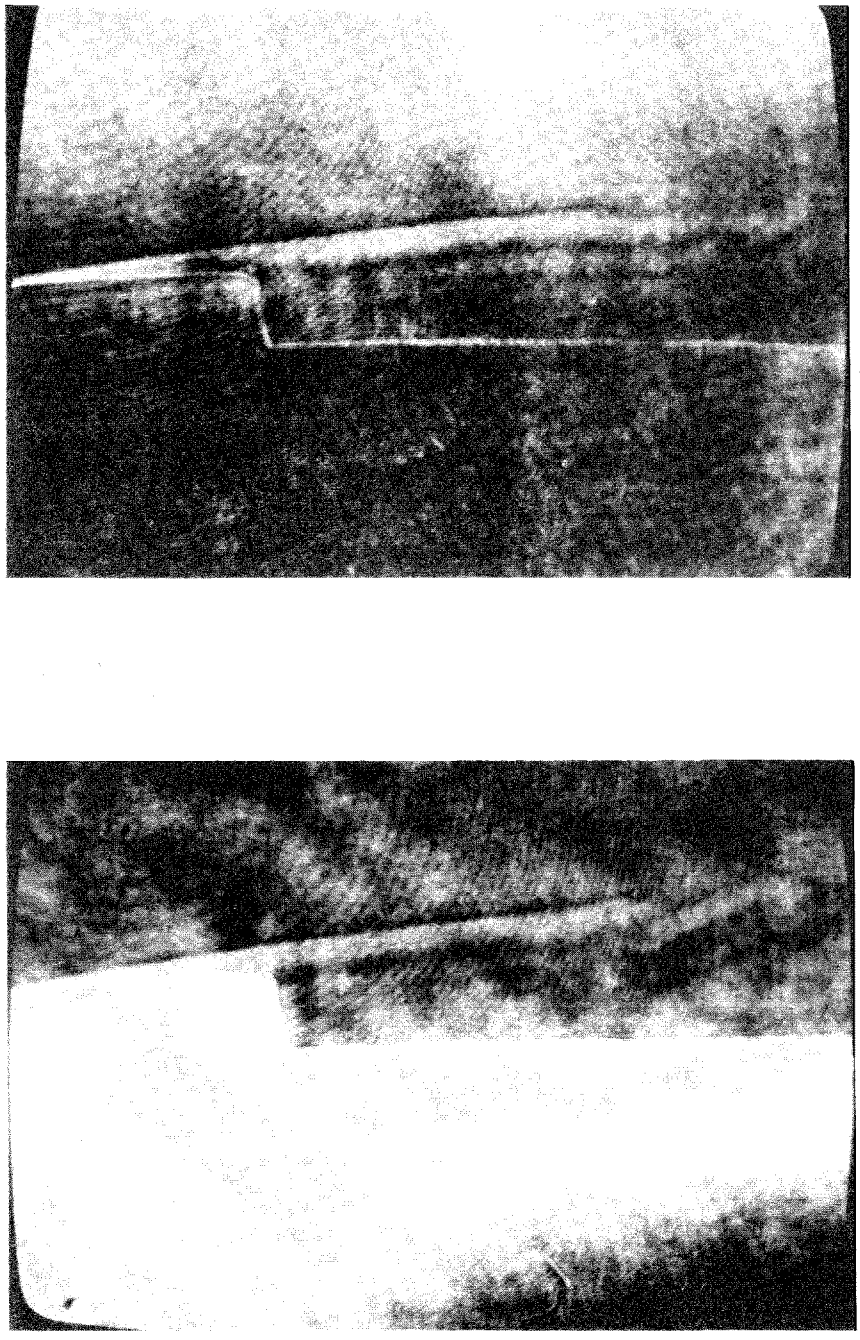

Fig. 2.25. Schlieren reconstructed holograms of the separation zone on the surface of the step body in various velocities: a) $u_\infty = 8.6$ ft/sec , $Re_D = 1.4 \times 10^5$; b) $u_\infty = 10.9$ ft/sec , $Re_D = 1.7 \times 10^5$; c) $u_\infty = 13.8$ ft/sec , $Re_D = 2.2 \times 10^5$; d) $u_\infty = 16.1$ ft/sec , $Re_D = 2.6 \times 10^5$.

(c)

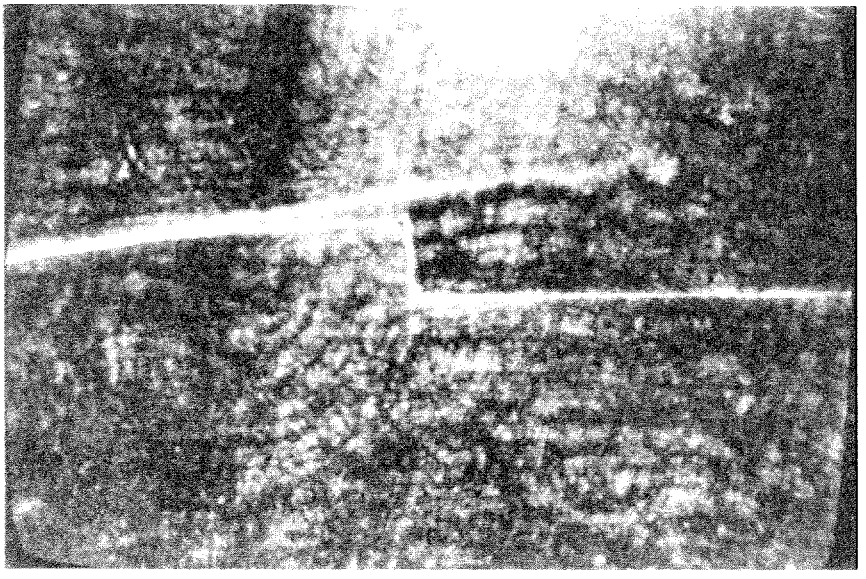

(d)

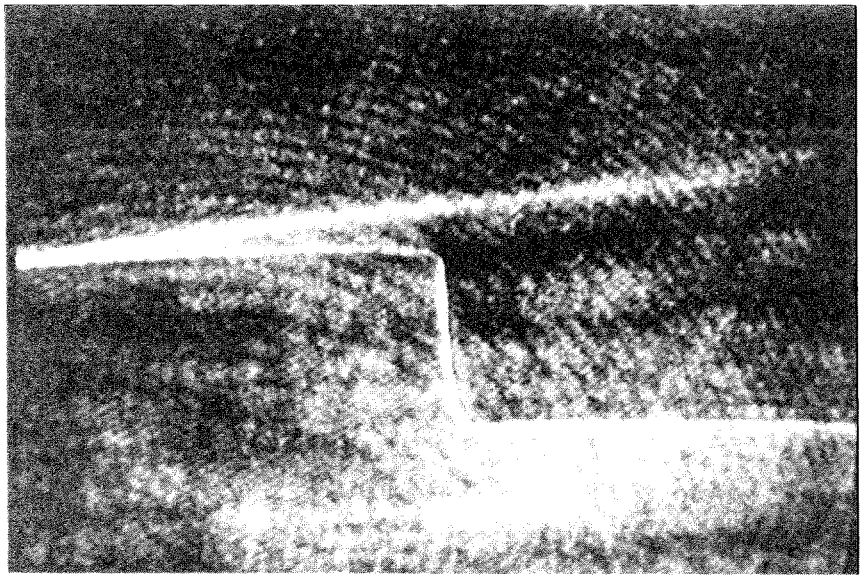

Fig. 2.25

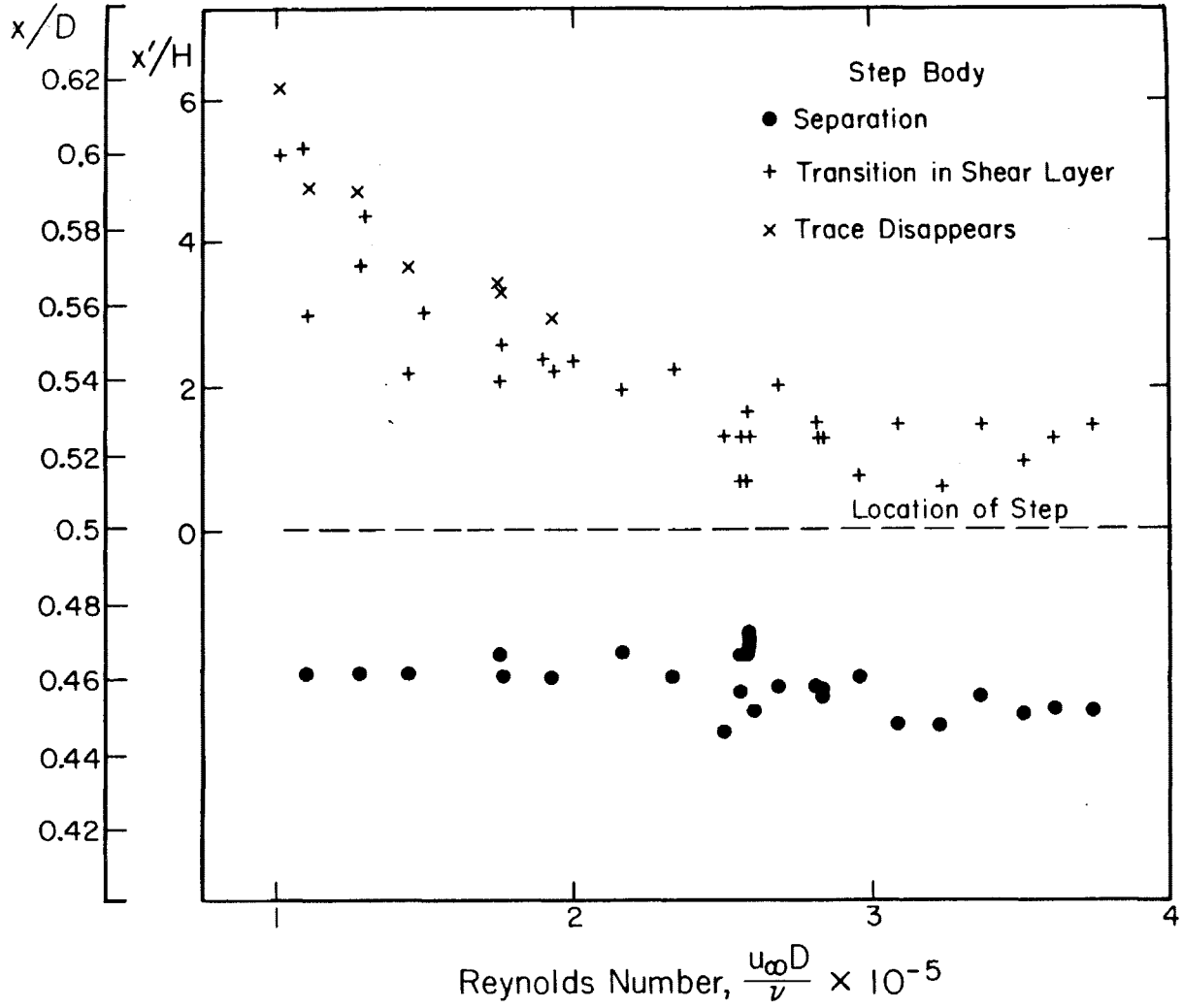

Figure 2.26. The location of separation and transition on the surface of the step body.

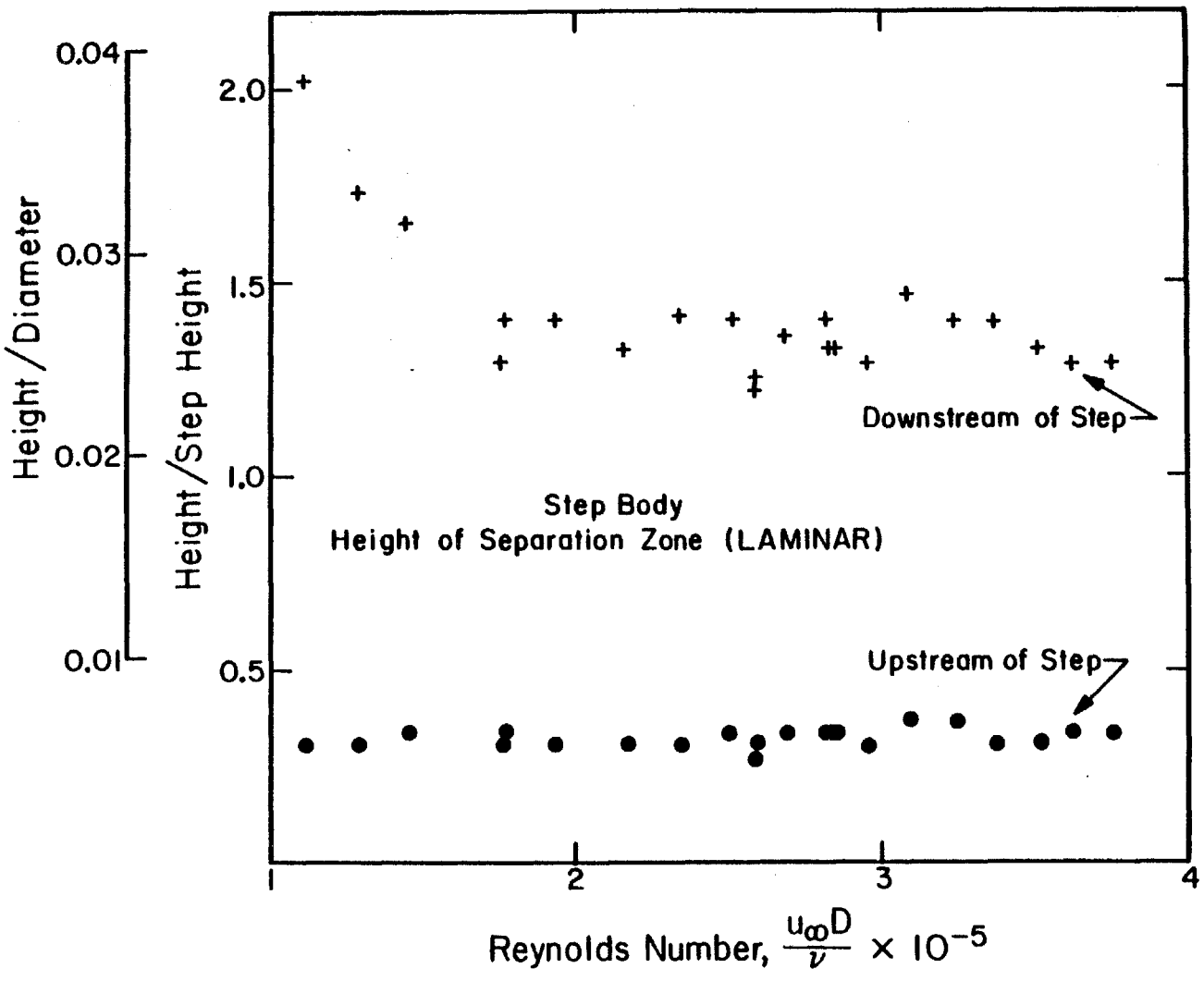

Figure 2.27. The height of the separation zone upstream and downstream of the step.

III. PRESSURE FLUCTUATION MEASUREMENTS

An important part of the pressure field in separated flows is that of the pressure fluctuations. Detailed measurements of these fluctuations were made on the surfaces of the bodies tested, and the experimental findings are presented in this chapter.

III.1 Apparatus

A piezoelectric pressure transducer (Model PCB 105A02) with a circular sensing area, 0.099 inches in diameter was used as the pressure sensor. The transducer contained a built-in amplifier and its output could be read directly on any measuring device. It was mounted on a special sliding carrier and could be positioned on any point along the body surface. The slot along which the transducer and the supporting carrier moved was covered by a 0.125-inch wide timing belt, through which only the transducer's sensing area appeared. The belt and the transducer were flush mounted. Four pulleys located inside the body tightly supported the belt which was also cemented to the transducer carrier. To reduce fluttering, the belt was seated on two flanges (each 0.015 inches wide) that were located under both sides of the slot on the body surface. A schematic description of the body and the carrier is presented in Figure 3.1. The cemented section of the belt isolated the transducer from possible vibrations of the free part of the belt.

The carrier itself was driven by a threaded rod that was connected to a flexible shaft which passed through the sting support, a lead-in

pipe and sealed connector to the external walls of the tunnel. By rotating the shaft, it was possible to position the transducer in any desired location along the slot. The shaft was connected to a mechanical counter which indicated the position of the transducer to within 0.008 inches.

With the system described it was possible to control the location of the transducer without opening the water tunnel; and it was possible to choose any desired spot for the measurements without leaving an open gap or a groove on the surface of the body.

The only part that had to be changed during the experiments was the nose. (It was planned to use the same system for all three noses. Some difficulties during the measurements forced a different set-up for the hemispherical nose which will be described later). The traversed length of the transducer was different for each test configuration. For example, the center of the transducer could reach to within 0.656 inches (x/D = 0.328) downstream of the blunt nose edge, and to within 0.05 inches downstream of step on the step nose (just behind the step). These limitations did not prevent a coverage of all the region of interest.

The output of the transducer was recorded with a seven-channel Ampex FM tape recorder during the experiments with the blunt and step noses, and with a four-channel HP-3960 instrumentation recorder during the experiments with the hemisphere (mainly due to the higher frequency range of the HP recorder). In order to reduce the relative effect of the noise generated by the recording equipment, the transducer signal was preamplified to the maximum recorder input band by a Burr-Brown 3640 amplifier. This

amplification, together with the tape recorder amplification, was calibrated by recording a sine wave at various frequencies from a signal generator. The frequency response of the Ampex recorder was flat up to 3 kHz and 5 kHz for the HP recorder which proved satisfactory for the present measurements.

The pressure response of the transducer was calibrated by mounting it together with a statically calibrated accelerometer on a water filled small horizontal tank, one foot long. The tank was bolted to a shake-table whose acceleration (frequency and amplitude) could be controlled. By monitoring the accelerometer and the transducer output and using the following relation between the pressure and acceleration

$$P - P_{atm} = \rho \ell' a$$

it was possible to calibrate the transducer up to 50 Hz. The output was found to be equal to that provided by the manufacturer's calibration (done in a pressure tank with a quick opening valve); namely, 26.2 mv/psi. This output did not show any dependence on the frequencies of the calibration range, namely, from one to fifty Hz.

By tapping on the transducer surface while it was submerged in water, it was verified that no resonance existed below 100 kHz. When the calibration tank was filled with air the response of the transducer was about one percent of its output when the tank was filled with water, proving that the transducer response to acceleration was negligible for the present experiments. Several calibrations done during the course of the experiments did not show any change in the output.

III.2 Results

III.2.1 Blunt Nose

The rms values of the fluctuating pressure were measured by a Hewlett Packard digital voltmeter, and the results represent an average of at least ten seconds sample time.

Figures 3.2 and 3.3 show the rms pressure fluctuations on the surface of the blunt nose. In Figure 3.2 the values of the fluctuating pressure coefficient, c_p', are plotted against the body Reynolds number, Re_D, and each line represents a different location along the surface. Figure 3.3 displays the rms values plotted against axial location on the surface by keeping the velocity constant and varying the transducer's position. The plot also shows the averaged results of Figure 3.2. The graphs show that the scaled rms values of pressure fluctuations strongly depend on the location of the measurements, but here they are independent of the Reynolds number. The rms values vary from 5.5 to 7 percent when $x/D = 0.328$ and to 17 percent when $x/D = 1.078$. Farther downstream the rms values drop to 14 percent at $x/D = 2.2$ (the furthest point of measurements).

A curious result is that maximum rms values are observed upstream of the reattachment zone determined earlier by the average pressure measurements and flow visualization. Furthermore, these flow visualization results (see Figure 2.11) show that there is a relative fast reverse flow at $x/D = 1.078$, and the average pressure measurements show that this point is upstream of the pressure recovery region that indicates the reattachment zone. The same behavior was observed by Mohsen (1967) in experiments on an upstream-facing step.

The recorded transducer output was analyzed on a Spectral Dynamics Corporation model SD360 digital signal processor. The averages of signals of predetermined time periods were analyzed by the processor and the resulting Fourier transform, power spectrum, autocorrelation, probability density, and probability distributions were plotted. From the probability distribution function, four values of "peak" pressure fluctuations were accurately determined. These were the points where the probability distribution exceeded 0.1, 2.5, 97.5, and 99.9 percent. The first two points represented negative pressure "peaks" whose probability of occurrence were less than 0.1 and 2.5 percent and the last two points represented positive peaks whose probability of occurrence were less than 2.5 and 0.1 percent, respectively.

An example of the probability density and distribution histograms obtained for the blunt nose is shown in Figure 3.4. Before further display of these results, a few comments should be made. A significant part of the fluctuating pressure was at a very low frequency (even less than 1 Hz). Since most of the averaging periods used were 12 seconds, frequencies below 0.1 Hz would bias the results. Two examples of this effect can be seen in Figures 3.5 and 3.6 as follows: In Figure 3.5 the signal was filtered with a high pass filter, first with a cut-off frequency of 0.02 Hz and then with a cut-off frequency of 1 Hz. One can observe a perceptible change in the probability density; the signal filtered with the lower cut-off frequency is biased toward the negative side. In the second example in Figure 3.6, the sampling time was increased to 102 seconds, and by again using the 0.02 Hz and 1 Hz high pass filters, the differences between the probability densities disappeared.

For this reason part of the data was subsequently analyzed with an averaging time of 102 seconds, and the differences between the findings will be discussed later.

The signal was also observed on the screen of a storage scope. The peak values observed on the scope were compared to the 0.1 and 99.9 percent probability distribution points and the differences were negligible. The comparison was made for all the measurements. In most of the cases the scope peaks were slightly higher, often due to one or two peaks, thus having only a small effect on the total sample population. If the number of peaks exceeded this value, the outcome was quite noticeable on the probability density.

The signal analyzer was calibrated using known sine, square, and triangular waves of various frequencies and amplitudes. No dependence was found on either the frequency or the amplitude of the input.

We now return to the results obtained for the blunt nose. They are displayed in Figures 3.7 to 3.18. In Figures 3.7 to 3.14 the transducer was positioned in the same location and the velocity was changed. In Figures 3.15 to 3.18 the velocity was kept constant and the transducer was moved into various positions along the body surface.

Two interesting observations can be made from the results: The first is the difference between the positive peaks and the negative peaks, and the second is the difference between the peaks with 0.1 and those with 2.5 percent probability. Almost over all the range of measurements the ratio between the 0.1 percent values and the 2.5 percent values was a little less than 2:1, and it applied both to positive and negative peaks. These

fluctuating pressures and their likelihood (probability) of occurrence have an important bearing on the initiation of cavitation. The chance that the existence of cavitation nuclei and the low pressure peaks will occur at the same time will be discussed separately.

Another consistent feature of the peak values is the relation between the positive and negative peaks of the fluctuating pressure. At x/D = 0.328, 0.578, 0.828, 1.078, 1.828, and 2.078 (corresponding to Figures 3.7, 3.8, 3.9, 3.10, 3.13, and 3.14, respectively) the negative peaks are always larger than the positive ones. These observations apply both to the results of 12 seconds and 102 seconds averaging times. This behavior is reversed at x/D = 1.578 as shown in Figure 3.12. The positive peaks become larger than the negative ones, and this trend can be observed again in both averaging times. A contradictory behavior can be observed in Figure 3.11 (x/D = 1.328). While the negative peaks are larger than the positive ones when the averaging time is 12 seconds, their relative value is reversed when the sampling time is changed to 102 seconds. From the flow visualization observations and average pressure measurements discussed in Chapter II, one can observe that the point x/D = 1.578 lies within the reattachment zone. It seems that the negative peaks are larger than the positive ones when the measurements are made outside of the region of reattachment, while experiments done within the reattachment zone show the existence of large positive peaks that exceed the negative ones. Later it will be shown that the same behavior could be observed for the two other noses. The 2.5 percent probability values display a similar tendency, that is, far from the reattachment

zone the negative peaks are much larger than the positive ones, and close to reattachment the negative and positive peaks are almost equal. The same trend can be observed in Figures 3.15 to 3.18, wherein the velocity is kept constant and the position of the transducer is varied.

As in the rms results,the peaks of the fluctuating pressure reach a local maximum between x/D = 0.9 and x/D = 1.3 (Figures 3.15 to 3.18). However, while the rms values and the peaks with 2.5 percent probability of occurrence become smaller downstream, the 0.1 percent negative peaks start growing again after a short region of lower values. This trend indicates the existence of a few large negative peaks whose frequency of occurrence is so low that they do not affect either the 2.5 percent peaks or the rms values.

Within the region of the separated zone, i.e., x/D < 1.7, the maximum negative peaks reached by the fluctuating pressure are 64, 69, 77, and 85 percent of the dynamic head corresponding to free stream velocities of 8.77, 14.05, 17.99, and 21.24 ft/sec, respectively. One can also observe that the point of maximum fluctuations moves slightly upstream as the velocity is increased, but the small available range of velocities in the LTWT precludes a decisive statement. Downstream of the reattachment zone,but within the range of measurements the maximum negative peaks are 70, 86, 82, and 104 percent of the dynamic head corresponding again to velocities of 8.77, 14.05, 17.99, and 21.24 ft/sec. These values are higher than the maximum negative peaks observed inside the separated zone.

It should be noted that the results presented in Figures 3.7 to 3.14 and those presented in Figures 3.15 to 3.18 are of two different sets of measurements.

The final remark here concerns the effect of the present results on cavitation inception. If we add the average pressure coefficient to the present negative peaks of the fluctuating pressure, it will still be impossible to explain cavitation inception numbers higher than 1.5 (see Figure 4.7. The present measurements exclude the possibility of inception of cavitation on the surface of the blunt nose, a conclusion well proven both by the holograms (see Chapter 4) and the series of inception photographs taken during the experiments. It follows, of course, that the fluctuating pressure must be lower at other points far from the surface to account for the observed cavitation there.

III.2.2 Step Nose

Figures 3.19 and 3.20 display the rms values of the fluctuating pressure coefficient as a function of location on the surface of the step nose for various velocities. Here again, the nondimensional pressure fluctuations do not show a strong dependence on velocity, but do show a strong dependence on position. These values range from around 2 percent at $x/D = 0.524$ ($x'/H = 1.25$) to more than 6.5 percent at $x/D = 0.689$ ($x'/H = 9.844$). Downstream of the point $x/D = 0.734$ ($x'/H = 12.188$) the rms values drop to 2-3 percent at $x/D = 0.885$ ($x'/H = 20$).

Even though there is no strong dependence on velocity, one can still observe that when $u = 8.48$ ft/sec the scaled rms fluctuations are higher than the measured values for higher velocities. In addition, the region of relatively high rms values is also larger.

On the other hand, when u = 22.50 ft/sec and u = 21.30 ft/sec (Figure 3.20) there seems to be a much faster drop in rms values downstream of the maximum and they are slightly lower. We are not certain if these differences are due to a change in the length of the separated zone, since the present range of test velocities is small.

According to other experiments (Mohsen (1967), Fricke (1971), and Greshilov et al. (1969)) conducted downstream of a backward facing step, the maximum rms values are observed close to the reattachment zone. Since the present experiments do not include determination of the reattachment point on this body, this relationship cannot be verified.

Similar to the procedure described earlier, the peak values of pressure fluctuations were calculated using the probability density and probability distribution functions, corresponding to 0.1, 2.5, 97.5, and 99.9 percent of the cumulative distribution. These results are plotted on Figures 3.21 to 3.28. Here again, and more obvious than in the blunt nose results, one can observe the relation between the positive and the negative peaks. Upstream and downstream of the reattachment zone the positive peaks are lower than the negative ones, but near reattachment the situation is reversed. This behavior is much more pronounced for the 0.1 and 99.9 percent probabilities than the intermediate ones, even though it is evident in both. One can always speculate about the reason for such a behavior. Perhaps it is the result of the impingement of the reattaching free shear layer on the surface which causes the positive peaks to grow above the negative ones, but it is hard to make a conclusive statement based only on the present results.

There is on this body, as on the blunt nose, a big difference between the 0.1 and 2.5 percent probability values. This ratio in the present case is around 1.5. As noted before, the difference between the probabilities may have an important bearing on the initiation of cavitation.

In order to know what portion of the pressure fluctuation spectrum is the main contributor to the relations mentioned earlier, the signal was filtered with a high pass filter (24 db/octave) at 90 Hz. This resulted in a reduction of the maximum rms values to around 5.5 percent, the minimum rms values to around 1.1 percent, and in a partial disappearance of the large positive peaks. Figure 3.29 is an example of the peak values of the filtered signal (corresponding to Figure 3.25, the unfiltered signal). This is an extreme example, since in other cases the positive peaks were still slightly higher than the negative ones, at least in part of the reattaching zone. This result strengthens the speculation that the large positive peaks are a result of the impingement of the reattaching shear layer on the surface. Since the oscillations of the separating streamline will usually contribute to the lower frequency portion of the spectrum, one may expect that any phenomenon resulting from such an effect will vanish when the low frequency part of the spectrum is filtered. This statement will be discussed further later.

The maximum negative peaks show very little dependence on velocity. For example, these peaks were 25.0, 22.4, 23.8, 22.5, 22.2, 23.3, 21.4, and

21.8 percent for velocities of 8.6, 11.5, 14.2, 16.3, 17.9, 19.6, 21.2, and 22.5 ft/sec, respectively. There is a corresponding slight decrease in the maximum rms values.

We can comment here that, as for the blunt nose, the sum of the average pressure coefficient in the separated zone and the highest peak values of the fluctuating pressure do not result in a sufficiently low value of instantaneous pressure to explain the cavitation inception numbers obtained for this body. Here again, as expected, cavitation inception never occurred on the body surface. This is shown in Chapter IV by the holograms and the photographs taken during the cavitation experiments.

III.2.3 Hemispherical Nose

Unlike the step and the blunt nose experiments, some difficulties occurred while trying to measure the pressure fluctuations on the surface of the hemisphere. Either the slight change in body shape where the belt emerged from the interior of the body onto the surface,or a possible leakage from the interior of the body into the separated zone prevented obtaining any valid results based upon our previous knowledge of this test body. In particular, it was found that by injecting hot water from the stagnation point and observing the flow with a laser beam, the separated zone appeared to be shorter near the belt when compared to other points around the body. For this reason the same nose was mounted on another cylinder and the transducer was flush mounted at a fixed point. Then the separated zone appeared to be symmetric, having the expected dimensions. Due to the sensitivity of this parti-

cular flow to very small changes in body shape, it was decided to make fluctuation measurements at various discrete points with a flush-mounted transducer.

No changes could be observed either in the frequency or in the rms and peak values of the fluctuating pressure when the blunt and step nose experiments were repeated with a similarly mounted fixed transducer. Since the nose of the step body covered the point where the belt emerged onto the surface, and due to the large dimensions of the separated zone of the blunt body (compared to the 0.005 inch groove at the belt exit) these noses did not have a significant shape imperfection. Thus, we concluded that the possible leakage did not have any effect on the experiments.

The hemispherical nose body used for the present measurements was the very same one used by Arakeri (1975) in his experiments. The fluctuating pressure was measured in six different locations downstream of the point of separation. These measuring points were at values of $x/D = 0.519$, 0.556, 0.609, 0.659, 0.681, and 0.744, x being the axial distance from the stagnation point. The arc-distance ratios corresponding to these positions are $S/D = 0.804$, 0.841, 0.894, 0.944, 0.966, and 1.029, respectively, S being the distance along the surface. As noted before, the output was amplified and then recorded on the HP 3960 instrumentation tape recorder.

Figures 3.30 to 3.32 display the rms values of the fluctuating pressure. In Figure 3.30 the scaled pressure fluctuations are plotted against

the Reynolds number for all six positions. Unlike the blunt and the step noses, the present results show a strong dependence on velocity and transducer location. At x/D = 0.519 (S/D = 0.804) there is no sign of any peak, indicating that the transducer location is always within the boundaries of the separated bubble. The rms pressure fluctuation varies from 1.2 percent at a low velocity to 0.6 percent at a high velocity.

At x/D = 0.556 (S/D = 0.841) the rms value is 2.33 percent at low velocity and drops to 0.75 percent at u = 13.9 ft/sec. From then on, the fluctuations grow monotonically to 1 percent at the highest velocity of the tunnel.

At x/D = 0.609 (S/D = 0.894) the rms reaches a maximum of 3.1 percent when u = 14.5 ft/sec ($Re_D = 2.34 \times 10^5$) and remains constant up to a velocity of 22.6 ft/sec ($Re_D = 3.60 \times 10^5$) where it drops to 2.4 percent. These results possibly indicate that the flow reattaches on the transducer surface over the range of tunnel velocities starting from about 12.5 ft/sec ($Re_D \simeq 2 \times 10^5$) up to 22 ft/sec ($Re_D \simeq 3.6 \times 10^5$).

At x/D = 0.659 (S/D = 0.944) there is a narrow peak at a velocity of 8.75 ft/sec ($Re_D = 1.41 \times 10^5$) where the rms reaches a maximum of 3.8 percent. When the velocity is increased the rms drops monotonically to 1 percent at the highest possible velocity. The present measuring point is 0.1 inch downstream of the previous one, a distance equal to the transducer diameter. The disappearance of the high rms values measured at the previous point and the present appearance of a new rms peak at a lower velocity reenforces the suggestions concerning the position of the reattachment zone.

At x/D = 0.681 (S/D = 0.966), a 5.5 percent rms peak occurs at a velocity of 6.83 ft/sec ($Re_D = 1.1 \times 10^5$). At higher velocities the rms of the fluctuating pressure drops monotonically to 0.7 percent.

At x/D = 0.744 (S/D = 1.029) the maximum value measured is 5.25 percent at u = 4.56 ft/sec ($Re_D = 7.36 \times 10^4$). No measurements were made at lower speeds. When the velocity is increased the rms values drop to 0.55 percent at the highest tunnel velocity.

Figures 3.31 and 3.32 show the same results but plotted against the transducer position. As mentioned before, the peaks in the rms values are taken to indicate the position of reattachment of the separated boundary layer. The results are summarized in the following table:

TABLE 3-1 Estimated position of reattachment of the separated boundary layer on the surface of the hemispherical nose based on pressure fluctuation measurements

Reynolds Number	Velocity (ft/sec)	x/D of Reattachment	S/D of Reattachment
0.84×10^5	4.56	≥ 0.744	≥ 1.029
1.1×10^5	6.83	0.681	0.966
1.41×10^5	8.75	0.659	0.944
$\geq 2 \times 10^5$ & $\leq 3.6 \times 10^5$	≥ 12.5 & ≤ 22	0.609 ± 0.025	0.894 ± 0.025
3.75×10^5	> 23.23	< 0.556	< 0.841

The present results do not agree with previous measurements made with the same body in a different water tunnel by Arakeri (1975). According to him, the maximum rms value obtained for a velocity of 7 ft/sec and S/D = 0.951 was almost ten percent. Even though the location of the

corresponding peak does match, the present rms value is a little more than half of Arakeri's results (i.e., 5.5 vs 10 percent). Several calibrations of the transducer during the experiments and repeated measurements always led to the same observations. Since Arakeri's measurements were made with a larger transducer than the present one, and therefore with a poorer high frequency response, we cannot account for the discrepancy.

The present results are also much smaller than Huang's rms values (1975 and 1979) obtained in a wind tunnel measurement using a large body and a pinhole microphone. Further reference to Huang's results will be made when the effect of the transducer size on the measurements is considered. (See Appendix III A and section III.4.4)

The transducer signal was analyzed following the previously described procedure of using the probability density and distribution functions for providing a consistent measure of the peaks of the fluctuating pressure. Figures 3.33 to 3.38 show the plotted results. These graphs display the large positive peaks corresponding to the expected points of reattachment tabulated in Table 3-1. However, one can observe in Figure 3.33 ($x/D = 0.519$, $S/D = 0.804$) that even though the transducer was positioned under the "laminar part" of the separated zone, the positive peaks were slightly higher than the negative ones for low velocities. For all the other positions, velocities, and bodies, the negative peaks were higher than the positive ones over the entire region where measurements were made, excluding the reattachment zone where large positive peaks overcame the negative ones. Two examples of the skewness of the probability density histograms can be seen in Figures 3.39 and 3.40 (both

are part of the data presented in Figure 3.35). In Figure 3.39 the negative peaks are higher and the probability density is skewed to the right; and in Figure 3.40 the positive peaks are larger and the density is skewed to the left. In both cases the most probable value is not the average value.

It should be noted that the values presented in Figures 3.33 to 3.38 were taken from a digital display of the signal analyzer and not from the plotted histograms. This remark is made to avoid confusion concerning the ability to detect a 0.1 percent change in the plotted probability distribution.

At the expected points of reattachment the negative peaks reach maximum values of 9, 11, 18, and 18 percent, corresponding to x/D = 0.609, 0.659, 0.681, and 0.744, respectively. In contrast to the other two noses, the sum of the average static pressure in the separated zone and the negative peak of the fluctuating pressure lead to a tension in the fluid. This can therefore explain the possibility of inception of band type cavitation obtained on this body as seen in Figure 4.17.

The big discrepancy between the present rms values and those of Arakeri does not exist in the peaks of the fluctuating pressure. His maximum peak is 25 percent, compared to 18 percent in the present measurements.

III.3 Spectral Measurements of the Fluctuating Pressure

III.3.1 Introduction

Determination of the power spectrum of the pressure fluctuations was one of the main objectives of this present work. Since the onset of cavitation

on the blunt and the step bodies occurred in the "free shear layer", far from the body surface, the measurement of surface pressure fluctuations cannot contribute directly to the understanding of cavitation phenomena occurring in this layer. However, a knowledge of the main frequencies involved in these fluctuations may help in comparing the present results to other experiments made in other turbulent shear flows this may shed some light on the pressure levels in the shearing region where cavitation was observed to start. The available literature on free shear layers is quite large, but relatively little seems to have been done in measuring pressure fluctuations in these flows. Among the existing works one can mention the measurements by Fuchs (1972); Lau, Fisher, and Fuchs (1972); Michalke and Fuchs (1975); Fuchs (1974); and Fuchs, Mercker, and Michel (1978). The first four references describe experiments in axisymmetric jets, and the last one discusses experiments in the wake of different disks. All these references provide the power and cross spectra in different axial, radial and azimuthal positions. The report of Fuchs and Michalke (1975) is of special interest, since it provides also the difference between rms levels in the potential core and the shear layer in the boundaries of a jet. Fuchs et al. (1978) provide information on the effect of axial position on the power spectrum of a jet and a series of results for a sharp-edged disk. Unfortunately, the closest point in which the disk measurements were made was $x = 3D$, i.e., downstream of the point where the free shear layer became a wake. The work of Lau et al. (1972) contains a series of correlated data between the pressure and the radial and axial velocity fluctuations. A strong correlation between these fluctuating quantities is shown, and the writers associate these correlations with a motion of large eddies in the mixing zone.

Surface pressure fluctuations of separated flows has also received attention. For example, B. Stahl (1980) gives information on the flow in a pipe with sudden expansion; Arakeri (1975); Greshilov et al. (1969) provided similar data behind a downstream facing step; Fricke and Stevenson (1968) and Fricke (1971) behind a fence positioned normal to a wall; Mohsen (1967) behind an upstream and downstream facing steps; and Huang (1975, 1979) among other bodies on the surface of a hemispherical nose. The present experimental results will be presented and later analyzed and compared to these works.

III.3.2 Apparatus and Procedure

The power spectra of the pressure fluctuations was computed by a Spectral Dynamics Corporation Model SD360 digital signal processor. The system has an internal digitizer so that analog data can be loaded directly from the tape recorder. The sampling rate depends on the predetermined frequency range; 1024 points are sampled during a basic time unit equal to $500/f_{max}$ where f_{max} is the highest frequency in the analysis range. Thus a sample is taken every $0.5/(1.024\ f_{max})$ seconds, approximately two points during a cycle of the highest frequency. To increase the accuracy of the results, the values of f_{max} and the number of calculated points on the spectrum were doubled. The results presented are actually half of the total range of frequencies calculated. As a result, eight points were sampled during the period of the highest displayed frequency of each power spectrum figure. Each of the spectra was an average of a large number of basic time units, leading to a total sampling period of at least 20 seconds.

Another necessary preliminary remark is that no attempt was made to

reduce the background noise, or the mechanical vibrations of the water tunnel and the sting support on which the bodies were mounted. Traces of these vibrations can be seen on almost all the calculated spectra. Verification that certain peaks observed on the spectrum are a result of vibrations were made by tapping on the body when the tunnel was silent, and analyzing the resulting transducer signal.

III.3.3 Blunt Nose

The lowest frequencies were observed on the surface of the blunt nose. The first peaks in the spectrum appeared below 1 Hz and were at least 30 db lower at 500 Hz in all the range of measurements (velocities and locations). Below -30 db the validity of the results is doubtful, since the signal-to-noise ratio of the tape recorder was around 35 db (stated by the manufacturer and tested with various signals). By keeping the velocity constant and varying the position of the transducer a series of plotted spectra (one for each point) was obtained, corresponding to the rms data on Figure 3.3. As noted before, each of the graphs represents an average of more than 20 seconds of data. A few examples can be seen in Figures 3.41, 3.42, and 3.43. They all represent the pressure fluctuations when u = 21.24 ft/sec, in various positions along the surface. The first one is for x/D = 0.453, the second for x/D = 1.203, and the third for x/D = 1.953. Each of the figures contains two plots, the first one shows the spectrum from zero to 500 Hz, and the second shows the details between zero and 100 Hz.

The peaks at 55 Hz and 135 Hz are immediately evident. These peaks are due to vibration of the test nose in the water tunnel. As noted before,

this point was verified by recording the transducer response while tapping on the body in a stationary tunnel (these peaks did not appear when the transducer was calibrated in a different set-up). These vibrations generated, in certain conditions, sub- and superharmonics, and an example of this behavior is the peak at 68.5 Hz and 28.5 Hz in Figure 3.42b. This nonlinear response of the flow field to induced vibrations is a characteristic of turbulent shear layers (see, for example, Browand (1966), in which the response of a shear layer to artificially generated sound waves is observed, and it is found that subharmonics develop in the velocity fluctuations). Note that these subharmonics do not appear in the spectrum when x/D = 0.453.

Other peaks can also be observed besides the effect of vibrations. When x/D = 0.453 (Figure 3.41b) a few peaks can be seen in a very low frequency (4-12 Hz) creating a single "natural" (not induced by external excitation) peak in the spectrum. However, more peaks can be seen downstream of x/D = 0.828 (Figure 3.42b at 22 and 29 Hz). Downsteam of reattachment, the peaks become wider and less distinct, even though the main frequencies remain unchanged (compare Figure 3.42b and 3.43b). The existence of a single peak in the upstream part of the separated zone, and the formation of at least a second one was a characteristic behavior of the blunt body. Better examples can be seen in Figures 3.44, 3.45, and 3.46 which represent the spectra for u = 14.05 ft/sec. The effect of velocity on the power spectra is demonstrated in Figures 3.45, 3.48 and 3.49 corresponding to x/D=0.828, 1.078, and 1.328. The data in these figures are taken from a series of computed power spectra that are not shown here. As is evident from the

results there are two distinct groups of spectral peaks. The first group include the low frequency peaks (below 12 Hz) and the second group include the higher frequency peaks that follow the trend.

$$f \propto u_\infty$$

hence

$$S_t = \frac{fD}{u_\infty} = \text{constant}$$

The frequency of these peaks appears to be independent of location on the body surface (again provided that $x/D \geq 0.828$). One can also note the appearance of a peak at 28.5Hz; this is believed to be a subharmonic of the mechanical vibrations.

III.3.4 Step Nose

Perhaps the biggest surprise was the results for the spectra of the step nose. At first observation, it seemed that there was very little in common between the spectrum of this body and that of the hemisphere. Considering the small difference between the two shapes, the results indicated that the small step, located within the separated zone enforced a complete change in the characteristics of these two separated flows. As in the case of the blunt nose, the spectrum contained fluctuations created by mechanical vibrations of the test facility, namely, peaks around 55 Hz and 135 Hz. In addition, there were very intense low-frequency fluctuations starting below 1 Hz. In the region close to the step only low-frequency fluctuations could be observed, and an example of a typical spectrum can be seen in Figure 3.50 which corresponds to u_∞ = 16.28 ft/sec and x'/H = 1.250. As the transducer was moved downstream a second peak gradually appeared on the spectrum. This peak became distinct at

$x'/H = 5.9$ and from then on remained on the spectrum far downstream of the reattachment zone. Typical examples are shown in Figures 3.51 and 3.52, corresponding to $x'/H = 9.8$ and 14.53, respectively. A very similar behavior was observed on the surface of the blunt nose, i.e., only a single group of low-frequency peaks in the upstream part of the separated bubble and an appearance of a second peak as the transducer was transversed downstream. In Figure 3.52 one can observe some traces of a small third peak in the high frequency side of the spectrum. This peak will be discussed, together with the results of the hemispherical nose.

In order to determine the effects of velocity and location on the frequency, a series of spectra was computed and the centers of the main peaks were plotted against body Reynolds number in Figure 3.53. Two important trends can be observed on this plot. First, there seems to be very small effect of location on the main frequency, and it applies both to points upstream and downstream of reattachment ($x'/H = 9.8$ and 14.5, respectively). Second, unlike the blunt nose it seems that

$$f \propto u^n$$

or

$$\frac{fD}{u} \propto u^{n-1}$$

and

$$n \simeq 1.3$$

which might indicate that the diameter is not the proper length scale in the dimensionless frequency. Obviously, finding a length scale that has the proper dependence on velocity is not self-evident. However, unlike the blunt nose, it seems that the diameter of the body is not as important as

the height of the step or the length and the height of the separated zone. A few suggestions for a proper length scale will be made later.

As a final remark in this section, we would like to draw attention to the order of magnitude difference between the frequencies of fluctuations observed on the surface of the blunt and the step noses. This difference might also suggest the proper choice of length scale for the dimensionless frequency.

III.3.5 Hemispherical Nose

The spectrum of the hemispherical body contained a much wider range of frequencies than the other two bodies. The changes of this spectrum with velocity and location helped, in addition to understanding these phenomena, in explaining some of the characteristics of the other two noses. Similar to the previous two noses, the spectrum contains peaks caused by mechanical vibrations in the water tunnel. In addition to the previously mentioned frequencies (55 Hz, 135 Hz), a third peak was observed at 4.1 kHz. By tapping on the test body in a stationary tunnel it was verified that the source of this peak was also mechanical, after excluding the possibility of a transducer resonance. However, the "naturally" excited pressure fluctuations were again the main contributor to the spectrum. The low frequency peaks (below 20 Hz) that existed in the spectra of the other two noses existed also in the spectrum of the hemisphere, but unlike these bodies, two major peaks appeared at higher frequencies. The highest frequency peak existed also in the "laminar" part of the separated bubble (the region upstream of transition in the boundary of the separated zone). When the transducer was located under the transition region and even farther

downstream, a second peak appeared at a lower frequency, and they both existed all over the turbulent part of the separated zone. When the transducer was located far downstream of reattachment (depending on velocity) the higher peak disappeared, leaving only the lower frequency one. A demonstration of this behavior can be seen in the spectra shown in Figures 3.54 to 3.59. In Figure 3.54 the transducer is located under the stable laminar part of the separation zone at a tunnel speed of 12.6 ft/sec. A single peak is evident between 1000 and 1600 Hz. At a somewhat higher velocity (17.4 ft/sec) and at the same location the flow undergoes transition upstream of the transducer (x/D = 0.556); a second peak starts to become noticeable at 500 Hz (Figure 3.55). Farther downstream and at the lower tunnel speed of 12 ft/sec, the transducer is downstream of the point of transition, two obvious peaks appear, one at 370 Hz and the other at 1410 Hz (Figure 3.56). Mechanical vibrations are also evident at 4190 Hz. The transducer is positioned directly under the reattachment zone in Figure 3.57 at a tunnel speed of 5.95 ft/sec and x/D = 0.681. Two peaks are still readily seen. As the tunnel speed is increased at this location, the higher frequency peak becomes diminished (Figure 3.58) and at a speed of 21.3 ft/sec it nearly disappears (Figure 3.59).

These are a few examples of the consistent results obtained for the hemisphere. To recapitulate, a relatively high frequency peak is seen in the laminar part of the separated bubble; two peaks are observed in both the turbulent part of the bubble and within a close distance downstream of reattachment; and the high frequency peak disappears farther downstream of reattachment.

The behavior of the pressure fluctuations leads us to suspect that the high frequency peak is associated with the laminar boundary layer upstream of separation, and with the laminar part of the separated bubble. The lower frequency peak then we expect to be due to the turbulent shear layer downstream of transition in the separated zone. In the laminar part of the flow, disturbances to the boundary layer can be described by the Orr-Sommerfeld equation. The most amplified wave should accordingly have a frequency corresponding to the high frequency peak seen in the spectrum. The dependence of this amplification on frequency was calculated using the computed stability charts by Wazzan, Okamura, and Smith (1968) following the technique described by Arakeri (1973, 1975). The boundary layer characteristics of the hemisphere were estimated using Thwaites' method for axisymmetric bodies (see White (1974)) and by using the parameters of boundary layers that were reported by Gadd et al. (1963).

Figure 3.60 shows the calculated results of the boundary layer parameters and Figure 3.61 shows the dependence of the amplification on frequency for various Reynolds numbers. All the above calculations were made following the boundary layer until the point of separation was reached. Following a technique suggested by Van Ingen (1956, 1975) for flows downstream of separation, an attempt was made to follow the stability analysis further downstream along the separated flow. The stability charts for reverse flows were calculated by Taghavi and Wazzan (1974), but the most amplified frequencies did not change significantly from the results presented in Figure 3.61. Due to a series of approximations needed for the application of these estimates to the hemisphere, the possible errors

may be too large to provide a conclusive statement about the importance of the stability calculations downstream of separation.

A comparison between the calculated frequencies and the experimental peaks is shown in Figure 3.62. The plot clearly shows how close the measured high frequency peaks and the calculated ones are. We conclude, as did Arakeri, that these high peaks correspond to Tollmien-Schlichting waves created by a spatially growing instability in the laminar boundary layer upstream of separation. These disturbances are probably further amplified in the laminar part of the separation streamline. We believe that this is the reason for their appearance in every part of the separated zone and for their decay downstream of reattachment when turbulent fluctuations overcome them.

Figure 3.62 contains both the high frequency and the low frequency peaks obtained for the location x/D = 0.609. Once it appeared, the frequency of the low frequency peak did not depend on location and the above point was chosen for the discussion, since it was, for most of the test velocities, in the turbulent part of the separated zone (thus providing the two peaks). From the graph it appears that:

$$f \propto u_\infty^{3/2}$$

As noted before, a proper choice of the length scale would provide a dimensionless number that would be independent of velocity. The task is fairly easy for the higher peak since it is clearly associated with the laminar boundary layer. A commonly used length scale for laminar boundary layers is the momentum thickness, θ. Since $\theta \propto u_\infty^{-1/2}$, it follows that

$f\theta/u_\infty$ should be constant and thus that $f \propto u_\infty^{3/2}$, a relation clearly shown in Figure 3.62.

The choice of a length scale for the lower peak is not quite so straightforward. In the discussion to follow, an attempt will be made to find such a scale, one that will also explain the differences between the spectra of the three noses.

III.4 Discussion

III.4.1 Comparison to Other Sources

We begin with a comparison between the present results and the available literature. Measurements made by Mohsen (1967) are probably the most detailed available study of pressure fluctuations in separated flows. His measurements, made with a 0.25-inch microphone, were carried out on a downstream facing step, an upstream facing step, and a fence. The first two are similar to the step and blunt noses, respectively. Mohsen also made average pressure measurements and injected smoke to determine the dimensions of the separated bubbles. His average static pressure distribution on the upstream facing step is similar to the present blunt nose results, although his dimensions of the separated bubbles are quite different (his were x/H=2.5 and 5 for the upstream and downstream steps). The maximum rms values of the fluctuating pressure obtained by him were 5.5 and 11 percent for the backward and forward facing steps, respectively, similar to the present results after taking into account that Mohsen filtered out the low frequency part of the spectrum. He also found that the point of maximum rms on the forward facing step was far upstream of reattachment, unlike the backward facing step where the maximum occurred close to the reattachment

zone. Mohsen's power spectra obey the same characteristic behavior observed in the present experiments; that is, formation of a peak in the spectrum only in the downstream part of the separated zone and downstream of reattachment. Considering that his measurements were made under different flow conditions, namely, in a very thick turbulent boundary layer, the similarity in the results is quite remarkable.

The same characteristics of the spectra were observed by Greshilov et al. (1969) behind a downstream facing step and by Fricke and Stevenson (1968) and Fricke (1971) downstream of a fence. The rms values obtained by Greshilov and Fricke compared favorably with the present step nose results and they were also similar to the rms values obtained by Stahl (1980) behind a sudden expansion in a pipe. Measurements made in jets by Michalke and Fuchs (1975) showed that the peaks in the pressure fluctuations spectrum varied as they proceeded downstream along the jet. They found further that the characteristic wavelength was proportional to axial distance; that is, the Strouhal number was proportional to $1/x$. Similar results are shown by Fuchs et al. (1978) in Figure 5. They interpreted their results as being due to the growth of vortices in the free shear layer created by the jet. Their model is that of a series of vortex rings which interact to create larger vortices. The existence of a large coherent structure in mixing layers was reported in several experiments made in plane free shear layers by Brown and Roshko (1974), Dimotakis and Brown (1976), Konrad (1976), and Winant and Browand (1974). In all these works the size of the vortices grew linearly with distance from the starting point. The measured frequencies of velocity fluctuations, together with flow visualization, confirmed this linear growth. As mentioned before, correlations between velocity

fluctuations (both components) and pressure fluctuations made by Lau, Fisher, and Fuchs (1972) showed that the pressure fluctuations correlated strongly with the fluctuating velocities and had the same dependence on the motion of the large scale turbulent eddies.

Measurements made by Eaton and Johnson (1980) behind a downstream facing step show that the difference between a plane mixing layer and a reattaching separated flow is concentrated in the region close to the wall, and the main characteristics of the shear layer remained almost unchanged. Their spectral measurements of velocity fluctuations (measured above the separated zone) showed, at least qualitatively, that the peak frequency was shifted to lower values with distance. The peaks became rounded (much broader band) when the same measurements were made within the mixing zone. Based on these results, it seems quite surprising that neither the present measurements nor any other pressure fluctuation measurements on the surface of a body within a separated zone contain any trace of the motion and growth of those vortices. This is taken to mean that the pressure fluctuation measurements on the surface of the body do not contain any information about the development of the fluctuating pressure in the free shear layer above, or at least the information is "screened" by the flow inside the recirculating zone. The reasons for this "screening" effect are not clear, but its existence makes the calculations done by Fricke (1971) doubtful. He assumed that the main source of noise came from the turbulent fluctuations in the shear layer above the measuring microphone.

III.4.2 The Turbulent Spectral Peaks

The question yet to be answered is, if the transducer does not sense

the development of the free mixing layer, what does it sense and what is the source of the peak in the spectrum obtained in all three noses? The probable answer is based on the observation that the spectral peak becomes distinct under the turbulent part of the separated zone and especially in the reattachment region. Even though, for some reason, the existence of the growing eddies in the mixing layer is screened by the reverse flow, there seems to be no flow mechanism that would shield these eddies from the transducer near the reattachment zone. Thus, one might suspect that the source of this "preferred" frequency comes from the characteristic size of the mixing layer eddy at reattachment. If all the above is true, the characteristic frequency obtained should correspond to the length and the height of the separated zone, and especially to the turbulent part of this zone. These dimensions might be expected to determine the size and the spacing of any large-scale vortex structure. Brown and Roshko (1974) and Dimotakis and Brown (1976) showed that in a plane mixing layer:

$$3.5\,\delta\omega \leq \ell < 5.0\,\delta\omega$$

where ℓ is the spacing between two vortices, and $\delta\omega$ is the slope thickness defined as:

$$\delta\omega = \frac{\Delta u}{\left(\frac{\partial u}{\partial y}\right)_{max}}$$

where Δu is the velocity difference across a shear layer and $(\partial u/\partial y)_{max}$ is

the maximum average velocity gradient in the layer. They also show that:

$$\frac{d\delta\omega}{dx} = 0.181 \frac{\Delta u}{2u_{Av}}$$

leading to:

$$0.63(x-x_0) \leq \ell \leq 0.91(x-x_0)$$

If the convection velocity at reattachment is half of the free stream velocity, then:

$$f = \frac{0.5u}{\ell}$$

where u is the velocity outside of the separated zone.

In order to apply these relations to the reattaching separated flow, one must bear in mind that these relationships do not take into account the curved streamlines and the large pressure gradients in the reattachment zone. However, the results of Eaton and Johnson (1980) show that the slope thickness behind a downstream facing step obey the relation mentioned above, and their result for the vortex spacing is:

$$\ell \simeq 5.5\ \delta\omega$$

a result close to the upper bound of Dimotakis and Brown. As a result, it seems appropriate to choose this upper bound as an approximated expression for ℓ, leading to:

$$\ell \simeq 0.9(x-x_0)$$

and by neglecting x_0

$$f = \frac{0.5u}{0.9x}$$

If x is chosen to be the length of the separated zone and assuming that

the velocity at reattachment is u_∞ then

$$f = \frac{0.5u_\infty}{0.9L}$$

So a characteristic Strouhal number would be:

$$S_t = \frac{fL}{u_\infty} = 0.56$$

One should bear in mind that this argument ignores the fact that part of the separation streamline is laminar, not obeying the turbulent similarity rules, and that the shear layer in separated flows has a curved path longer than the length of the separated bubble.

The next stage will be to compare the experimental results to the Strouhal number obtained. The average pressure measurements on the surface of the blunt nose, the jets injected from its surface, and the measurements by Ota (1975) show that the dimensions of the separated zone are independent of velocity and a characteristic length will be:

$$L = 1.7D$$

So, the expected frequency is given by

$$f = 0.56 \frac{u_\infty}{1.7D}$$

or

$$\frac{fD}{u_\infty} = 0.33$$

From Figures 3.47, 3.48 and 3.49

$$\frac{fD}{u_\infty} \simeq 0.28$$

The comparison is not straightforward for the other two noses, due to a lack of knowledge of the length of the separated zone. However, an attempt will be made to use the available data. The flow visualization techniques described in Chapter 2 can help in determining the points of laminar separation and transition in the separating stream line, but cannot locate the reattachment point. The presently available data about reattachment are the points where the fluctuating pressure reaches a maximum. Due to previously made remarks, the characteristic frequency will be calculated using two length scales. The first one will be the distance between the separation point and reattachment, L_1, and the second will be the distance between the point where the separating streamline starts "rolling up" and reattachment, L_2.

The calculated frequency of fluctuations on the surface of the hemisphere is presented in Table 3-2. The data on separation and transition were taken from Figure 2.23, and the location of the peaks in rms values were taken from Figure 3.30.

Table 3-2 Calculated frequencies of turbulent pressure fluctuations on the surface of the hemispherical nose

Re_D	u_∞ [ft/sec]	x_r/D	x_{sep}/D	x_{tr}/D	L_1/D	$f_1 = 0.56u_\infty/L_1$	L_2/D	$f_2 = 0.56u_\infty/L_2$
1.1×10^5	6.83	0.681	0.45	0.55	0.23	100 Hz	0.13	175 Hz
1.41×10^5	8.75	0.659	0.45	0.54	0.21	140 Hz	0.12	245 Hz
2.34×10^5	14.5	0.609	0.46	0.52	0.15	325 Hz	0.089	547 Hz

The results were plotted in Figure 3.63, and compared to the analyzed results of the pressure fluctuation measurements. As one can

observe, f_1 is lower than the measured value, and f_2 falls within the experimental results. The agreement is amazing, especially considering the rough approximations used.

The reattachment point on the surface of the step nose is estimated as the center of the region where the positive peaks exceed the negative ones in the probability plots (Figures 3.21 to 3.28). The separation and transition points are estimated from Figure 2.26. The results are tabulated in Table 3-3

Table 3-3 Calculated frequencies of turbulent pressure fluctuations on the surface of the step nose

Re_D	u_∞ [ft/sec]	x_r/D	x_{sep}/D	x_{tr}/D	L_1D	f_1(Hz]	L_2/D	f_2[Hz)
1.39×10^5	8.59	0.719	0.46	0.555	0.26	105	0.16	170
1.84×10^5	11.43	0.712	0.46	0.54	0.25	145	0.17	214
2.29×10^5	14.21	0.704	0.46	0.53	0.24	188	0.17	266
2.63×10^5	16.28	0.689	0.46	0.52	0.23	225	0.17	305
2.89×10^5	17.91	0.689	0.455	0.52	0.23	248	0.17	335
3.17×10^5	19.62	0.689	0.45	0.52	0.24	260	0.17	367
3.42×10^5	21.21	0.682	0.45	0.52	0.23	293	0.16	421
3.63×10^5	22.47	0.682	0.45	0.52	0.23	311	0.16	447

It should be noted that the values of L are quite crude, mainly due to the subtraction of two numbers which have nearly the same value. The above results are compared to the experiments in Figure 3.53. It seems that the experimental frequencies fall between the calculated values. Again, a very crude analysis achieved surprising agreement.

According to Mabey (1972), who collected results from various sources, the Strouhal number, fL/u, varied from 0.5 to 0.8 (his calculations included the results of Mohsen, Fricke, and Greshilov et al. mentioned before. He claimed that the "universal" Strouhal number implied a feedback process between conditions at the reattachment and separation points. Mabey claimed that this relation will be inappropriate when there was a strong coherent disturbance in the wake. The present analysis suggests that the peak in the spectrum is an outcome of the coherent structure in the wake. By incorporating the results on a plane shear layer to estimate the size of the eddy near reattachment, it was possible to calculate the frequency of the peak in the spectrum once the dimensions of the separated zone were known. As noted before, the question of why the spectra did not display the characteristic frequencies of the free shear layer upstream of reattachment cannot be answered at this time.

Another surprising result is the disappearance of the pressure fluctuations associated with the laminar boundary layer upstream of separation from the step nose spectrum. Since the pressure distribution on the surface of this nose is quite similar to the hemisphere, one may suspect that the boundary layer development will be similar, and as a result the same instabilities will develop. It is quite surprising that no such trace can be observed. We believe that this is a result of the same "screening" behavior of the reverse flow responsible for the disappearance

of the shear layer peaks. Some small traces of high frequency peaks can be seen on the spectrum presented in Figure 3.52. According to Figures 3.61 and 3.62, it is the proper frequency of an amplified boundary layer disturbance, but the level of these peaks is very low compared with the turbulent part of the spectrum.

III.4.3 Low Frequency Fluctuations

It was noted before that by filtering the signal of the fluctuations on the step nose with a high-pass filter at 90 Hz (24 db per octave) the maximum rms level dropped from 7 to 5.5 percent, which was a significant difference. These low frequency peaks, originating either from the background noise of the tunnel, or from the fluctuations in the dimensions of the separated zone and should not be ignored. According to Eaton and Johnson, more than 30 percent of the turbulence intensity was at frequencies lower than a third of the peak associated with coherent structure in the shear layer. They coupled these low spectral peaks with the motion of the free shear layer. In the present results, the disappearance of the high positive pressure peaks near reattachment when the signal is filtered (compare Figures 3.25 and 3.29), supports the suggestion that these high positive peaks are caused by the motion of the boundary of the separated zone and by the impingement of the reattaching free shear layer. It should be noted that the existence of low frequency fluctuations was also reported in plane free shear layer experiments. Some remarks concerning these fluctuations are made by Dimotakis and Brown

(1976) and Jimenez (1979).

III.4.4 Effect of Transducer Size on the Measurements

A detailed discussion about the effect of the transducer on the measurements is given in Appendix III-A. From the discussion in this appendix it seems that the only results significantly affected by the dimensions of the transducer are the measurements on the surface of the hemisphere, and especially the high frequency part of these measurements. The spectra of the fluctuating pressure on the surface of either the blunt or the step nose contain peaks whose corresponding wavelength is sufficiently large compared to the transducer diameter, preventing any serious doubt concerning the validity of these results.

III.4.5 Summary

The present chapter describes and discusses the measurements of pressure fluctuations on the surface of bodies whose boundary layer undergoes laminar separation and turbulent reattachment.

The maximum rms values of the fluctuating pressure are 19, 7, and 3 - 5.5 percent of the dynamic head for the blunt, step, and hemispherical noses, respectively. The peak values obtained from the probability distribution histograms are at least three to four times larger. The magnitude of the peaks with a probability of occurrence of 2.5 percent are half to two-thirds of those with 0.1 percent probability. The negative peaks are larger than the positive ones at almost any point of measurement excluding the reattachment zone where the positive peaks exceed the negative ones. These high positive peaks are originated from the low frequency part of

the spectrum and are probably associated with the motion of the separating stream line.

The spectra contain peaks that appear in the turbulent part of the separated zone, and downstream of the reattachment point. It is suggested that these frequency peaks are associated with the turbulent coherent structures of the free shear layer near reattachment. The Strouhal number based on the length of the separated zone and the free stream velocity is approximately equal to 0.56 for all the noses tested. The spectrum of the hemisphere contains peaks associated with the Tollmien Schlichting waves. These waves are not detected on the surface of the step and blunt noses for reasons yet unknown.

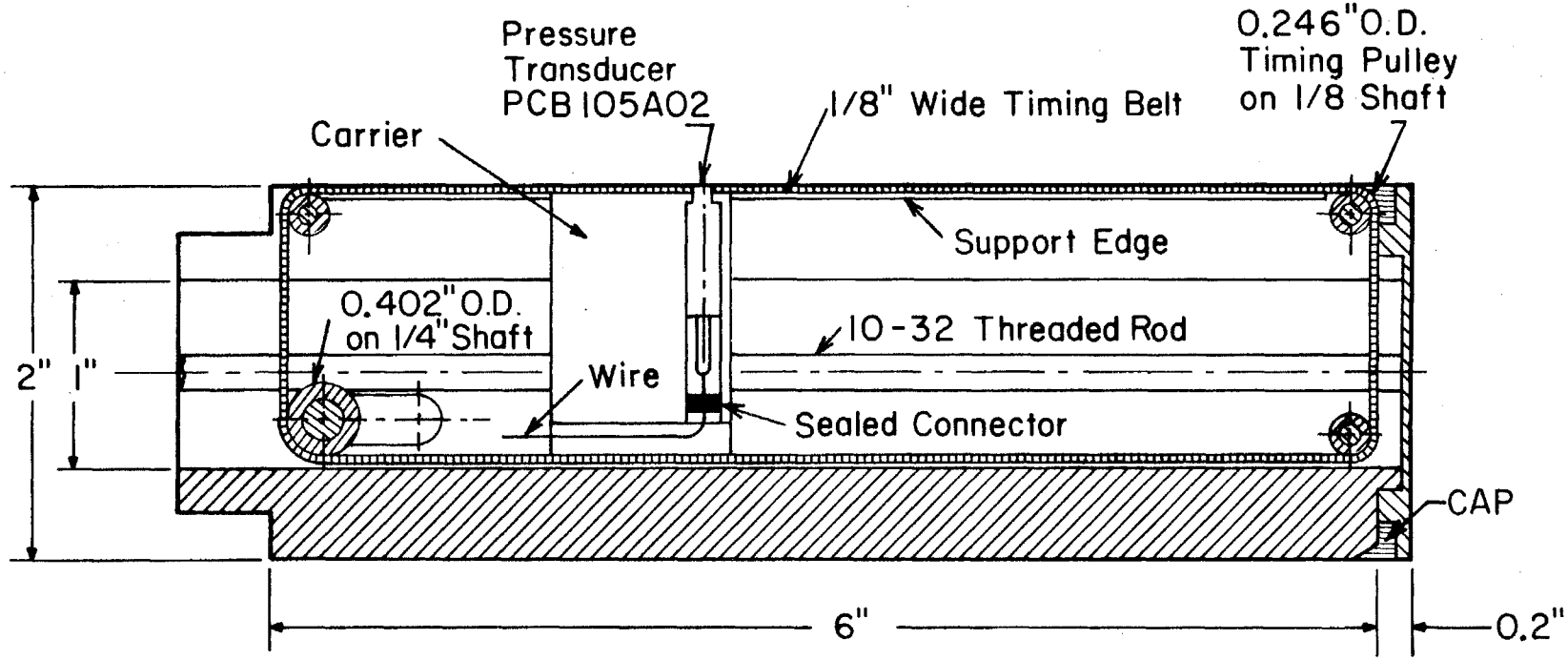

Figure 3.1. A schematic description of the system for pressure fluctuation measurements.

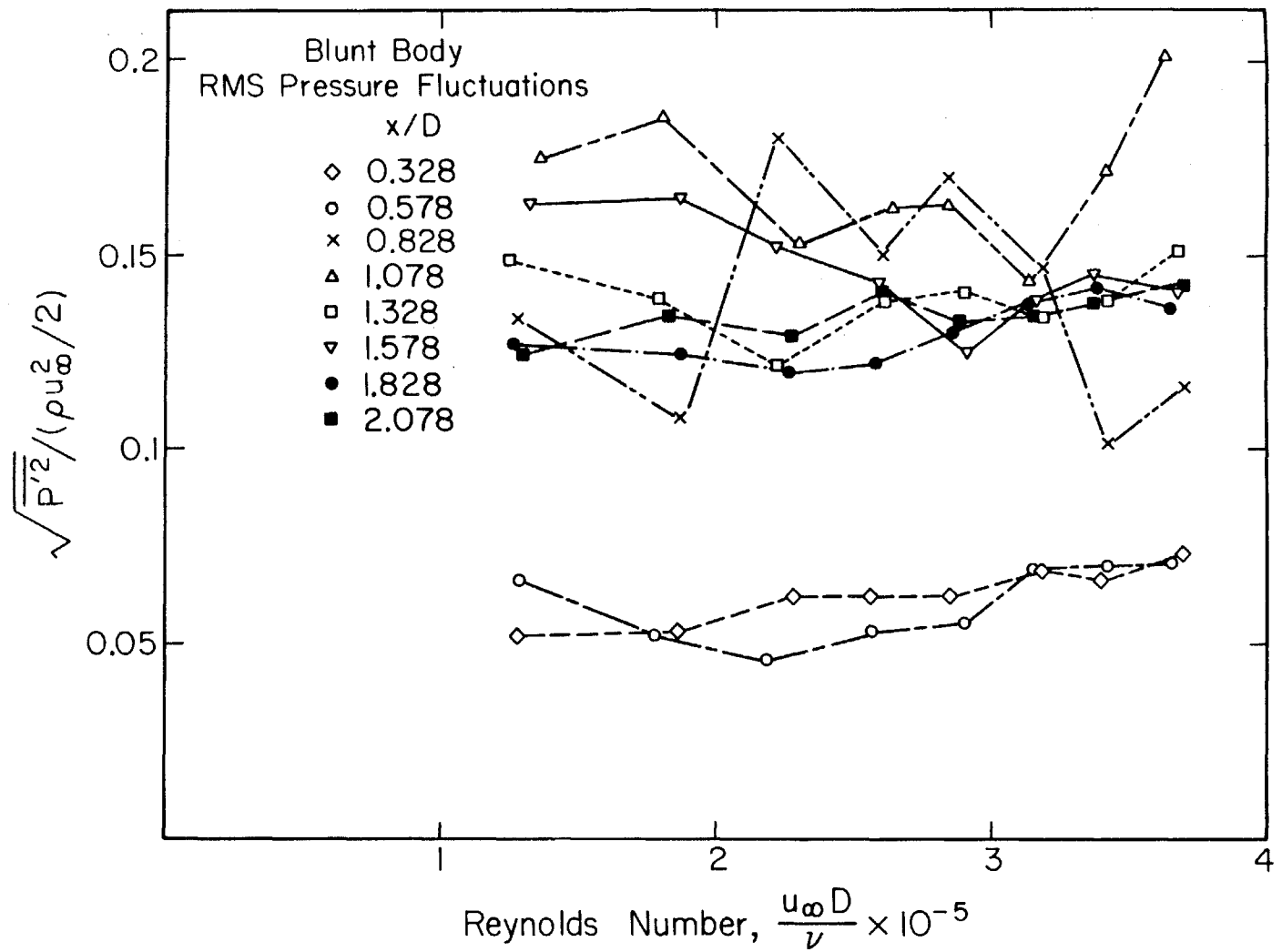

Figure 3.2. Rms values of the fluctuating pressure on the surface of the blunt body plotted against the Reynolds number.

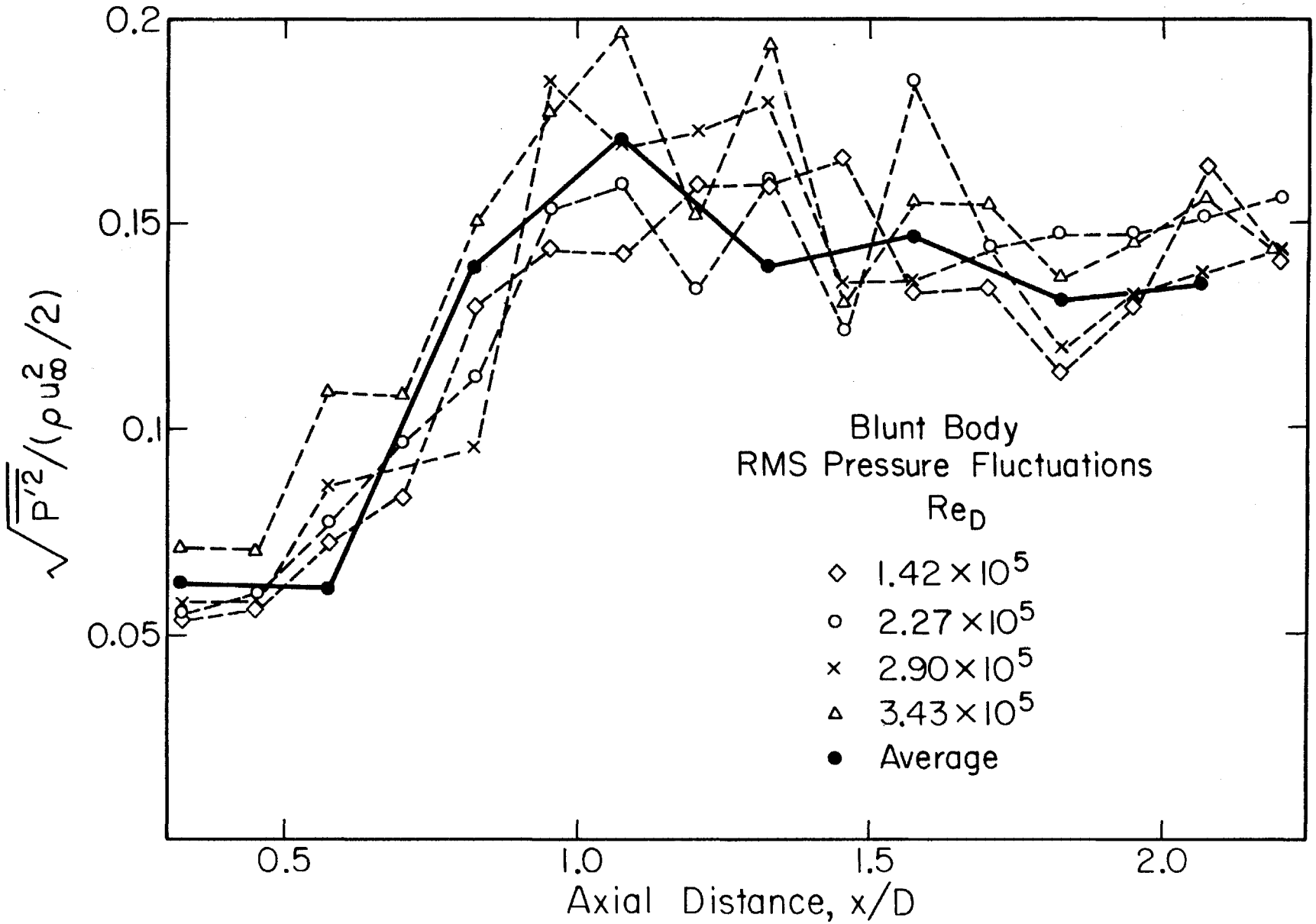

Fig. 3.3 Rms values of the fluctuating pressure on the surface of the blunt body.

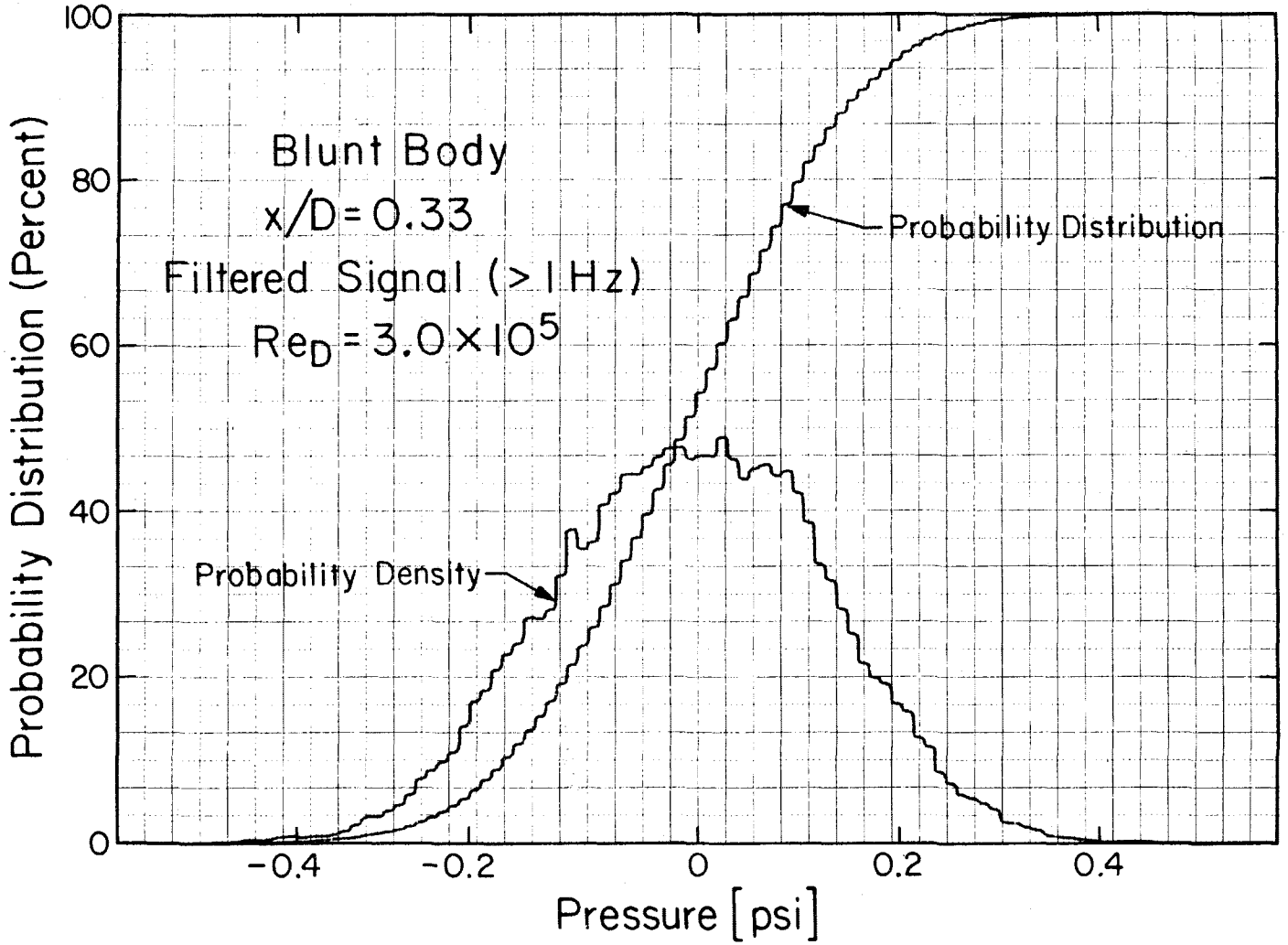

Figure 3.4. Probability density and distribution histograms of pressure fluctuations at x/D=0.328, u_∞=18 ft/sec, Re_D=3.0x10^5.

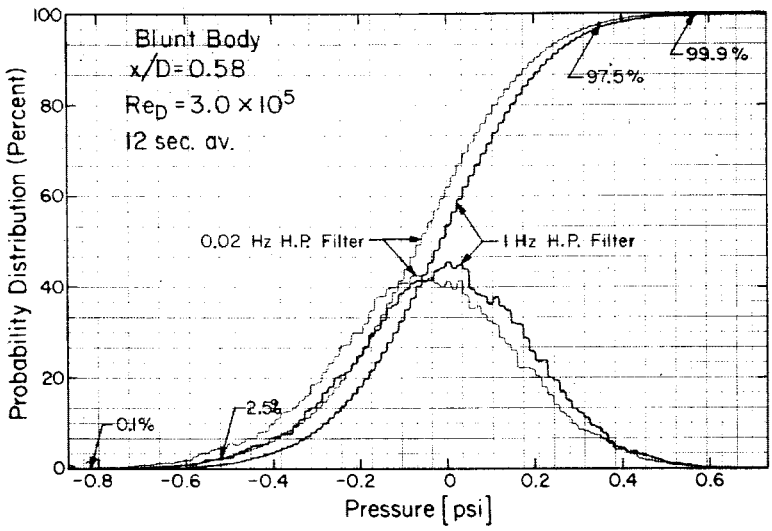

Fig. 3.5. Probability density and distribution histograms of pressure fluctuations at x/D=0.578 and $Re_D = 3.0 \times 10^5$ displaying the effects of signal filterings.(Sampling time is 12 seconds.)

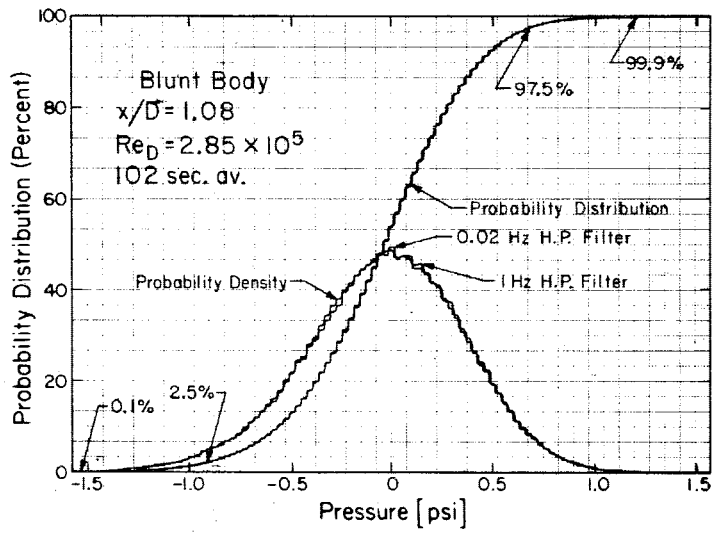

Fig. 3.6. Probability density and distribution histograms of pressure fluctuations at x/D=1.078 and $Re_D = 2.85 \times 10^5$ displaying the effects of filtering when the sampling time is 102 seconds.

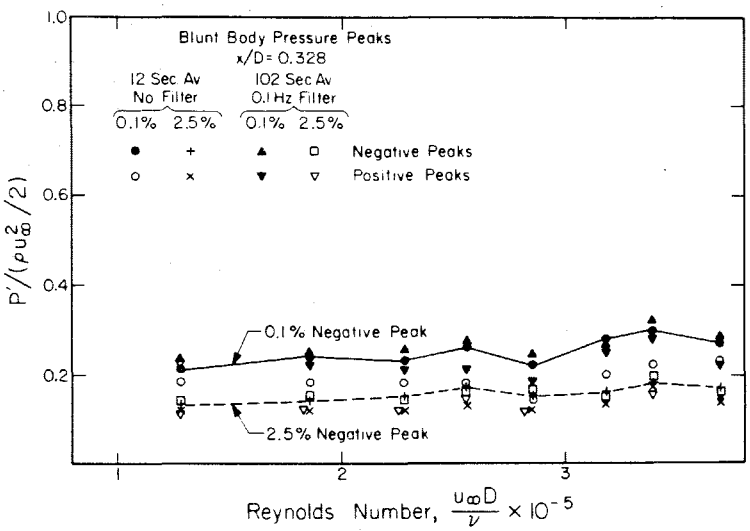

Fig. 3.7. Peak values of pressure fluctuations on the surface of the blunt body at x/D = 0.328.

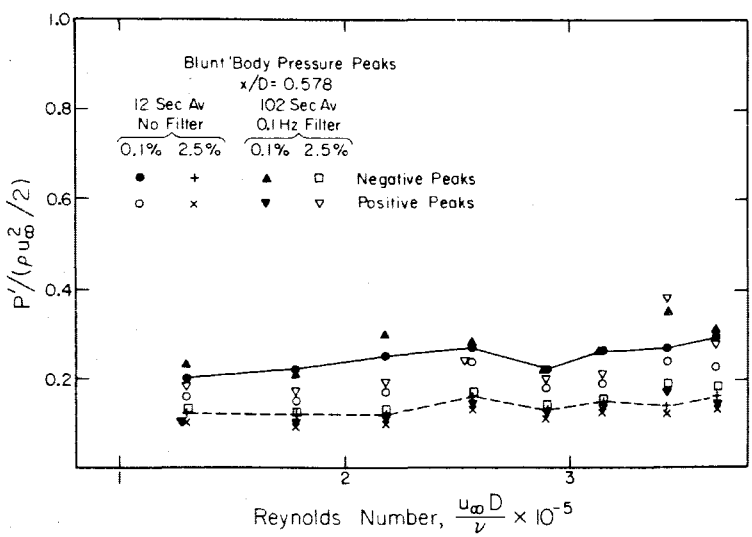

Fig. 3.8. Peak values of pressure fluctuations on the surface of the blunt body at x/D = 0.578.

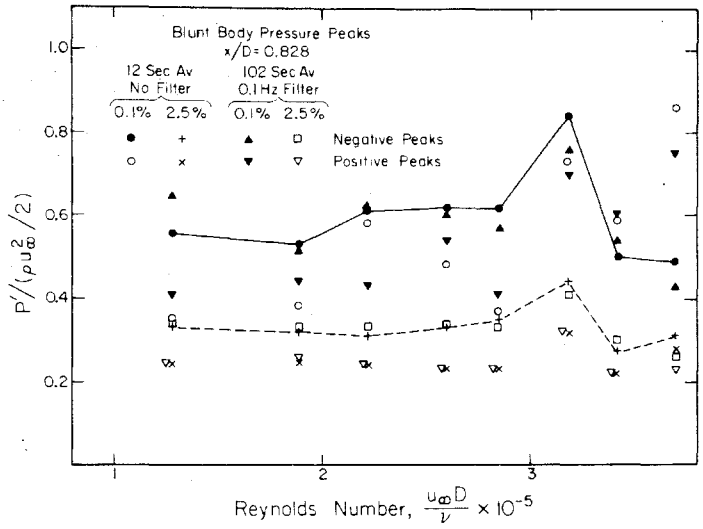

Fig. 3.9. Peak values of pressure fluctuations on the surface of the blunt body at x/D = 0.828.

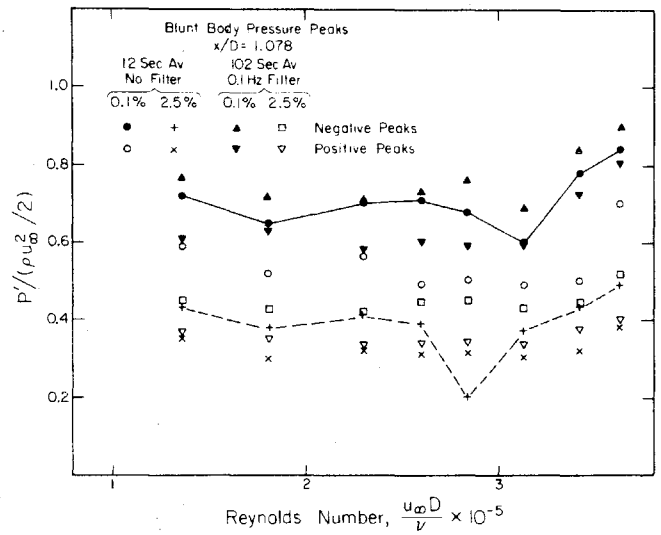

Fig. 3.10. Peak values of pressure fluctuations on the surface of the blunt body at x/D = 1.08.

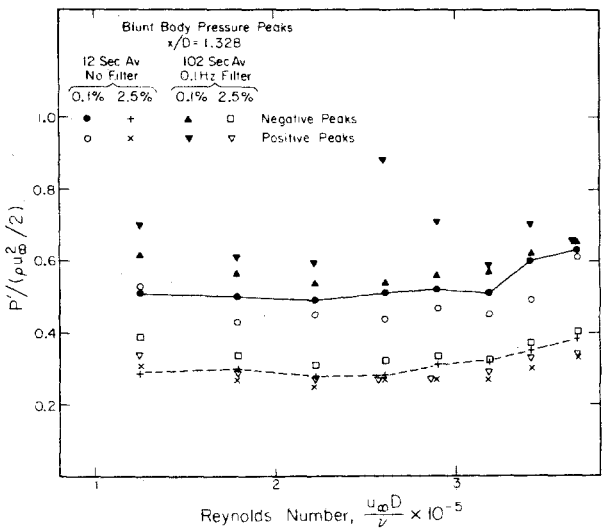

Fig. 3.11. Peak values of pressure fluctuations on the surface of the blunt body at x/D = 1.328.

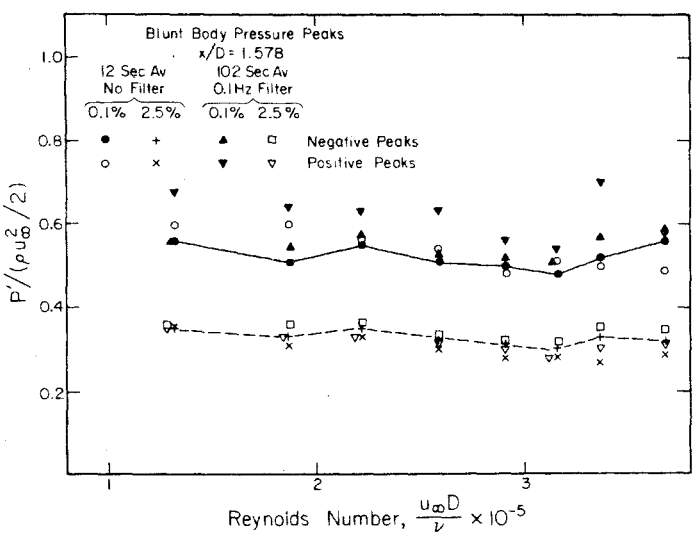

Fig. 3.12. Peak values of pressure fluctuations on the surface of the blunt body at x/D = 1.578.

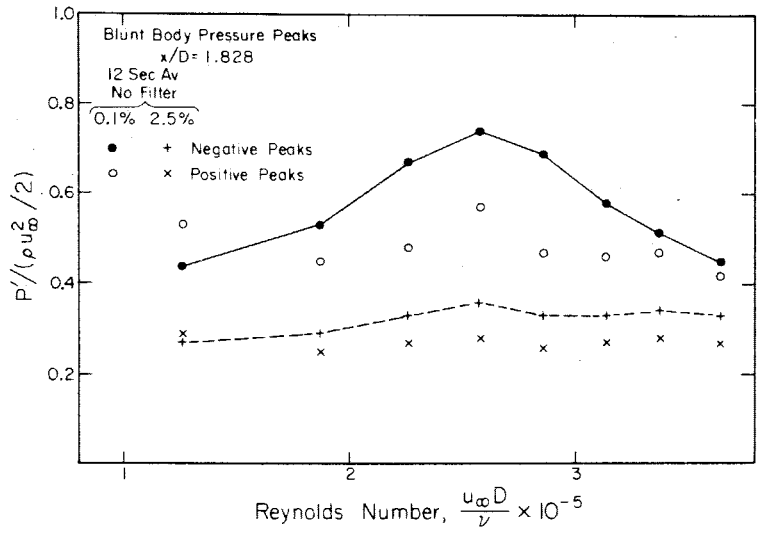

Fig. 3.13. Peak values of pressure fluctuations on the surface of the blunt body at x/D = 1.828.

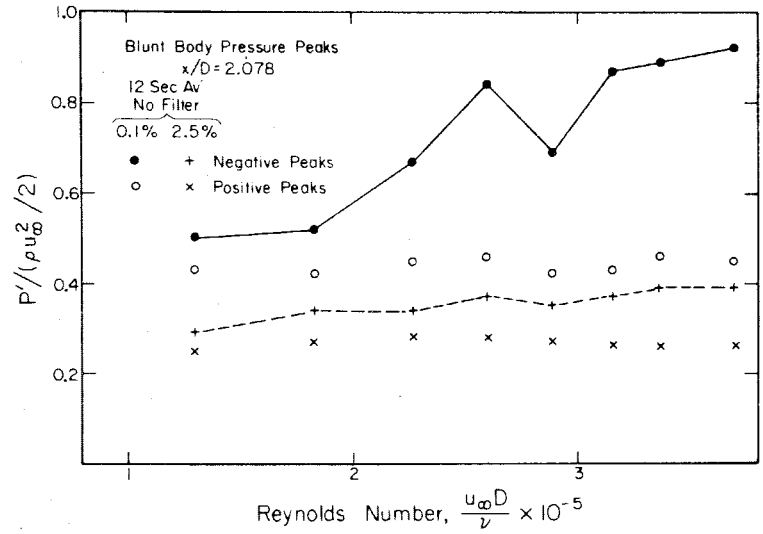

Fig. 3.14. Peak values of pressure fluctuations on the surface of the blunt body at x/D = 2.078.

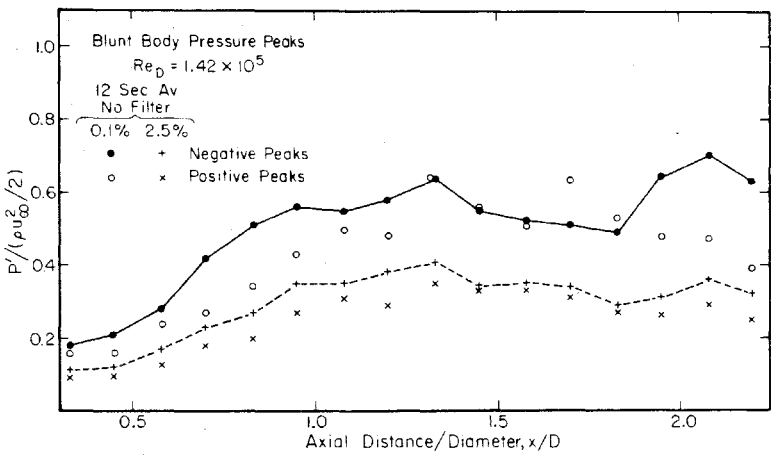

Fig. 3.15. Axial distribution of the pressure fluctuation peaks on the surface of the blunt body. $u_\infty = 8.8$ ft/sec , $Re_D = 1.4 \times 10^5$.

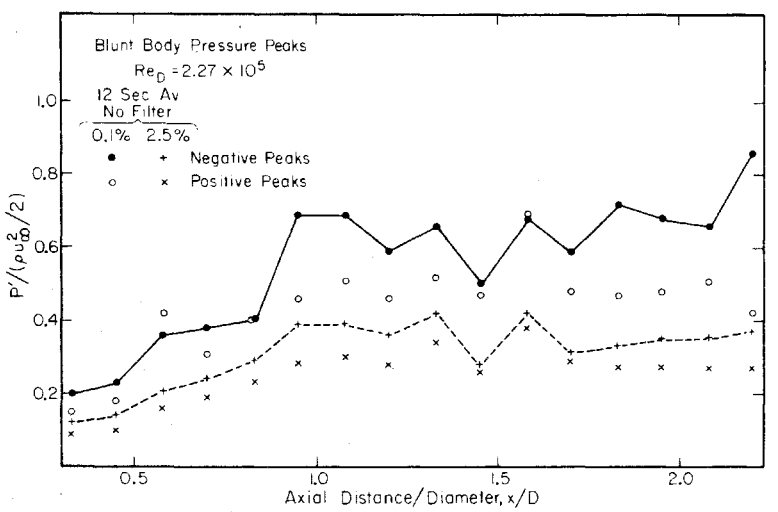

Fig. 3.16. Axial distribution of the pressure fluctuation peaks on the surface of the blunt body. $u_\infty = 14$ ft/sec, $Re_D = 2.3 \times 10^5$.

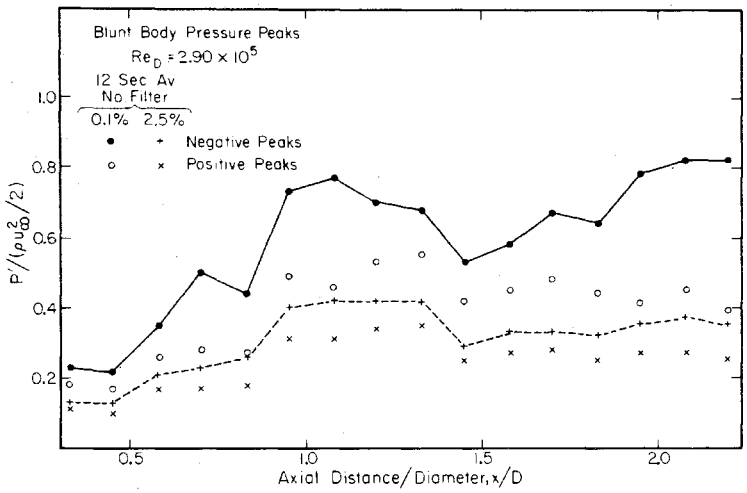

Fig. 3.17. Axial distribution of the pressure fluctuation peaks on the surface of the blunt body. $u_\infty = 18$ ft/sec , $Re_D = 2.9 \times 10^5$.

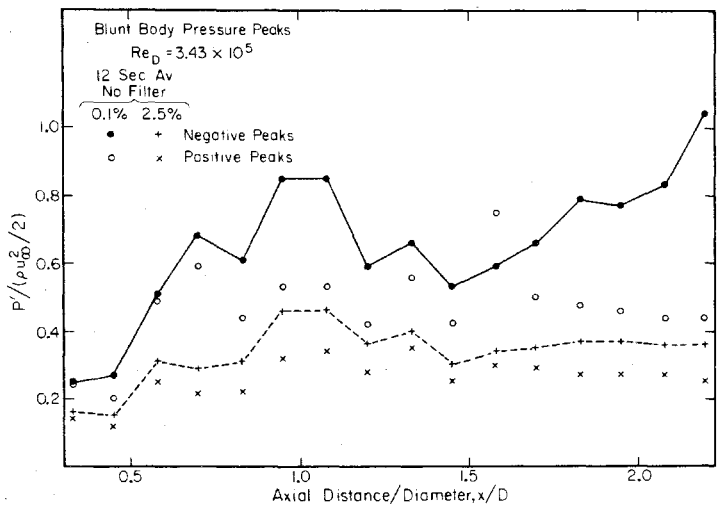

Fig. 3.18. Axial distribution of the pressure fluctuation peaks on the surface of the blunt body. $u_\infty = 21$ ft/sec , $Re_D = 3.4 \times 10^5$.

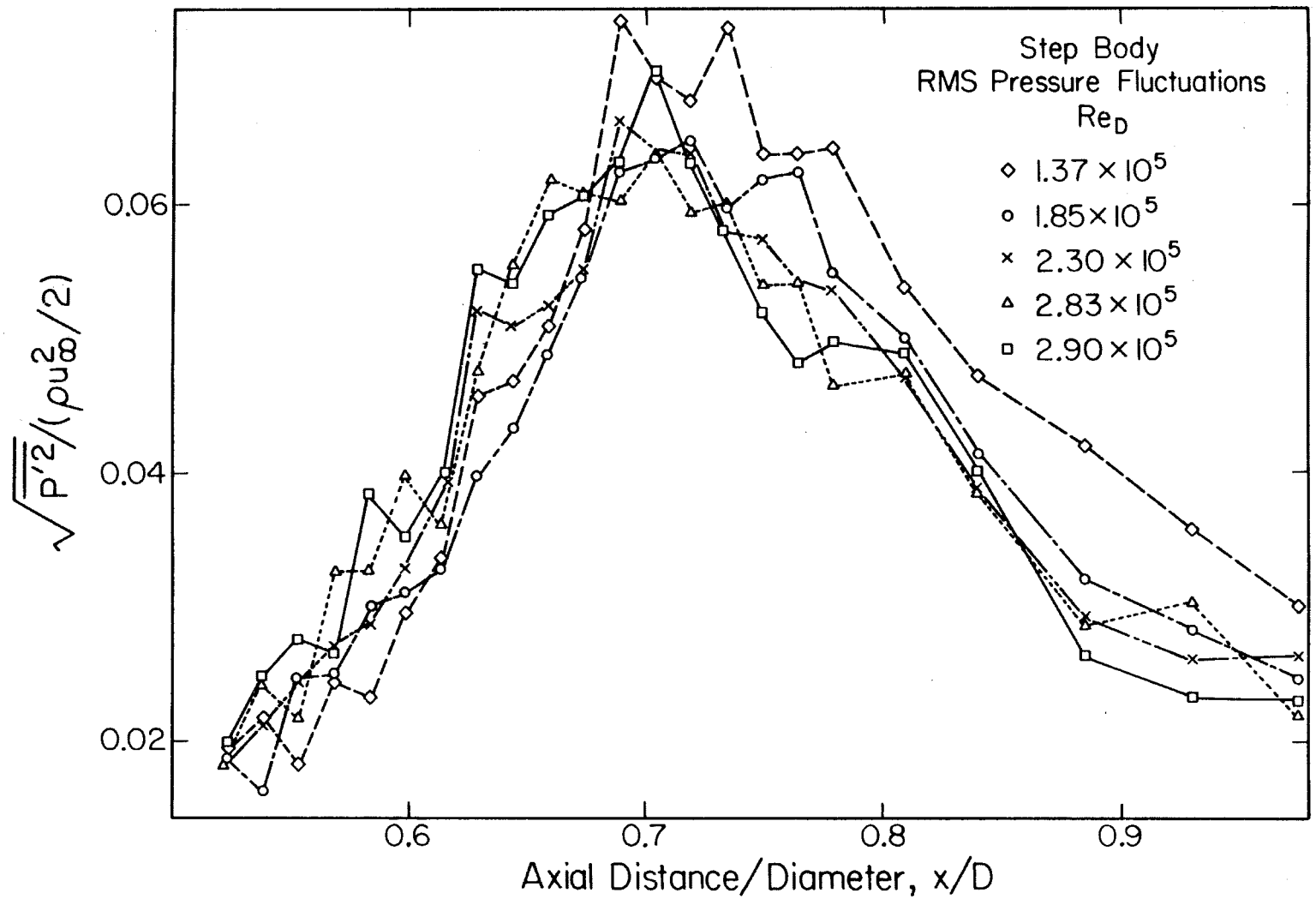

Figure 3.19. Rms values of the fluctuating pressure on the surface of the step body plotted against the axial location.

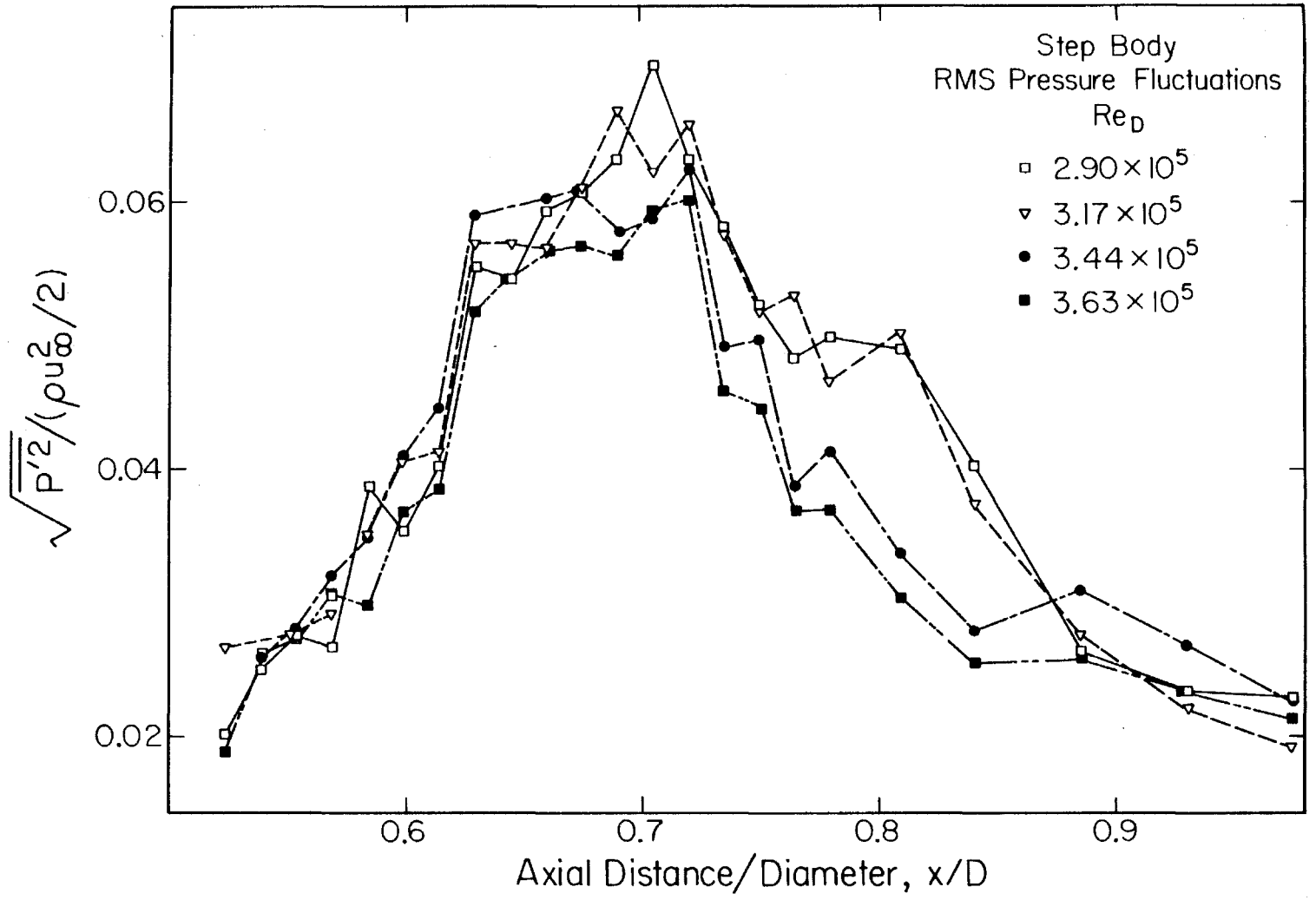

Figure 3.20. Rms values of the fluctuating pressure on the surface of the step body plotted against the axial location.

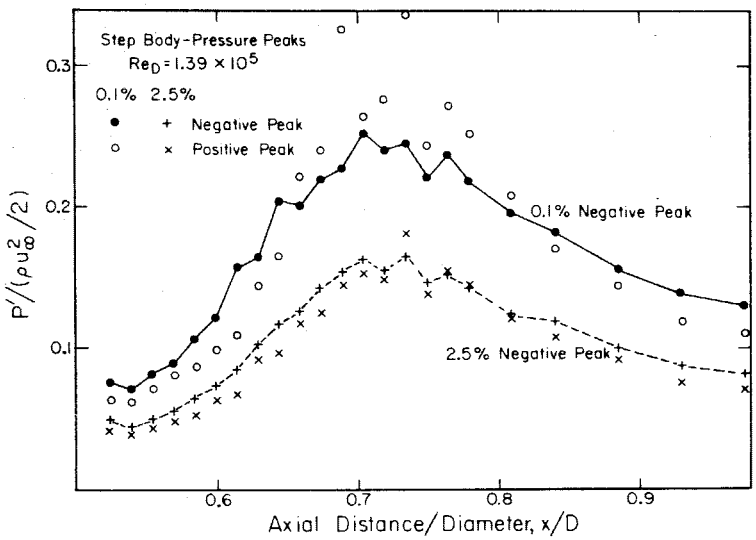

Fig. 3.21. Axial distribution of pressure fluctuation peaks on the surface of the step body. $u_\infty = 8.6$ ft/sec , $Re_D = 1.4 \times 10^5$.

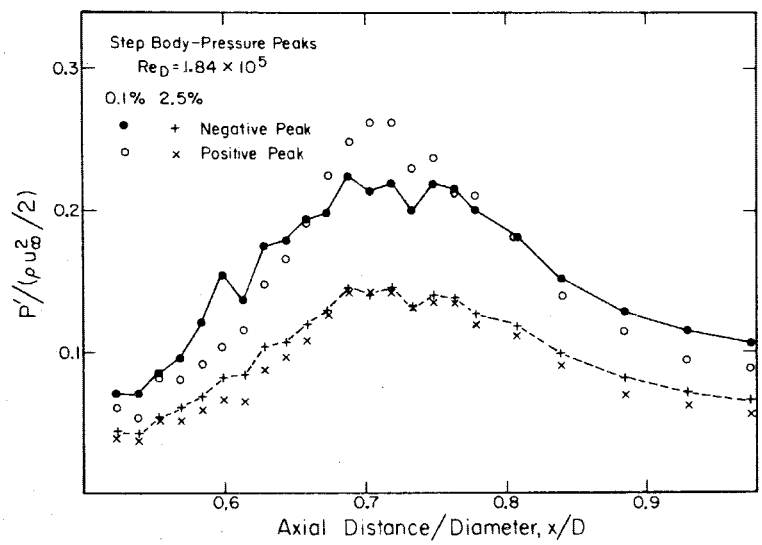

Fig. 3.22. Axial distribution of pressure fluctuation peaks on the surface of the step body. $u_\infty = 11.4$ ft/sec , $Re_D = 1.84 \times 10^5$.

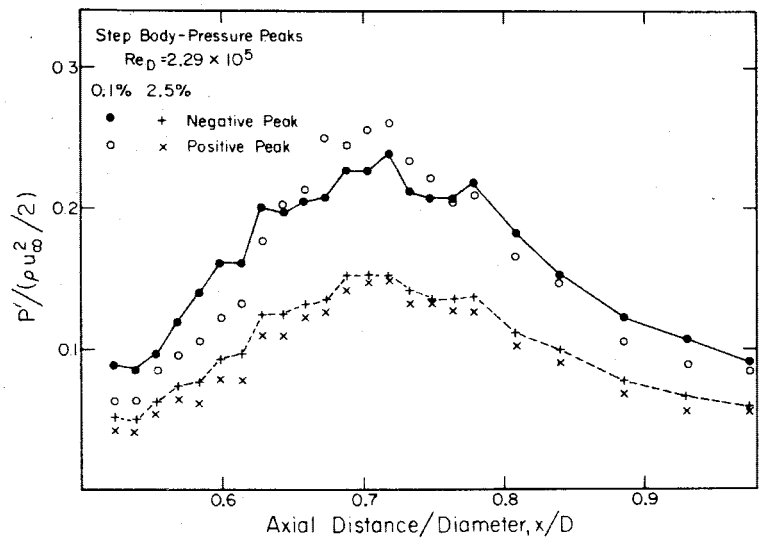

Fig. 3.23. Axial distribution of pressure fluctuation peaks on the surface of the step body. $u_\infty = 14.2$ ft/sec , $Re_D = 2.29 \times 10^5$.

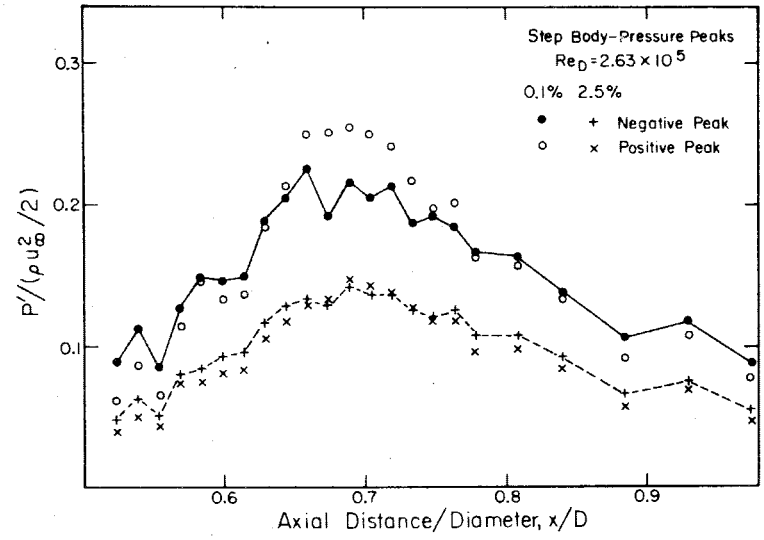

Fig. 3.24. Axial distribution of pressure fluctuation peaks on the surface of the step body. $u_\infty = 16.3$ ft/sec , $Re_D = 2.63 \times 10^5$.

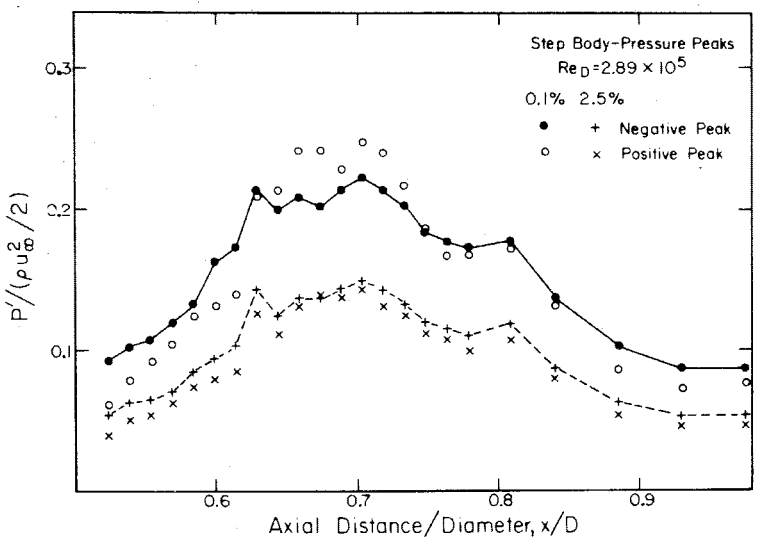

Fig. 3.25. Axial distribution of pressure fluctuation peaks on the surface of the step body. $u_\infty = 17.9$ ft/sec , $Re_D = 2.89 \times 10^5$.

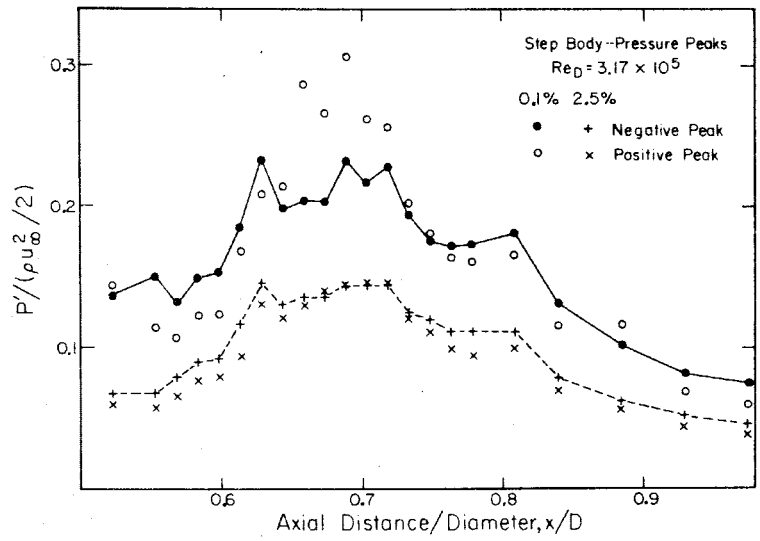

Fig. 3.26. Axial distribution of pressure fluctuation peaks on the surface of the stop body. $u_\infty = 19.6$ ft/sec , $Re_D = 3.17 \times 10^5$.

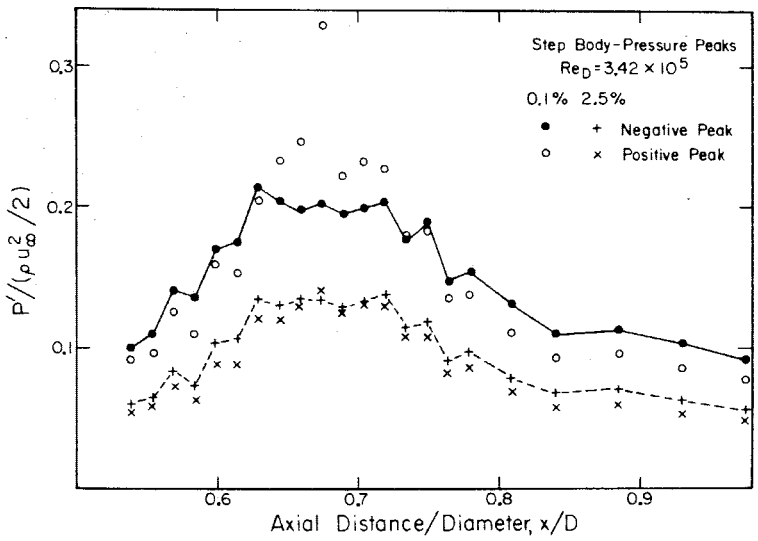

Fig. 3.27. Axial distribution of pressure fluctuation peaks on the surface of the step body. $u_\infty = 21.2$ ft/sec , $Re_D = 3.42 \times 10^5$.

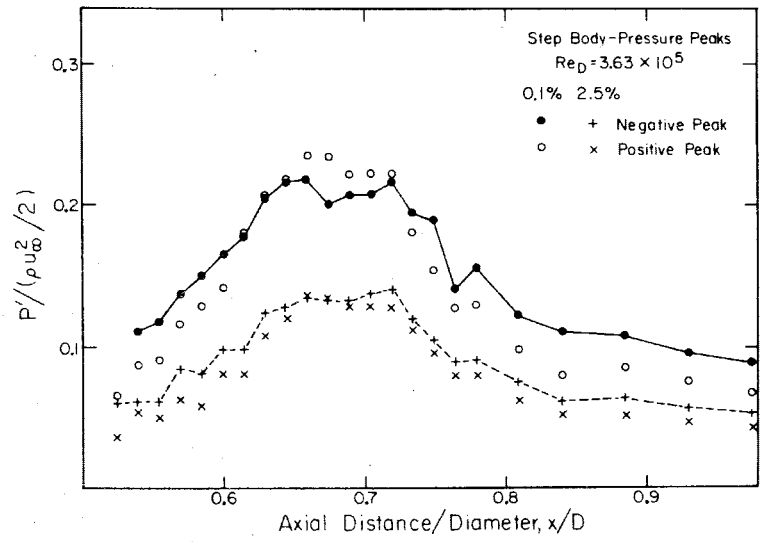

Fig. 3.28. Axial distribution of pressure fluctuation peaks on the surface of the step body. $u_\infty = 22.5$ ft/sec , $Re_D = 3.63 \times 10^5$.

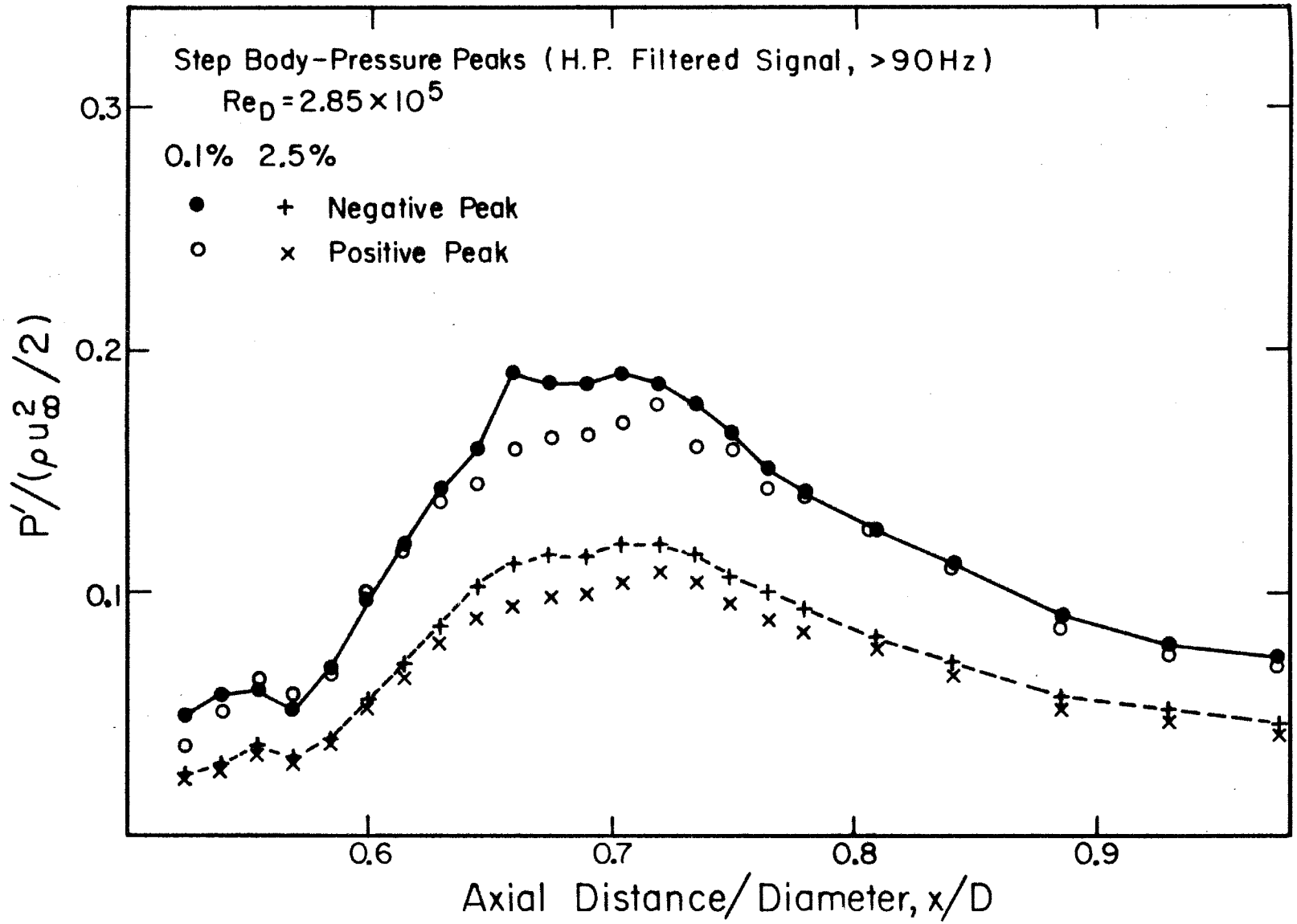

Figure 3.29. Axial distribution of pressure fluctuation peaks on the surface of the step body. The signal is filtered with a high pass filter at 90 hz. $u_\infty = 17.9$ ft/sec, $Re_D = 2.89 \times 10^5$.

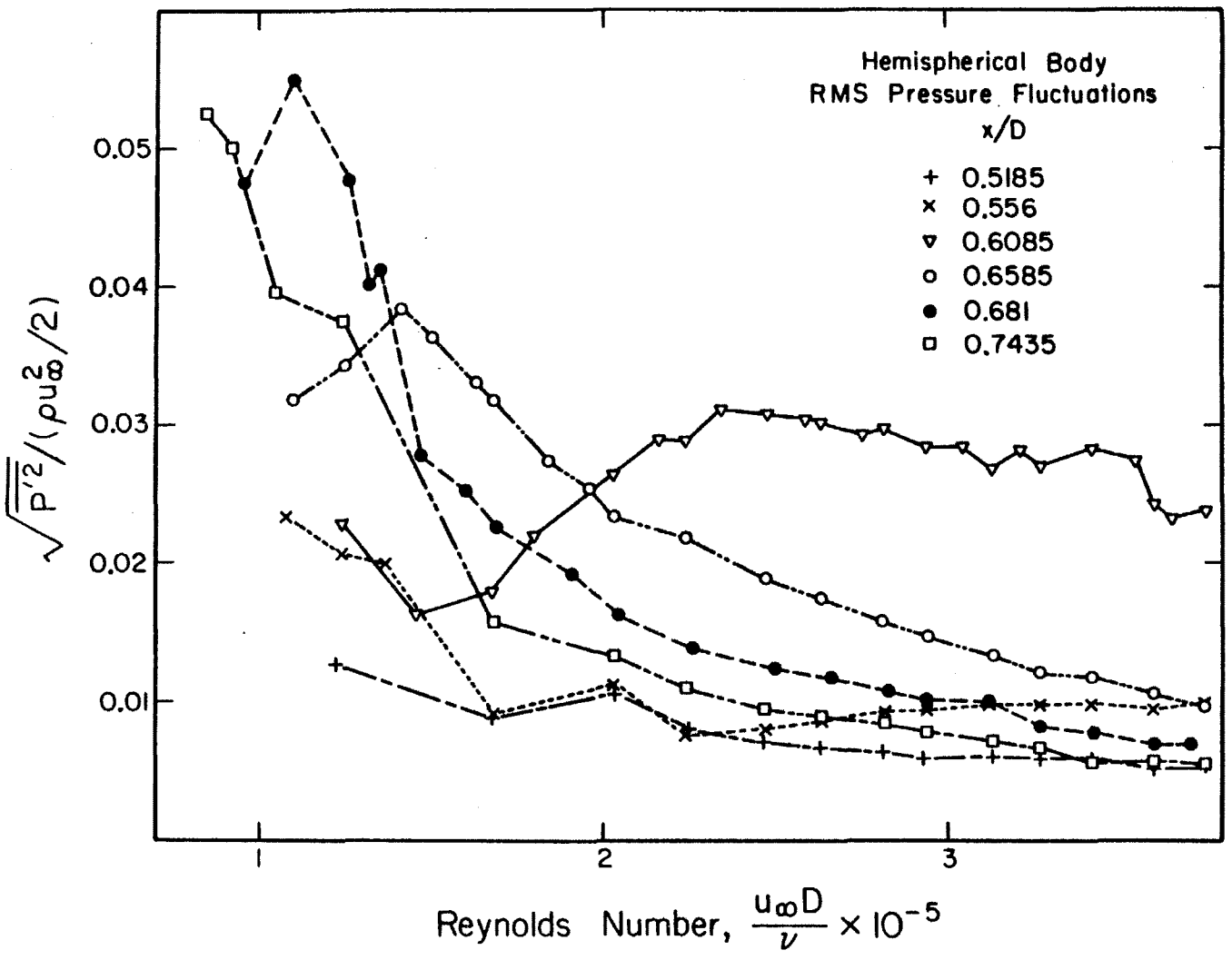

Figure 3.30. Rms values of the fluctuating pressure on the surface of the hemispherical body plotted against the Reynolds number.

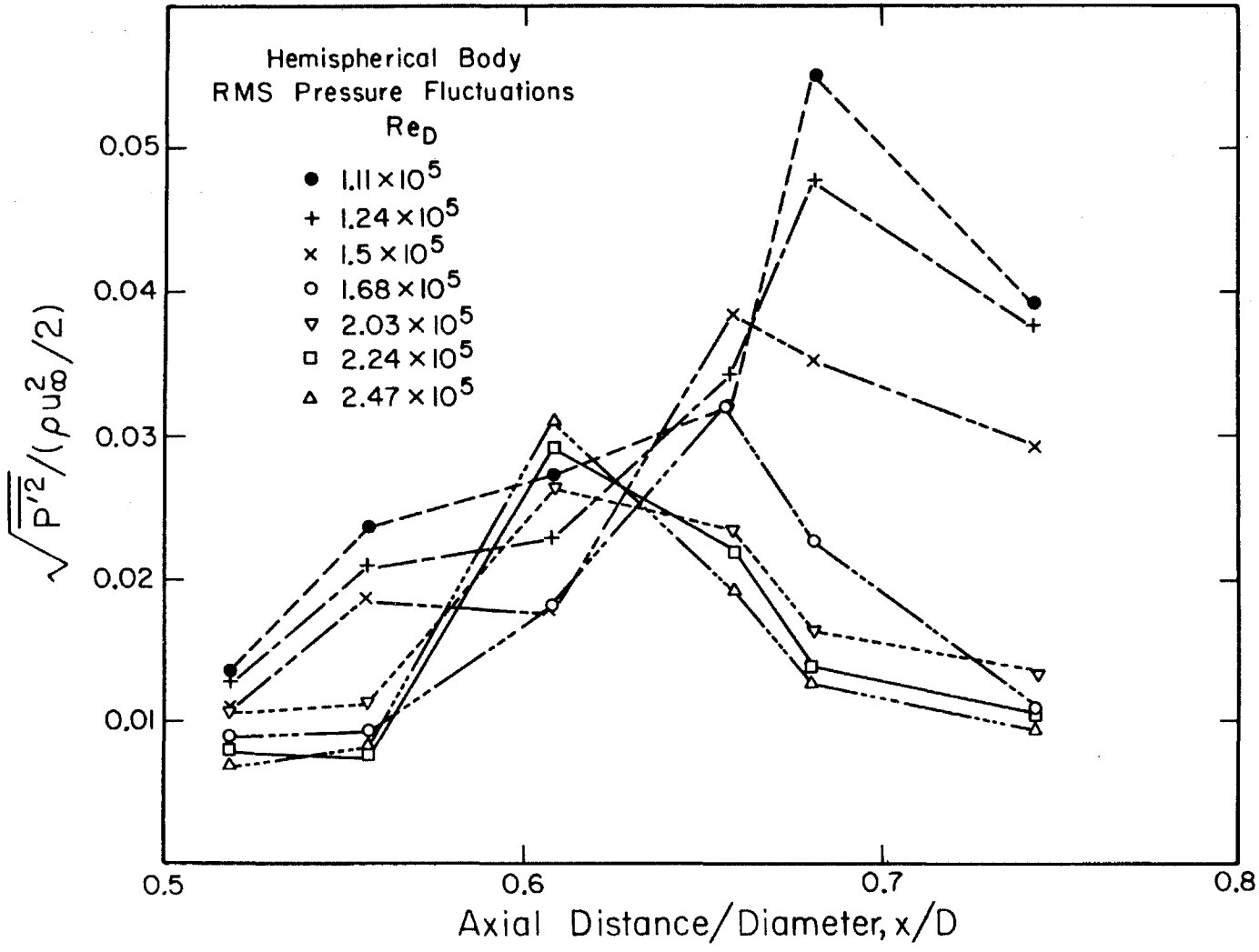

Figure 3.31. Rms values of the fluctuating pressure on the surface of the hemispherical body plotted against the axial location.

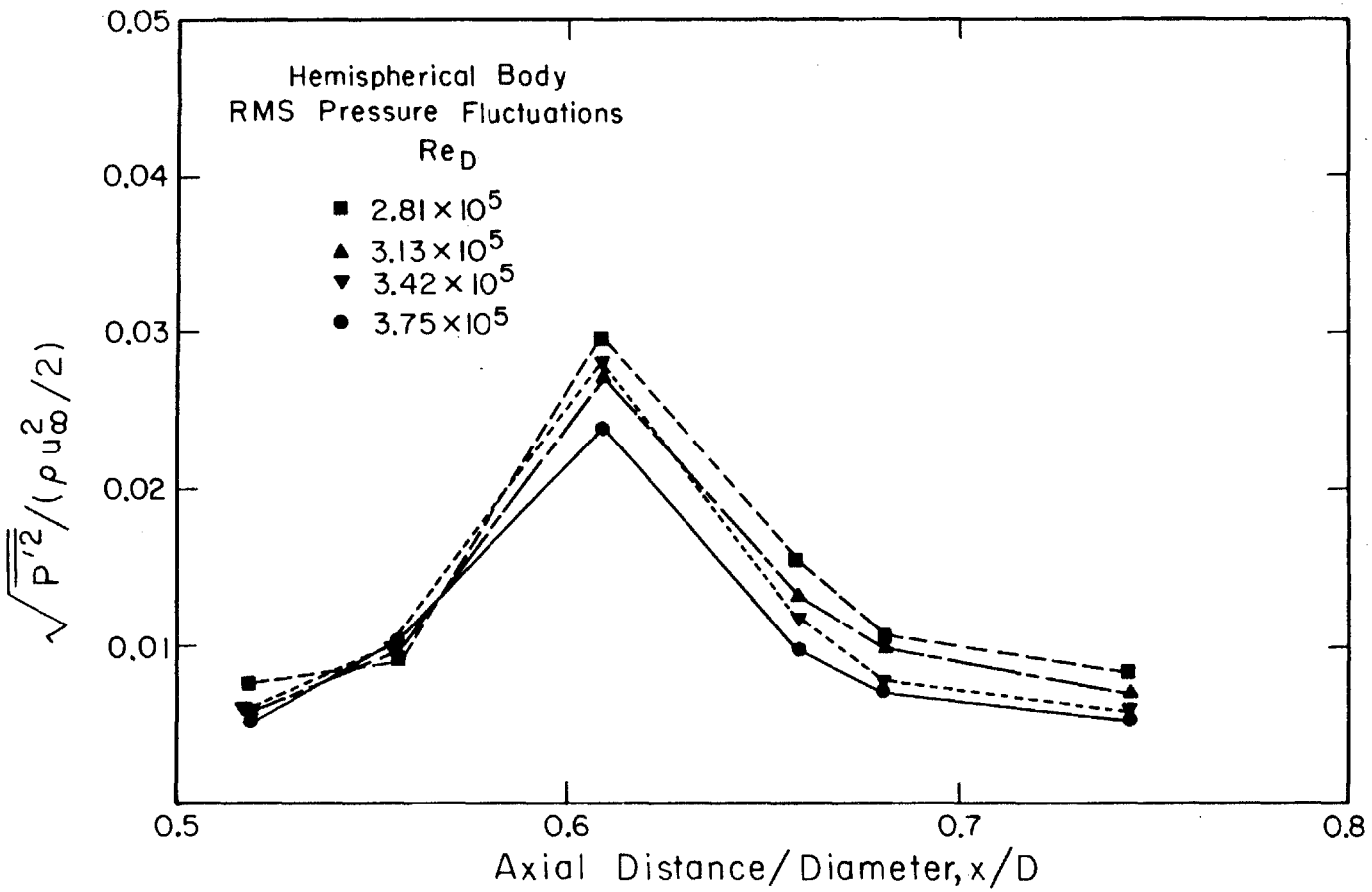

Figure 3.32. Rms values of the fluctuating pressure on the surface of the hemispherical body plotted against the axial location.

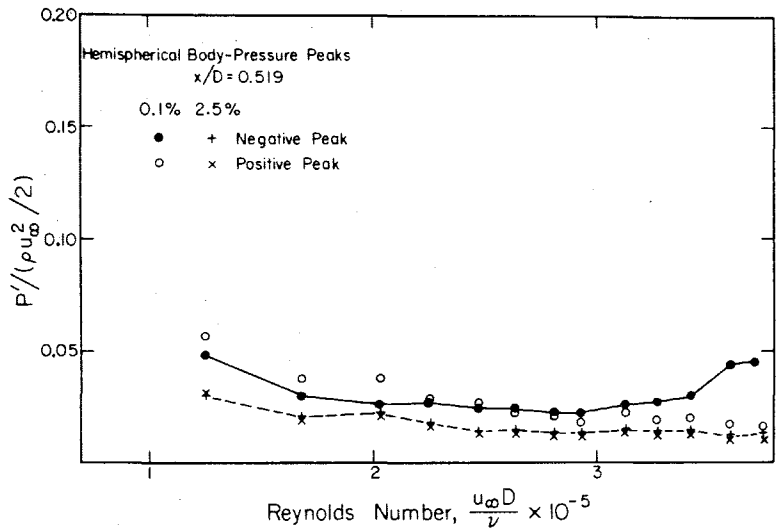

Fig. 3.33. Peak values of pressure fluctuations on the surface of the hemispherical body at x/D = 0.519.

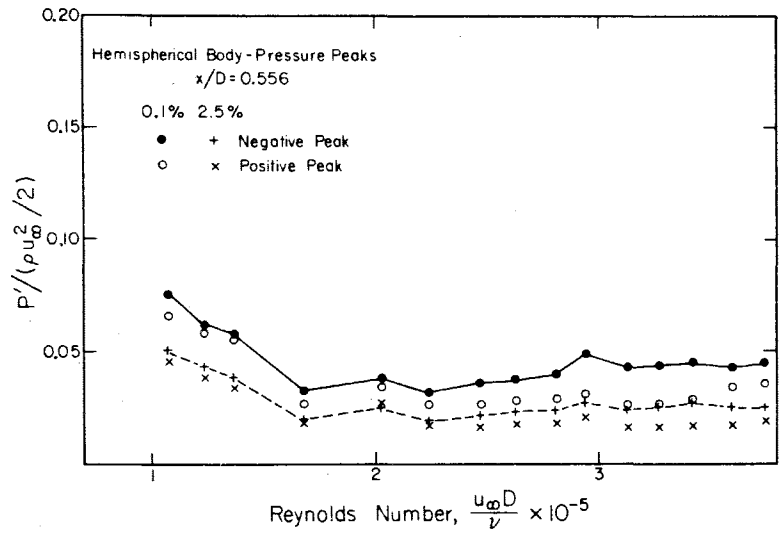

Fig. 3.34. Peak values of pressure fluctuations on the surface of the hemispherical body at x/D = 0.556.

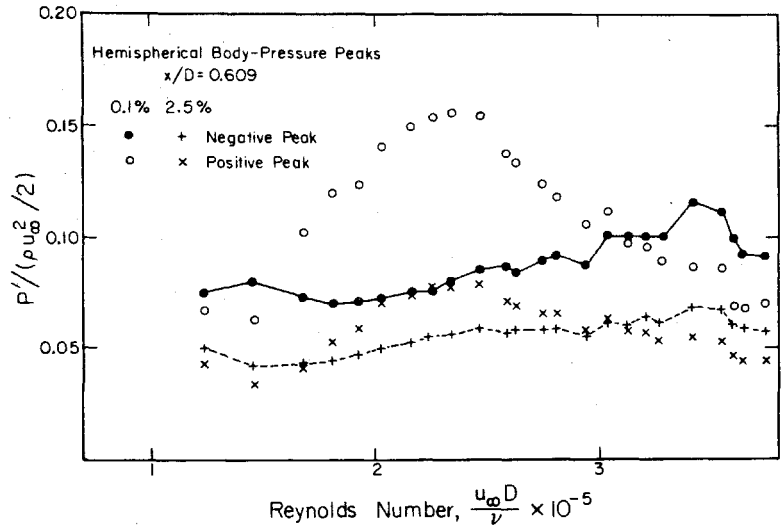

Fig. 3.35. Peak values of pressure fluctuations on the surface of the hemispherical body at x/D = 0.609.

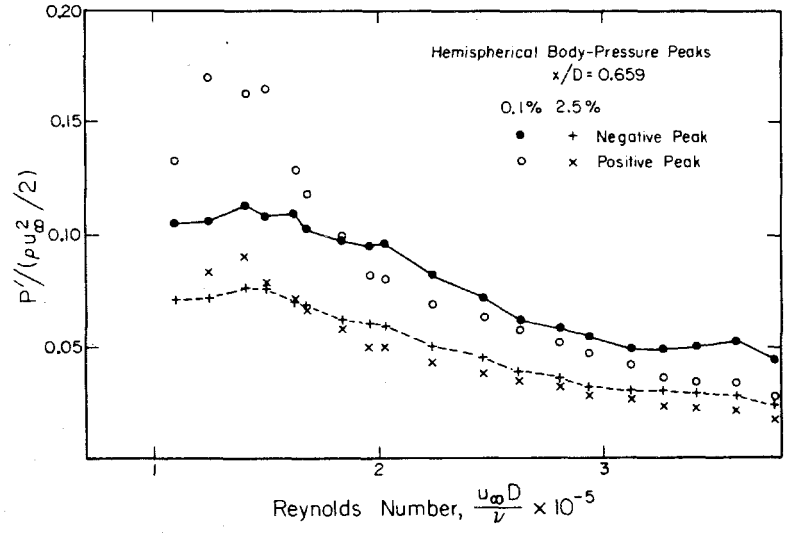

Fig. 3.36. Peak values of pressure fluctuations on the surface of the hemispherical body at x/D = 0.659.

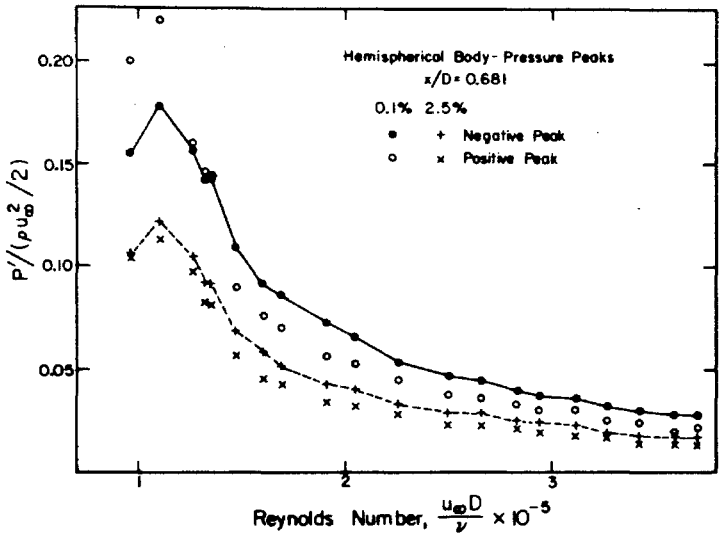

Fig. 3.37. Peak values of pressure fluctuations on the surface of the hemispherical body at x/D = 0.681.

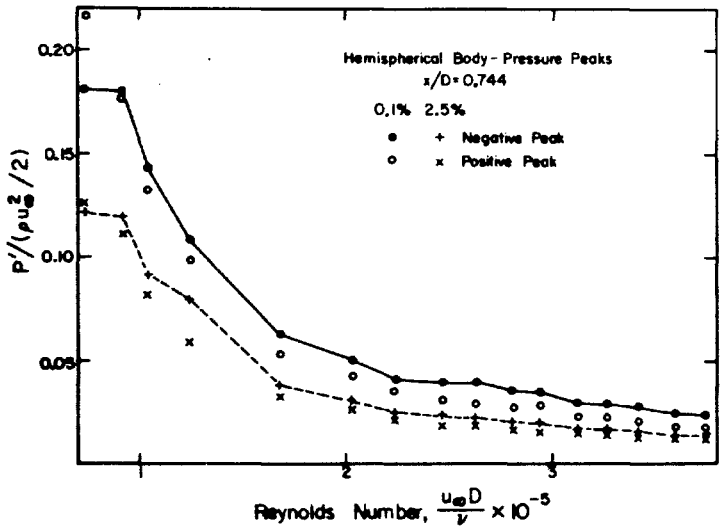

Fig. 3.38. Peak values of pressure fluctuations on the surface of the hemispherical body at x/D = 0.744.

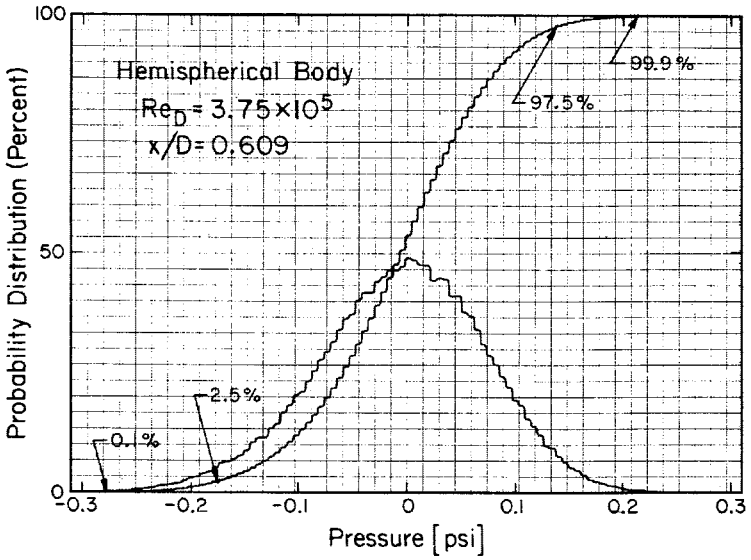

Fig. 3.39. Probability density and distribution histograms of pressure fluctuations on the surface of the hemispherical body. x/D = 0.609, $Re_D = 3.75 \times 10^5$.

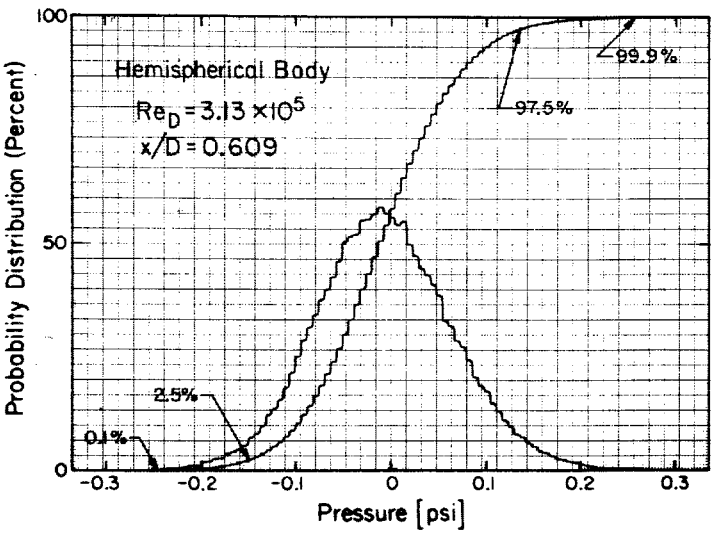

Fig. 3.40. Probability density and distribution histograms of pressure fluctuations on the surface of the hemispherical body. x/D = 0.609, $Re_D = 3.13 \times 10^5$.

(a)

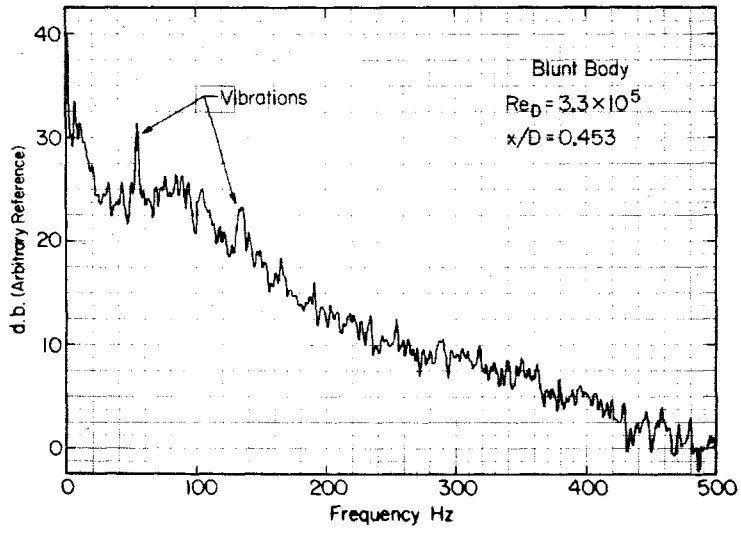

Fig. 3.41. Spectrum of pressure fluctuations on the surface of the blunt body. x/D = 0.453, u_∞ = 21.2 ft/sec . a) 0-500 Hz , b) 0-100 Hz.

(b)

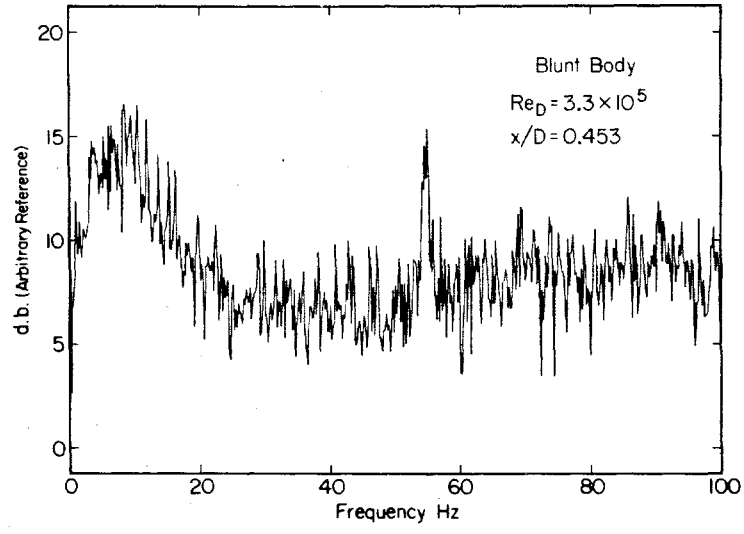

(a)

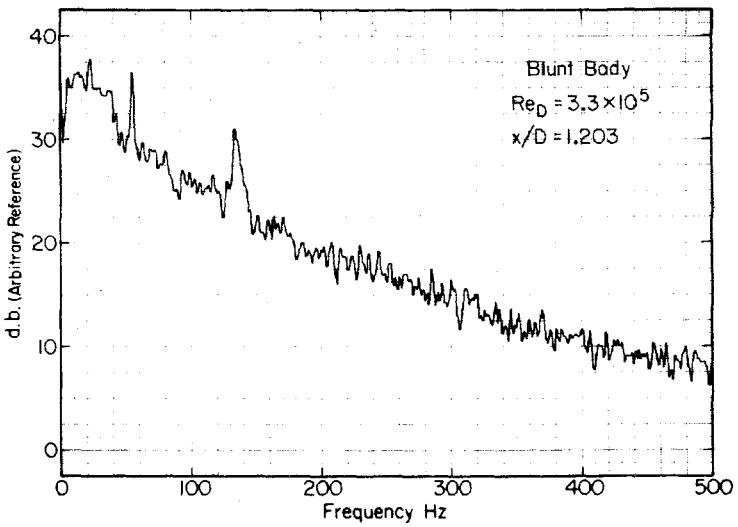

Fig. 3.42. Spectrun of pressure fluctuations on the surface of the blunt body. x/D = 1.203, u_∞ = 21.3 ft/sec . a) 0-500 Hz , b) 0-100 Hz .

(b)

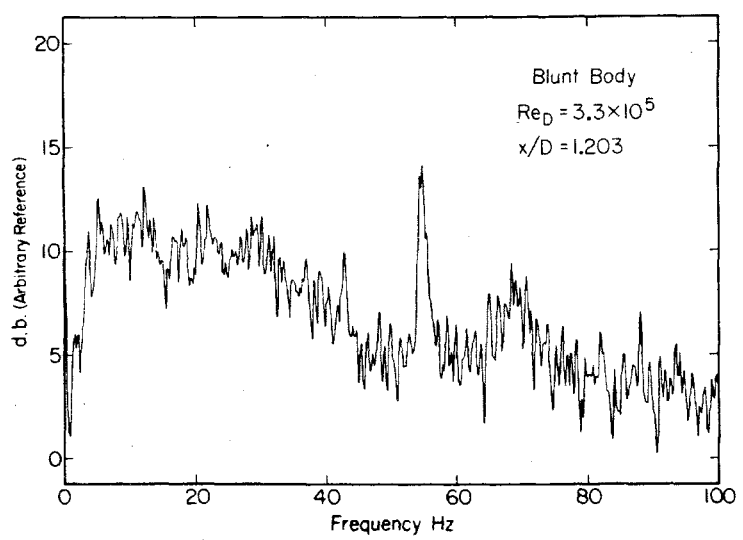

(a)

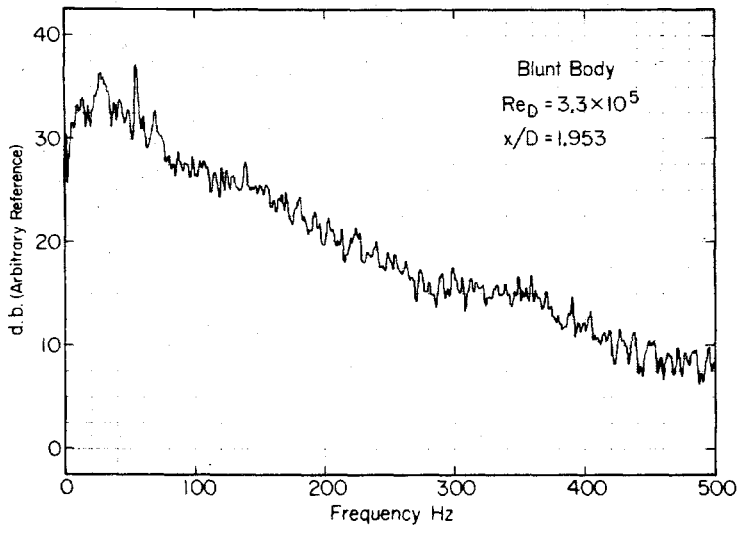

Fig. 3.43. Spectrum of pressure fluctuations in the surface of the blunt body. x/D = 1.953, u_∞ = 21.2 ft/sec , a) 0.500 Hz , b) 0-100 Hz .

(b)

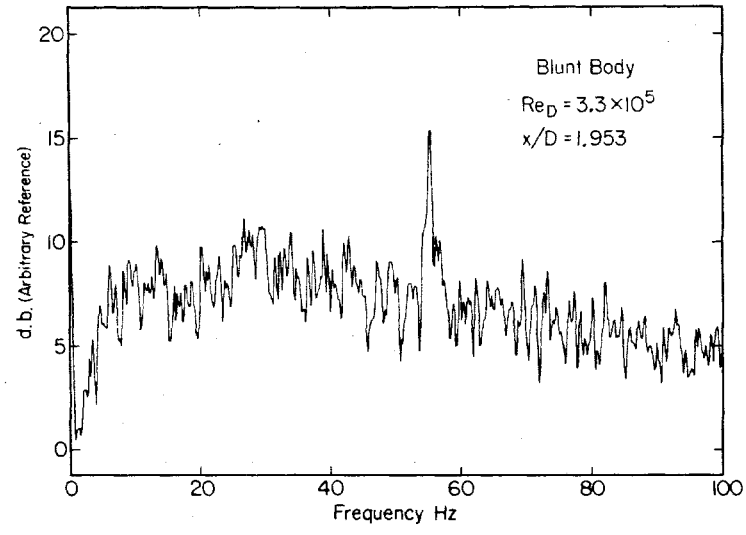

3.44

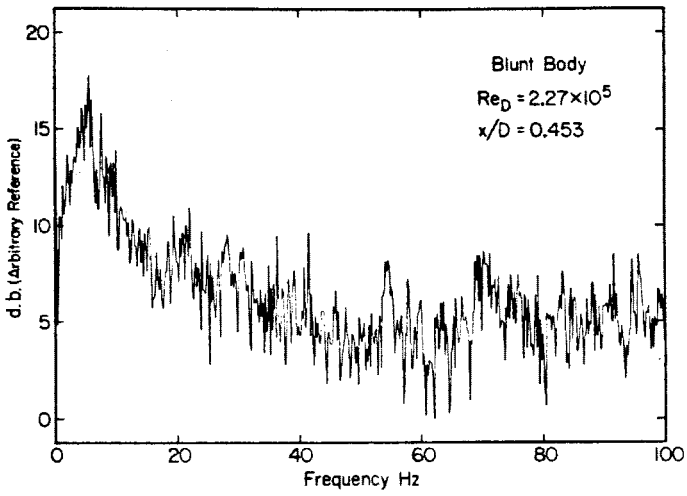

3.45

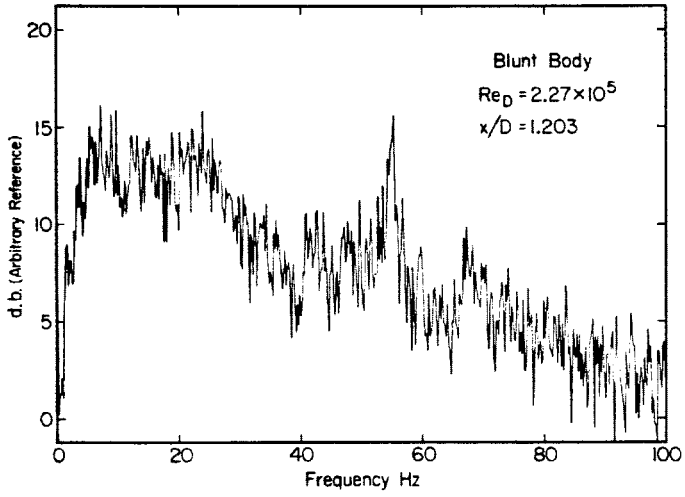

3.46

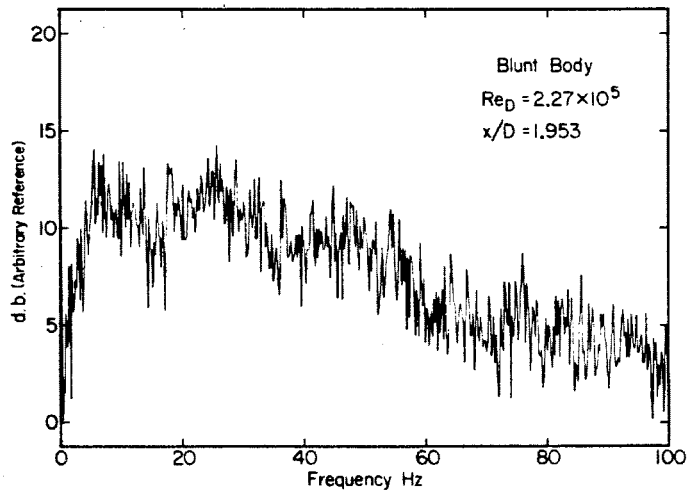

Figs. 3.44,45,46. Spectra of pressure fluctuations on the surface of the blunt body. $u_\infty = 14.1$ ft/sec , $Re_D = 2.3 \times 10^5$. 3-44) x/D = 0.453; 3-45) x/D = 1.203; 3-46) x/D = 1.953.

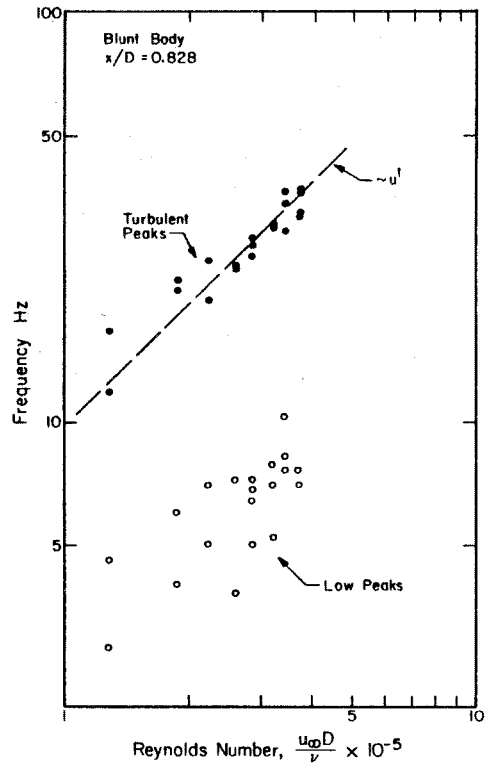

3.47

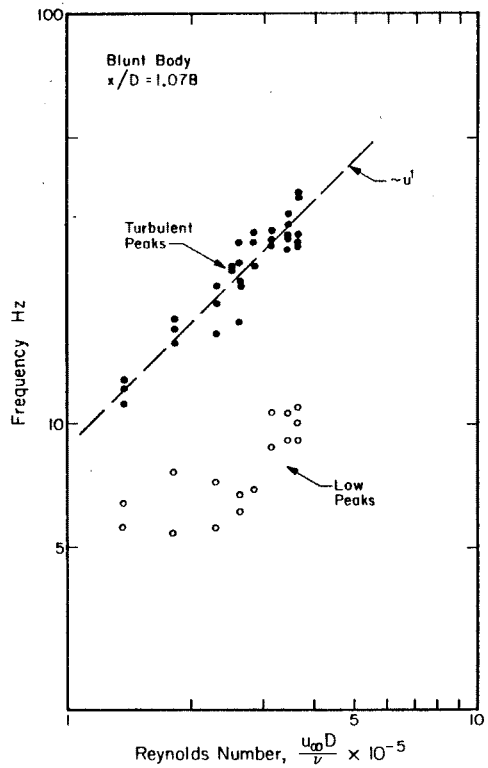

3.48

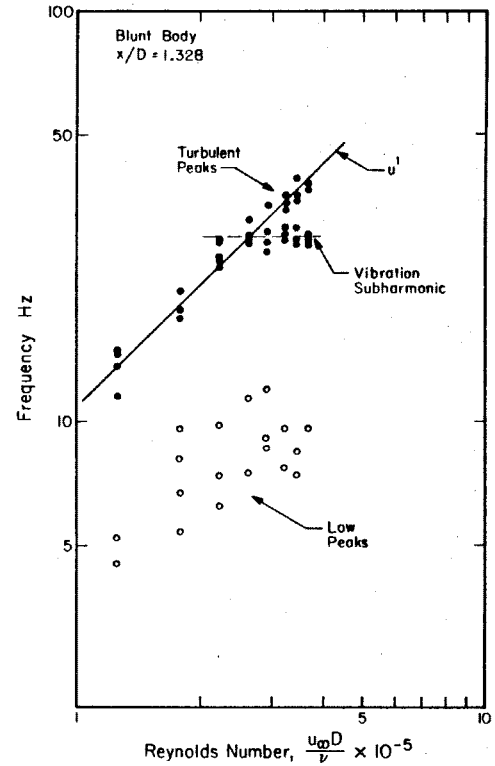

3.49

Figs. 3.47,48,49. Frequency of the peaks in the spectra of pressure fluctuations on the two inch blunt body. 3.47) x/D = 0.828; 3.48 x/D = 1.078; 3.49) x/D = 1.328.

3.50

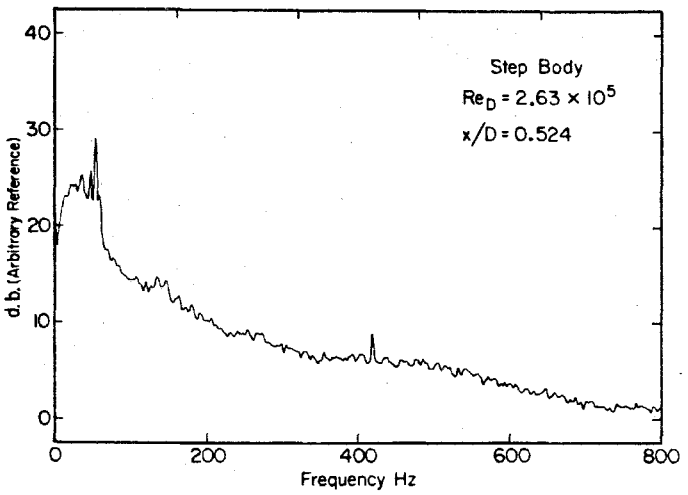

3.51

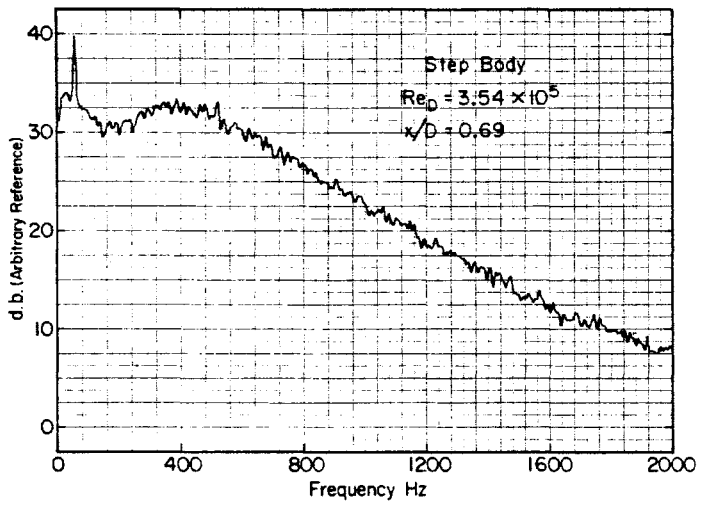

3.52

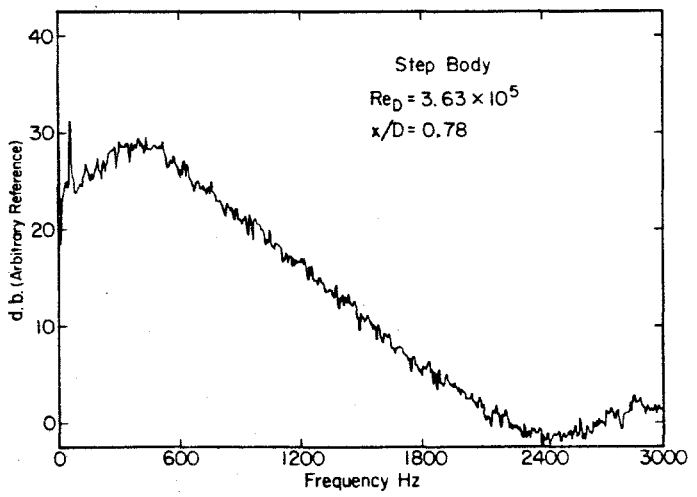

Figs 3.50,51,52. Spectra of pressure fluctuations on the surface of the step body. 3.50) $x'/H = 1.25$, $Re_D = 2.63 \times 10^5$; 3.51) $x'/H = 9.8$, $Re_D = 3.54 \times 10^5$; 3.52) $x'/H = 14.53$, $Re_D = 3.63 \times 10^5$.

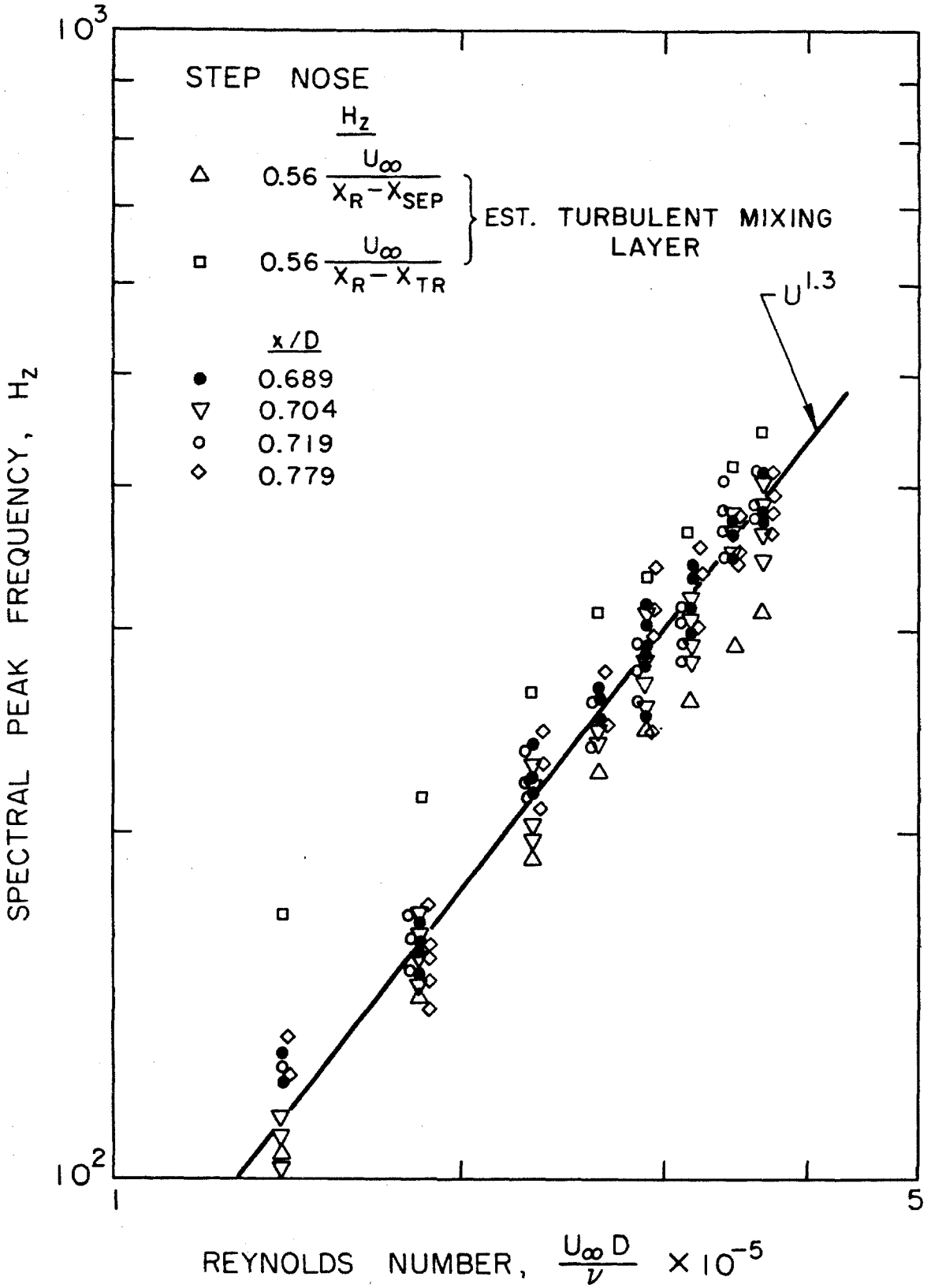

Figure 3.53. A comparison between the step body spectral peaks and the estimated peak frequencies of turbulent fluctuations.

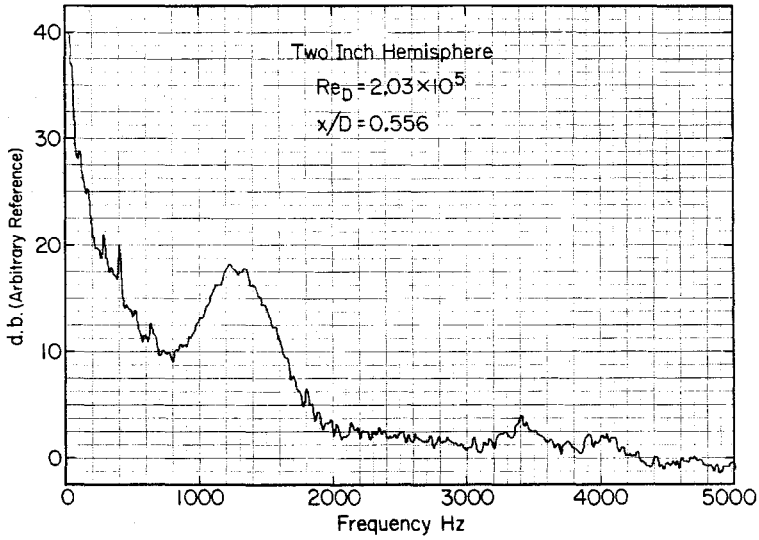

Fig. 3.54. Spectrum of pressure fluctuations on the surface of the hemispherical body. $x/D = 0.556$, $u_\infty = 12.6$ ft/sec , $Re_D = 2.0 \times 10^5$.

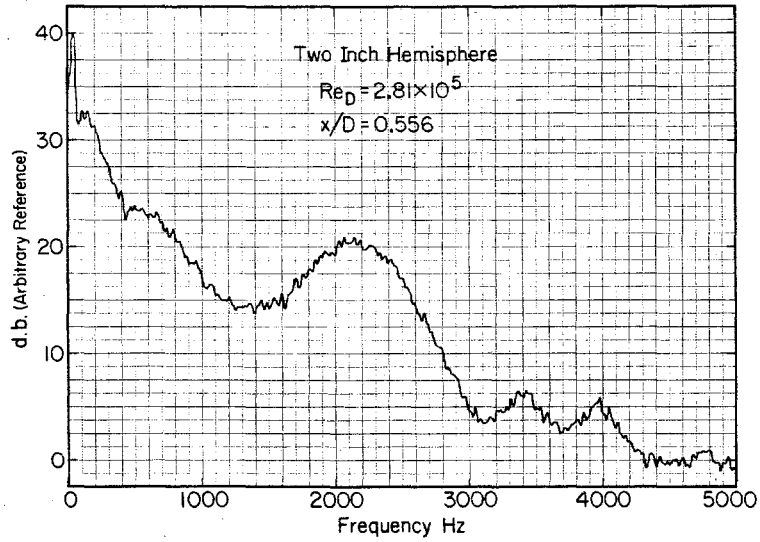

Fig. 3.55. Spectrum of pressure fluctuations on the surface of the hemispherical body. $x/D = 0.556$, $u_\infty = 17.4$ ft/sec , $Re_D = 2.8 \times 10^5$.

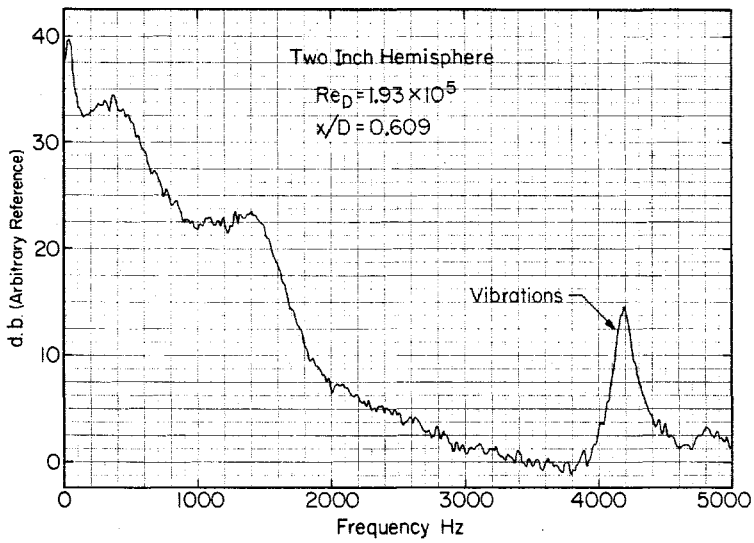

Fig. 3.56. Spectrum of pressure fluctuations on the surface of the hemispherical body. $x/D = 0.609$, $u_\infty = 12.0$ ft/sec , $Re_D = 1.9 \times 10^5$.

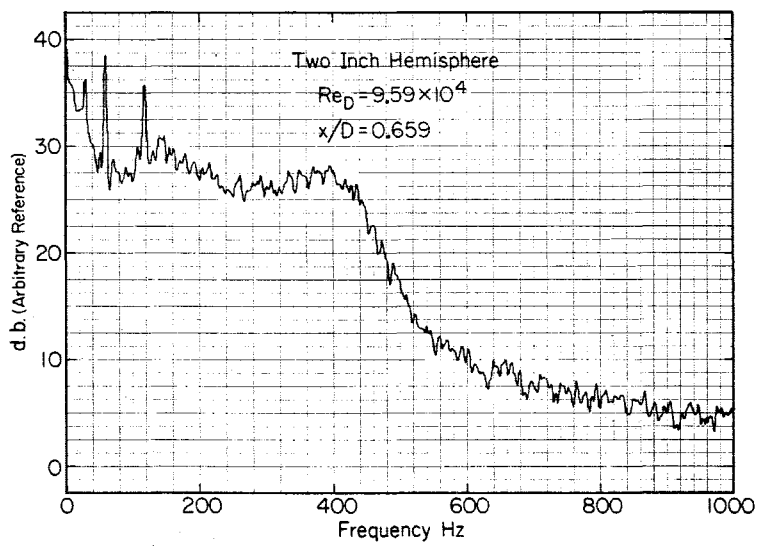

Fig. 3.57. Spectrum of pressure fluctuations on the surface of the hemispherical body. $x/D = 0.681$, $u_\infty = 6$ ft/sec , $Re_D = 9.6 \times 10^5$.

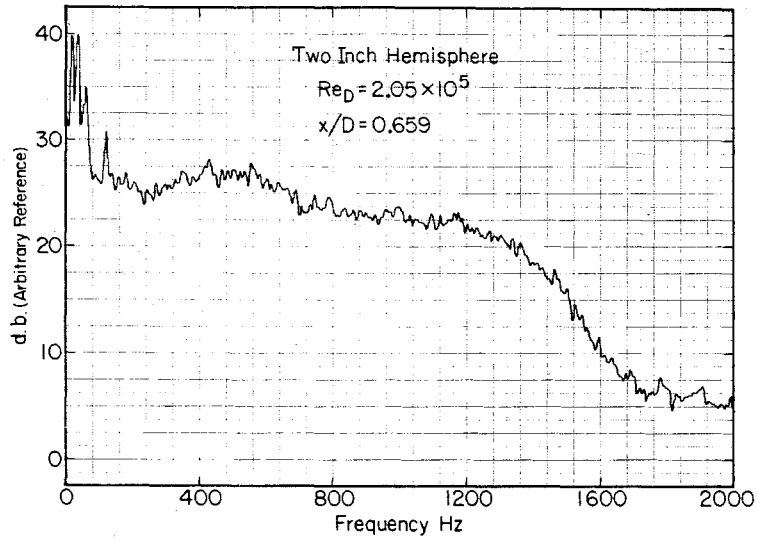

Fig. 3.58. Spectrum of pressure fluctuations on the surface of the hemispherical body. $x/D = 0.681$, $u_\infty = 12.7$ ft/sec , $Re_D = 2.1 \times 10^5$.

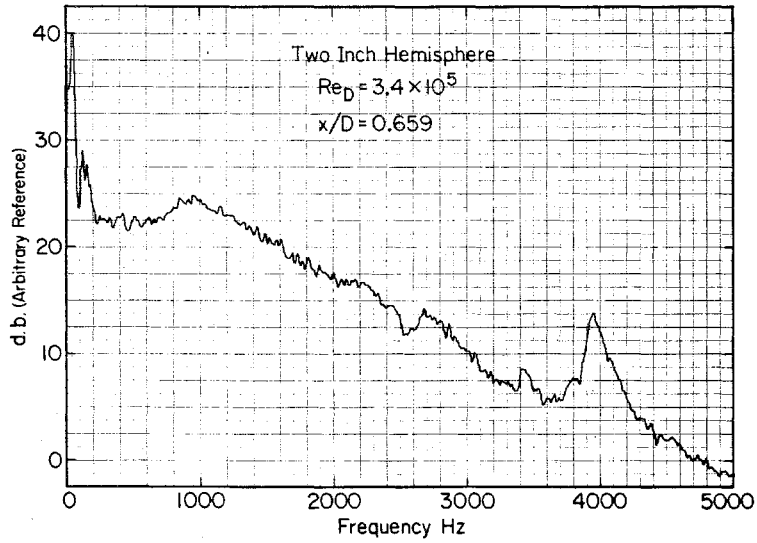

Fig. 3.59. Spectrum of pressure fluctuations on the surface of the hemispherical body. $x/D = 0.681$, $u_\infty = 21.3$ ft/sec , $Re_D = 3.4 \times 10^5$.

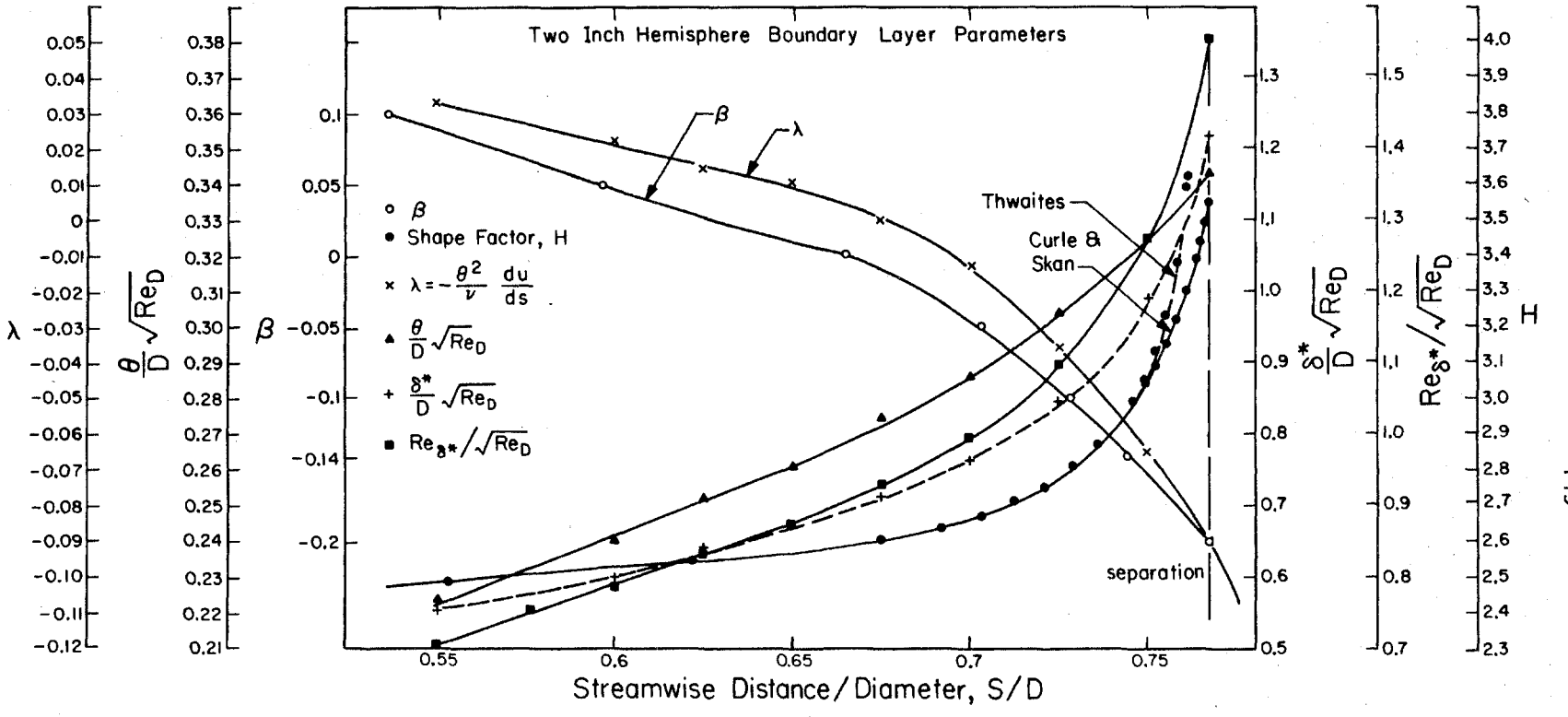

Figure 3.60 Calculated values of the hemispherical body boundary layer parameters.

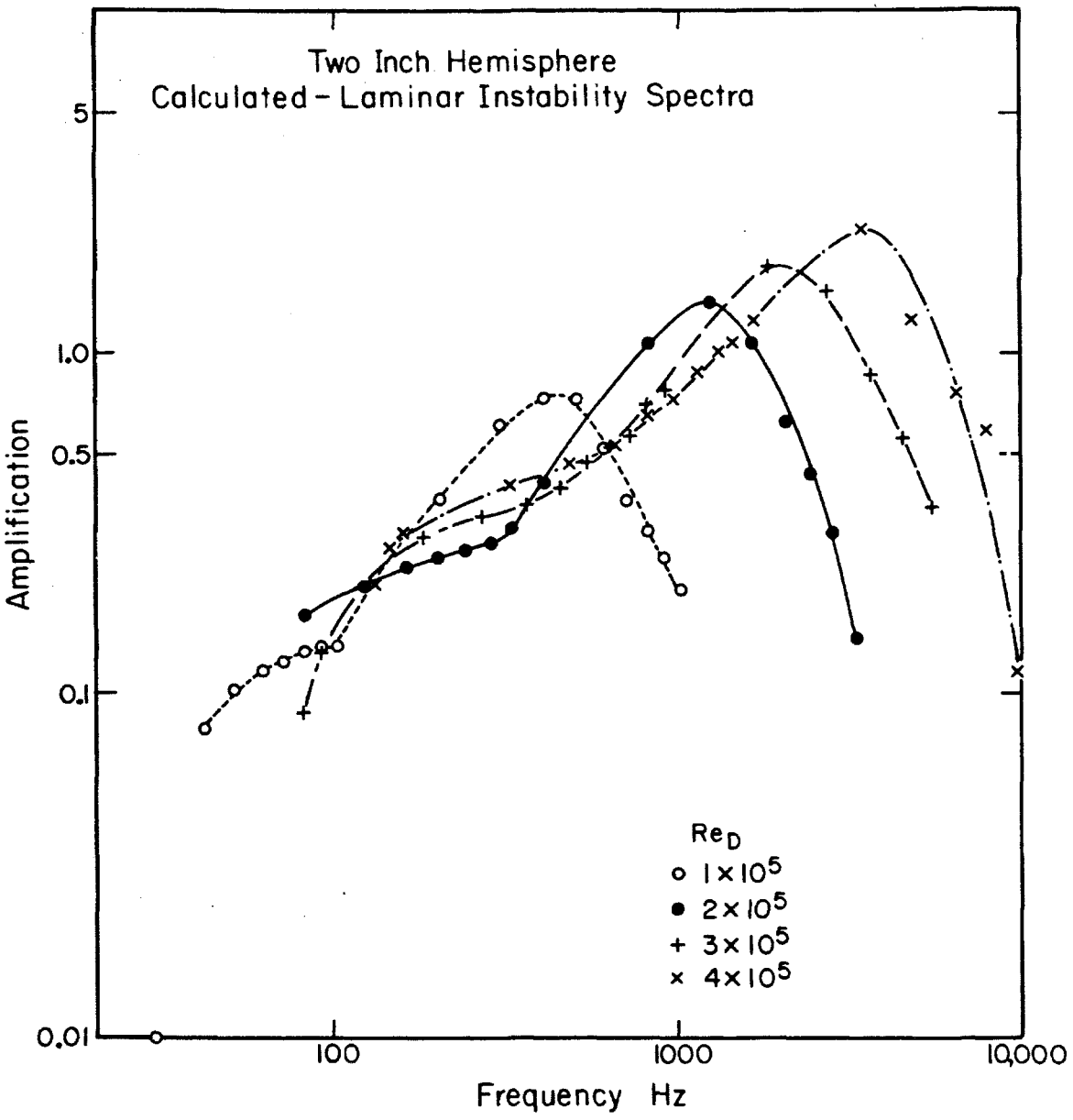

Figure 3.61. Calculated amplification of the laminar boundary layer waves in the separation point of the hemispherical body.

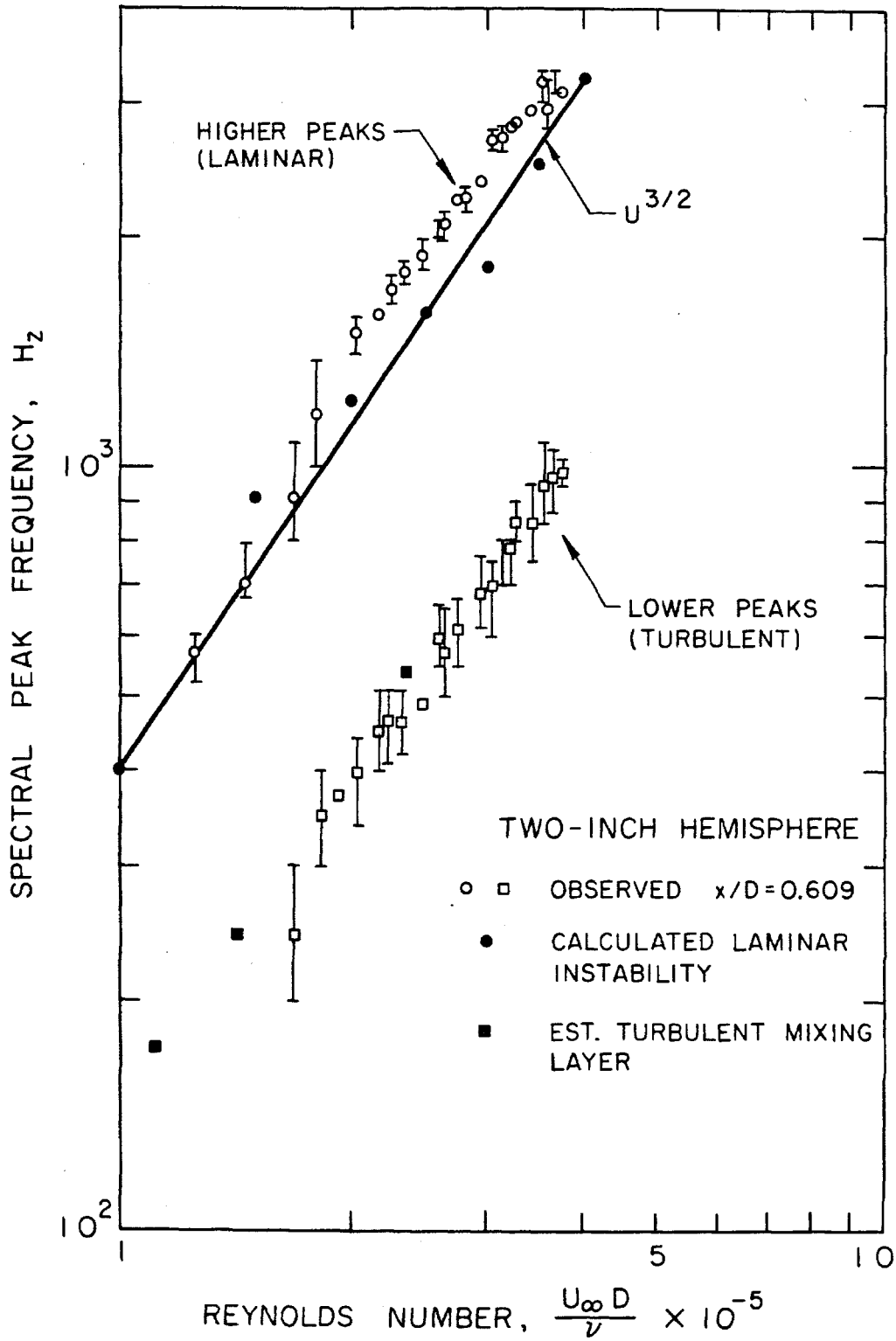

Figure 3.62. Frequency of the peaks in the spectra of pressure fluctuations at x/D=0.609 on the hemispherical body surface. Also included are the calculated peaks of the boundary layer waves.

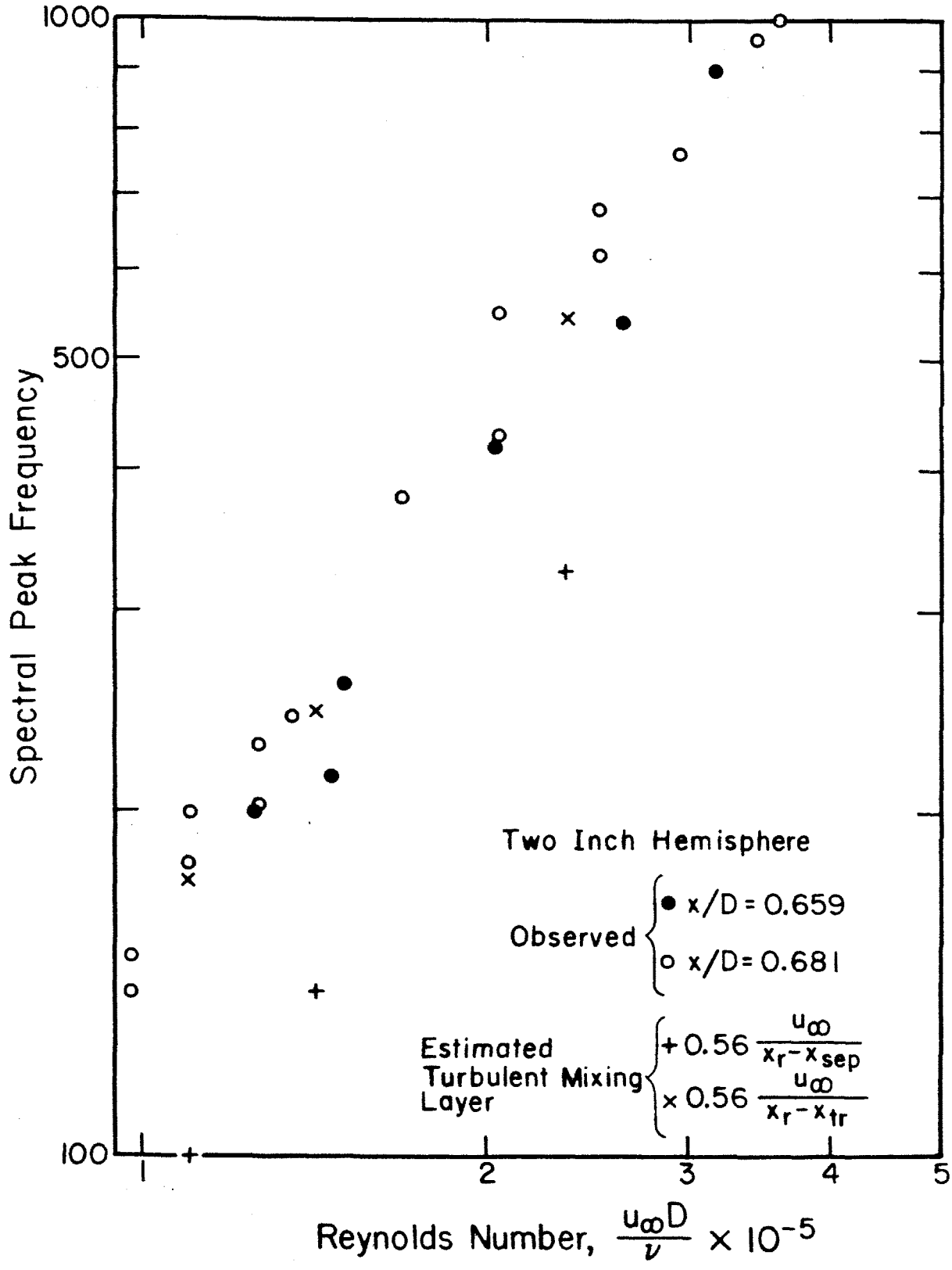

Figure 3.63. A comparison between the hemispherical body low frequency peaks and the estimated peaks of turbulent fluctuations.

IV. CAVITATION PHENOMENA

Introduction: This chapter will focus on cavitation phenomena associated with the flow around the test bodies. The first section contains a brief description of the equipment and the procedures of measurement followed by a presentation of the experimental results in the second section. These results include photographic and holographic illustrations, measurements of cavitation,inception and desinence indices, measurements of the population of bubbles in different sections of the flow field prior to and during cavitation,and the relations between several fully wetted flow phenomena and the location of cavitation inception. These experimental results will be discussed and compared with the existing literature in the last section.

IV.1 Experimental Procedures

IV.1.1 Cavitation Inception and Desinence Measurements

The inception of cavitation was determined visually under stroboscopic light. The tunnel velocity was kept constant and the pressure was gradually reduced from ambient conditions until the desired form of cavitation appeared. At that moment the output of the tunnel pressure transducer was frozen and recorded, together with the tunnel velocity. The vacuum pump was turned off after each test and the water was recirculated for at least ten minutes at atmospheric pressure. This length of time was required to reduce the amount of bubbles in the free stream. The desinence measurements were carried out by lowering the tunnel pressure

until cavitation appeared and then slowly increasing the pressure until the last signs of cavitation disappeared. The process was repeated only after recirculating the water as in the inception test.

The cavitation number was computed by recording the room temperature and obtaining the proper vapor pressure from steam tables. The correction of tunnel velocity and pressure due to the expansion of the test section area was similar to the corrections made during the computations of the average pressure coefficient. The amount of air dissolved in the water varied from 10 to 11 ppm (molar) and was measured with a Van Slyke apparatus. This air content was achieved by running the water tunnel in a low pressure for several hours before starting the experiments.

IV.1.2 Holographic and Photographic Methods

In a manner similar to the flow visualization experiments, holograms were recorded with the ruby laser holocamera and reconstructed either by using the conventional procedure or the schlieren reconstruction described in Chapter I. The population of bubbles in different sections of the flow field was determined by counting the number of bubbles in the reconstructed image with a magnification of 220X. The exact position and the size of the counted volume is indicated prior to the presentation of the results for each of the bodies and they include several sections within and outside of the separated zones. The results are presented, either by tabulating the number of bubbles counted in different sections of the flow field or by plotting the number density distribution function defined as

$$N\left(\frac{R_1 + R_2}{2}\right) = \frac{\text{Number of bubbles per unit volume with radii between } R_1 \text{ \& } R_2}{R_2 - R_1}$$

against the bubble radius.

The photographs presented in this chapter were recorded with a 35 mm camera and by using a flashlamp that provided a 2-3 microsecond light pulse.

IV.2 Observations and Measurements of Cavitation Phenomena

IV.2.1 Two-Inch Blunt Body

Two photographs of cavitation on the two-inch blunt body are shown in Figures 4.1 and 4.2, the first being of inception and the second of a more developed state. As is evident from these pictures, the first cavities appear far from the surface, forming a series of rings around the body that remind us of the series of vortices observed during the flow visualization measurements (see Figure 1.15). A closer look at the first cavitating bubbles with the help of the holocamera is demonstrated in Figure 4.3. These nonspherical bubbles are located at $x/D = 0.89$ and 0.96 and $y/D = 0.13$ and 0.22 respectively, lower than the upper boundary of the mixing layer determined in Chapter 2, but in agreement with the points of maximum shear measured by Ota and Motegi 1980). Bubbles of such size and shape do not exist in any point upstream of the region displayed in these holograms.

The relation between the shear layer and the cavitating bubbles is best demonstrated in Figure 4.4. This hologram demonstrates the bubble population above and below the mixing layer, between $x/D = 0.23$ and 0.45 and $y/D = 0.11$ and 0.27, when the body is fully cavitating downstream. The larger nonspherical bubbles appear in a clearly defined line whose

dimensions agree with the maximum shear points according to Ota (1980) ($y/D = 0.16$ and 0.27 at $x/D = 0.1$ and 0.5, respectively). The region below is full of smaller spherical bubbles, probably fed by the macroscopic cavities that exist downstream, but very few bubbles can be seen above the line defined by the larger bubbles.

This clear relation between the bubble population and the flow field when the body is cavitating can also be observed prior to cavitation inception. These observations were made by comparing the population of bubbles in different sections above the body surface prior to the appearance of the large cavities. The holograms examined were recorded in a "steady state" condition, meaning that the tunnel pressure and velocity were kept constant for at least ten minutes before the firing of the laser. Three examples of bubble distribution are presented in Figures 4-5a,b,c, corresponding to cavitation numbers of 3.55, 3.00 and 2.56, respectively. Each figure displays the number of bubbles found in several half-inch deep sections that together cover the separated zone and part of the external field. A comparison between the bubble population in two different sections defined by the dashed lines in Figure 4.5 are plotted in Figures 4.6a-j (Figures 4.5a,b,c correspond to Figures 4.6b,g,j, respectively). These graphs and the more detailed distributions in Figure 4.5 suggest that the population of bubbles inside the recirculation zone is larger than the population just above the mixing layer boundaries. This difference is more pronounced in the lower cavitation indices, but is still evident in all the flow conditions. For example, in Figures 4.6a and 4.6b ($\sigma = 4.74$ and 3.55, respectively) the discrepancies are very small and the

second graph shows that some large bubbles exist in the free stream and none within the separated zone. However, when the cavitation index is lowered to about three (Figures 4.6c,e,f, and g) larger bubbles appear in the entire flow field and the population within the separated zone becomes much larger than the population outside. A further reduction in the cavitation index (Figures 4.6d, h, i, and j) to about 2.5 brings this difference in the population of the larger bubbles to more than an order of magnitude. The details in Figures 4.5b and c suggest also that the population of bubbles within the separated zone is not uniform being larger between $y/D = 0.07$ and 0.21 and $x/D = 0.25$ and 0.5. The differences are even larger than shown in these figures, since the depth of each counted volume (= 0.5 inch) causes an overlap in the distance from the surface of the body.

These growing differences in bubble population, and especially the nonuniformity in bubble density inside the separation zone causes us to suspect that the flow is already cavitating, at least in a limited scale. However, the radius of the largest bubble does not exceed 160 microns, much smaller than the cavities shown in Figures 4.1 and 4.3, and the presently displayed steady state results lack any sign of explosive growth or collapse of bubbles. Thus, we suggest that the large shearing forces and the slower recirculating flow that increases the residence time of a bubble inside the separated zone are also major contributors to the increasing differences in bubble population. This suggestion does not exclude the possibility that some occasional microscale cavitation has already occurred somewhere in the separated zone. However, the size and

the population in any of these holograms is still at least an order of magnitude smaller than the population of bubbles during macroscopic cavitation as demonstrated in Figure 4.4.

The cavitation inception and desinence indices are plotted against the body Reynolds number in Figures 4.7 and 4.8. Unlike presently measured flow parameters, (the dimensions of the separated zone, the average pressure distribution and the rms and peak values of the fluctuating pressure) the cavitation inception and desinence numbers do depend on velocity growing both from about 1.3 to 1.9 when the Reynolds number is increased from 2×10^5 to 3.8×10^5. The minimum pressure coefficient measured on the surface of this body (average plus the largest negative peak) being around -1.3 to -1.4 may justify the cavitation inception indices for the lower velocities, but is definitely insufficient for the higher Reynolds numbers. These results are in agreement with the observation that the first cavitating bubbles appear in the center of the shear layer far from the surface of the body. Further discussion will follow the presentation of the rest of the results.

IV.2.2 Half-Inch Blunt Body

Similar to the larger blunt nose, the first cavitating bubbles appear far from the surface and form a series of rings around the body. Two holographic illustrations are presented in Figures 4.9 and 4.10 displaying the explosive nature and the nonspherical shape of these cavities.

Two probability density histograms, the first being of the axial and the second of the radial location of cavitation inception are presented in Figures 4.11a and b. These results are accumulated from a series of 25 holograms, all of them recorded in the same velocity, 21 ft/sec. As is

evident from these figures, the most probable location of cavitation inception is centered between x/D = 0.8 and 1.1 and around y/D = 0.18. This clearly defined section of the separation zone is located upstream of reattachment and far downstream of the separation point. The radial location is in agreement with the maximum shear line that according to Ota and Motegi (1980) is located around y/D=0.2 at x/D=1.0, but his results do not give any justification for the axial location of cavitation inception. However, the present measurements on the surface of the two-inch blunt body indicate that the minimum average pressure (Fig. 2.3) and the peak in the pressure fluctuations (Fig. 3.11 and 12) are also located around x/D = 1.0. Moreover, the first high positive peaks of pressure fluctuations that are presently associated with the reattachment zone appear at x/D = 1.25, just downstream of the major cavitating section. The location of cavitation inception was not determined in such a detail on the two-inch body. However, the few holograms checked were in agreement with the present observation (Figure 4.3).

The population of bubbles under noncavitating conditions was determined in two different sections of the flow field (Figure 4.12). The first section is enclosed almost entirely by the upper boundary of the mixing layer, and the second section is located in the free stream above. The results, representing two different experimental procedures are presented in Figure 4.13 a-i; the first group (a-g) being of a non-steady state condition meaning that the tunnel pressure was gradually reduced from $\sigma \simeq 5.0$ to the values shown in each of the figures, and the second group (h and i) being of steady state conditions.

Similar to the results for the larger blunt body,the population of bubbles within the separated zone is almost always larger than the population outside. The difference is clearer when the cavitation number is lower and when the hologram is recorded in steady state conditions. For example, a comparison between the last two figures shows a small difference in the population of bubbles when σ = 1.783 (Fig. 4.13h) and a clear and large difference when σ = 1.52 (Fig. 4.13i). The same trend exists also in Figures 4.13a-g but the differences in bubble density are smaller and in two of the holograms (4.13a and e) the population is identical.

Another clear observation is the large difference between the population of bubbles in the steady and the nonsteady state conditions. This difference reaches a 2:1 ratio in the population of small bubbles (0-10 microns radius) and almost an order of magnitude in the density of the larger ones. Moreover, the population in Figures 4.13a-g is almost equal to the results obtained earlier for cavitation indices of 2.5-4 (Figure 4.6). This observation suggests that the rate of pressure reduction in the present cavitation inception experiments is sufficiently fast to avoid a significant change in free stream bubble population.

There is also quite a large scatter in the nonsteady state results themselves even for the same velocities and cavitation indices. For example there is a 2.5:1 ratio between the bubble population in Figures 4.13b and c,and a 2:1 ratio between the population of large bubbles (>10 microns radius) in Figures 4.13f and g.

The cavitation inception and desinence indices are plotted against the Reynolds number in Figures 4.14 and 4.15, respectively. The

inception data is scattered all over the graph, the highest being 1.2 and the lowest being 0.3. Since the base pressure coefficient measured on this body is equal to -0.5 (Figure 2.8) these results imply that under certain conditions cavitation inception occurs when the water inside the separated zone is under tension, even without bringing the fluctuations in pressure into consideration. These quite surprising results are probably related to the differences in the population of free stream bubbles observed earlier and require further consideration. The desinent cavitation indices are more organized growing from 1.25 to 1.45 when the Reynolds number is changed from 5.7×10^4 to 9.4×10^4.

A comparison between the present results and the data for the two-inch blunt body suggests that the cavitation inception (or desinence) indices depend on the Reynolds number. The present results are in agreement with the experiments of Kermeen and Parkin (1957) on a series of sharp edged disks. Their cavitation inception indices vary from 1.3 to 1.5 for Reynolds numbers between 6×10^4 and 9×10^4, and from 1.5 to 2.0 for Reynolds numbers between 1×10^5 and 3.5×10^5. Their data display a large scatter in the inception numbers (between 0.2 and 1.6) for the quarter inch diameter disk, and a smaller but still significant scatter, for the 3/4 inch diameter disk.

IV.2.3 Hemispherical Headform Body

Three distinct forms of cavitation can be visually observed on the hemispherical body. The first form, not necessarily associated with separated flows, is the travelling bubble cavitation, illustrated in a photograph in Figure 4.16 and in a holographic image in Figure

4.24. The second form, whose connection to separated flows was first established by Arakeri (1973) and later verified by Gates (1977) and Van Der Meulen (1977), is the band type cavitation, demonstrated in a photograph in Figure 4.17 and in a hologram in Figure 4.22. When the water tunnel is filled with a large number of free stream bubbles the band type cavity partially disappears, and the cavitating zone appears to be less organized containing a mixture of band and travelling bubble cavitation as illustrated in Figure 4.18. Another form, the bubble ring cavitation observed by Parkin and Kermeen (1953) and by Holl and Carroll (1979) was not observed in the present experiments, at least not to the naked eye.

The major interest in the present study is in the band type cavitation, particularly in the origin of the cavities in the separated zone. All the sources mentioned above confirm that several bubbles whose dimensions are comparable to the height of the separated zone can be observed prior to the formation of the band, first, near the reattachment point, and then within the recirculation zone. These bubbles exist either in a "steady" form (bubble ring cavitation), or as an intermediate stage that transforms very fast to a large cavity that occupies most of the separation zone. However, none of these sources provide any evidence for the source of these relatively large cavitating bubbles. The holograms presented in Figures 4.19 and 4.20 demonstrate a very early stage of cavitation inception and provide us with a clear suggestion for the origin of these cavitating bubbles. They seem to be concentrated in a narrow region, near $x/D = 0.6$ in Figure 4.19 and 0.58 in Figure 4.20, slightly downstream of the previously predicted

reattachment points (Fig. 2.23). None of these bubbles is attached to the surface, and their diameter varies from 10 to 300 microns (actually only one bubble is larger than 200 microns) in the first hologram and from 10 to 100 microns in the second one. The vertical location of the bubbles upstream of the inception point, some of them appearing as far as 1.5 mm from the surface, almost an order of magnitude higher than the size of the laminar part of the separated zone, (Figure 2.24) excludes the possibility that these bubbles are swept upstream by the reverse flow. This observation suggests that the first sign of a large number of visible ($\geq$ 10 micron diameter) cavitation nuclei appears in the turbulent shear layer upstream of the cavitation inception point. This observation is also demonstrated by a detailed distribution of bubble population shown in Figure 4.25. The main cavitating zone appears to be concentrated near x/D = 0.6 and an increased bubble population can be detected 1.6 mm upstream (x/D = 0.57) and 0.5 mm (x/D = 0.73) downstream. One can notice that several bubbles larger than 20 microns in diameter are found also in the section above y/D = 0.024 and between x/D = 0.57 and 0.6, but not in any other section upstream of the cavitation inception zone, including the interior and the region above and upstream of the separation zone. These observations raise a serious doubt about the direct role of the laminar boundary layer and the pressure field upstream of the separation point in the inception of cavitation.

Free stream bubbles that do grow due to the potential pressure field may become the source of nuclei for the present cavitation process. This possibility is demonstrated in Figure 4.21 that shows a

hologram of a 300 micron bubble being torn apart while being entrained by the shear layer upstream of the reattachment zone, but far from the surface. As noted by Gates (1977), when the free stream bubbles are sufficiently large (as the one shown in Figure 4.24) they affect the flow field around the body resulting in the form of cavitation that is demonstrated in Figure 4.18. However, when these large bubbles are absent (as in Figure 4.19 and 20) the growth of free stream bubbles from a microscopic size (≃10 microns diameter) to a visible form of cavitation occurs in a limited section of the flow field - in the turbulent mixing layer developed downstream of the transition point up to the reattachment zone.

The transition from this micro cavitation to a fully developed band occurs very fast usually starting at an arbitrary point (but at the same axial location) and expanding all around the body. The fully developed cavity is demonstrated in Figures 4.22 and 4.23, the first one,in a small magnification,displaying a major part of the cavitating zone,and the second one,in a higher magnification,concentrating on the laminar and cavitation separation points. As observed by Arakeri (1973), the leading edge of the cavity is contained within the laminar separated bubble being smooth and stable in the upstream part and becoming unstable further downstream. The distance between the leading edge of the cavity and the laminar separation point is plotted against the cavitation index in Figure 4.26. The results, scaled with the body diameter,are scattered between 0.024 and 0.032 and show some dependence on velocity but not on the cavitation index. The point of laminar separation, also plotted in Figure 4.26, moves upstream

when the cavitation number is reduced but does not show a noticeable dependence or velocity. This trend is in agreement with the detailed observations by Arakeri (1973) and earlier results of Brennen (1969)* but the present results are slightly lower when compared for the same velocity and cavitation index (he measured a larger distance between the laminar and cavitation separation points and a higher angle of laminar separation).

The population of bubbles counted in the sections described in Figure 4.27, prior to cavitation inception, but at a comparable pressure, are presented in Figure 4.28a-h. All the holograms were recorded under nonsteady state conditions; the first group (a-f) was recorded after lowering the tunnel pressure from ambient conditions, and the second group (g and h) after keeping the cavitation index in the test section equal to three for at least ten minutes. Due to the present low cavitation indices and the lack of any means for bubble removal in the water tunnel, it was impossible to maintain the flow in steady state conditions without filling the tunnel with an enormous quantity of large bubbles (possibly due to cavitation inception somewhere else in the test facility).

The most important observation concerning the present cavitation inception measurements is the low population of bubbles with radii larger than ten microns in Figures 4.28a-f. There are nine in one of the holograms (4.28a), and a single bubble all over the sample volume in two of the others (4.28d and f). The population of these relatively large bubbles in Figures 4.28b, c and e is comparable to the non-steady state results in Figures 4.13a-g, but much lower than any of the steady state populations (Figure 4.6 and 4.13 h and i) in any cavitation

*Cavitation State of Knowledge, ASME, p. 141.

index. The density of small bubbles ($\leq$10 microns radius), however, is quite large and has the same order of magnitude as most of the previously presented results. These observations provide us with an idea about the characteristic size of bubbles that may act as cavitation nuclei during the present cavitation inception index measurements, since the experimental procedures are identical. The population of bubbles in the last two figures (4.28g and h) is significantly larger, and the results are of the same order of magnitude as the steady state populations in Figures 4.6 and 4.13. This agreement between figures 4.28g and h and Figure 4.6, and the large differences between the results obtained for two different experimental procedures presented in Figure 4.28 suggest again that the rate of pressure reduction during the present cavitation inception measurements is sufficiently high to prevent a significant change in free stream bubble population. The implication of these observations will be discussed later.

The section that covers the separation zone (section No. 1 in Fig. 4.27) contains almost the same amount of bubbles as the fluid above, and so are the results for the rest of the counted sections. Moreover, there is not even one single bubble with a radius larger than ten microns within the separation zone in all the presently-counted holograms. One can notice by looking back at Figure 4.25 that the same observation still holds for those parts of the separation zone that are not affected yet by the inception of cavitation.

The inception indices for travelling bubble cavitation are plotted against the Reynolds number in Figure 4.29. The results that scatter between 0.6 and 0.82 are fairly close to the minimum pressure measured

on this body (-0.7). The inception indices for band type cavitation, plotted in Figure 4.30 are scattered between 0.35 and 0.6 and the desinence indices, plotted in Figure 4.31, are scattered between 0.46 and 0.56. The available literature contains a large number of cavitation inception experiments with the hemispherical body. For example, Gates (1977) measured inception indices between 0.55 and 0.65, Arakeri (1979) - between 0.57 and 0.59, Holl and Carroll (1979) - around 0.56 (for the present velocities), Huang (1979) - 0.61 (for a higher Reynolds number), Arakeri (1973) - between 0.75 and 0.85, and above all those of Keller (1979) that vary from 0.2 to 1.4. Most of these results are in agreement with the upper bound of the present observations but some, especially those of Keller, are much higher. There was no visible form of cavitation on the present body in such high indices, not even by running the tunnel for 20 minutes, keeping the cavitation index equal to 1.2, and flooding the test section with bubbles.

IV.2.4 Step Body

Figure 4.32 is a photograph of an early stage of cavitation on the step body as it appears to the naked eye. The cavities seem to appear either in one or two distinct points behind the step creating a ring that surrounds the body. When the cavitation index is sufficiently low, around 0.6, the cavities climb over the step, as demonstrated in Figure 4.33, and finally form a band type cavity, similar to the hemispherical body.

Several holograms that were recorded during cavitation inception are presented in Figures 4.34-38, the first one being of cavitation still in a microscale form, and the rest in a visible state. The earliest

traces of cavitation (Figure 4.34a and b) appear as a large number of bubbles, only one of them with a radius larger than 50 microns concentrated in part of the separation zone,far from the surface of the body. This large bubble population is clearly demonstrated in Figure 4.34b which is a magnified image of the most populated region of Figure 4.34a. The whole picture becomes clearer in the holograms presented in Figure 4.35 and 36 that were recorded with a heated body. These holograms provide evidence that the first cavitating bubbles appear in two distinct sections, the first one being the transition region of the shear layer,and the second and bigger "cavitation center" appears almost at the same height far downstream. The bubbles that do exist, either upstream of the transition zone or below the shear layer, do not cavitate, as demonstrated in Figure 4.35 and 4.36b. These holograms that display the image of the cavitating bubbles in the transition zone, also show 10 micron (radius) bubbles in the laminar part of the shear layer and several noncavitating circular bubbles below. The shape and the distinct position of these cavities,and the previous observations of the coherent eddy structure in the turbulent shear layer,suggest that the inception of cavitation and the mixing layer vortices are closely related.

The separation zone upstream of the step when the flow is cavitating downstream (same hologram as Figure 4.36) are demonstrated in Figure 4.37. Several small bubbles that may have been swept by the reverse flow can be detected on the surface of the body downstream of the separation point but none can be seen upstream. There is no sign of cavitation anywhere in this region.

The holograms in Figures 4.34-37 represent the form of cavitation for a free stream velocity of 17 ft/sec. When the tunnel speed is increased to 22 ft/sec some changes occur as demonstrated in Figure 4.38. The distance between the cavities becomes smaller and the main cavitating zone moves upstream. This observation led to a detailed study of the cavitation inception points in two different velocities, 17.3 and 22.2 ft/sec,and the results are accumulated in the probability density histograms that are presented in Figures 4.39a and b, respectively. At 17.3 ft/sec there are two cavitation centers, the first one is located at x'/H = 3.25 (x' being the axial distance from the step and H the step height) and the second one at 5.75. At 22.2 ft/sec the inception points move upstream, the first one is located at x'/H = 2.5 and the second one at 3.75. Both results are far upstream of the reattachment zone determined from pressure fluctuation measurements (see Table 3-2),and both have a noncavitating section upstream extending to x'/H = 2 at 17.3 ft/sec and 1 at 22.2 ft/sec. The upstream motion of the cavitation centers may be due to the earlier transition and reattachment when the free stream velocity is increased. The large positive peaks of the surface pressure fluctuations, that are presently associated with the reattachment zone, first appear at x'/H = 6.9 (x/D = 0.63 in Figure 3.28) and x'/H = 6.0 (x/D = 0.614 in Figure 3.31) for free stream velocities of 17.9 and 21.0 ft/sec, respectively. These points are just downstream of the present major cavitation center. One can recall that cavitation inception on the blunt body also occurs just upstream of these large positive peaks. This common behavior suggests that the most probable point for cavitation

inception in both bodies is located in the most developed section of the free shear layer, but upstream of the region that is affected by the re-attachment. The reason for this phenomenon has yet to be explored.

The distance between the cavitation centers is probably related to the characteristic distance between neighboring eddies in the shear layer. Since the first center is located in the transition region, the wavelength of a disturbance can be related either to the laminar boundary layer instability waves or can be already part of the coherent eddy structure downstream. The wavelengths of the boundary layer waves can be estimated from the hemispherical body spectra (figure 3.62) and by assuming that the disturbances are convected with half of the local external velocity. These estimates lead to wavelengths of 1.49 mm and 1.36 mm corresponding to free stream velocities of 17.3 and 22.2 ft/sec, respectively. The distance between neighboring turbulent shear layer eddies, being proportional to the axial location, can be estimated by using the previous results (see the discussion in Chapter III)namely that $fL/u = 0.56$. By assuming a convection velocity of half the local velocity, and by replacing L with the axial distance from the transition point, the resulting wavelength is

$$\lambda \simeq 0.89\ (x' - x'_{tr}) \quad .$$

The length x' can be estimated by choosing it to be the central point between the cavitation centers and obtaining x'_{tr} from Figure 2.28. The calculations are tabulated in Table 4-1.

Re_D	frequency from Fig. 3.26	λ[mm] laminar instability (estimated)	x'[mm] (observed)	x'tr[mm] (observed)	λ[mm] turbulent shear layer (estimated)	distance between cavitation centers [mm] (observed)
2.77×10^5	2270 Hz	1.49	4.5	1.4	2.8	2.5
3.55×10^5	3200 Hz	1.36	3.1	1.2	1.7	1.25

Table 4-1. A comparison between the characteristic estimated wavelength of the laminar instability, the wavelengths of the estimated turbulent shear layer eddies, and the observed distance between cavitation centers.

These comparisons indicate that the estimated wavelengths and the observed distance between cavitation centers have the same order of magnitude and display a similar trend with velocity.

These distinct centers of inception can also be observed when cavitation is still in a microscale form as demonstrated in Figure 4.40 that displays the bubble population in various sections of the flow field during cavitation inception. The highest population is detected in the neighborhood of x'/H = 2.4 and 6.4 (the exact location of the cavitating bubbles in this hologram is included in Figure 4.39a), but the bubble density is relatively high (compared to the upper two rows) in most of the sections that are within and below the shear layer. There is no sign of increased bubble population in the sections above the step. The accumulated density of bubbles in the first three rows behind the step is compared to the results for the fourth and fifth rows, and to the population in the upstream sections (marked by a dashed line) in Figures 4.41a-c (Figure 4.41b presents the results shown in Figure 4.40). All three counted holograms were recorded under non-steady state conditions, when the tunnel pressure was lowered from ambient conditions (similar to Figures 4.28a-f), and when cavitation was still in a microscale form. The large difference between the population

of bubbles inside the separation zone and the population either above the shear layer or upstream of separation is evident from these figures, but especially in 4.41b and c. One can also notice that there is no significant difference between the bubble population upstream and above the separation zone. The present "free stream" bubble density is a little larger than the results presented in Figure 4.28a-f, but the previous statements concerning the small number of bubbles with radii larger than ten microns still hold. There are nine in Figure 4.41a, only one in 4.41b (as shown in Figure 4.40), and three bubbles in Figure 4.41c. These results will be included in the discussion that follows.

The cavitation inception and desinence indices are plotted against the Reynolds number in Figures 4.42 and 4.43, respectively. They both grow from around 0.95 to 1.25 when the Reynolds number is increased from 2.4×10^5 to 3.8×10^5. The only available results in the literature are those of Arakeri (1979) who measured inception indices of 1.3 and 1.35 in higher Reynolds numbers, 4.54×10^5 and 5.7×10^5, respectively. Figure 4.42 contains also the cavitation indices of inception of band type cavitation, and the results are in agreement with those obtained for the hemispherical headform (see Figure 4.30).

IV.3 Discussion: The Effect of Bubble Population on Cavitation Inception

There are a few major factors that have to be considered during an attempt to determine the effect of free stream bubbles on cavitation inception. The first and most important factor is the population of bubbles and their size distribution in the neighborhood of the cavitating region. As will be shown later, the results in Figures 4.6, 13, 28 and 41 provide quite a detailed answer to this question, at least for the present test facility. Secondly, one should determine the pressures that will force the existing free stream bubbles to an unstable state and explosive growth rate. Thirdly, the bubble has to be exposed to a low pressure for a sufficiently long time, or when pressure fluctuations are considered, their period must be long enough for the bubble to respond. Finally, there remains the question of the probability that all these conditions will be met simultaneously, meaning that a bubble will exist in the proper section of the flow field for a sufficiently long time and will be exposed to a pressure field to which it can respond. The following discussion is an attempt to provide some answers to these questions.

IV.3.1 Free Stream Bubble Population

The present results suggest that the rate of pressure reduction during the cavitation inception measurements is sufficiently fast so that the bubble population at any cavitation index depends mainly on the original tunnel pressure before it is reduced. For example, the population of bubbles in Figure 4.6 that represents steady state con-

ditions (σ = 2.5 ÷ 4) is almost equal to the results in Figure 4.13a-g (σ = 1.5 ÷ 1.8) and Figure 4.28g and h (σ = 0.6 ÷ 0.7) that represent the population when the pressure is reduced after being kept for ten minutes at σ =3÷4. On the other hand, the results presented in Figures 4-28a-f (σ=0.6÷0.7) and Figures 4.41a-c (σ=1.1) that display the bubble population when the tunnel pressure is reduced from ambient conditions (similar to the cavitation inception measurements) are much smaller. Some examples that demonstrate these effects of experimental procedures on bubble population are presented in Figure 4.44 (the results are taken from Figures 4.13g and i and 4.28c). These differences are extremely significant for the population of bubbles with radii larger than 10 microns. Several reasons can be argued for and against these phenomena starting from the fact that the water in the test section is super-saturated (being ≃10 ppm) for most of the displayed conditions, but is under-saturated in the stagnation chamber or the sections of slow motion below. There is also the question of the time needed for undissolved gas to go into the solution in under-saturated water and vice versa. There is also a possibility of cavitation in the tunnel pump and this may be the reason that the tunnel cannot be kept at σ = 0.5 ÷ 0.7 for more than 10 seconds without flooding the test section with bubbles. Thus, it is difficult to make a clear cut argument to explain these phenomena.

The resolution limits of the present holography system prevents a clear distinction between the bubbles and solid particles in the range of 0-10 microns radius,unlike the bigger nuclei. Thus, there is no certainty that the results for the smallest range represent only bubbles,even though the water in the tunnel was filtered before

recording the holograms and as a result a negligible amount of larger particles was detected in the test section.

The differences between the population of bubbles within and above the separation zone were discussed during the presentation of the results for the blunt bodies. Since these differences depended on the cavitation index and applied mainly to the steady state conditions there is no certainty that some limited amount of cavitation did not occur somewhere inside the shear layer. Thus, the results that will be used in the present discussion are the population of bubbles above the separation zone found when the tunnel pressure was lowered from ambient conditions. There will be, however, some reference to the steady state results and to the resulting population inside the separation zone. A series of averaged results are tabulated in Table 4-2. The right column in this table contains the density of bubbles, $n(\bar{R})$, with radius between R_1 and R_2 defined by

$$n(\bar{R}) = n\left(\frac{R_1+R_2}{2}\right) = N(\bar{R}) \cdot (R_2-R_1)$$

	Bubble radius (microns)	Number density, $N(R)$ [Bubbles/m^4]	Density, $n(\bar{R})$ [Bubbles/m^3]
Steady state	0-10	1.13×10^{13} *	1.13×10^{8} *
$\sigma = 2.5 \div 4$	10-25	1.63×10^{12}	1.07×10^{7}
	25-37.5	8.9×10^{10}	7.1×10^{5}
Above the separation	37.5-50	6.2×10^{10}	5.0×10^{5}
zone	50-75	2.0×10^{10}	8×10^{4}
Figure 4.6	75-100	3.4×10^{10}	1.36×10^{5}
	100-125	-	-
*only 4.6a-b	125-150	3.4×10^{10}	1.36×10^{5}

Steady state	0-10	1.86×10^{13}	1.86×10^{8}
$\sigma = 1.5 \div 1.8$	10-25	4.47×10^{12}	2.98×10^{7}
	25-37.5	1.28×10^{12}	1.02×10^{7}
Above the separation	37.5-50	4×10^{11}	3.2×10^{6}
zone	50-75	1.2×10^{11}	4.8×10^{5}
Figure 4.13h-i	75-100	4×10^{10}	1.6×10^{5}
	100-125	-	-
	125-150	-	-
Non steady, $\sigma_o \cong 3.0$	0-10	9×10^{12}	9.5×10^{7}
$\sigma = 1.5 \div 1.7$	10-25	1.03×10^{12}	6.9×10^{6}
Figure 4.13a-g	25-37.5	2.3×10^{11}	1.84×10^{6}
	37.5-50	2.3×10^{10}	1.84×10^{5}
Non steady, $\sigma_o \cong 3.0$	0-10	2.4×10^{13}	2.4×10^{8}
$\sigma=0.5 \div 0.7$	10-25	1.8×10^{12}	1.2×10^{7}
Figure 4.28g-h	25-37.5	1.8×10^{11}	1.44×10^{6}
Non steady, from ambient	0-10	2.7×10^{13}	2.7×10^{8}
$\sigma \cong 1.1$	10-25	2.9×10^{11}	1.9×10^{6}
Figure 4.41a-c	25-37.5	-	-
Non steady from ambient	0-10	1.6×10^{13}	1.6×10^{8}
$\sigma \cong 0.5 \div 0.7$	10-25	4.3×10^{11}	2.9×10^{6}
Figure 4.28a-f	25-37.5	-	-
	37.5-50	2×10^{10}	1.6×10^{5}

Table 4-2 Averaged number density ($N(R)$) and density ($n(\overline{R})$) of bubbles counted in the holograms in various experimental procedures. All the results are of the sample volume above the separation zone. The last two sections represent the population of bubbles during the cavitation inception measurements.

IV.3.2 Conditions for Instability

The pressure, P, that is required to bring a vapor bubble to an unstable state satisfies the equation

$$P-P_V = -\frac{4T}{3R}$$

T being the surface tension and P_V the vapor pressure. This relation can be derived from the Rayleigh-Plesset equation (see Knapp et al (1970)). Some numerical values are presented in Table 4-3.

R (microns)	$P-P_V$ psi	$\Delta\sigma$ (u_∞=15 ft/sec)	$\Delta\sigma$ (u_∞=20 ft/sec)	$\Delta\sigma$ (u_∞=25 ft/sec)
1	-14.3	-9.3	-5.2	-3.35
2	- 7.13	-4.6	-2.6	-1.67
5	-2.85	-1.9	-1.04	-0.67
10	-1.43	-0.93	-0.52	-0.34
20	-0.713	-0.46	-0.26	-0.17
50	-0.285	-0.19	-0.104	-0.067
100	-0.143	-0.093	-0.05	-0.034
200	-0.071	-0.046	-0.026	-0.017

Table 4-3 The pressure and the pressure coefficient that are needed to bring a bubble to instability. $\Delta\sigma = (P-P_V)/\frac{1}{2}\rho u_\infty^2$.

The results imply that an enormous tension (almost one atmosphere) is required for a one micron bubble but a negligible negative pressure will bring a 100 micron bubble to instability. Obviously, the effect on the cavitation index becomes smaller as the velocity is increased.

IV.3.3 Response Time of Bubbles vs Spectra of Fluctuations

The characteristic response time of a bubble can be estimated from its natural frequency

$$t_{B_1} = \frac{2\pi}{\omega} = 2\pi\sqrt{\frac{\rho R^3}{2T}} = 4.4\sqrt{\frac{\rho R^3}{T}}$$

Another possibility, as suggested by Arndt and George (1978), is the ratio between the bubble radius and its asymptotic growth rate:

$$\dot{R} = \sqrt{\frac{2}{3}\frac{P_v - P}{\rho}}$$

This relation can be derived by integrating the Rayleigh-Plesset equation (Knapp et al (1970)). By substituting the conditions for instability the following time scale is obtained

$$t_{B_2} = \frac{R}{\dot{R}} = R\sqrt{\frac{3}{2}\left(\frac{3\rho R}{4T}\right)} = 1.06\sqrt{\frac{\rho R^3}{T}}$$

Both approaches lead to a time scale of the same order of magnitude. Some numerical values are presented in Table 4-4

R(microns)	t_{B_1} [sec]	t_{B_2} [sec]
1	5.2×10^{-7}	1.2×10^{-7}
2	1.5×10^{-6}	3.4×10^{-7}
5	5.8×10^{-6}	1.4×10^{-6}
10	1.6×10^{-5}	3.9×10^{-6}
20	4.6×10^{-5}	1.1×10^{-5}

50	1.8×10^{-4}	4.3×10^{-5}
100	5.2×10^{-4}	1.2×10^{-4}
200	1.5×10^{-3}	3.4×10^{-4}

Table 4-4. Estimated characteristic response time for a bubble.

There is an uncertainty concerning the characteristic frequency of fluctuations to which a bubble is exposed, since the present measurements (see Chapter 2) are made in a fixed point and the bubble moves with the fluid. Better data, however, is not available and thus, the characteristic time scale will be estimated from the present pressure fluctuation measurements. The spectral peaks for the blunt, step, and hemispherical head form bodies are presented in Figures 3.50-52, 3.56 and 3.65-66, respectively. The corresponding periods are present in Table 4-5.

u_∞ [ft/sec]	Re_D	Boundary Layer Waves Hemisphere	Turbulent Hemisphere	Step Body	Blunt Body
10	1.6×10^5	1.25×10^{-3} sec	3.8×10^{-3} sec	7.4×10^{-3} sec	6.1×10^{-2} sec
15	2.3×10^5	5.7×10^{-4}	2.1×10^{-3}	4.4×10^{-3}	4×10^{-2}
20	3.1×10^5	3.7×10^{-4}	1.4×10^{-3}	3.1×10^{-3}	3.0×10^{-2}
24	3.8×10^5	3.03×10^{-4}	1×10^{-3}	2×10^{-3}	2.5×10^{-2}

Table 4-5 Characteristic period of pressure fluctuations based on measured spectral peaks.

As is evident from the data in Table 4-5 the characteristic period of the blunt body is much larger than the results presented in Table 4-4. The step body time scale is still sufficiently large for bubbles that are smaller than 100 microns but since its spectra

(see Figure 3.53, 54,and 55) extend to higher frequencies (to around 2 k Hz - period of 5×10^{-4} sec),only 20 micron bubbles will fully respond to these pressure fluctuations. The characteristic periods of the hemispherical body,however, and especially those of the boundary layer instability waves (it was argued before that waves of a similar frequency must also exist in the step body shear layer), are already comparable to the natural period of bubbles that are larger than 20 microns. As a result,the bubbles will not respond "instantaneously" to these high frequency pressure fluctuations and the required tension mentioned earlier may be insufficient. Being excited by its natural frequency,however,forces the bubble into large oscillations as discussed by Plesset and Prosperetti (1977) and makes the problem of estimating the favorable conditions for cavitation much more complex.

The present discussion is limited to a narrow range of velocities, but we can extend the discussion now to a much wider range. It was argued before (see Chapter 3) that the frequency of these boundary layer waves can be made dimensionless by defining the Strouhal number as

$$\frac{f\theta_s}{u_\infty} = \text{const.}$$

This relation can be rewritten as

$$\frac{f\ D\ Re_{\theta s}}{u_s\ Re_D} = \text{const.}$$

For boundary layer flows where the pressure coefficient is not a function of velocity

$$\frac{u_s}{u_\infty} = (1-Cp_s)^{\frac{1}{2}} \; ; \qquad \frac{Re_{\theta s}}{\sqrt{Re_D}} = \text{const.}$$

Thus

$$\frac{f\ D}{u_\infty \sqrt{Re_D}} = \text{const.}$$

This relation means that we may face a different pressure fluctuation spectra, and as a result, a different response of bubbles even for the same Reynolds number. For example, if we use a body with half the diameter and run the experiment in twice the velocity we keep the same Reynolds number but the frequency of fluctuations will be four times larger. As a result, the bubbles will respond to a smaller portion of the spectrum.

Similar arguments can be developed for the turbulent section of the pressure fluctuation spectrum, being dependent on the length of the separated zone and the free stream velocity (zee the discussion in Chapter 3). This length scale, however, depends on so many flow parameters (such as the step height in a downstream facing step, the body diameter in blunt bodies, the axial location in the shear layer, the Reynolds number, etc.) that any detailed discussion will exceed the scope of the present work.

As for the present range of measurements, the only troublesome results apply to bubbles larger than 20 microns (radius) and to a small section of the spectrum. We can proceed now with some confidence that most of the bubbles do fully react to almost all of the existing

pressure changes.

IV.3.4 Rate of Cavitation Events

The information that was provided earlier can assist us in estimating the rate of cavitation events; that is, the rate at which the free stream bubbles will be exposed to a sufficiently low pressure to become unstable. Unfortunately, the present surface pressure fluctuation measurements do not provide us with the size of negative peaks in the region of cavitation inception (excluding the hemispherical body). They do provide us, however, with a measure for the fraction of time that such peaks do exist. As demonstrated in Chapter 3, there is a 2:1 ratio between the amplitude of the negative peaks with 0.1 percent and 2.5 percent probability of occurrence. Thus, a reasonable choice for the fraction of time that a pressure peak occurs is 0.1 percent.

The present observations suggest that cavitation inception occurs in small sections of the flow field. They are the reattachment zone on the hemispherical body, the turbulent shear layer mainly just upstream of reattachment on the step body, and around $x/D = 1$ and $0.15 \leq y/D \leq 0.25$ on the blunt bodies. The flow rate of bubbles in these sections can be estimated by assuming that the velocity is half of the free stream velocity, and by using the measured density of bubbles in the last section of Table 4-2.

Hemispherical body - The width of the mixing layer, δ, near the reattachment zone is estimated from the spread rate of shear flows (see the discussion in Chapter 3) to be

$$\delta \simeq 0.2(x_r - x_{tr})$$

The cross section of the free shear layer around the body is

$$\pi(D + \tfrac{1}{2}\delta)\delta$$

The flow rate of bubbles through this cross section, Q, is

$$Q(\overline{R}) = n(\overline{R}) \cdot \tfrac{1}{2} u_\infty \cdot \pi(D + \tfrac{1}{2}\delta)\delta$$

where $n(\overline{R})$ is the density of bubbles with radii between R_1 and R_2, $\overline{R}$ being the average radius.

Since the pressure peaks exist only for 0.1 percent of the time

$$Q_c(\overline{R}) = 0.001\ Q(\overline{R})$$

where Q_c is the rate at which bubbles are exposed to pressure peaks

$$Q_c(R) = \pi D^2\ u_\infty\ n(\overline{R})(1+0.1(\frac{x_r-x_{tr}}{D}))(\frac{x_r-x_{tr}}{D})\ x10^{-4}$$

Since

$$0.1(\frac{x_r-x_{tr}}{D}) << 1$$

$$Q_c(R) = \pi D^2\ u_\infty\ n(\overline{R})(\frac{x_r-x_{tr}}{D})\ x10^{-4}$$

Some numerical results are presented in Table 4-6.

R(microns)	u_∞(ft/sec)	Re_D	$Q_c(\overline{R})$(Bubbles/sec)	$\Delta\sigma$ required
0-10	15	$2.3x10^5$	53	-0.93
10-25			0.96	-0.46
> 25			0.05	-0.19

0-10	20	3.1×10^5	63	-0.52
10-25			1.2	-0.26
> 25			0.06	-0.10
0-10	25	3.8×10^5	79	-0.34
10-25			1.4	-0.17
> 25			0.08	-0.07

Table 4-6 Estimated possible rate of cavitation events and the tension required for the hemispherical body. The values for $\Delta\sigma$ are taken from Table 4-3 for 10, 20 and 50 micron bubbles.

These results are of special interest since this is the only case for which the pressure fluctuations peaks are measured near the cavitation inception region. The sum of most of the inception indices, being between 0.45 and 0.56 (Figure 4.30), the pressure coefficient in the separation zone being -0.56, and the negative pressure fluctuations peaks being -0.18 (Figure 3.40 and 3.41), is

$$\sigma_i + C_{PB} + \frac{p'}{\frac{1}{2}\rho u_\infty^2} = -0.29 \div -0.18$$

Table 4-6 suggests that the required bubble size in a free stream velocity of 20 and 25 ft/sec is in the range of 10-25 microns (radius) and that the possible rate of cavitation events in this range is around one per second. This may be an explanation for the observation that cavitation is initiated in a single point around the body. A few inception indices are below -0.4 leading to a local peak of -0.34, a sufficient tension for a 10 micron bubble to become unstable at 25 ft/sec. sec.

We can conclude now that the measured pressure field and the bubble density and size distribution are in agreement with the cavitation inception indices. These estimates confirm the previous observations that the growth of bubbles from less than 10 micron radius to macroscopic cavitation can and does occur near the reattachment zone on the hemispherical body. In order to become unstable it is not necessary for the bubble to be exposed to the low pressure region upstream of the separation point. This last statement does not exclude the possibility of cavitation due to the potential pressure field; as a matter of fact, the travelling bubble cavitation is a result of such a process. The present estimates do suggest, however, that cavitation inception in the reattachment zone can and does occur no matter what the pressure is in any other section of the flow field.

If we repeat the estimates for the density of bubbles found after the tunnel pressure is lowered from $\sigma = 3.0$ (fourth section of Table 4-2), the resulting rate of cavitation events (for 10-25 micron bubbles) is four, five and six per second for velocities of 15, 20 and 25 ft/sec. The rate for larger bubbles being 0.45, 0.54 and 0.72, is still less than one but already within a close range for a possible effect on the cavitation inception index. One would expect a slightly higher inception index in such cases, between 0.55 and 0.65. A larger bubble population may already affect the flow field around the body as noted by Gates and Acosta (1978) and confirmed by the present observations. These estimates, by themselves, suggest that the inception index will increase even to more than 0.7 in higher velocities, but as noted before,

more attention should be given to the pressure fluctuations time scales.

Blunt Bodies - The present observations suggest that the characteristic height of the cavitating zone is $0.15 \leq y/D \leq 0.25$. Thus the bubble flow rate is:

$$Q(\overline{R}) = n(\overline{R}) \cdot \tfrac{1}{2}u_\infty \cdot \pi(D + 0.2D) \cdot 0.1D$$

and

$$Q_c(\overline{R}) = 6\times10^{-5}\ \pi u_\infty D^2\ n(\overline{R})$$

Some numerical results are presented in Tables 4-7 and 4-8 for the one half and the two inch bodies respectively.

R(microns)	u_∞(ft/sec)	Re_D	$Q_c(\overline{R})$[Bubbles/Sec]	$\Delta\sigma$ required
0-10	15	5.8×10^4	22	-0.93
10-25			0.4	-0.46
> 25			0.02	-0.19
0-10	20	7.8×10^4	30	-0.52
10-25			0.54	-0.26
> 25			0.03	-0.10
0-10	25	9.5×10^4	37	-0.34
10-25			0.67	-0.17
> 25			0.04	-0.07

Table 4-7 Estimated rate of cavitation events and the local tension required for the one-half inch blunt body. $\Delta\sigma$ is taken from Table 4-3 for 10, 20 and 50 micron bubbles.

R(microns)	u_∞(ft/sec)	Re_D	$Q_c(R)$[Bubbles/Sec]	$\Delta\sigma$ required
0-10	15	2.3×10^5	356	-0.93
10-25			6.5	-0.46
> 25			0.36	-0.19
0-10	20	3.1×10^5	474	-0.52
10-25			8.6	-0.26
> 25			0.47	-0.10
0-10	25	3.8×10^5	593	-0.34
10-25			10.8	-0.17
> 25			0.59	-0.07

Table 4-8 Estimated rate of cavitation events and the local tension required for the two inch blunt body. $\Delta\sigma$ is taken from Table 4-3 for 10, 20 and 50 micron bubbles.

Since the estimated rate of cavitation events is proportional to the square of the body diameter there is a 16:1 ratio between the results obtained for the two bodies. An important observation is the low rate for the half inch body especially in the range of 10-25 microns. These results imply that a single bubble becomes unstable once every two seconds, a time scale that is comparable to the present rate of pressure reduction in the water tunnel (around 1 psi/sec). Thus, we should not be surprised that the cavitation inception data for this body show a considerable scatter (see Figure 4.14). The cavitation rate for the larger body however, is quite large and this result is consistent with the agreement between the inception and desinence indices (Figures 4.7 and 4.8). The results for the larger bubbles are quite small for both

bodies but are already quite significant for the larger one.

The lack of experimental values of pressure fluctuation peaks in the cavitation inception zone limits our ability to interpret the present results. One can estimate the size of these peaks by assuming that cavitation is initiated from a 20 micron bubble. They are around 1.2 and 1.0 at 20 ft/sec for the two and one-half inch body, respectively. These results are higher than the 0.85 peaks on the surface of the two inch body (Figure 3.21) but are already of comparable size. There is obviously a need for further pressure fluctuation measurements.

Step Body - The width of the mixing layer is estimated from the spread rate of a free shear layer, and the axial position of cavitation inception x_i is assumed to be the location of the first large positive peaks of pressure fluctuations (Figures 3.24 to 31). Then

$$\delta = 0.2\ (x_i - x_{tr})$$

$$Q(\overline{R}) \simeq \pi D\delta \cdot \tfrac{1}{2} u_\infty \cdot n(R)$$

$$Q_c(\overline{R}) = \pi x 10^{-4}\ D^2\ u_\infty\ n(\overline{R})\ \left(\frac{x_i - x_{tr}}{D}\right)$$

Some numerical results are presented in Table 4-9.

R(microns)	u_∞(ft/sec)	Re_D	$Q_c(\overline{R})$[Bubbles/sec]	$\Delta\sigma$ required
0-10	15	2.4×10^5	83	-0.93
10-25			1.5	-0.46
> 25			0.08	-0.19

0-10	20	3.2×10^5	85	-0.52
10-25			1.5	-0.26
> 25			0.09	-0.10
0-10	25	4.0×10^5	96	-0.34
10-25			1.7	-0.17
> 25			0.10	-0.07

Table 4-9 Estimated rate of cavitation events and the local tension required for the step body. $\Delta\sigma$ is taken from Table 4-3 for 10, 20 and 50 micron bubbles.

The results indicate that there is a sufficient number of 10-25 micron bubbles to initiate cavitation. The cavitation indices being 0.95, 1.1 and 1.25 and the average pressure coefficient being -0.65 suggest that pressure fluctuation peaks of -0.76, -0.71 and -0.77 are required for free stream velocity of 15, 20 and 25 ft/sec. These values are much larger than the surface peaks (around -0.23) but as noted before cavitation never starts on the body surface. Since the required peaks are very close to each other one is tempted to suggest that $P'/(0.5\rho u_\infty^2)$ does not depend on the Reynolds number and that the increase in σ is due to the reduction in $\Delta\sigma$ when the velocity is increased. This is not the case however, for the present blunt bodies and the collection of inception indices for sharp edged disks that are presented by Arndt (1981). His collection shows that the cavitation inception index keeps on growing to around 3.0 at $Re_D = 1.6 \times 10^6$ and some measured results exceed even 4.0. These values must be the result of significant dependence of the pressure fluctuation peaks on the Reynolds number.

IV.3.5 Summary and Comments

The present estimates suggest that the free stream bubble population is sufficient to initiate cavitation on the two inch bodies provided that the corresponding pressure fluctuation peaks exist in the cavitation inception zone (assuming that the probability of occurrence of a peak is 0.1 percent).

For the hemispherical body it is shown that all the elements that are required for cavitation inception exist near the reattachment point. These elements include a sufficient supply of 10-25 micron (radius) bubbles, and the corresponding peaks of pressure fluctuations whose frequency is low enough so that these bubbles can fully respond. These statements are supported by the holographic observations that demonstrate that the growth of microscale bubbles to macroscopic cavitation can be confined to the reattachment zone.

As for the rest of the tested bodies, the required pressure peaks are higher than the present experimental results, suggesting that cavitation inception cannot occur on the surface of these bodies. These conclusions are also demonstrated by the holograms.

The possible rate of cavitation events on the half inch body is relatively low (for bubbles larger than 10 microns radius), and this result may explain the large scatter in the cavitation inception data.

The role of the free stream velocity in the inception of cavitation can be expressed by the required tension in the water

$$\sigma_i + C_{PB} + P'/(\tfrac{1}{2}\rho\, u_\infty^2) = \Delta\sigma = -\frac{4T}{3R} \cdot \frac{1}{\tfrac{1}{2}\rho\, u_\infty^2}$$

Thus, σ_i depends on u_∞ even if C_{PB} and $\frac{P'}{\frac{1}{2}\rho u_\infty^2}$ do not. This dependence is due to the division by u_∞^2 in the right-hand side and due to the dependence of R on the free stream velocity. To clarify this statement we recall that the rate of cavitation events is expressed as

$$Q_c(\overline{R}) = K\, u_\infty\, D^2\, n(\overline{R})$$

where K is a constant that depends on the body shape and the choice of the duration of the pressure peaks. We require for cavitation inception that Q_c is at least in the order of one. Thus

$$n(\overline{R})_{min} \simeq \frac{1}{K\, D^2\, u_\infty}$$

Even if $n(\overline{R})$ is independent of the flow conditions a change in u_∞ or the body diameter changes the required minimum density, and thus the corresponding bubble radius. As a result, the choice of R in the expression for $\Delta\sigma$ depends also on the free stream velocity.

When u_∞ is large, or when there is a sufficient number of bubbles with radii larger than 100 microns $\Delta\sigma$ becomes negligible as is usually assumed in the cavitation literature. This is not the case however, either for the present measurements, or for most of the size distributions of bubbles in various experimental facilities that are presented in Figure 1.1.

The Reynolds number dependence of the inception indices on the bodies with a large separation zone, such as blunt bodies, the sharp edged disks, and hydrofoils in large angles of Attack (see Arakeri and Acosta (1979), Arndt (1981), and Van Der Meulen (1980)

cannot be explained only with the present arguments. This dependence indicates that P' - the pressure fluctuation peaks - changes with the Reynolds number. These types of flow fields are discussed in the next section.

The present estimates differ from those of Schiebe (1969), Gates and Acosta (1978), and others that were mentioned in the introduction, who made an attempt to calculate the rate of cavitation events near the surface of a streamlined body. They used the Rayleigh Plesset equation and the potential pressure field around the test body in order to predict the behavior of a bubble as it moves along the surface. Their estimates, however, do not apply to separated flows where the pressure fluctuations, the development of a turbulent mixing layer, and the changes in the potential pressure field due to boundary layer separation play a dominant role. The present rough estimates are an attempt to provide similar answers when separated flows are concerned. The lack of pressure fluctuation data in the inception region prevents us from carrying out more accurate calculations since we presently do not know the size of the pressure peaks and their probability of occurrence. When such information is available one can combine the probability that the pressure will reach a certain peak with the rest of the information (dimensions of the inception region and bubble population), instead of arbitrarily choosing a probability of 0.1 percent.

The last remark concerns the measurements of "cavitation susceptibility" of water by exposing a sample volume to a low pressure in the throat of a venturi tube, as suggested by Oldenziel (1979). On the

one hand,since the bubble population depends mainly on the steady state conditions we may expect that the water susceptibility will not be affected by the short passage through the venturi tube (upstream of the throat). Thus, this instrument provides valuable information about the bubble population and the required tension for cavitation inception. On the other hand, one must be cautious to provide the same values of Q_c to both the venturi throat and to the cavitating zone on the tested body. As one can see, this is not an easy problem.

IV.4 Discussion: The Effect of the Flow Field on Cavitation Inception

IV.4.1 Summary

The relatively large separated zone, the development of a large eddy structure in the shear layer, and the strong dependence of the cavitation index on the Reynolds number classify the step and the blunt bodies in one group. It was demonstrated on the step body that the inception of cavitation is associated with these shear layer eddies, and that location of the first cavities on the blunt bodies agrees with the location of the mixing layer maximum shear stresses. The axial distance of cavitation inception is located upstream of the reattachment region, between $x/D = 0.8$ and 1.1 on the half inch blunt body and in two discrete points downstream of transition on the step body.

The dimensions of the separated zone on the hemispherical body are much smaller, the dependence of the cavitation inception index on the Reynolds number is weak (not noticed in the present experiments) and the first signs of cavitation appear near the reattachment zone, but detached from the surface. These flow field and cavitation phenomena are different

from the first group of bodies as is also suggested by Arakeri and Acosta (1979).

IV.4.2 Cavitation and the Shear Layer Eddies

The existence of a coherent eddy structure in free shear layers and the present cavitation observations suggest that the flow field can be modeled as a series of vortices. This idea is not new, Kermeen and Parkin (1957) developed such a model for the pressure field behind a sharp edged disk,and quite a large body of theoretical and numerical work has been done since then (see Saffman and Baker (1974)). Moore and Saffman (1975) suggest that the circulation Γ around each vortex can be estimated as

$$\Gamma = \Delta u \cdot \lambda$$

where Δu is the velocity difference across the shear layer and λ the spacing between neighboring eddies. The pressure in a vortex core,P_c, can be estimated as

$$P_c = P_\infty - \frac{\rho}{2}\left(\frac{\Gamma}{2\pi r_c}\right)^2$$

where r_c is the radius of the core.
As a result

$$\frac{P_c - P_\infty}{\frac{1}{2}\rho(\Delta u)^2} = -\left(\frac{\lambda}{2\pi\, r_c}\right)^2$$

Thus, any changes in this pressure coefficient must be accompanied with changes in the ratio λ/r_c. The existing literature of plane shear flows

(see the discussion in Chapter 3) suggests that both λ and the width of the shear layer (or the slope thickness) grow linearly with the axial distance from an initial point x_o. If we assume that the radius of the core is proportional to the mixing layer width, then λ/r_c is independent of x. Thus, the pressure in the core of all the vortices in the shear layer must be identical. Moreover, since the spread rate and λ show a little dependence on the Reynolds number, provided that the separating flow is either laminar or turbulent (see, for example, Hussain and Ledan (1978)) then the core pressure coefficient is also independent of the Reynolds number. Kermeen and Parkin (1957) came to the same conclusion with a slightly different approach. Such a simplified model cannot explain either the strong Reynolds number dependence of the cavitation inception index or the reason for the consistent axial location of the first cavitating bubbles on the blunt body.

Arndt (1976) modified this model by assuming that the eddy core contains only the fluid that was originally in the boundary layer prior to separation. Thus, he obtained

$$r_c^2 \propto (Re_D)^{-\frac{1}{2}};$$

$$\frac{P - P_\infty}{\frac{1}{2}\rho u_\infty^2} \propto (Re_D)^{\frac{1}{2}}$$

From these relations and from the vortex shedding frequency that was found by Kermeen and Parkin, Arndt developed an empirical relation between the cavitation inception index and the Reynolds number. Arndt's

assumptions however, are questionable. Flow visualization experiments (see, for example, Winant and Browand (1974) and Freymuth (1965) show that the entrained fluid and the boundary layer fluid wrap up together into a spiral. Thus, the assumption that all the boundary layer fluid is concentrated in a core that does not contain any entrained fluid is incorrect. Moreover, the width of the mixing region does not depend on the Reynolds number, at least not to the levels that are suggested by Arndt (in some works such as Brown and Roshko (1974) this width is determined by the size of the vortices), and it seems unlikely that the vortex core does. Finally, according to Moore and Saffman (1974), r_c and λ are related because of the velocity that is induced by one vortex on its neighbors. They estimated this distance and their results are in agreement with those of Brown and Roshko (1974). Thus, it seems that the ratio λ/r_c cannot depend on the Reynolds number.

The preceding argument, the previously mentioned experimental results of Ota (1975 and 1980)(who did not detect any Reynolds number effects on the rms values of velocity fluctuations in similar flows), and the present measurements of surface pressure fluctuations leave us at a dead end insofar as the vortex model is concerned for cavitation inception. A possible explanation for the dependence of the inception index on the Reynolds number is an increase in the size of the pressure fluctuation peaks that does not affect the rms values. Such a behavior can be presently detected only downstream of the reattachment point on the blunt body (see Figure 3.14 and compare the results in Figures 3.15 to 3.18). Unlike the 0.1 percent peaks that grow with the velocity, the corresponding rms values and the 2.5 percent probability

peaks do not display a similar dependence on the Reynolds number. There is a need for further exploration of the pressure field inside the shear layer before making any conclusive statement.

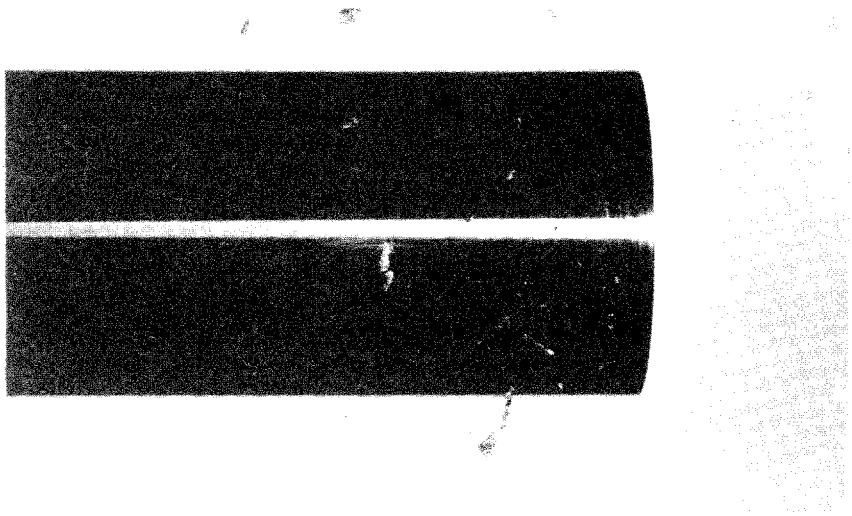

Fig. 4.1. A photograph of an early stage of cavitation on the two inch blunt body. $Re_D = 3.6 \times 10^5$, $\sigma = 1.70$.

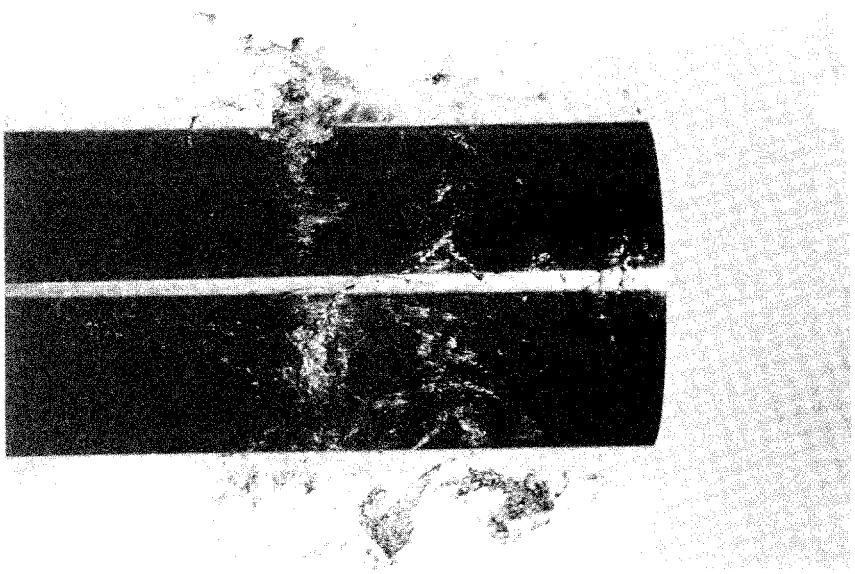

Fig. 4.2. A photograph of cavitation on the two inch blunt body. $Re_D = 3.6 \times 10^5$, $\sigma = 1.60$.

(a)

(b)

Fig. 4.3. Holograms of the first microscopic signs of cavitation near the surface of the two inch blunt body. $Re_D = 2.3 \times 10^5$, $\sigma = 1.21$. The "large" sheared bubbles are located at a) $x/D = 0.89$, $y/D = 0.13$; b) $x/D = 0.96$, $y/D = 0.22$.

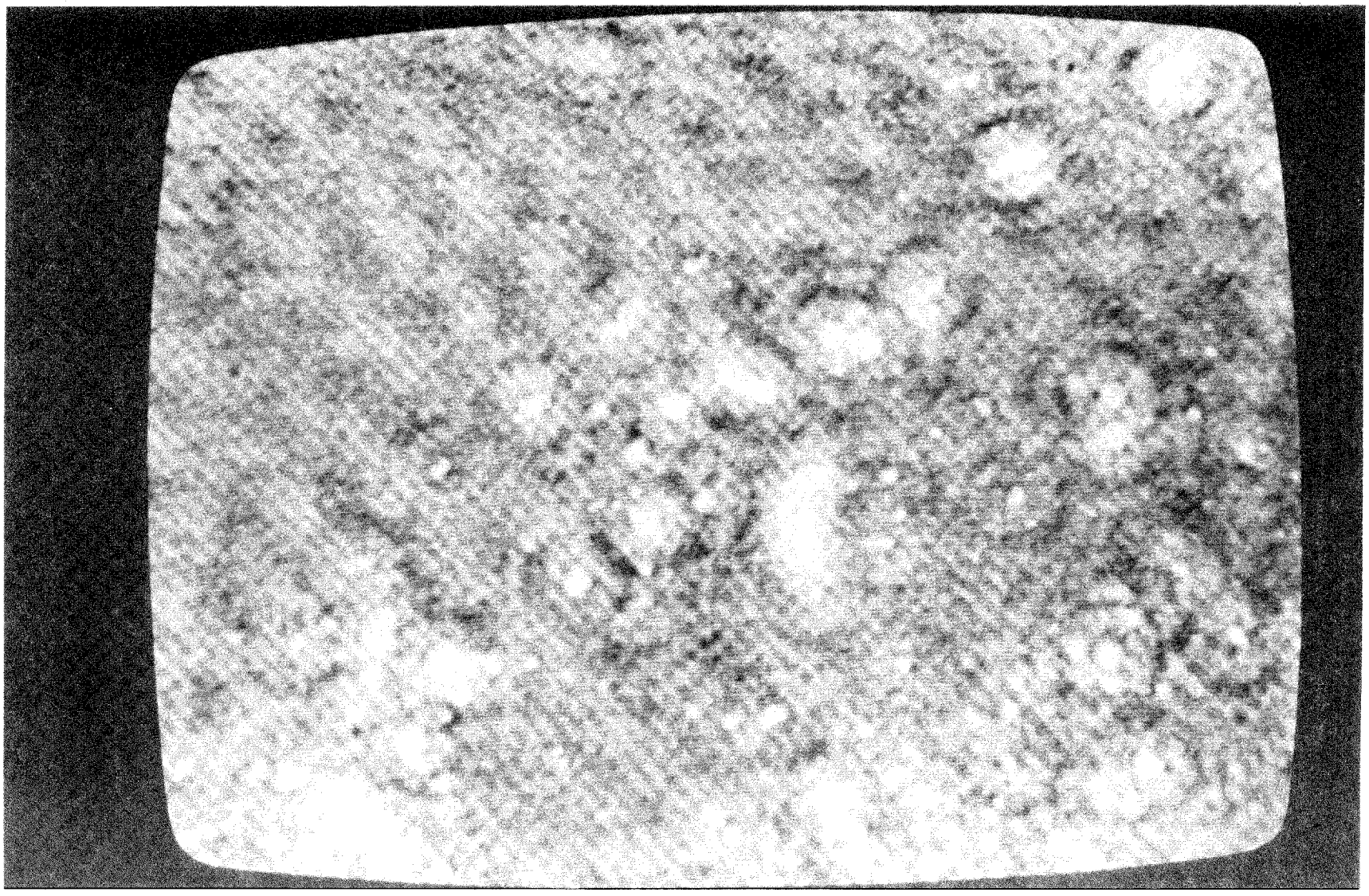

Figure 4.4. A hologram that displays the population of bubbles below and above the shear layer of the blunt body during cavitation inception. $Re_D = 2.3 \times 10^5$, $\sigma = 1.15$. The hologram covers the region between $x/D = 0.23$ and 0.45 and $y/D = 0.11$ and 0.27.

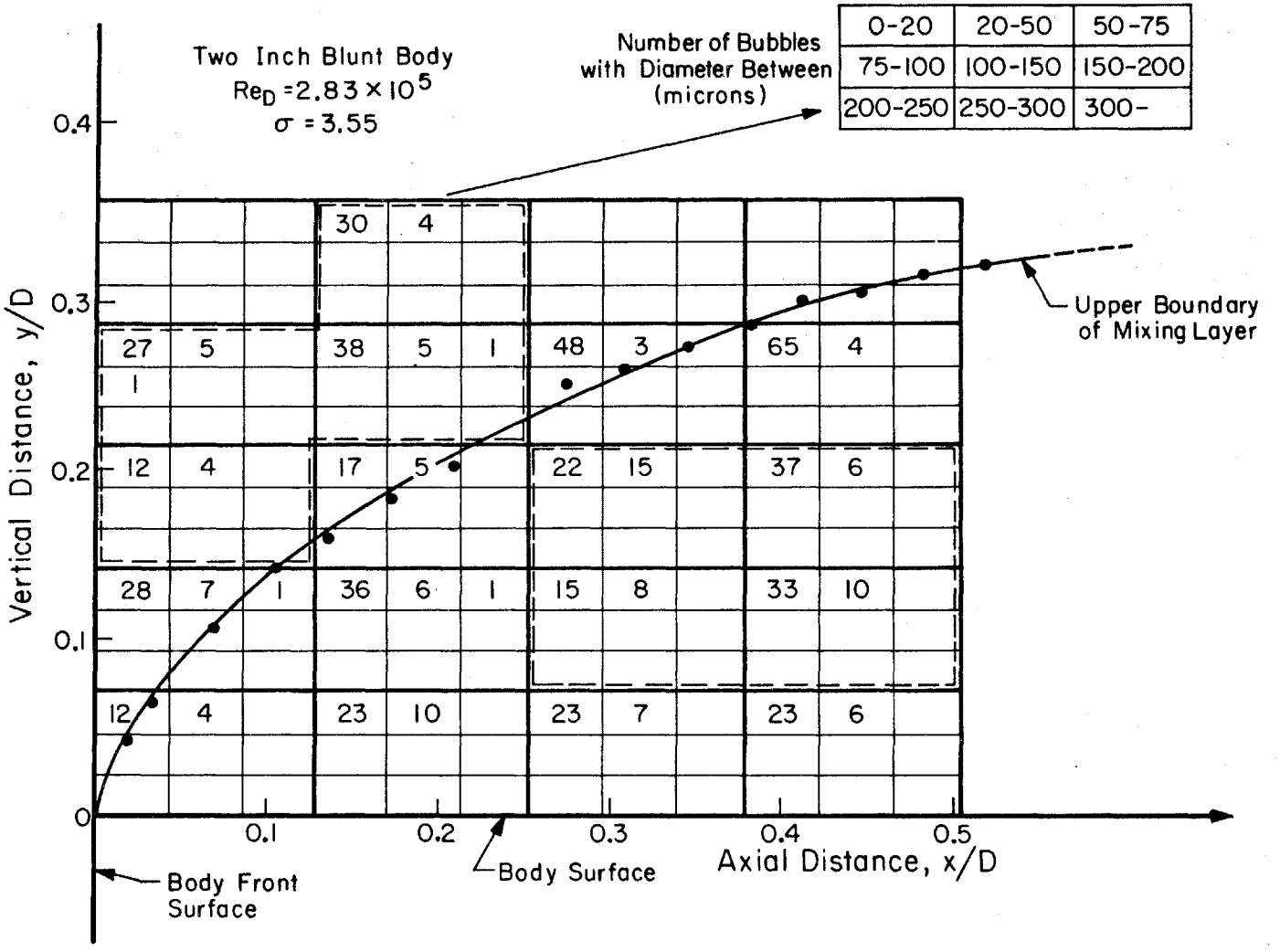

Figure 4.5a. Maps of bubble population near the surface of the two inch blunt body, $Re_D = 2.83 \times 10^5$.

(b)

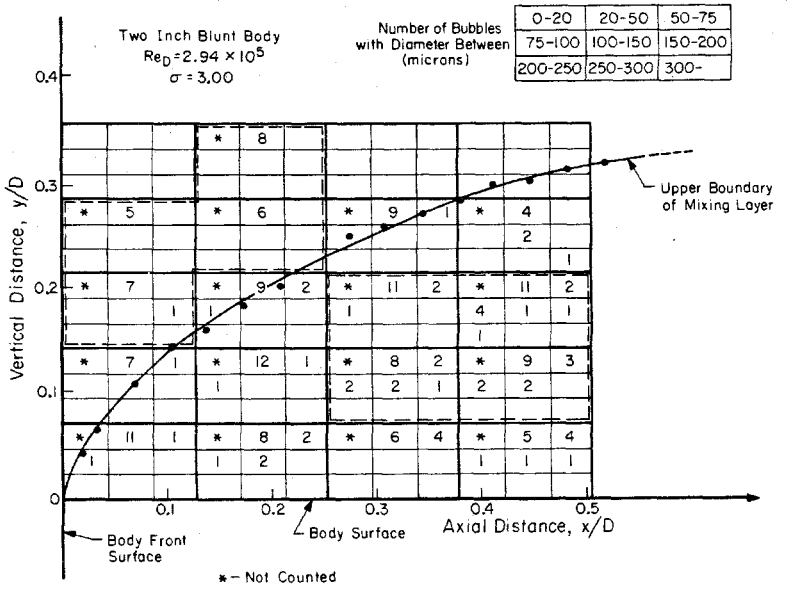

Fig. 4.5. Maps of bubble population near the surface of the two-inch blunt body. a) $Re_D = 2.83 \times 10^5$, $\sigma = 3.55$; b) $Re_D = 2.94 \times 10^5$, $\sigma = 3.00$; c) $Re_D = 3.06 \times 10^5$, $\sigma = 2.56$.

(c)

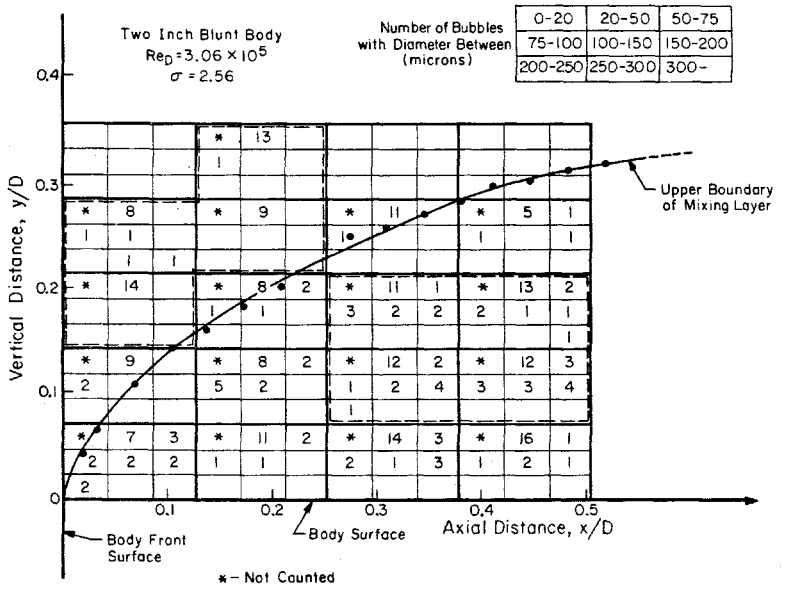

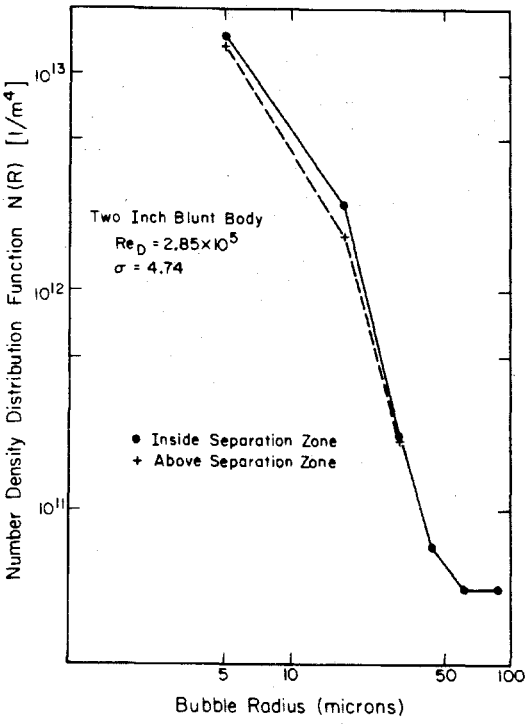

Fig. 4.6a

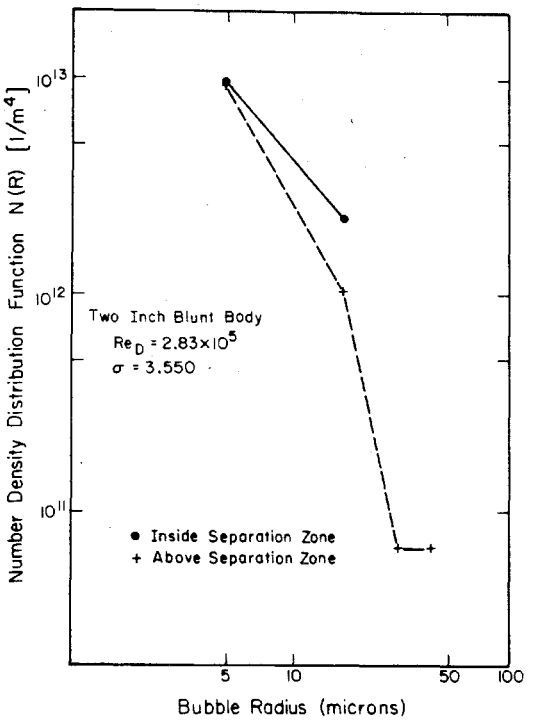

Fig. 4.6b

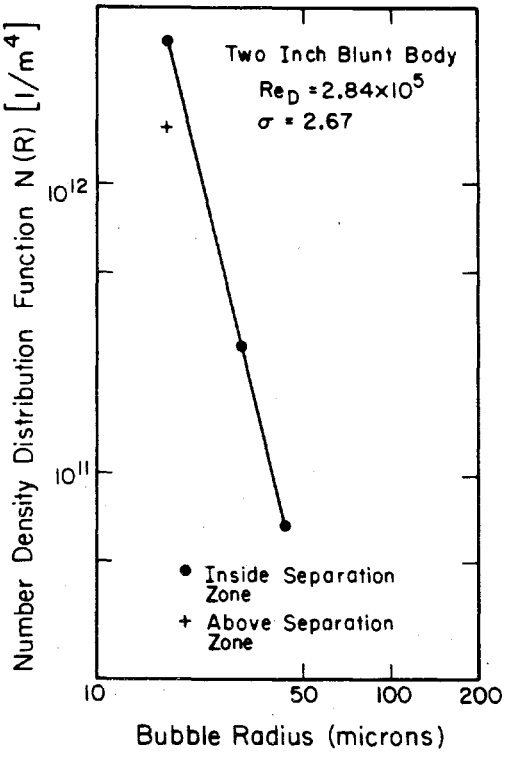

Fig. 4.6c

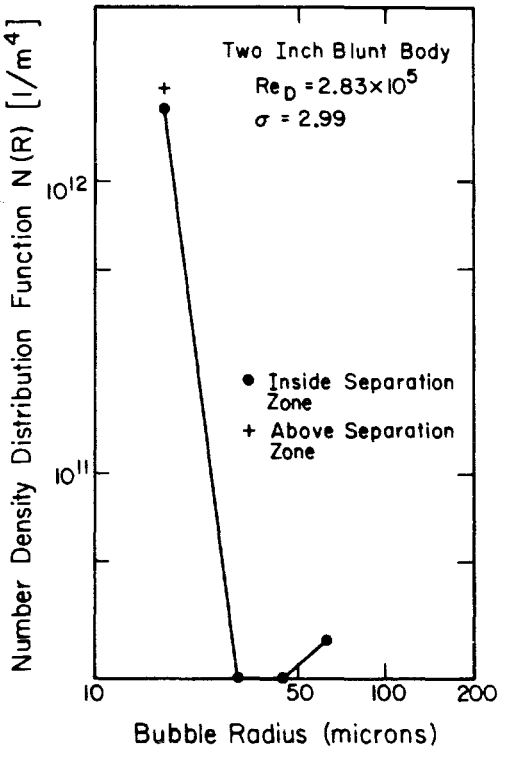

Fig. 4.6d

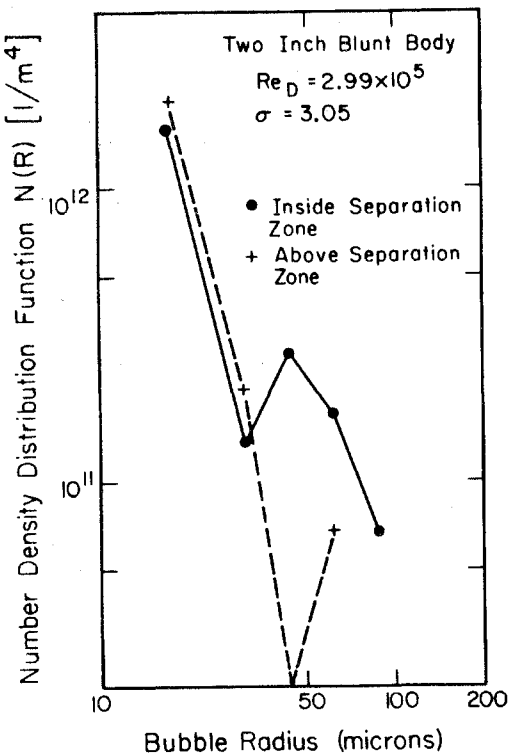

Fig. 4.6e

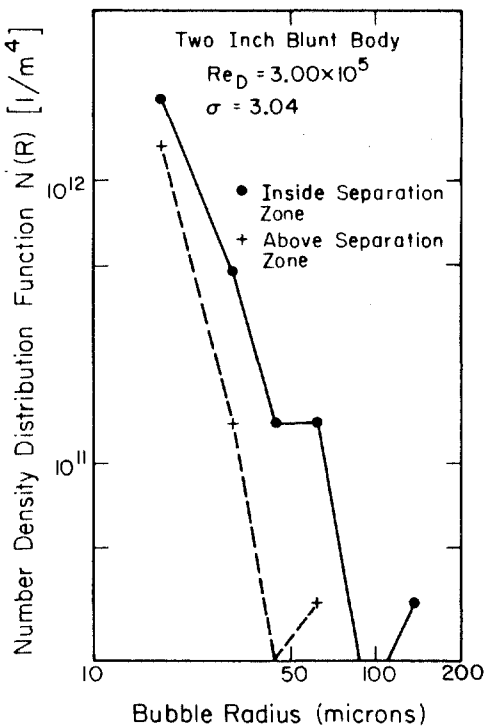

Fig. 4.6f

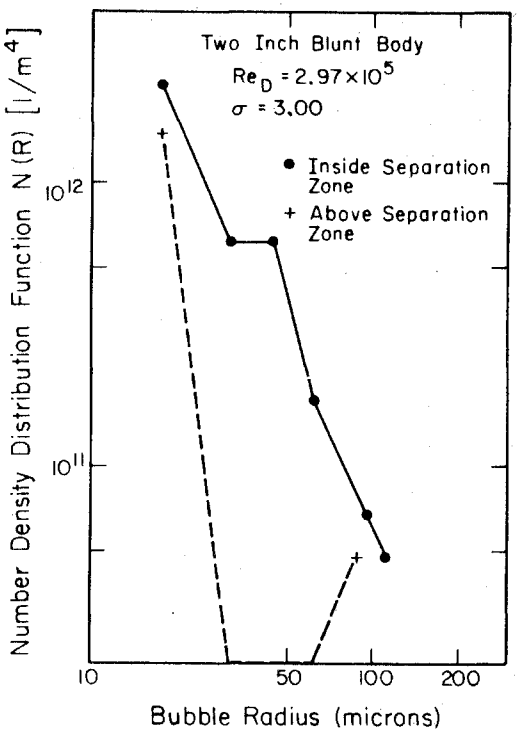

Fig. 4.6g

Fig. 4.6h

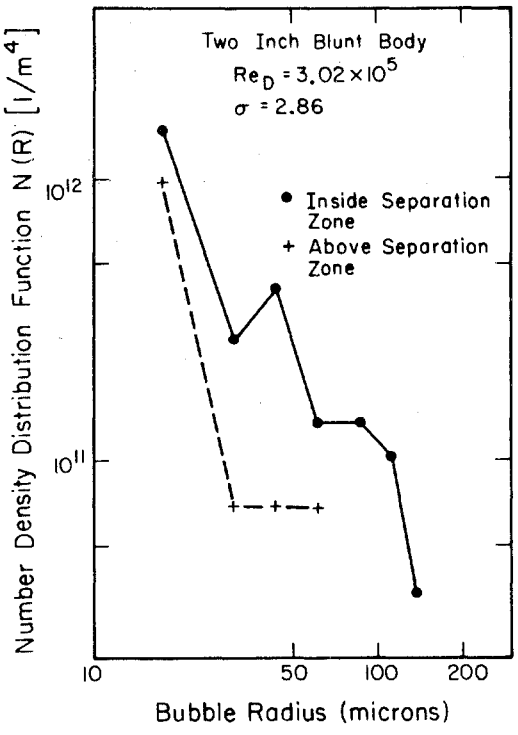

Fig. 4.6i

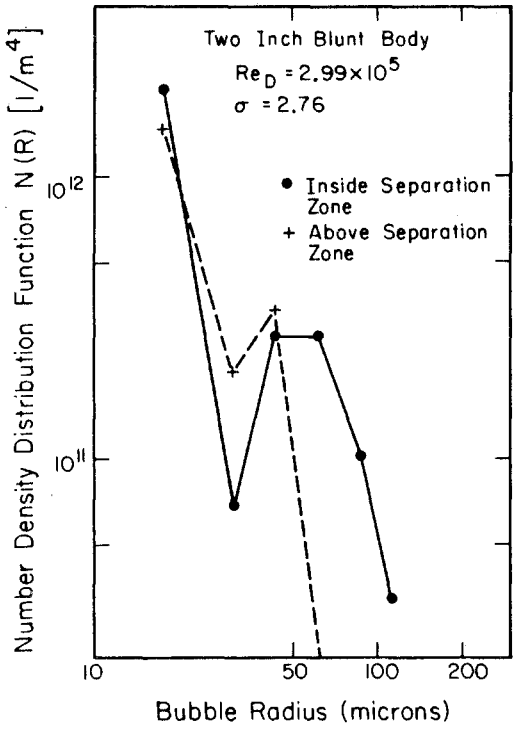

Fig. 4.6j

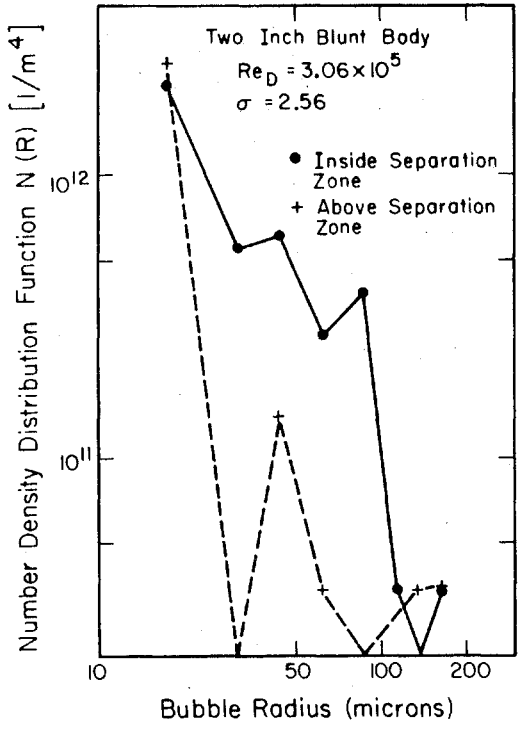

Fig. 4.6. The number density distribution function of bubbles that were counted near the surface of the two inch blunt body. The counted sections are defined by the dashed lines in Fig. 4.5 a) $Re_D = 2.85 \times 10^5$, $\sigma = 4.74$; b) $Re_D = 2.83 \times 10^5$, $\sigma = 3.55$; c) $Re_D = 2.83 \times 10^5$, $\sigma = 2.99$, d) $Re_D = 2.84 \times 10^5$, $\sigma = 2.67$; e) $Re_D = 2.99 \times 10^5$, $\sigma = 3.05$; f) $Re_D 3.00 \times 10^5$, $\sigma = 3.04$; g) $Re_D = 2.94 \times 10^5$, $\sigma = 3.00$; h) $Re_D = 3.02 \times 10^5$, $\sigma = 2.86$; i) $Re_D = 2.99 \times 10^5$, $\sigma = 2.76$; j) $Re_D = 3.06 \times 10^5$, $\sigma = 2.56$.

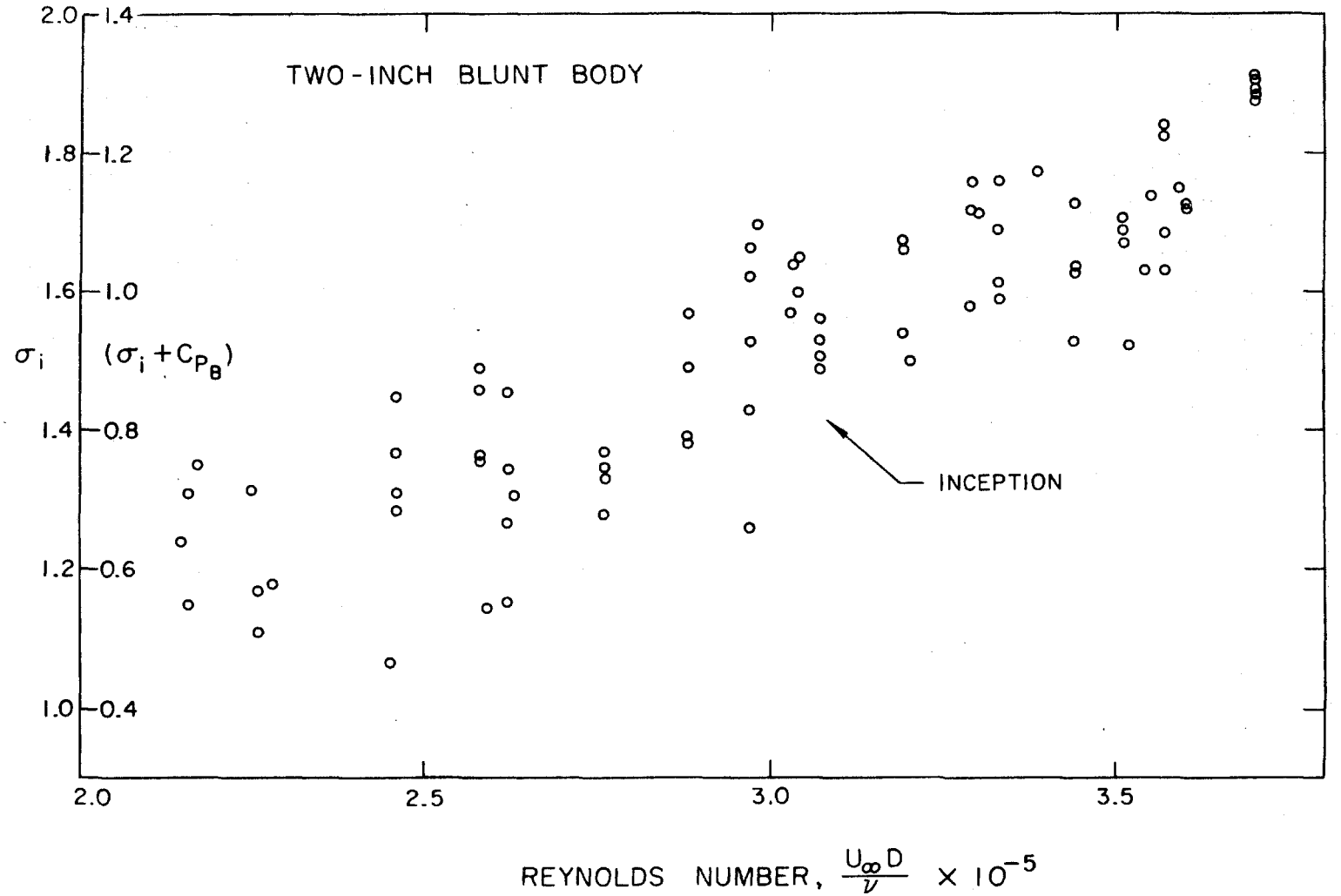

Figure 4.7. Cavitation inception indices on the two inch blunt body.

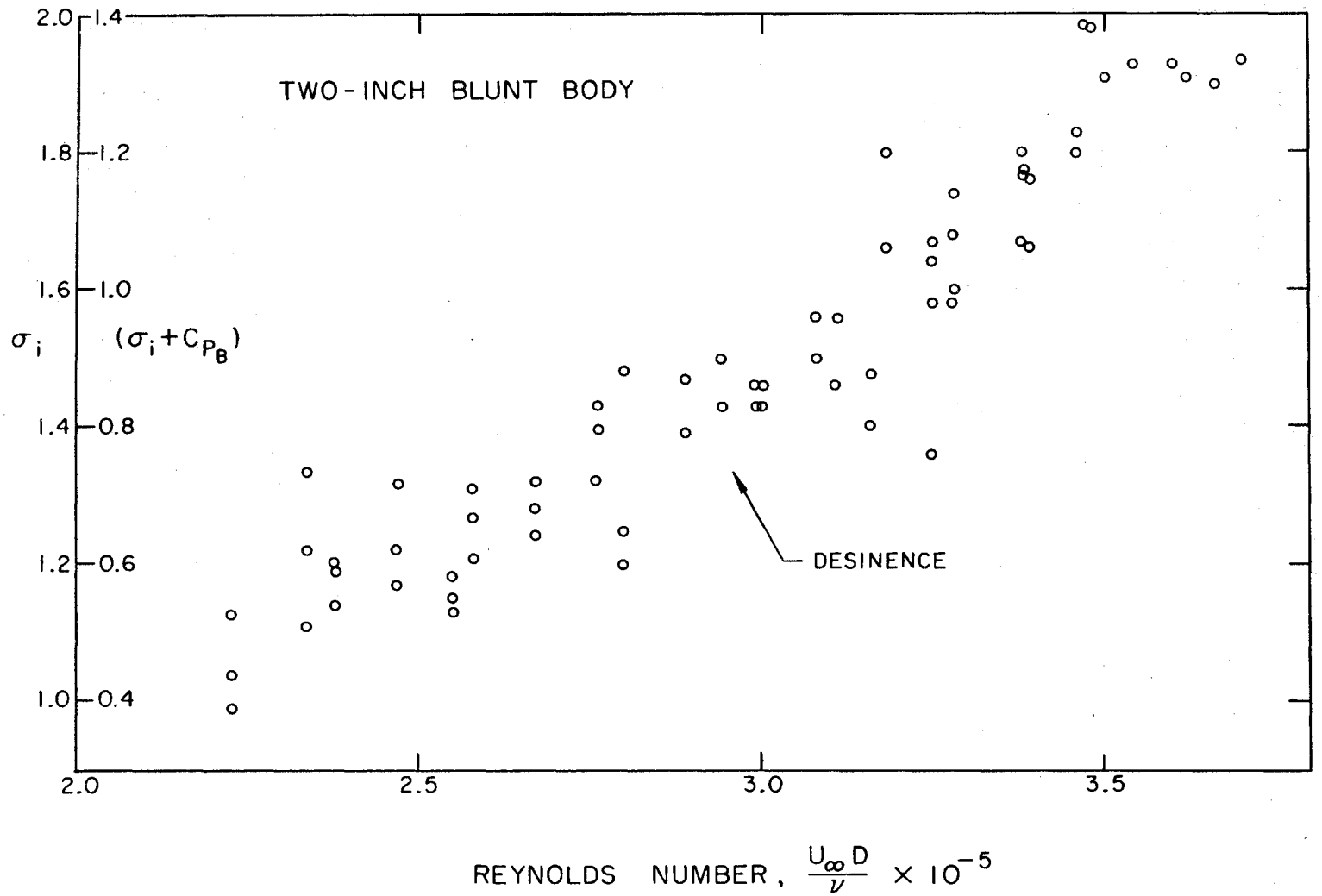

Figure 4.8. Cavitation desinence indices on the two inch blunt body.

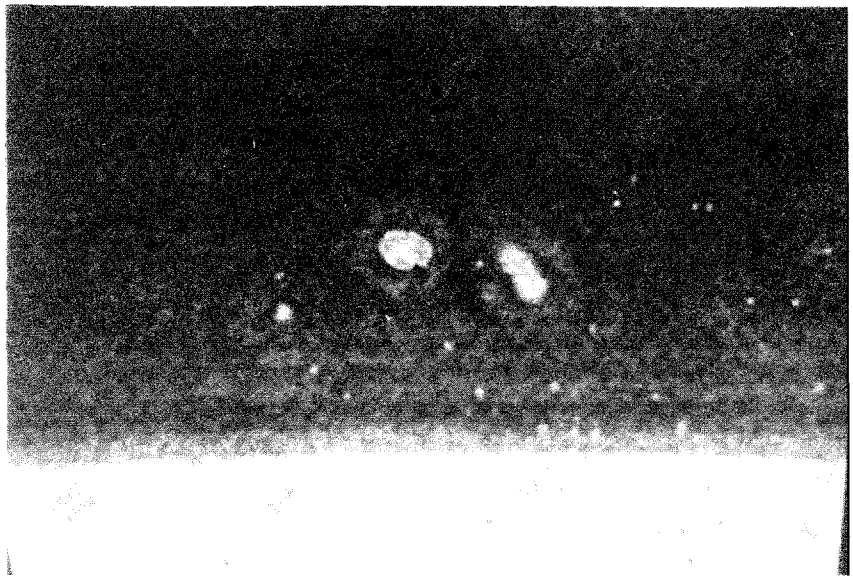

Fig 4.9. A hologram of cavitation inception on the one-half inch blunt body. u_∞ = 21.1 ft/sec , $Re_D = 8.42 \times 10^4$, $\sigma = 1.41$.

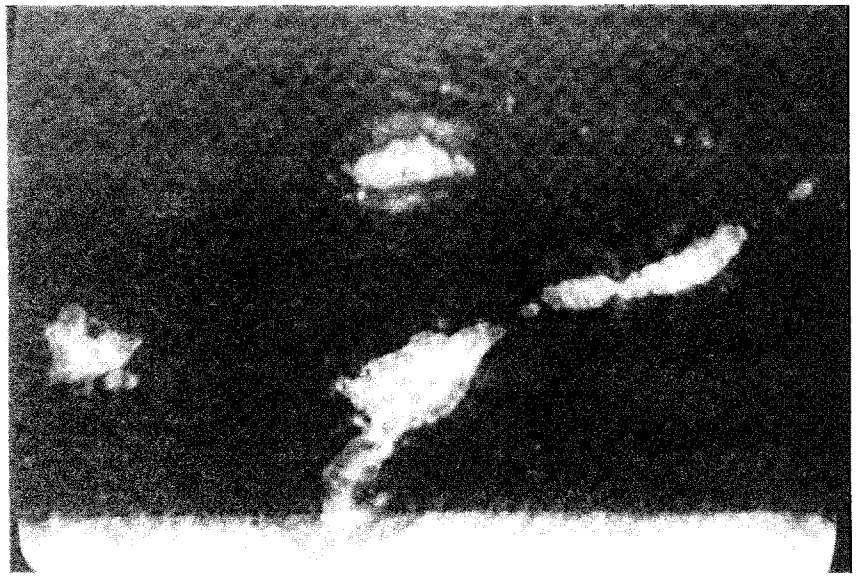

Fig. 4.10. A hologram of cavitation inception on the one-half inch blunt body. u_∞ = 21.1 ft/sec, $Re_D = 8.24 \times 10^4$, $\sigma = 1.41$.

(a)

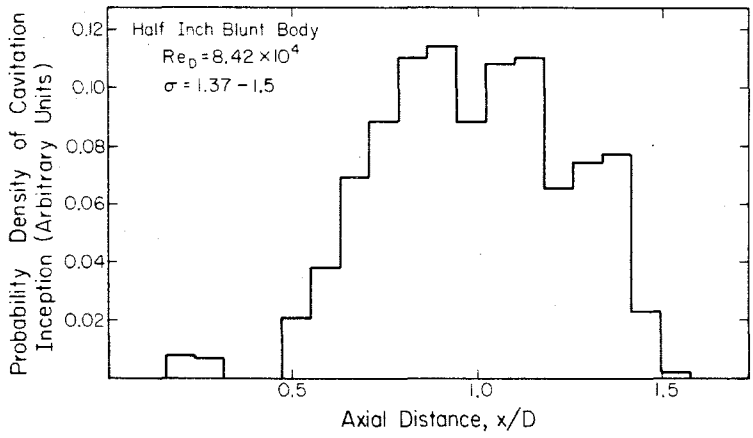

Fig. 4.11. Probability density histograms of the location of cavitation inception on the one-half inch blunt body. a) axial location, b) vertical location.

(b)

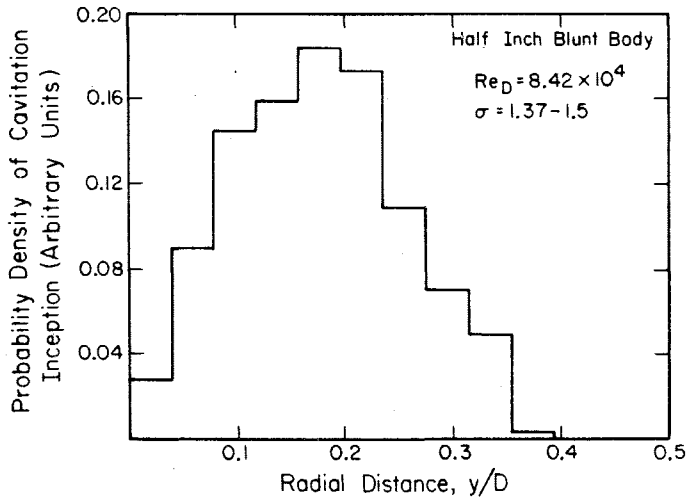

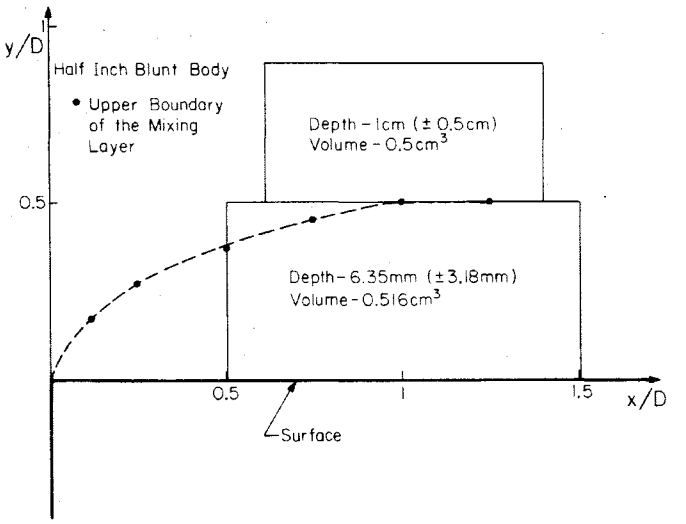

Fig. 4.12. A description of the counted sample volumes near the surface of the one-half inch blunt body.

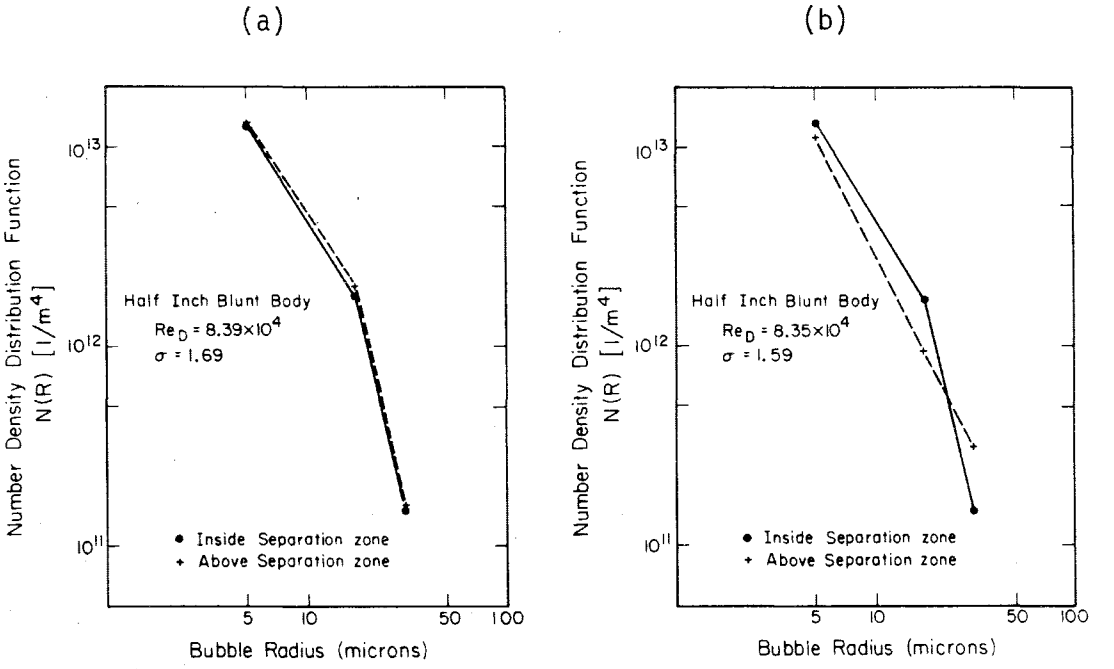

Fig. 4.13. The population of bubbles near the surface of the one-half inch blunt body. $u_\infty \cong$ 21ft/sec , $Re_D \cong 8.4 \times 10^4$; a)$\sigma = 1.69$; b)$\sigma = 1.59$; c)$\sigma = 1.58$; d)$\sigma = 1.52$; e) $\sigma = 1.51$; f) $\sigma = 1.46$; g) $\sigma = 1.46$; h) $\sigma = 1.78$. i) $\sigma = 1.52$.

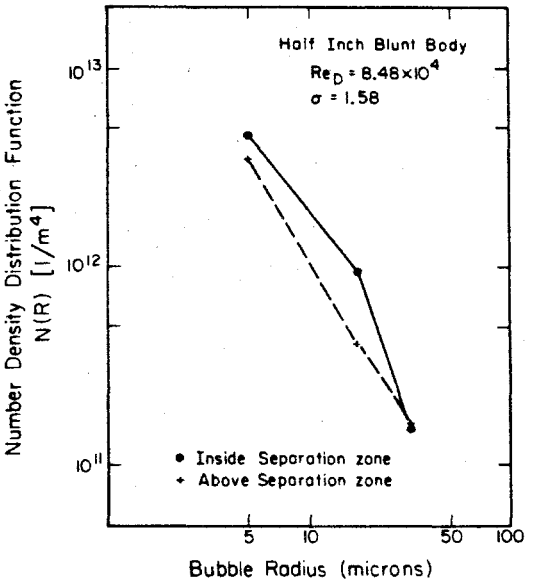
Half Inch Blunt Body
$Re_D = 8.48 \times 10^4$
$\sigma = 1.58$
Number Density Distribution Function N(R) [1/m⁴]
10^{13}
10^{12}
10^{11}
• Inside Separation zone
+ Above Separation zone
5
10
50
100
Bubble Radius (microns)

(c)

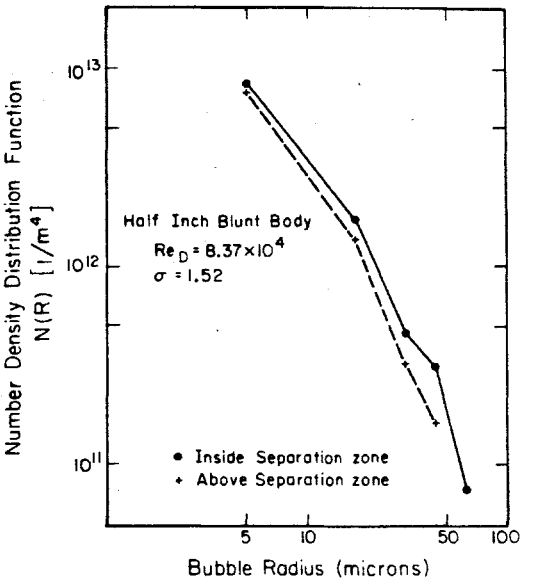
Half Inch Blunt Body
$Re_D = 8.37 \times 10^4$
$\sigma = 1.52$
Number Density Distribution Function N(R) [1/m⁴]
10^{13}
10^{12}
10^{11}
• Inside Separation zone
+ Above Separation zone
5
10
50
100
Bubble Radius (microns)

(d)

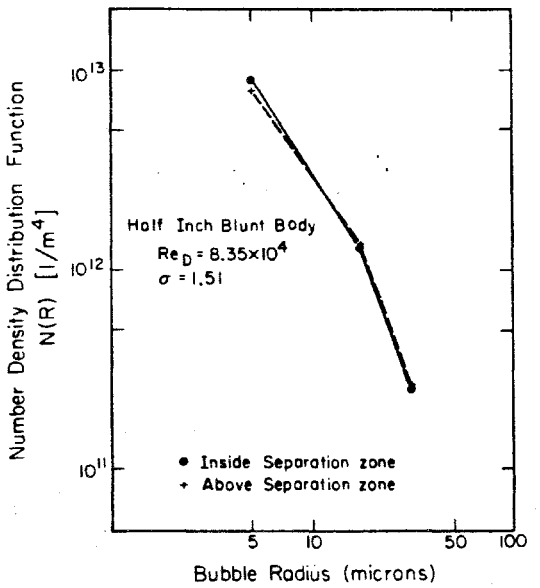
Half Inch Blunt Body
$Re_D = 8.35 \times 10^4$
$\sigma = 1.51$
Number Density Distribution Function N(R) [1/m⁴]
10^{13}
10^{12}
10^{11}
• Inside Separation zone
+ Above Separation zone
5
10
50
100
Bubble Radius (microns)

(e)

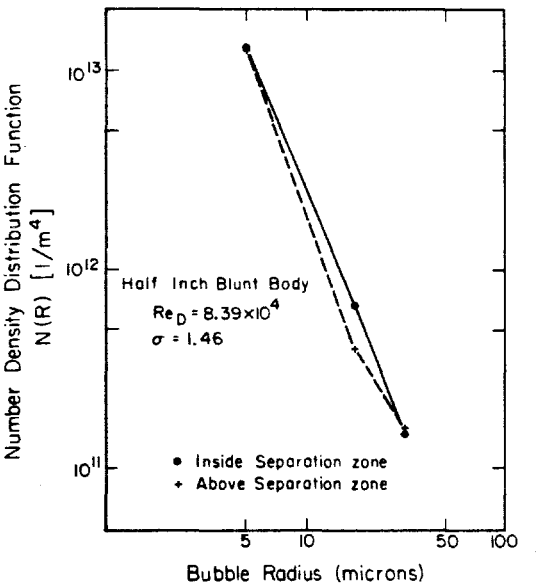
Half Inch Blunt Body
$Re_D = 8.39 \times 10^4$
$\sigma = 1.46$
Number Density Distribution Function N(R) [1/m⁴]
10^{13}
10^{12}
10^{11}
• Inside Separation zone
+ Above Separation zone
5
10
50
100
Bubble Radius (microns)

(f)

Fig. 4.13

(g)

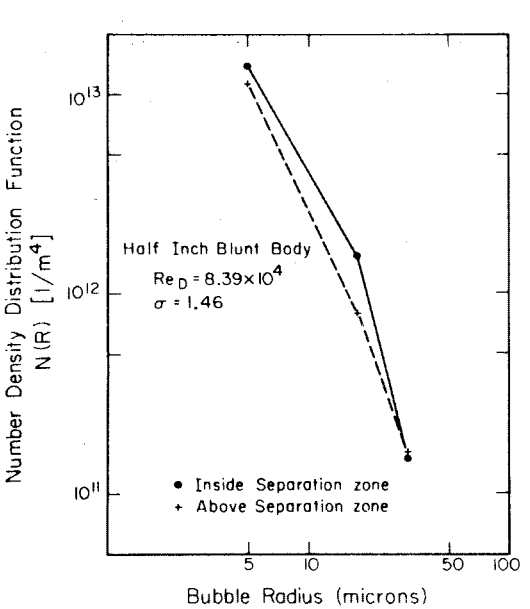
Number Density Distribution Function
N(R) [1/m⁴]
Half Inch Blunt Body
Re_D = 8.39×10⁴
σ = 1.46
• Inside Separation zone
+ Above Separation zone
Bubble Radius (microns)

(h)

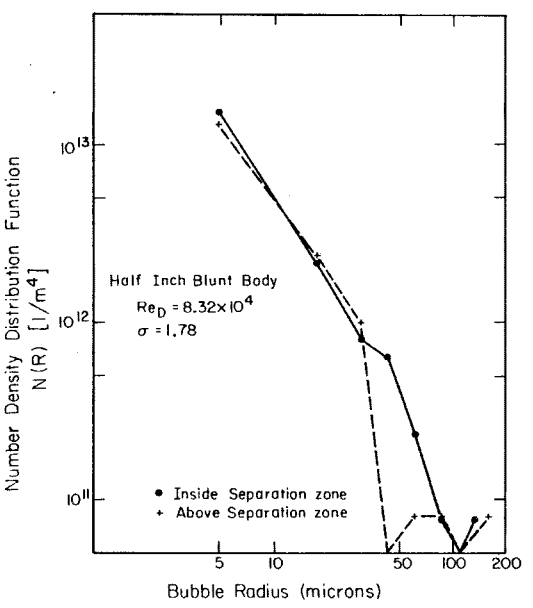
Number Density Distribution Function
N(R) [1/m⁴]
Half Inch Blunt Body
Re_D = 8.32×10⁴
σ = 1.78
• Inside Separation zone
+ Above Separation zone
Bubble Radius (microns)

(i)

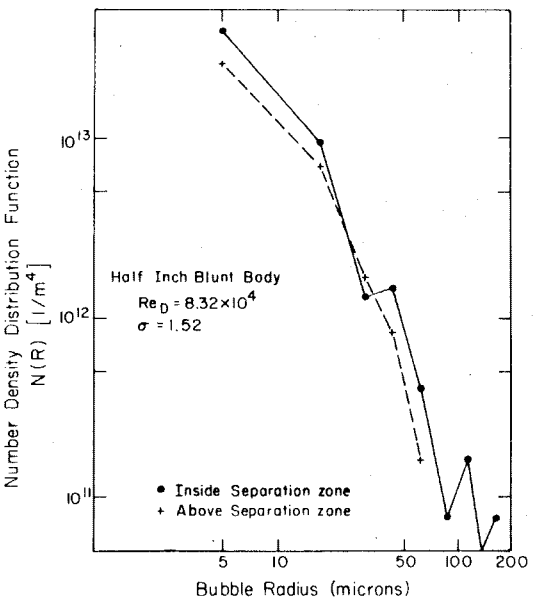
Number Density Distribution Function
N(R) [1/m⁴]
Half Inch Blunt Body
Re_D = 8.32×10⁴
σ = 1.52
• Inside Separation zone
+ Above Separation zone
Bubble Radius (microns)

Fig. 4.13

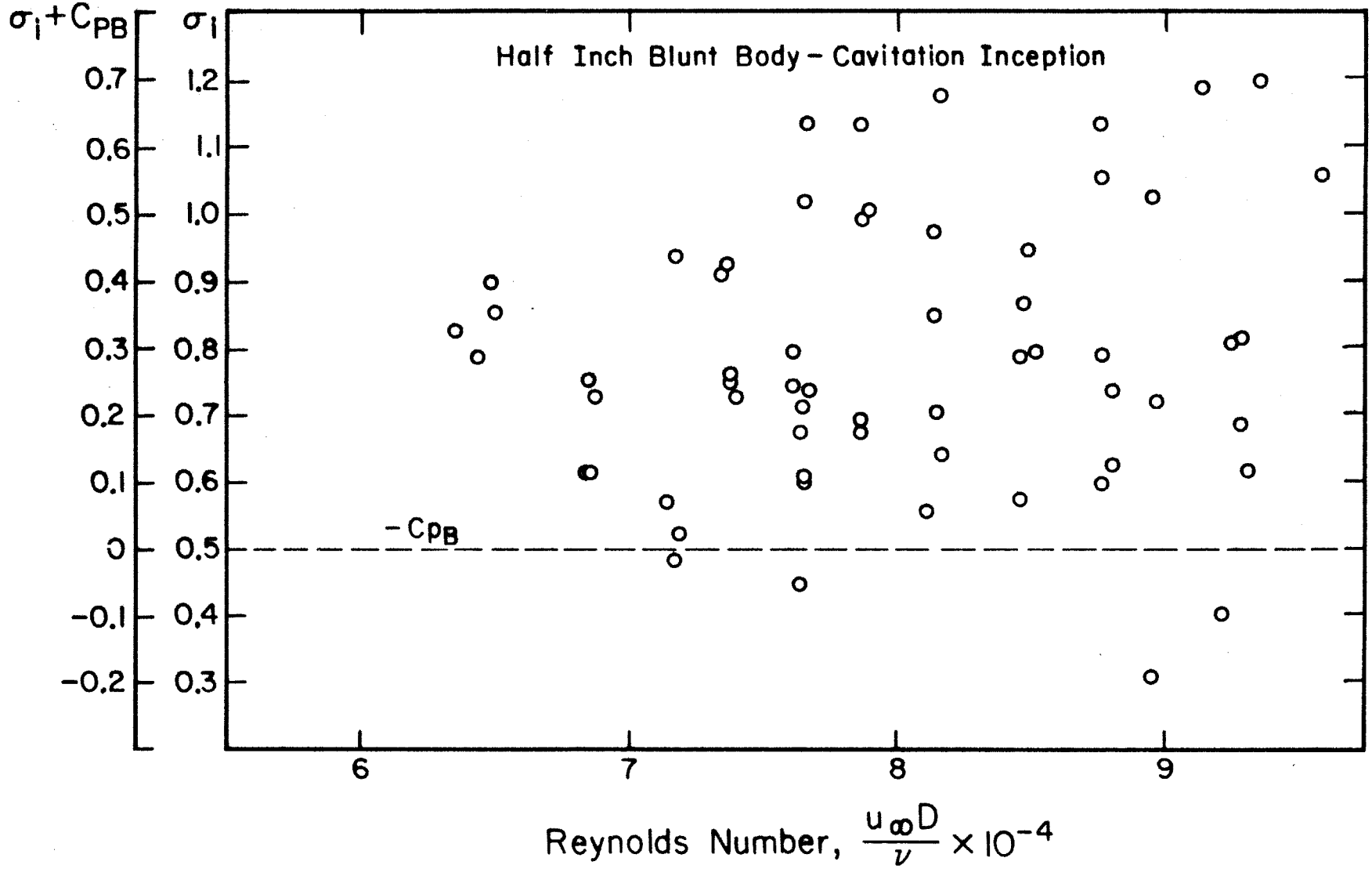

Figure 4.14. Cavitation inception indices on the one-half inch blunt body.

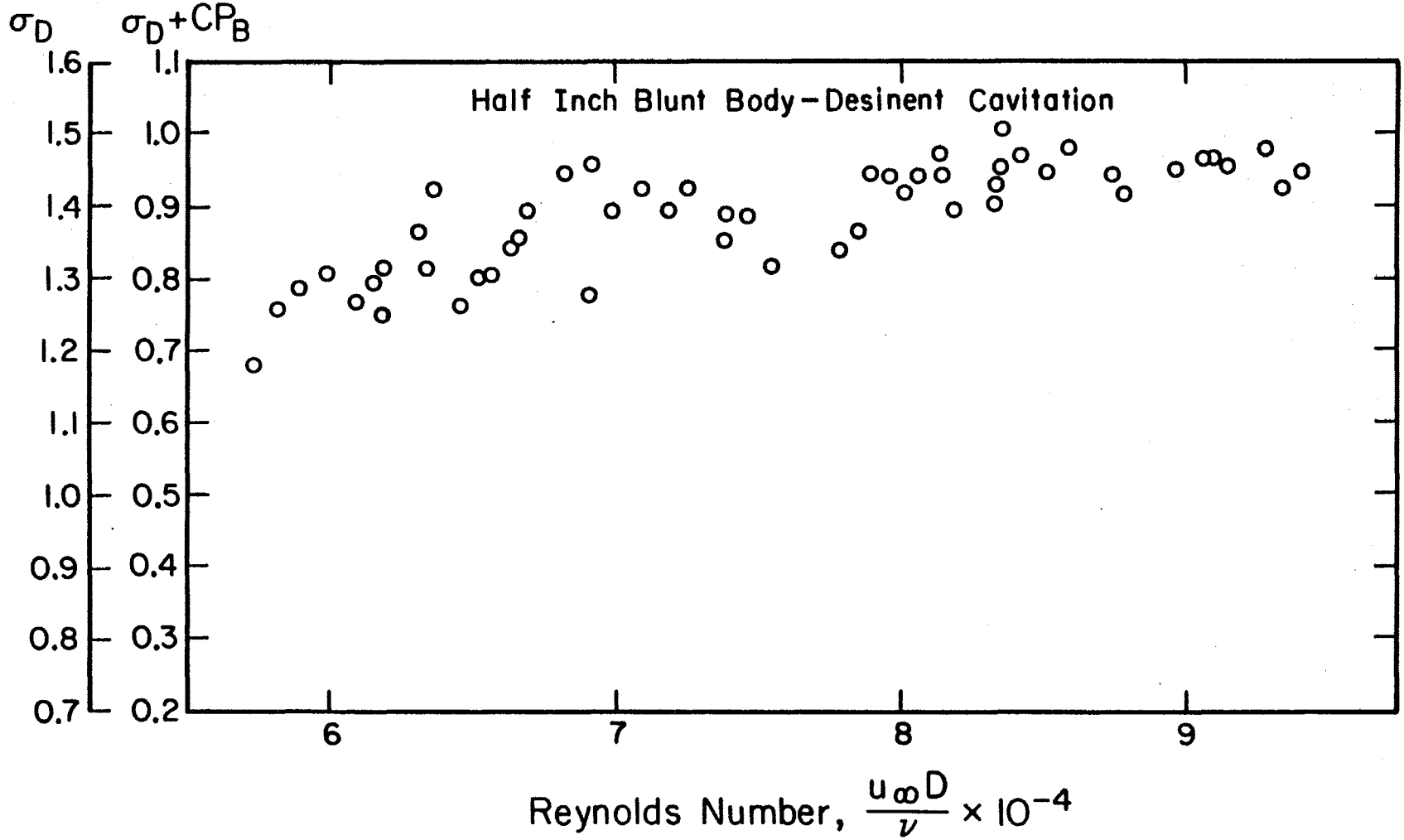

Figure 4.15. Cavitation desinence indices on the one-half inch blunt body.

Fig. 4.16. Travelling bubble cavitation on the hemispherical body. $Re_D = 3.70 \times 10^5$, $\sigma = 0.73$.

Fig. 4.17) Band type cavitation on the hemispherical body. $Re_D = 3.70 \times 10^5$, $\sigma = 0.55$.

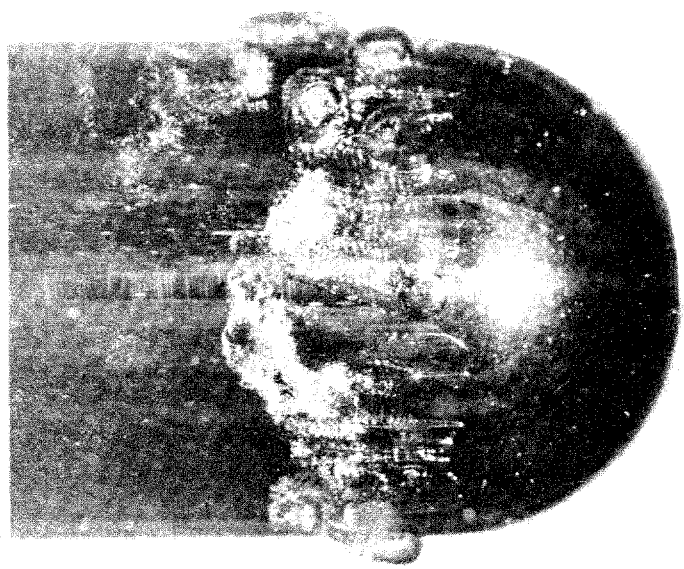

Fig. 4.18. A mixture of band and travelling bubble cavitation in a tunnel filled with a large number of bubbles. $Re_D = 3.70 \times 10^5$, $\sigma = 0.54$.

Fig. 4.19. A hologram of cavitation inception on the hemispherical body. $Re_D = 3 \times 10^5$, $\sigma = 0.607$. The hologram covers the region between $x/D = 0.53$ and 0.67. (the flow is from left to right).

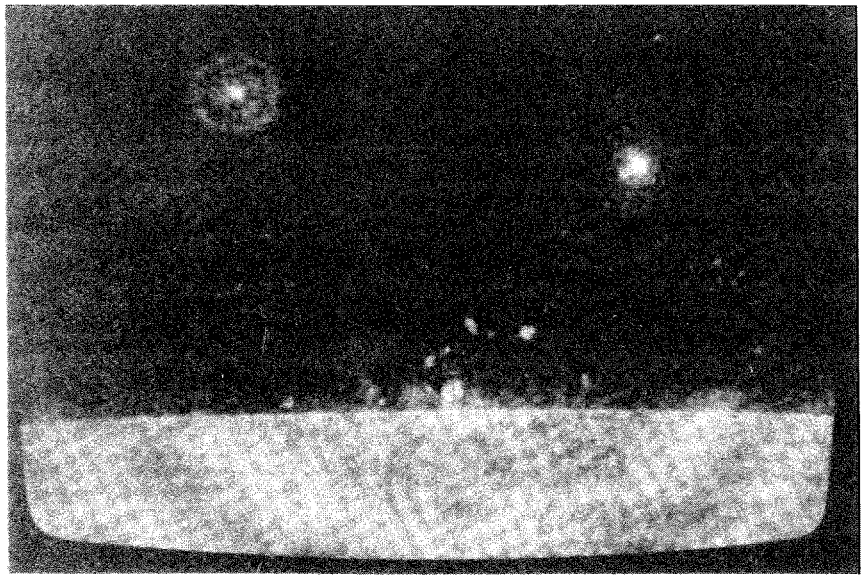

Fig. 4.20. A hologram of cavitation inception on the hemispherical body. $Re_D = 3.77 \times 10^5$, $\sigma = 0.630$. The hologram covers the region between $x/D = 0.51$ and 0.65.

Fig. 4.21. A sheared free stream bubble above the separation zone of the hemispherical body. $Re_D = 3.8 \times 10^5$, $\sigma = 0.63$. The width of the screen in 6.9mm and the bubble is located at $x/D = 0.55$.

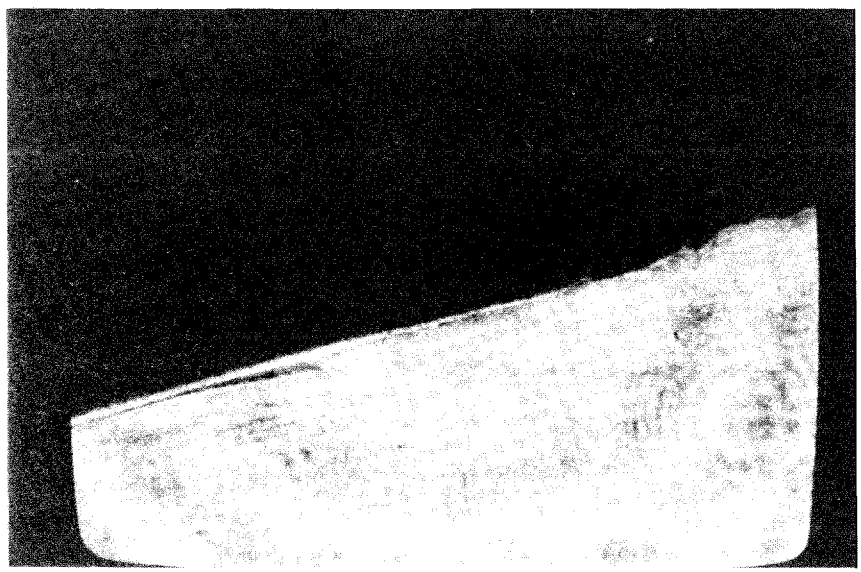

Fig. 4.22. A hologram of band type cavitation on a heated hemispherical body. $Re_D = 3.3 \times 10^5$, $\sigma = 0.46$. The width of the screen is 6.9mm and cavitation separation is at $x/D = 0.42$.

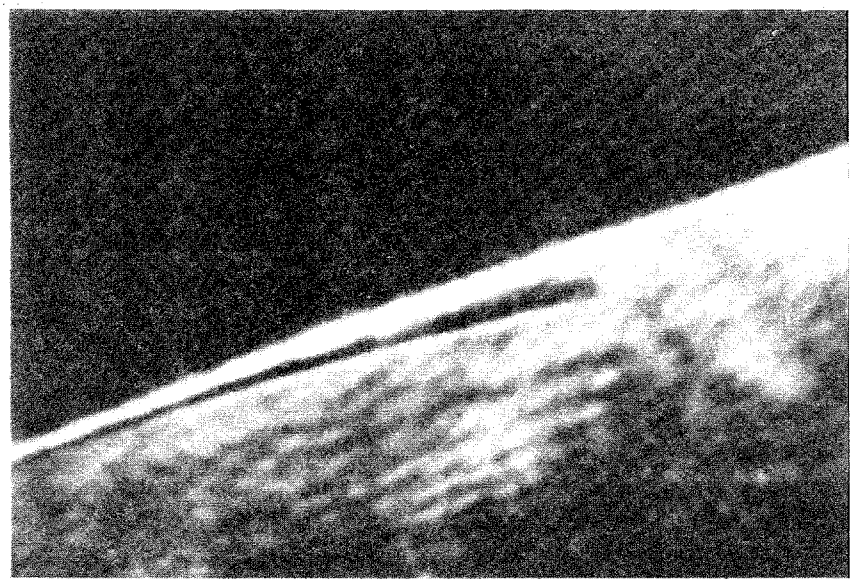

Fig. 4-23. A hologram showing the laminar and cavitation separation points on the hemispherical body. $Re_D = 3.54 \times 10^5$, $\sigma = 0.494$. The width of the screen is 3.25mm and cavitaion separation is at $x/D = 0.43$.

Fig. 4-24. A hologram of travelling bubble cavitation on the hemispherical body. $Re_D = 3.8 \times 10^5$, $\sigma = 0.63$. The photograph covers the region between $x/D = 0.32$ and $x/D = 0.46$.

HEMISPHERICAL BODY-BUBBLE POPULATION DURING INCEPTION

BUBBLE DIAMETER IN MICRONS

SECTION	0-20	20-50	50-75	75-100	100-150	150-250	250-350
a	30	13	2	1	1	1	
b	29	5	2	3	1	1	1
c	27	9	3	1		1	
d	12	2	1				
e	30	4	2	2	1		

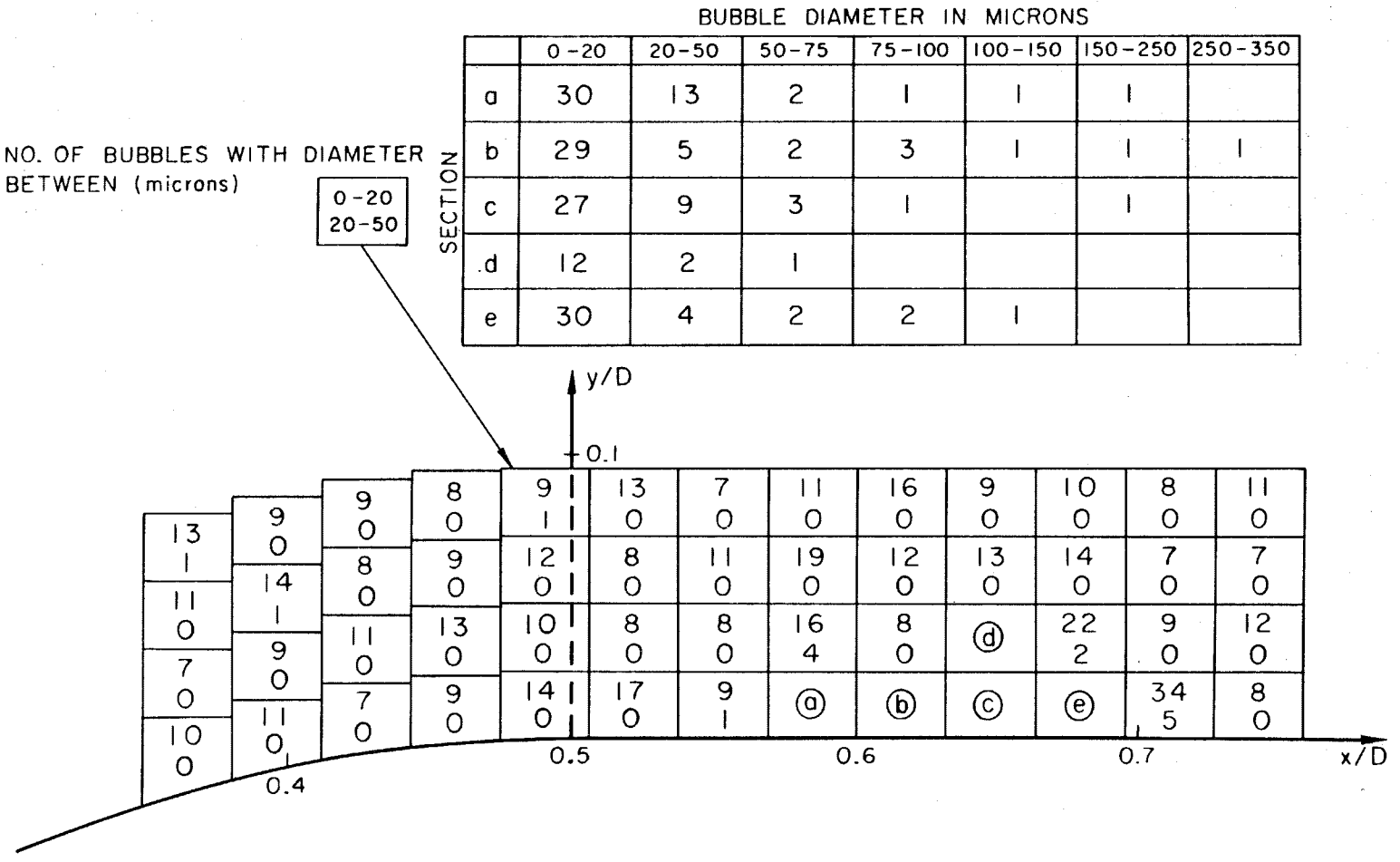

Figure 4.25. A map of bubble population during cavitation inception on the hemispherical body. $Re_D = 3.10^5$, $\sigma = 0.607$.

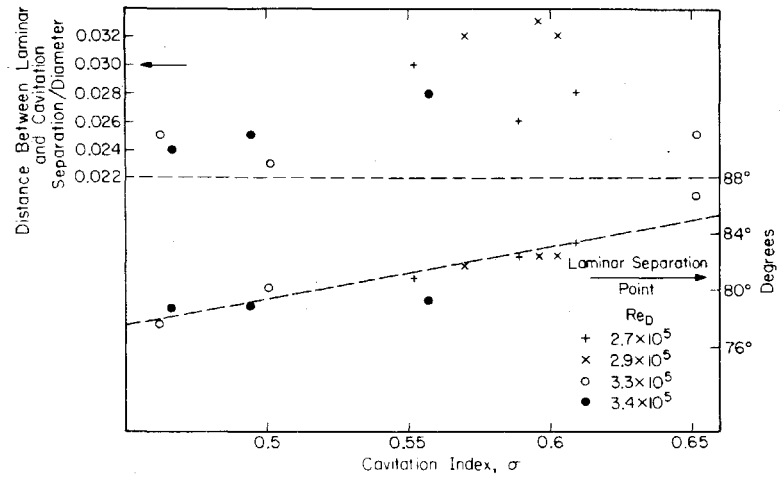

Fig. 4.26. The location of laminar separation point and the distance between this point and the cavitation separation on the hemispherical body.

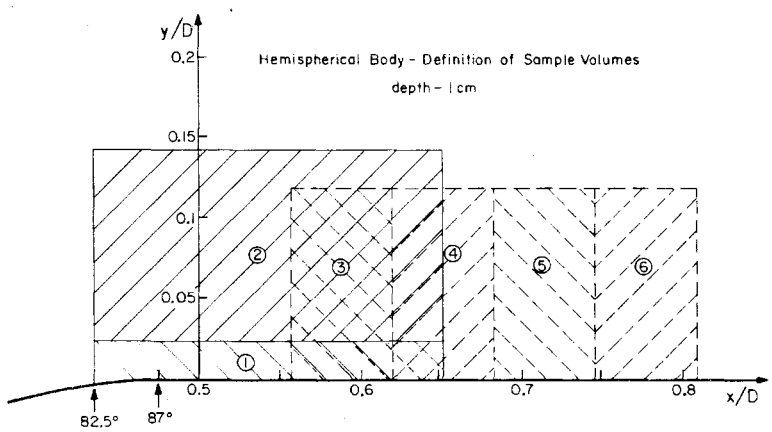

Fig. 4.27. A description of the counted sample volumes near the surface of the hemispherical body.

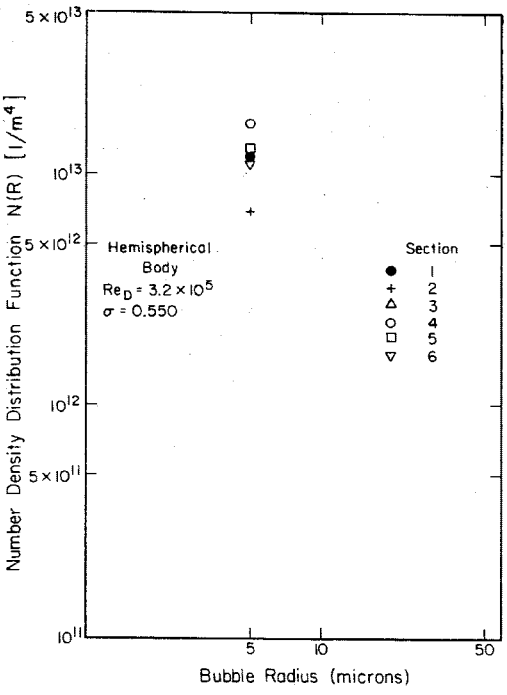

Fig. 4.28a

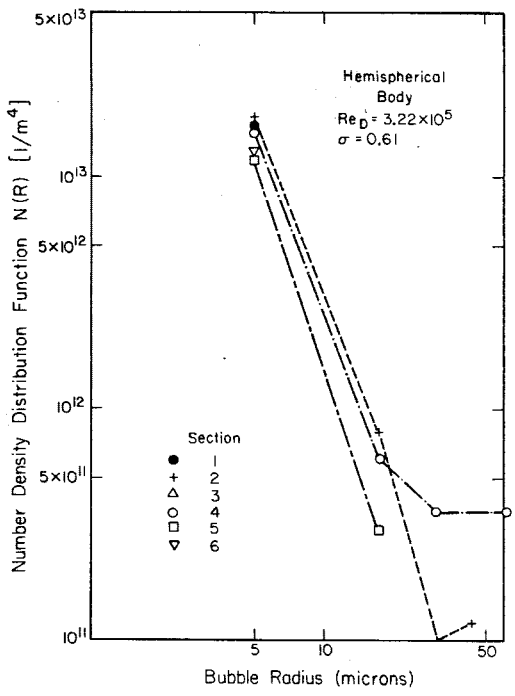

Fig. 4.28b

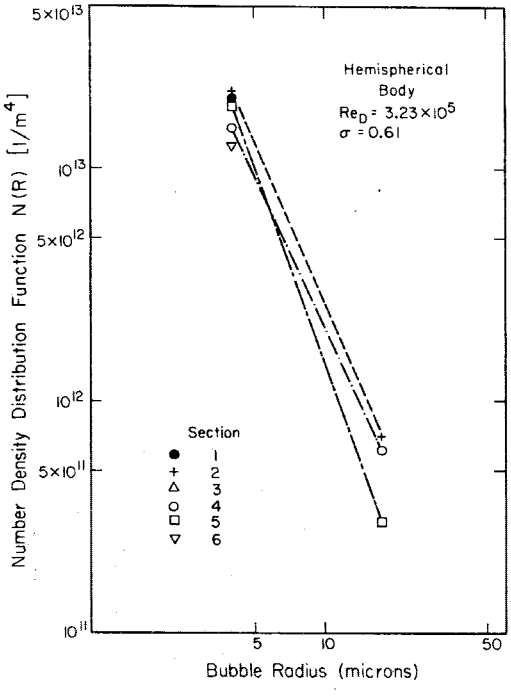

Fig. 4.28c

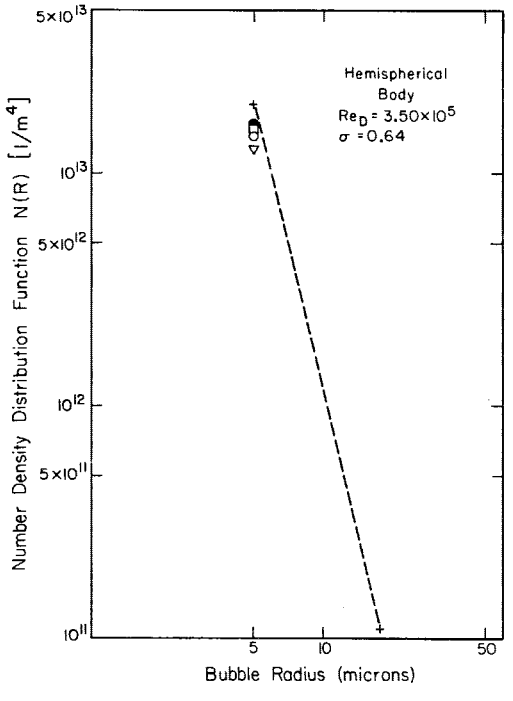

Fig. 4.28d

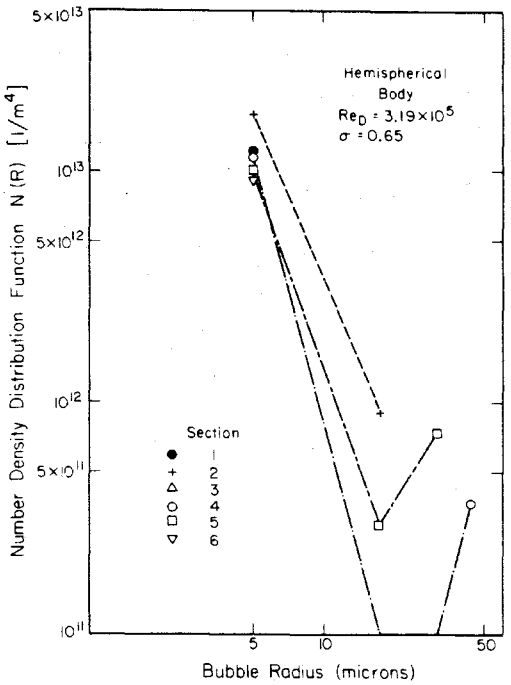

Fig. 4.28e

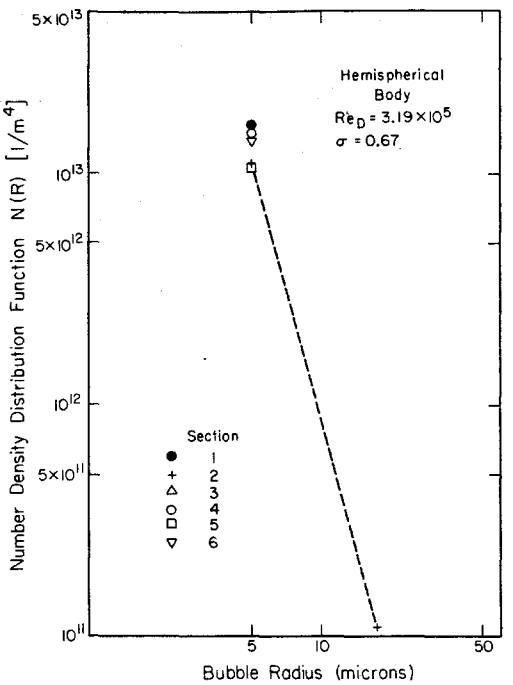

Fig. 4.28f

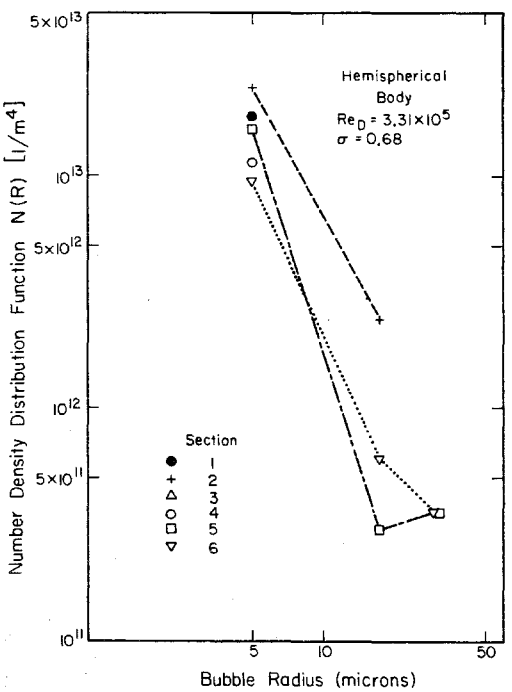

Fig. 4.28g

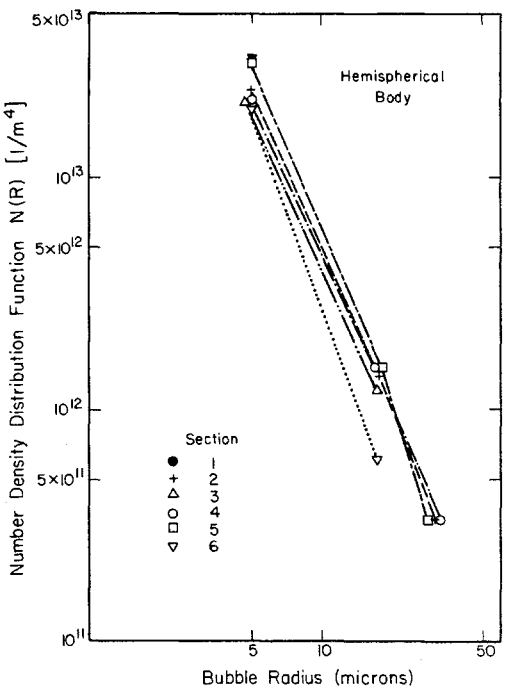

Fig. 4.28h

The population of bubbles near the surface of the hemispherical body. a) $Re_D = 3.23 \times 10^5$, $\sigma = 0.550$; b) $Re_D = 3.22 \times 10^5$, d=0.608; c) $Re_D = 3.23 \times 10^5$, $\sigma = 0.611$; d) $Re_D = 3.50 \times 10^5$, $\sigma = 0.643$; e) $Re_D = 3.19 \times 10^5$, $\sigma = 0.649$; f) $Re_D = 3.19 \times 10^5$, $\sigma = 0.699$; g) $Re_D = 3.31 \times 10^5$, $\sigma = 0.683$; h) $Re_D = 3.76 \times 10^5$, $\sigma = 0.586$.

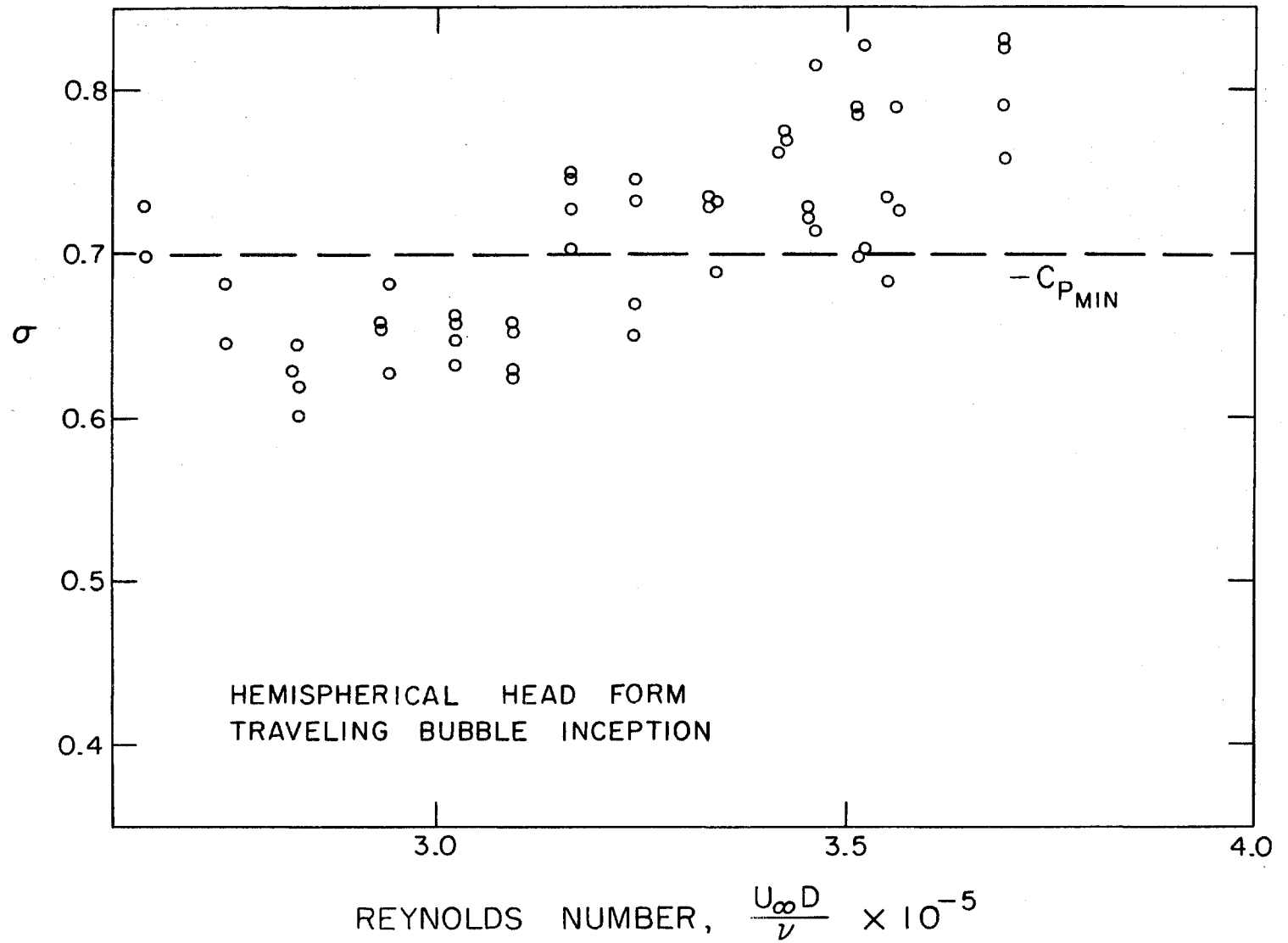

Figure 4.29. Inception indices of travelling bubble cavitation on the hemispherical body.

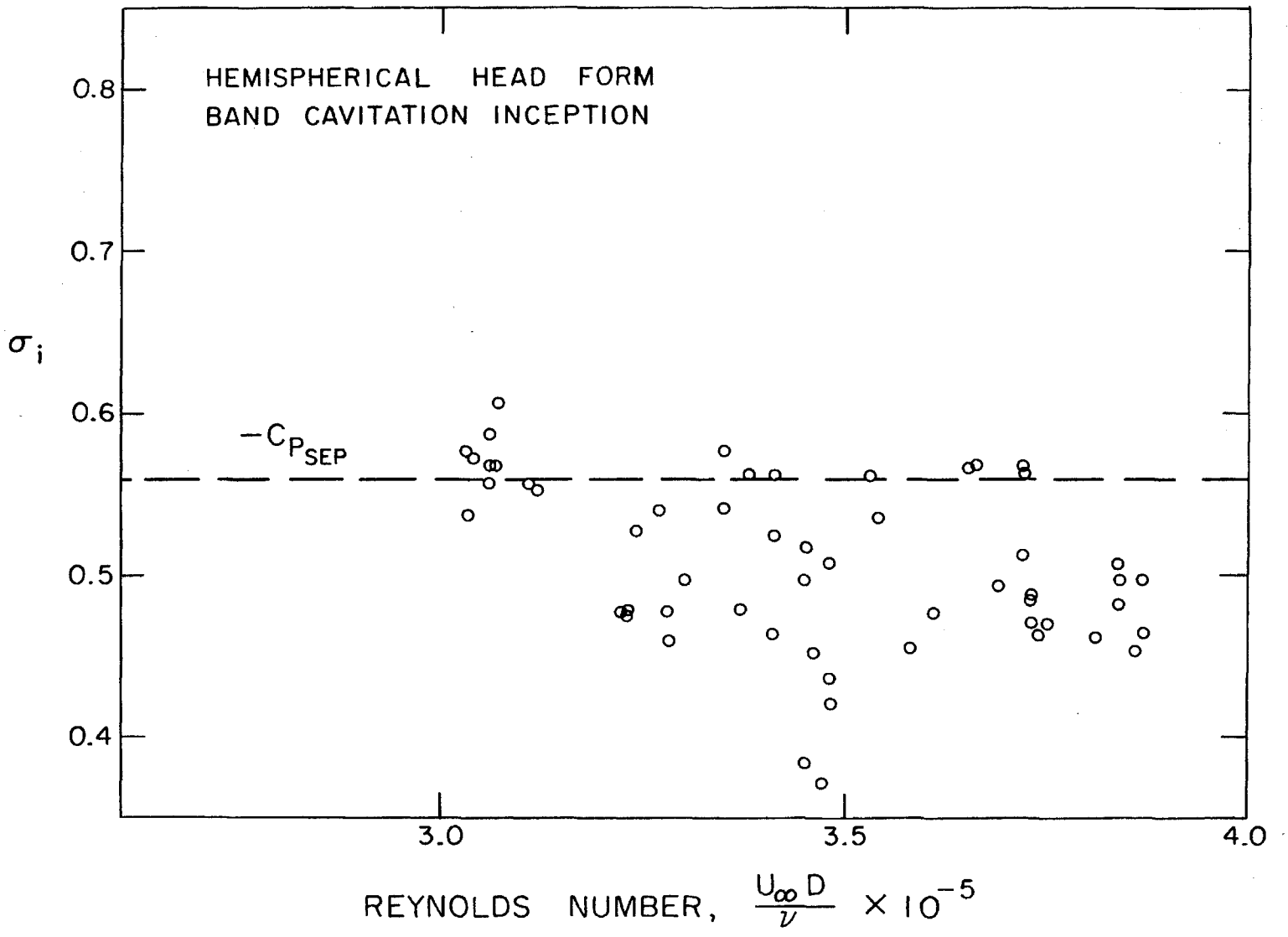

Figure 4.30. Inception indices of band type cavitation on the hemispherical body.

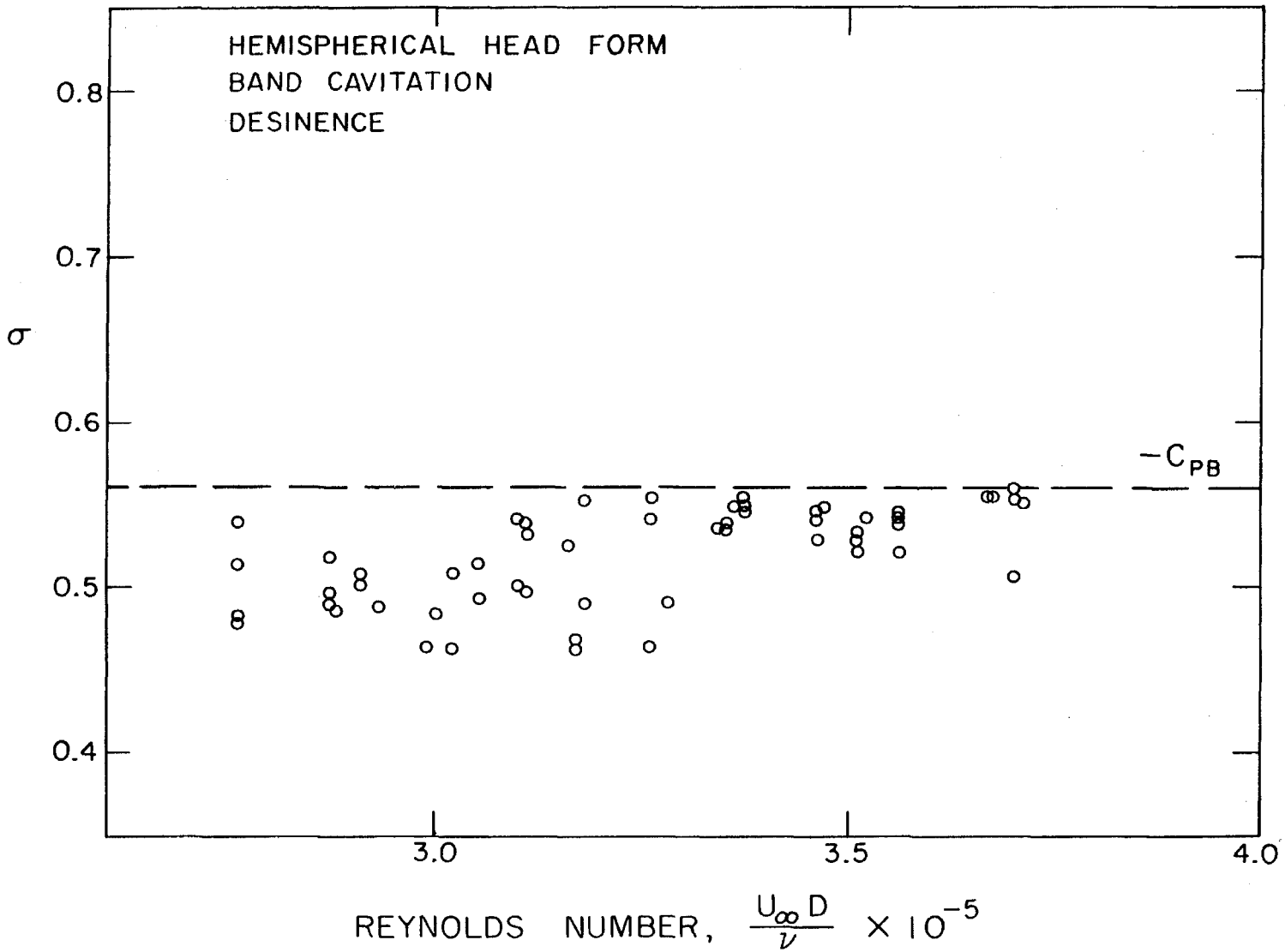

Figure 4.31. Desinence indices of band type cavitation on the hemispherical body.

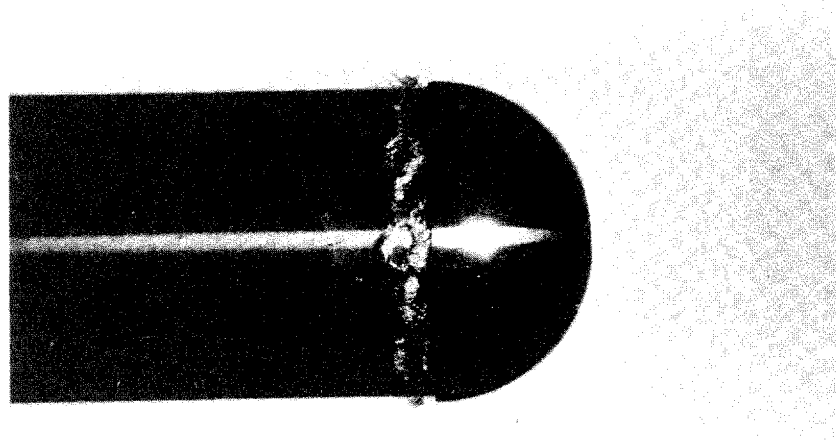

Fig. 4.32. Bubble ring cavitation on the step body. $Re_D = 3.60 \times 10^5$, $\sigma = 1.10$.

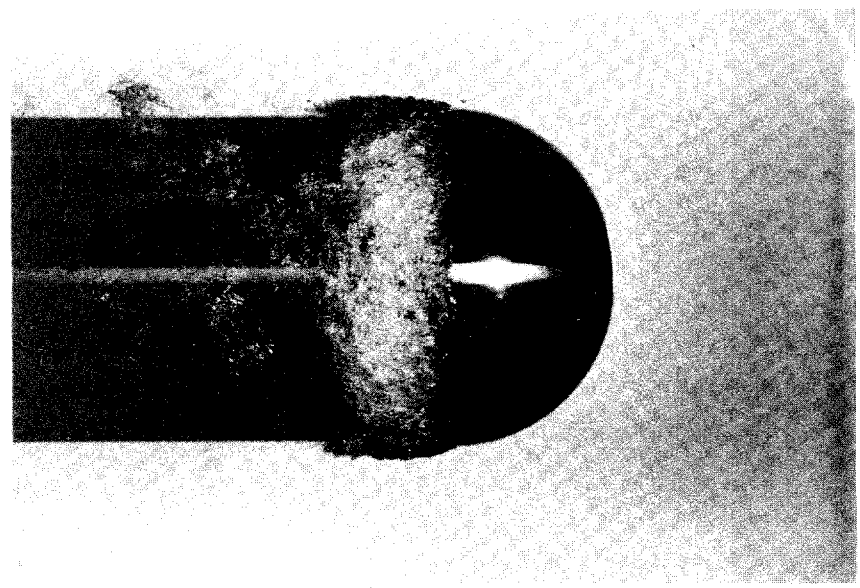

Fig. 4.33. Formation of band type cavitation on the step body. $Re_D = 3.60 \times 10^5$, $\sigma = 0.54$.

(a)

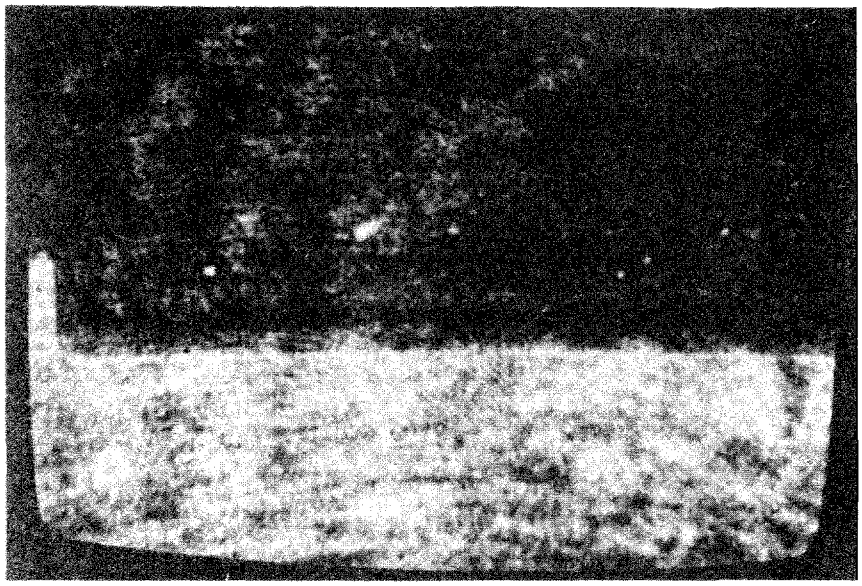

(b)

Fig. 4.34. Inception of cavitation on a non heated step body. $Re_D = 2.78 \times 10^5$, $\sigma = 1.07$. a) a total view of the cavitating zone; b) a close-up view of part of the region extending from 3.5 to 10.5mm behind the step.

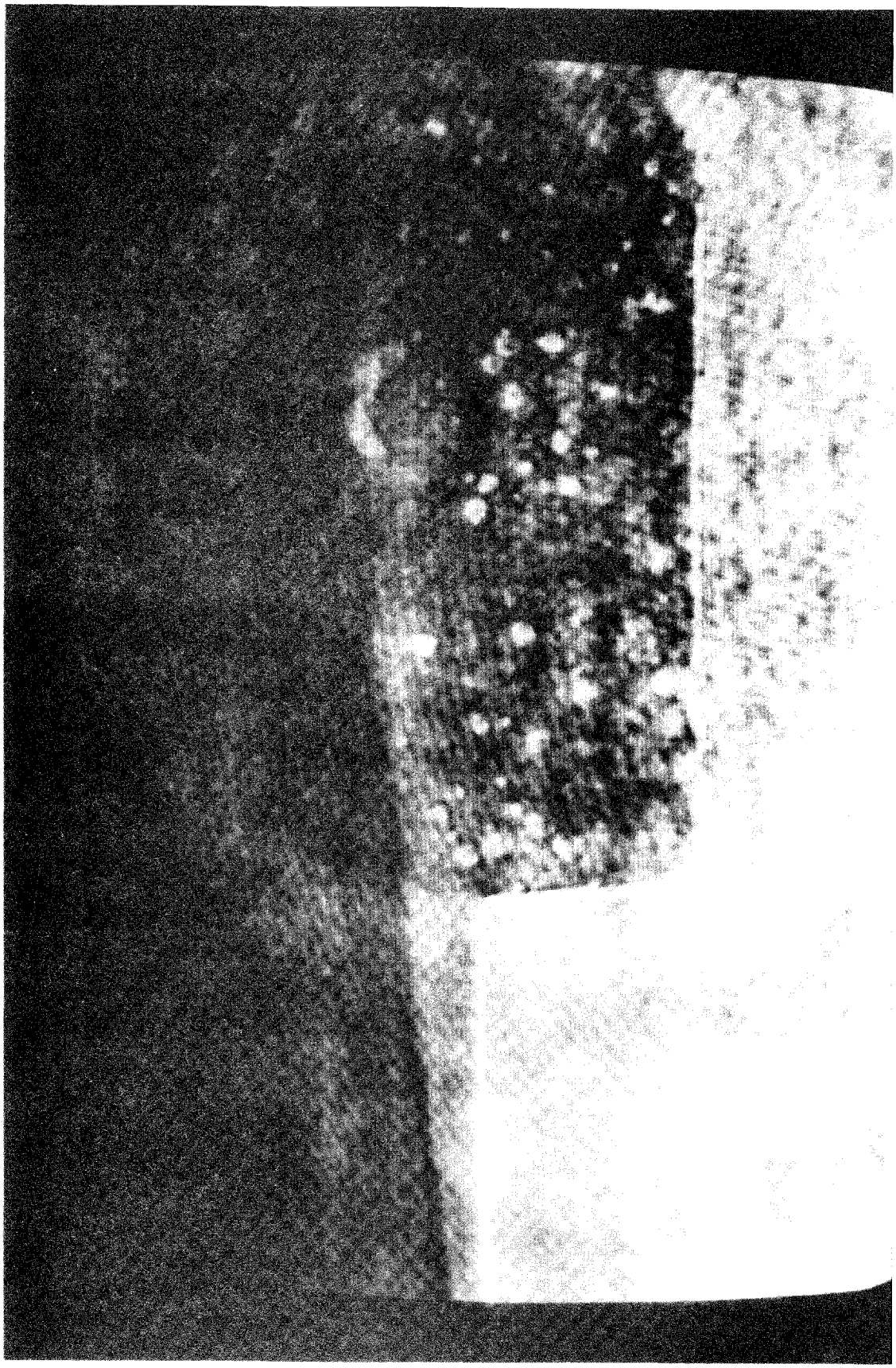

Figure 4.35. Inception of cavitation on a heated step body. $Re_D = 2.79 \times 10^5$, $\sigma = 1.07$.

(a)

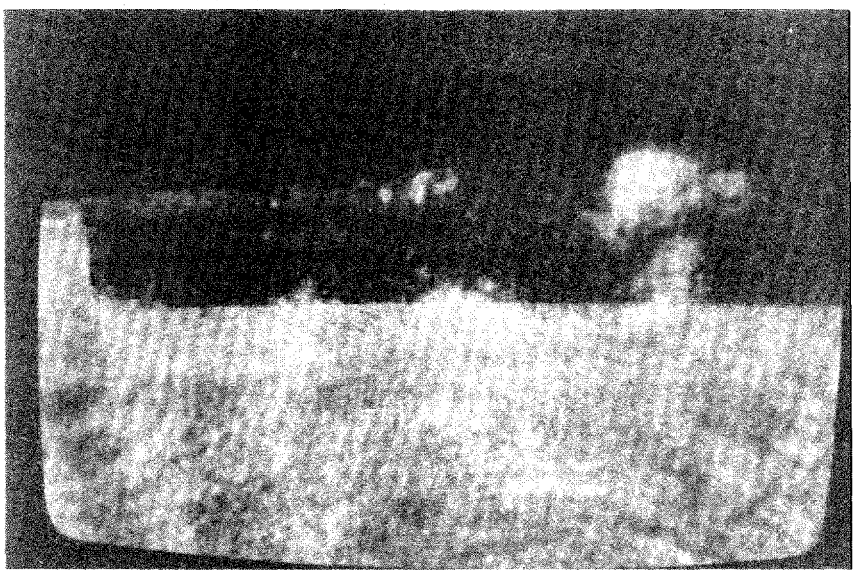

(b)

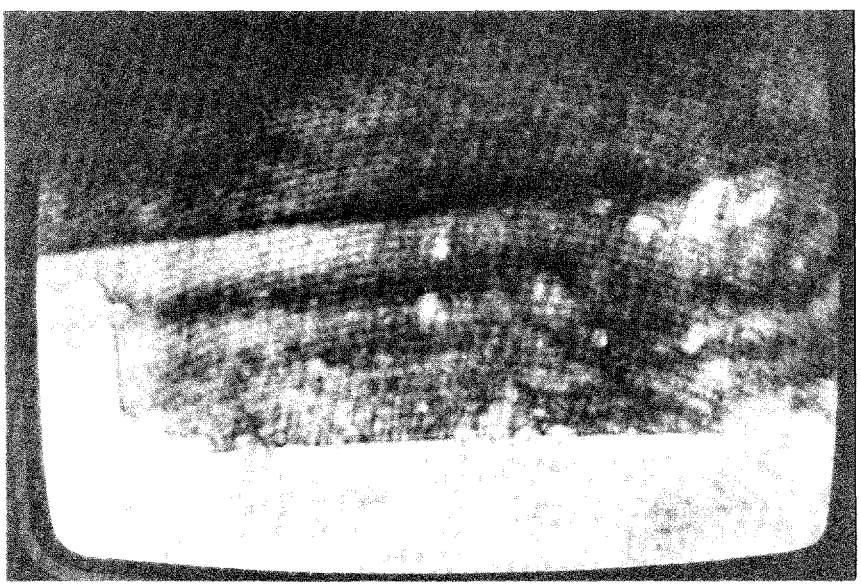

Fig. 4.36. Inception of cavitation on a heated step body. $Re_D = 2.78 \times 10^5$, $\sigma = 1.11$. a) a total view of the cavitating zone; b) a close-up view of the region behind the step.

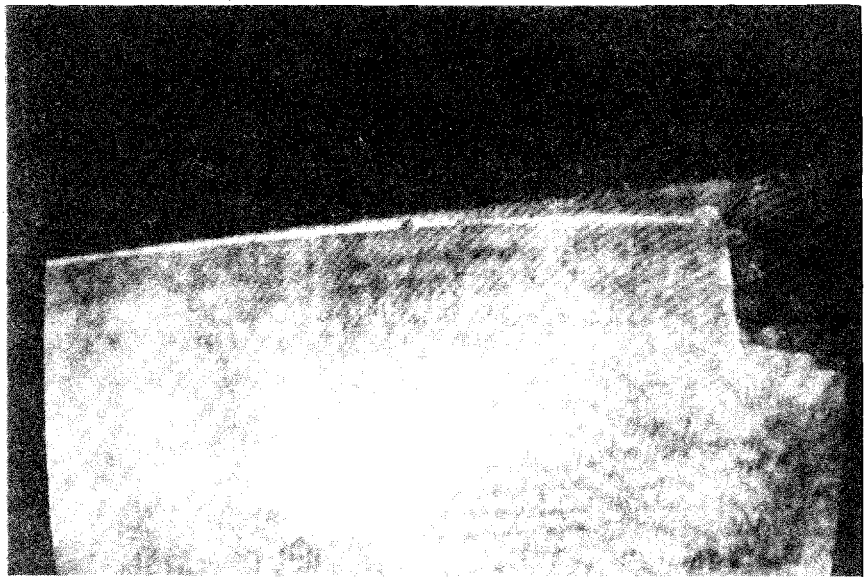

Fig. 4.37. The region near the separation point of the hologram shown in Fig. 4.36.

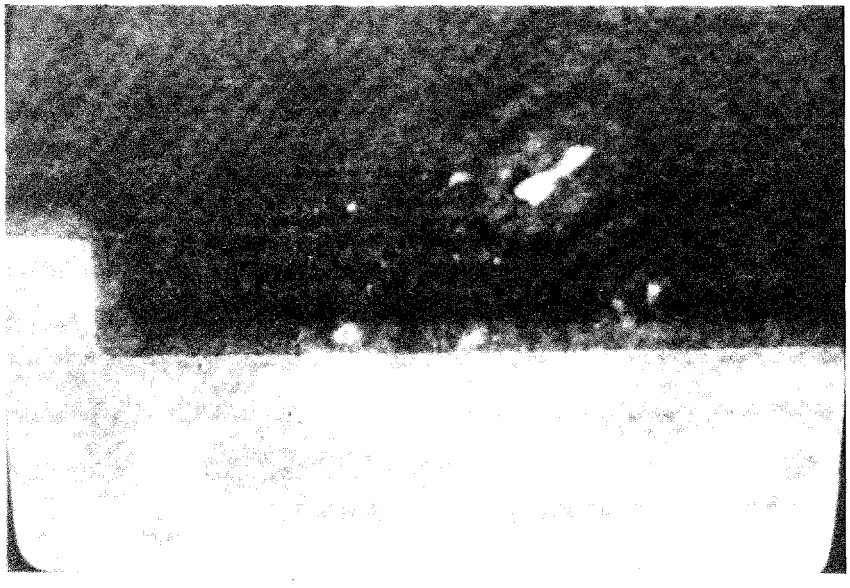

Fig. 4.38. Inception of cavitation on a non-heated step body. $Re_D = 3.62 \times 10^5$, $\sigma = 1.20$.

(a)

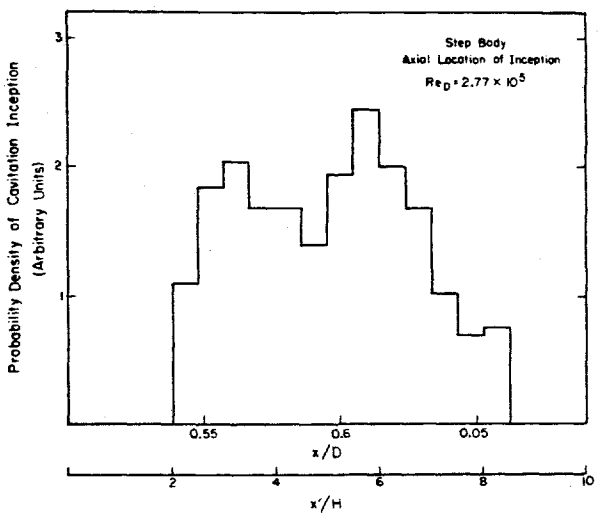

(b)

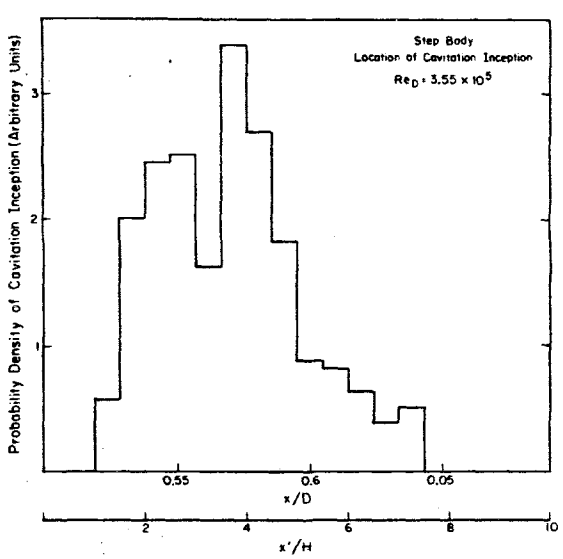

Fig. 4.39. Probability density histograms of the axial location of cavitation inception on the step body; a) $Re_D=2.77 \times 10^5$; b) $Re_D=3.55 \times 10^5$.

Step Body

$Re_D = 2.78 \times 10^5$

$\sigma = 1.11$

Bubble Diameter in microns

Section	0-20	20-50	50-75	75-100	100-150	150-200	200-250
a	11	1	2	-	-		
b	7	1	1				
c	10	-	1				
d	12	1	1	1			
e	10	2	1	-	-	-	1
f	4	1	-	-	-	2	
g	8	-	1				

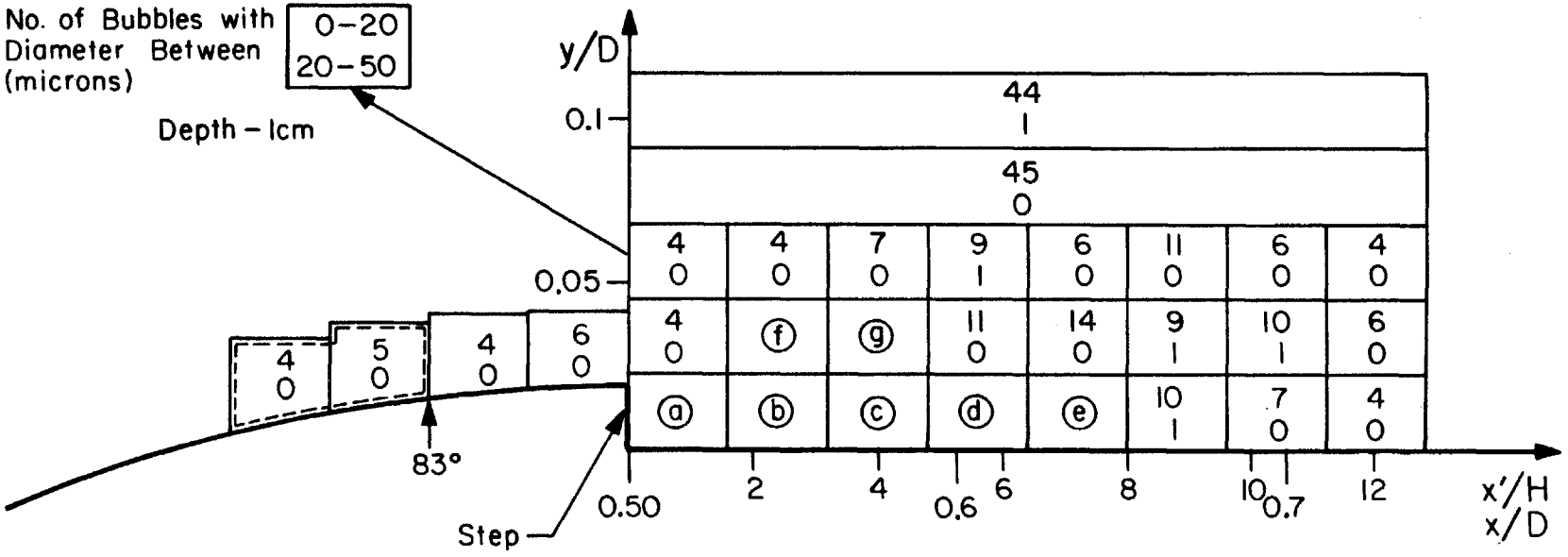

Figure 4.40. A map of bubble population during cavitation inception on the step body. $Re_D = 3.55 \times 10^5$, $\sigma = 1.11$.

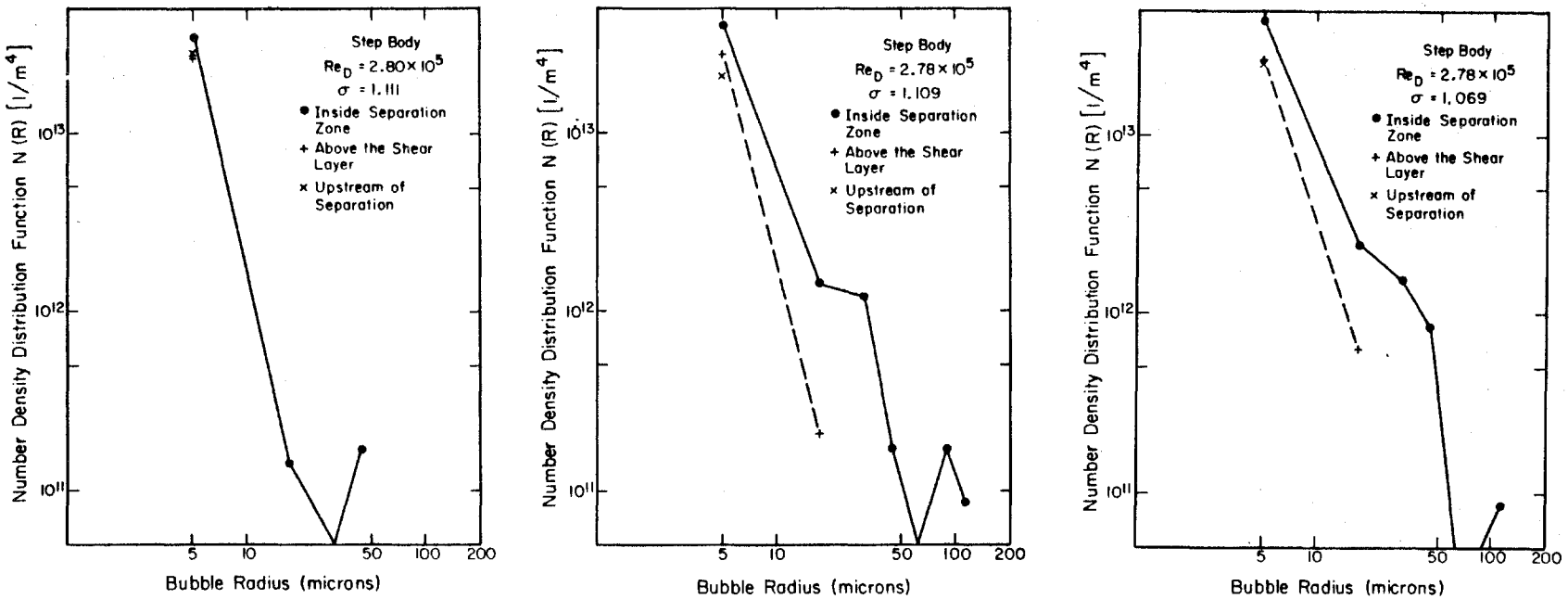

(a) (b) (c)

Fig. 4.41. The population of bubbles near the surface of the step body during cavitation inception; a) $Re_D = 2.8 \times 10^5$, $\sigma = 1.11$; b) $Re_D = 2.78 \times 10^5$, $\sigma = 1.11$; c) $Re_D = 2.78 \times 10^5$, $\sigma = 1.07$.

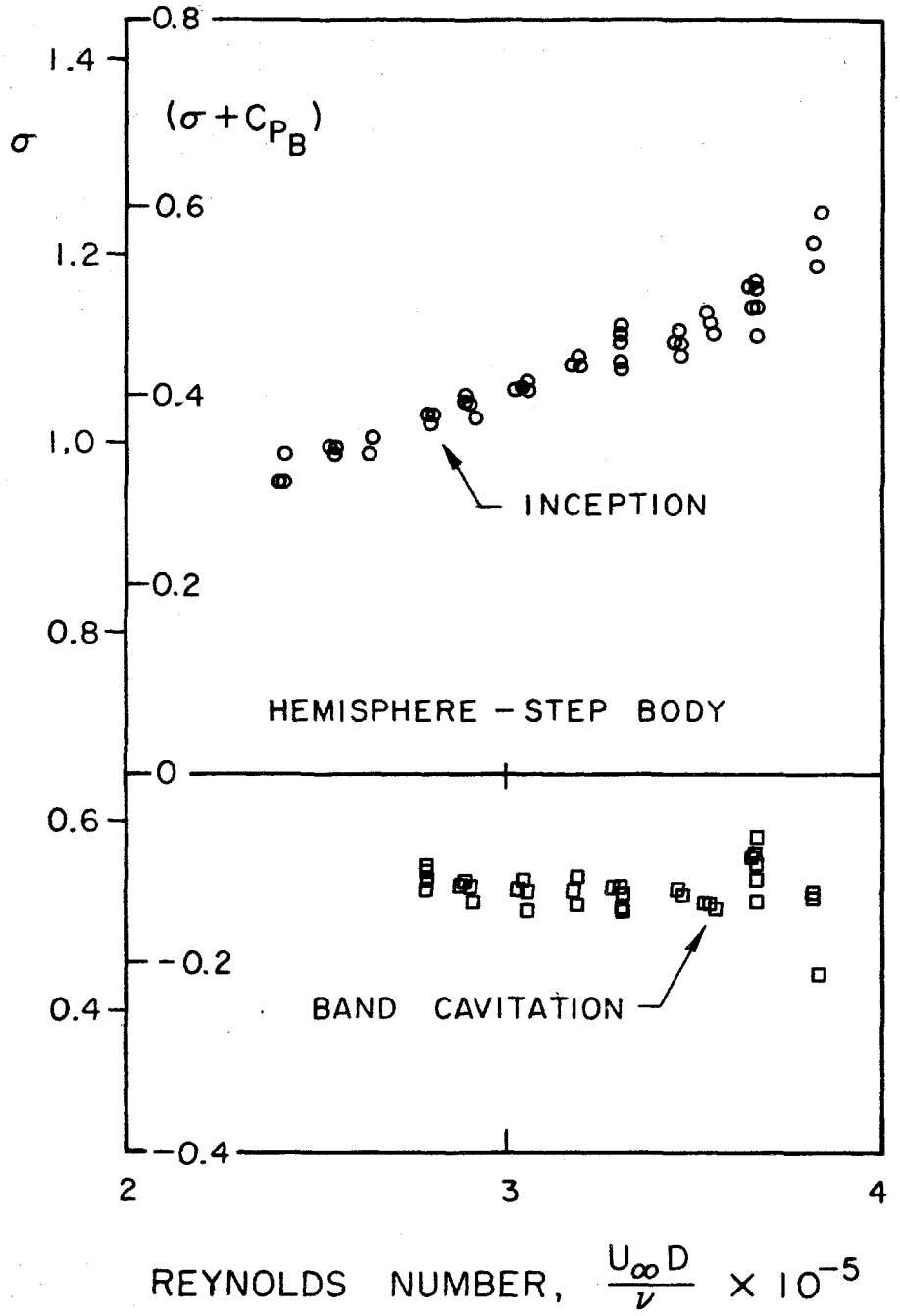

Figure 4.42. Cavitation inception indices on the step body.

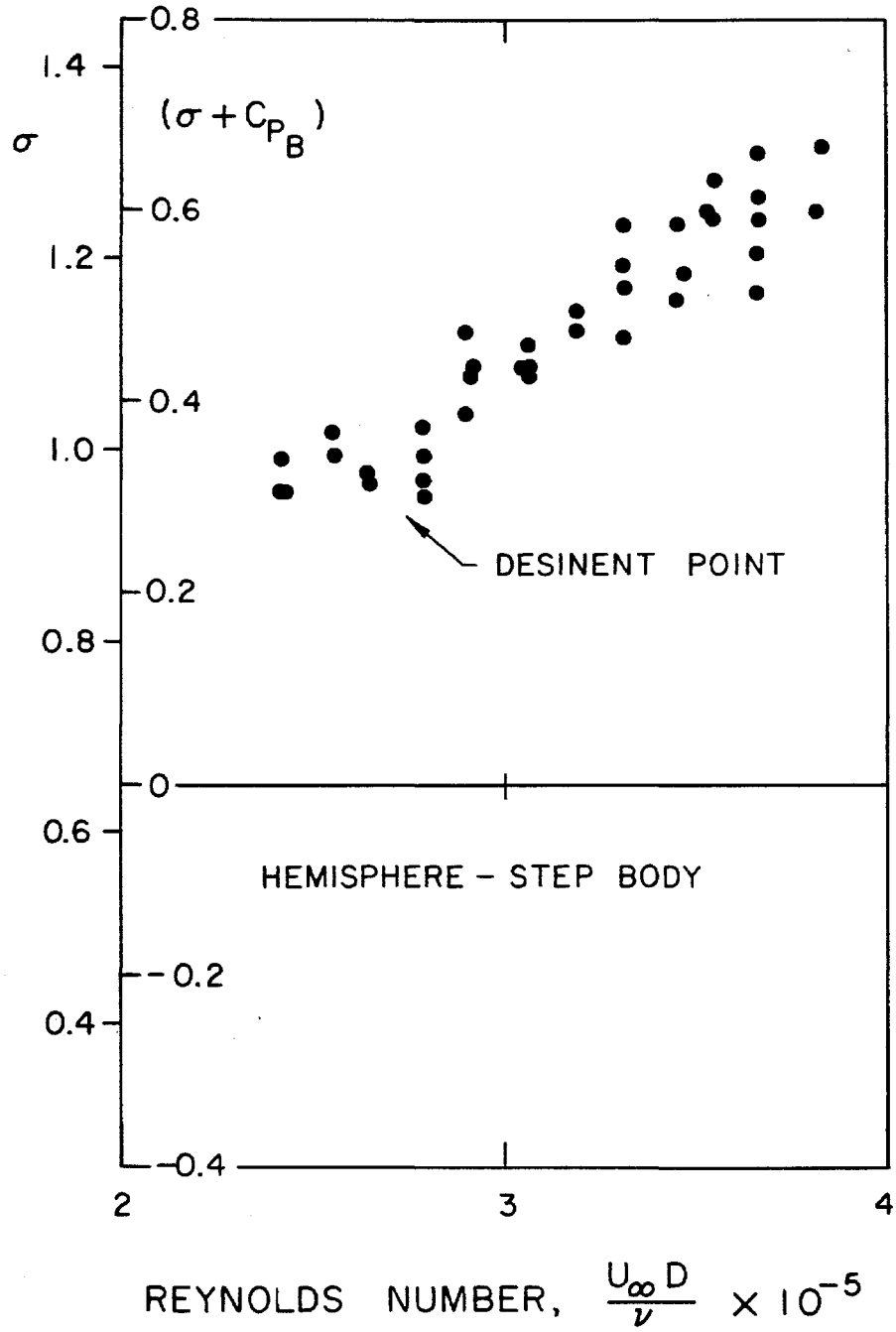

Figure 4.43. Cavitation desinence indices on the step body.

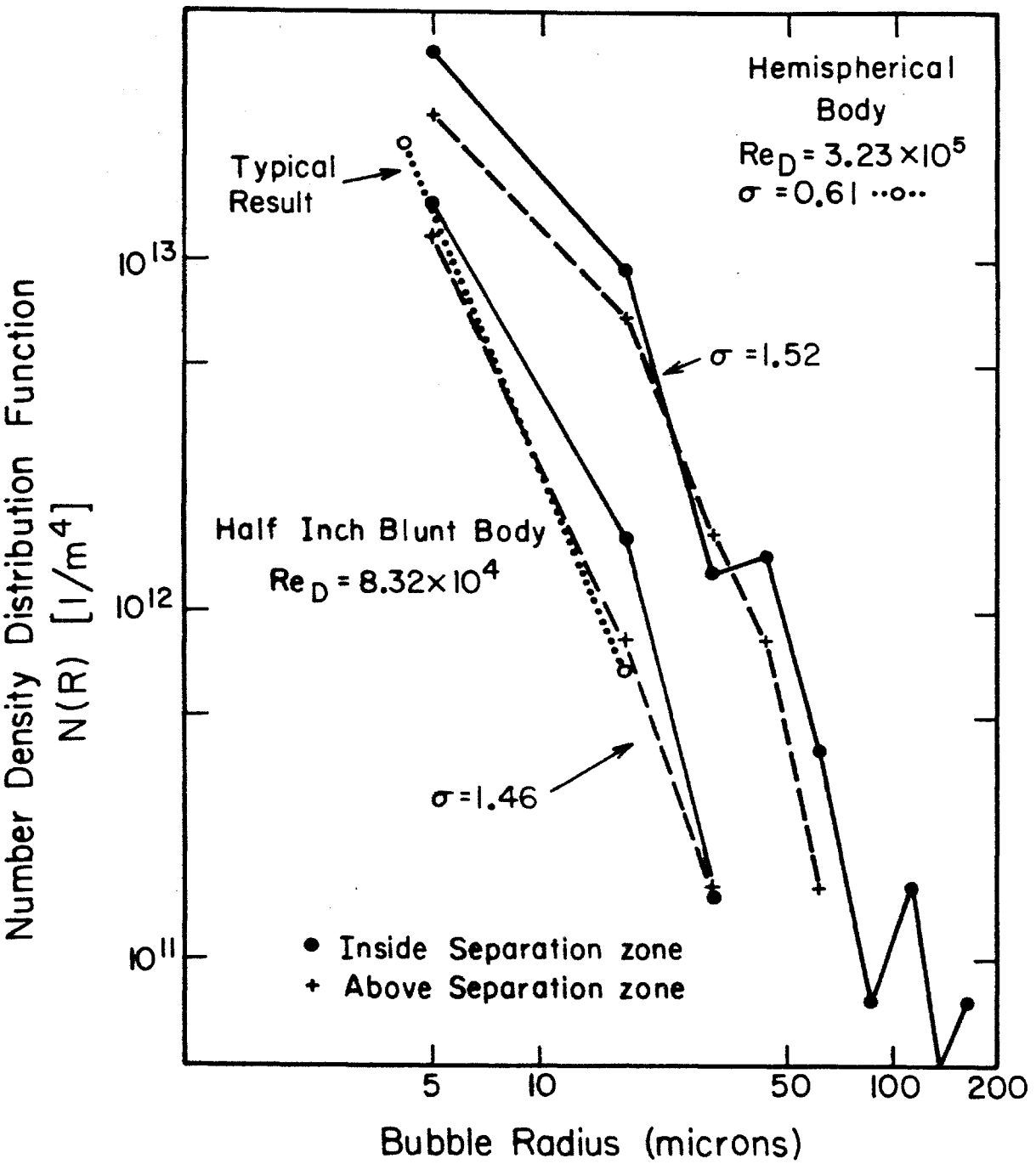

Figure 4.44. The population of bubbles in various conditions during the present experiments. The data are taken from Figures 4.13g, 4.13i and 4.28c.

V. SUMMARY AND CONCLUSIONS

The present thesis focuses on cavitation phenomena within regions of separated flows adjacent to axisymmetric bodies. In all of these flows the separation is laminar, followed by a free shear layer transition and turbulent reattachment. The test bodies and the dimensions of the associated separated regions differ widely from each other. They are a hemispherical body, a hemispherical head form with a downstream facing step at the tangency point, and a flat blunt circular cylinder. The noncavitating flow and the features of the separated regions around each of the test bodies was studied by different flow visualization techniques such as holography and schlieren photography (accomplished by either heating the bodies slightly or by injection of a denser fluid at discrete points). Surface distributions of the mean and the fluctuating pressures were measured over the range of Reynolds numbers available in the test facility (the Caltech Low Turbulence Water Tunnel). The occurrence of several forms of cavitation was noted, and the conditions for inception and desinence were measured for each of the test bodies. Several holograms of the water inside of and outside of the separated regions were recorded just prior and at the onset of cavitation. Reconstruction of these holograms then made possible the quantitative evaluation of the population of micro bubbles (of diameter 10 micrometer and larger) in various sections of the flow field. The location and the nature of the subsequent visible cavitation originating from these micro bubbles was also determined from these holograms.

A number of trends and conclusions can be drawn from the measurements and observations concerning the onset of cavitation in separated flows:

1. The mean pressure coefficient and the dimensions of the separated region on the blunt body do not depend on the Reynolds number (at least in the present range of measurements). The dimensions of the separated bubble on the hemispherical and the step bodies, however, become smaller as the velocity is increased but the mean pressure coefficient inside the separation zone remains unchanged.

2. The maximum rms values of the fluctuating pressure are 19, 7 and 3-5.5 percent of the dynamic head for the blunt, step and hemispherical bodies, respectively. The peak values that are obtained from the probability distribution histograms (chosen to be the peaks with a 0.1 percent probability of occurrence) are at least three to four times larger. The negative peaks are larger than the positive ones in all the points of measurements excluding the reattachment zone where the positive peaks exceed the negative ones. These high positive peaks are originated from the low frequency part of the spectrum and are probably associated with the motion of the separating stream line.

3. The spectra of pressure fluctuations contain peaks that appear in the turbulent part of the separated region, the reattachment zone and part of the flow field downstream. It is suggested that these spectral peaks are associated with the large eddy structure in the shear layer (whose existence is also demonstrated by flow visualization). The Strouhal number based on the length of the separation zone and the

free stream velocity is equal approximately to 0.56 for all the test bodies. The spectra of the hemispherical body contain also peaks due to laminar boundary layer instability waves.

4. The cavitation observations indicate that inception occurs in the turbulent part of the shear layer downstream of the transition point. In those cases where the shear layer is sufficiently far from the surface (the blunt and the step bodies) the inception region is located in the most developed section of this free shear layer but upstream of the reattachment zone. Some of the holograms also suggest that the onset of cavitation is related to the mixing layer large eddy structure. When the separation bubble is relatively small (hemispherical body) the inception region is located close to the reattachment zone but clearly detached from the body surface.

5. The sum of the negative pressure peaks and the mean pressure coefficient on the surface of the blunt and the step bodies do not explain the presently measured cavitation inception indices. These results support the observation that the onset of cavitation occurs far from these bodies surface. The inception indices on the hemispherical headform, however, are smaller than the absolute value of the surface minimum pressure. This result also indicates that inception may occur close to this body surface.

6. The appearance of visible cavities on all the present test bodies is preceded by the appearance of a cluster of microbubbles in the cavitation inception region. This local increase of bubble population does not appear in any other section of the flow field (including

parts of the separation zone) whose nuclei population remains fairly uniform. This observation clearly supports the assumption that cavitation is initiated from microscopic free stream nuclei.

7. The rate of cavitation events was roughly estimated on each of the test bodies by combining the measured bubble population, the dimensions of the turbulent mixing layer and the available pressure fluctuations data. This analysis demonstrates that the presently measured bubble size distribution affects the rate of cavitation events and the inception indices for the present free stream velocities and body sizes. The results for the two inch bodies suggest that at least one bubble with a radius between 10 and 25 micrometers and a large number of smaller bubbles are exposed every second to a pressure peak whose probability of occurrence is 0.1 percent. In the hemispherical body case, the estimates demonstrate that all the required conditions for cavitation inception are satisfied near the reattachment zone. The lack of pressure fluctuation data in the inception region of the other bodies prevents any similar conclusions about them.

The nuclei population in the water tunnel is very sensitive to the steady state pressure that preceded each of the cavitation tests. The instantaneous final cavitation index to which the tunnel is brought during these tests seems to be less important.

8. The cavitation inception indices measured on bodies with a large separation zone (such as the blunt and the step bodies) depend on the Reynolds number. The present measurements on these bodies' surface do not provide an explanation for this phenomenon and further

pressure fluctuations measurements in the inception region (the free shear layer) are still required.

REFERENCES

1. Acosta, A. J. and Hamaguchi, H., (1967), "Cavitation Inception on the ITTC Standard Head Form", Rep. No. E-149.1, Hydrodynamics Laboratory, California Institute of Technology, March.
2. Acosta, A. J., Parkin, B. R., (1975), "Cavitation Inception - A Selective Review", J. Ship Res., Vol. 19, No. 4, pp. 193-205.
3. Acosta, A. J., Parkin, B. R., (1980), "Report of the ATTC Cavitation Inception Committee", Proc. 19th American Towing Tank Conference, 2, pp. 829-858, Ann Arbor, Michigan.
4. Arakeri, V. H., (1973), "Viscous Effects in Inception and Development of Cavitation on Axi-Symmetric Bodies", Ph.D. dissertation, California Institute of Technology.
5. Arakeri, V. H., (1975a),"A Note on the Transition Observations on an Axisymmetric Body and Some Related Fluctuating Wall Pressure Measurements", Journal of Fluids Engineering, ASME, Vol. 97, Series 1, No. 1, Mar., pp. 82-87.
6. Arakeri, V. H., (1975b),"Viscous Effects on the Position of Cavitation Separation from Smooth Bodies", J. Fluid Mech., 68, pp. 779-799.
7. Arakeri, V. H., (1979), "Inception of Cavitation from a Backward Facing Step", International Symposium on Cavitation Inception, ASME Winter Annual Meeting, New York, Dec. 2-7.
8. Arakeri, V. H., Acosta, A. J., (1973), "Viscous Effects in Inception of Cavitation on Axisymmetric Bodies", Journal of Fluids Engineering, Dec., pp. 519-526.

9. Arakeri, V. H., Acosta, A. J., (1974), "Some Transition and Cavitation Inception Observations on a 1.5 Caliber Ogive", 17th American Towing Tank Conference, Pasadena, California.

10. Arakeri, V. H., Acosta, A. J., (1976), "Cavitation Inception Observations on Axisymmetric Bodies at Supercritical Reynolds Numbers", Journal of Ship Research, Vol. 20, No. 1, Mar, pp. 40-50.

11. Arakeri, V. H., Acosta, A. J., (1979), "Viscous Effects in the Inception of Cavitation", International Symposium on Cavitation Inception, ASME Winter Annual Meeting, New York, Dec. 2-7.

12. Arakeri, V. H., Carroll, J. A.,Holl, J. W., (1978), "A Note on the Effect of Short and Long Laminar Separation Bubbles on Desinent Cavitation", Measurements in Polyphase Flows, Annual Meeting - ASME, San Francisco, CA., Dec. 10-15.

13. Arndt, R. E. A., (1976), "Semiempirical Analysis of Cavitation in the Wake of a Sharp Edged Disk", J. Fluid Engineering, Vol. 98, pp. 560-562.

14. Arndt, R. E. A., (1981), "Cavitation in Fluid Machinery and Hydraulic Structures", Annual Review of Fluid Mechanics, Vol. 13, pp. 273-328.

15. Arndt, R. E. A., George, W. K., (1978), "Pressure Fields and Cavitation in Turbulent Shear Flows", 12th Symposium Naval Hydrynomics, Washington, D. C., pp. 327-339.

16. Arndt, R. E. A., Keller, A. P., (1976), "Free Gas Content Effects on Cavitation Inception and Noise in a Free Shear Flow", Proceedings of IAHR Symposium, Paris, France, pp. 3-16.

17. Beers, J. R., Reid, F. M. H., Stewart, G. L., (1973), "Microplankton of the North Pacific Central Gyre. Population, Structure, and Abundance", June 1973, Int. Revue. Ges. Hydrobiol., 60, 5, pp. 607-638.

18. Billet, M. L., Gates, E. M., (1979), "A Comparison of Two Optical Techniques for Measuring Cavitation Nuclei", International Symposium on Cavitation Inception, ASME, New York.

19. Born, M., Wolf, E., (1975), "Principles of Optics", Pergamon Press, Fifth Edition.

20. Browand, F. K., (1966), "An Experimental Investigation of the Instability of an Incompressible, Separated Shear Layer", J. Fluid Mechanics, Vol. 26, Part 2, pp. 281-307.

21. Brown, G. L., Roshko, A., (1974), "On Density Effects and Large Structure in Turbulent Mixing Layers", J. Fluid Mechanics, Vol. 64, Part 4, pp. 775-816.

22. Collier, R. J., Burkhardt, C. B., Lin, L. H., (1971), "Optical Holography", Academic Press Inc.

23. Corcos, G. M., (1963), "Resolution of Pressure in Turbulence", J. Acoustical Society of America, Vol. 35, No. 2, Feb., pp. 192-199.

24. Dimotakis, P. E., Brown, G. L., (1976), "The Mixing Layer at High Reynolds Number, Large Structure, Dynamics and Entrainment", J. Fluid Mechanics, Vol. 78, Part 3, pp. 535-560.

25. Eaton, J. K., Johnson, J. P., (1980), "Turbulent Flow Reattachment, an Experimental Study of the Flow and Structure Behind a Backward Facing Step", Stanford, Report MD-39, June.

26. Epstein, P. S., Plesset, M. S., (1950), "On the Stability of Gas Bubbles in Liquid-Gas Solutions", The Journal of Chemical Physics, Vol. 18, No. 11, Nov. 1950, pp. 1505-1509.

27. Feldberg, L. A., Shlemenson, K. T., (1973), "The Holographic Study of Cavitation Nuclei", Discussion to Proceedings IUTAM Symposium on Non Steady Flow of Water at High Speeds, Leningrad, USSR (English version; Moscow 1973), pp. 106-111.

28. Freymuth, P., (1965), "On Transition in a Separated Laminar Boundary Layer", J. Fluid Mechanics, Vol. 25, Part 4, pp. 683-704.

29. Fricke, F. R., (1971), "Pressure Fluctuations in Separated Flows", J. Sound and Vibrations, Vol. 17, No. 1, pp. 113-123.

30. Fricke, F. R., Stevenson, D. C., (1968), "Pressure Fluctuations in a Separated Flow Region", J. Acoustical Society of America, Vol. 44, No. 5, pp. 1189-1200.

31. Fuchs, H. V., (1972), "Space Correlations of the Fluctuating Pressure in Subsonic Turbulent Jets", J. Sound and Vibrations, Vol. 23, No. 1, pp. 77-99.

32. Fuchs, H. V., (1974), "Resolution of Turbulent Jet Pressure into Asimutal Components, AGARD-CP-131, Paper 27.

33. Fuchs, H. V., Mercker, E., Michel, U., (1978), "Large Scale Coherent Structure in the Wake of Axisymmetric Bodies", J. Fluid Mechanics, Vol. 93, Part 1, pp. 185-207.

34. Gadd, G. E., Jones, C. W., Watson, E. J., (1963), "Approximate Methods of Solution", in: Laminar Boundary Layers, Editor: Rosenhead L., Oxford University Press, pp. 258-345.

35. Gaster, M., (1966), "The Structure and Behavior of Laminar Separation Bubbles", AGARD Conference Proceedings on Flow Separation, No. 4, Part 2, May, pp. 813-854.

36. Gates, E. M., (1977), "The Influence of Freestream Turbulence Freestream Nuclei Populations and a Drag-Reducing Polymer on Cavitation Inception on Two Axisymmetric Bodies", California Institute of Technology, Report No. 183-2, April.

37. Gates, E. M., Acosta, A. J., (1978), "Some Effects of Several Freestream Factors on Cavitation Inception of Axisymmetric Bodies", 12th Symp. Naval Hydrodynamics, Washington, D. C., pp. 86-108.

38. Gates, E. M., Billet, M. L., Katz, J., Ooi, K. K., Holl, J. W., Acosta, A. J., (1973), "Cavitation Inception and Nuclei Distributions", Joint ARL/CIT Experiments, California Institute of Rechnology, Report No. E244.1,

39. Godefroy, H. W. H. E., Jansen, R. H. J., Keller, A. P., Lecoffre, Y., Oldenziel, D. M., Van Renesse, R. L., (1981), "Comparison of Measuring and Control Methods of the Water Quality with Respect to Cavitation Behaviour", Delft Hydraulic Laboratory, January.

40. Greshilov, E. M., Evtushenko, A. V., Lyamshev, L. M., (1969), "Spectral Characteristics of the Wall Pressure Fluctuations Associated with Boundary Layer Separation Behind a Projection on a Smooth Wall", Soviet Physics-Acoustics, Vol. 15, No. 1, pp. 29-34.

41. Gupta, S. K., (1969), "The Influence of Porosity and Contact Angle on Incipient and Desinent Cavitation", M. S. Dissertation, Department of Aerospace Engineering, Pennsylvania State University, December.

42. Harvey, E. N., Barnes, D. K., McElroy, W. D., Whiteley, A. H., Peace, D. C., Cooper, K. W., (1944), "Bubble Formation in Animals: I, Physical Factors", J. Cellular and Comp. Physiol., Vol. 24, No. 1, Aug., pp. 1-22.

43. Harvey, E. N., McElroy, W. D., Whiteley, A. H. (1947), "On Cavity Formation in Water", J. Appl. Phys. No. 18, pp. 162-172,

44. Holl, J. W. and Treaster, A. L., (1966), "Cavitation Hysteresis", Journal of Basic Engineering, Trans. ASME, Series D, Vol. 88, No. 1, Mar., pp. 199-212,

45. Holl, J. W., (1968), "Sources of Cavitation Nuclei", Presented at the 15th American Towing Tank Conference, Ottawa, Canada, June.

46. Holl, W. J., (1969), "Limited Cavitation", Cavitation State of Knowledge, ASME, pp. 26-63.

47. Holl, W. J., Carroll, J. A., (1979), "Observation of the Various Types of Limited Cavitation on Axisymmetric Bodies", International Symposium on Cavitation Inception, ASME Winter Annual Meeting, New York, Dec. 2-7.

48. Holl, J. W., Kornhauser, A. L., (1969), "Thermodynamic Effects on Desinent Cavitation on Hemispherical Nosed Bodies in Water of Temperatures from 80 Degrees F to 260 Degrees F", Joint Conference of Applied Mechanics and Fluid Engineering Divisions,

ASME, Northwestern University, June, ASME Paper No. 69-FE-1.

49. Huang, T. T., (1979), "Cavitation Inception Observations on Six Axisymmetric Bodies", International Symposium on Cavitation Inception, ASME Winter Annual Meeting, New York, Dec. 2-7.

50. Huang, T. T., Hannan, D. E., (1975), "Pressure Fluctuations in the Regions of Flow Transition", David Taylor Naval Ship Research and Development Center, Washington D.C., Report No. 4723.

51. Hussain, A. K. M. F., Ledan, M. F., (1978), "Effect of Initial Conditions on the Axisymmetric Free Shear Layer; Effects of Initial Momentum Thickness", The Physics of Fluids, Vol. 21, No. 7, July, pp. 1100-1112.

52. Jimenez, J., Martinez-Val, R., Rebollo, M., (1979), "The Spectrum of Large Scale Structure in a Mixing Layer" 2nd Turbulent Shear Flow Symposium, Imperial College, London, July.

53. Johnson, Jr., V. E., Hsieh, T., (1966), "The Influence of the Trajectories of Gas Nuclei on Cavitation Inception", Sixth Symposium on Naval Hydrodynamics, Washington D.C., Sept.

54. Johnsson,C. A., (1969), "Cavitation Inception on Head Forms, Further Tests", 12th International Towing Tank Conference, Rome, pp. 381-392.

55. Katz, J., (1979), "Construction and Calibration of a Holographic Camera Designed for Micro Bubbles Observation in Cavitation Research", California Institute of Technology, Report No. Eng. 183-4.

56. Keller, A. P.,(1972),"The Influence of the Cavitation Nucleus Spectrum on Cavitation Inception, Investigated with Scattered

Light Counting Method", Journal of Basic Engineering, December, 917-925.

57. Keller, A. P., (1973), "Investigations Concerning the Modeling of Flow Cavitation", The University of Michigan Cavitation and Multiphase Flow Laboratory, Rep. No. UMICH 01357-28-T, March.

58. Keller, A. P., (1979), "Cavitation Inception and Flow Visualization on Axisymmetric Bodies at Two Different Free Stream Turbulence Levels and Test Procedures", International Symposium on Cavitation Inception, ASME Winter Annual Meeting, New York, Dec. 2-7.

59. Keller, A. P., Prasad, R., (1978), "Influence of the Previous History of the Test Water on the Cavitation Inception on Submerged Bodies", Technical University of Munich, Report No. 39.

60. Keller, A. P., Weitendorf, E. A., (1976), Influence of Undissolved Air Content on Cavitation Phenomena at the Propeller Blades and on Induced Hull Pressure Amplitudes", Proceedings of IAHR-Symp., Paris, pp. 65-76.

61. Kermeen, R. W., (1952), "Some Observations of Cavitation on Hemispherical Head Models", Hydrodynamics Lab. Rep. No. E-35.1, California Institute of Technology, June.

62. Kermeen, R. W., Parkin, B. R., (1957), "Incipient Cavitation and Wake Flow Behind Sharp Edge Disks", California Institute of Technology, Hydrodynamic Lab., Report No. 85-4, August.

63. Killen, J. M., Ripken, J. F., (1964), "A Water Tunnel Air Content Meter", University of Minnesota, St. Anthony Falls Hydraulic Laboratory, Project Rep. No. 70, February.

64. Knapp, R. T., Daily, J. W.,Hammitt, F. G., (1970), "Cavitation", McGraw Hill, New York.

65. Koechner, W., (1976), "Solid State Laser Engineering", Springer-Verlag, New York.

66. Konrad, J. H., (1976), "An Experimental Investigation of Mixing in Two Dimensional Turbulent Shear Flows with Application to Diffusion Limited Chemical Reactions", Project Squid, Technical Report CIT-8-PU, GALCIT, California Inst. of Technology.

67. Lau, J. C., Fisher, M. J., Fuchs, H. V., (1972), "The Intrinsic Structure of Turbulent Jets", J. Sound and Vibrations, Vol. 22, No. 4, pp. 379-406.

68. Lindgren, H., Johnsson, C. A., (1966), "Cavitation Inception on Head Forms ITTC Comparative Experiments", Publications of the Swedish State Shipbuilding Experimental Tank, No. 58, Göteborg.

69. Mabey, D. G., (1972), "Analysis and Correlations of Data on Pressure Fluctuations in Separated Flows", J. of Aircraft, Vol. 9, No. 9, pp. 642-645.

70. Medwin, H., (1977), "In Situ Acoustic Measurements of Micro-bubbles at Sea", J. Geophys. Res., 82, 6, pp. 921-976.

71. Michalke, A., Fuchs, H. V., (1975), "On Turbulence and Noise of Axisymmetric Shear Flow", J. Fluid Mechanics, Vol. 70, Part 1, pp. 179-205.

72. Mohsen, A. M., (1967), "Experimental Investigation of the Wall Pressure Fluctuations in Subsonic Separated Flows", Boeing Co., Commercial Airplane Division, Renton, Washington, Report D6-17094 AD 669214.

73. Moore, B. W., Saffman, P. G., (1975), "The Density of Organized Vortices in a Turbulent Mixing Layer", J. Fluid Mechanics, Vol. 69, Part 3, pp. 465-473.

74. Morgan, W. B., (1972), "Air Content and Nuclei Measurements", 13th ITTC, Rep. of Cavitation Committee, Berlin/Hamburg, pp. 657-675.

75. Oldenziel, D. M., (1979), "Bubble Cavitation in Relation to Liquid Quality, Ph. D. Thesis, Technical University Twente, Delft Hydraulic Laboratory, Publication No. 211, Delft.

76. Oldenziel, D. M., (1979), "New Instruments in Cavitation Research", International Symposium on Cavitation Inception, ASME Winter Annual Meeting, New York, Dec. 2-7.

77. Oshima, R., (1961), "Theory of Scale Effects on Cavitation Inception on Axially Symmetric Bodies", Journal of Basic Engineering, Trans. ASME, Series D, No. 3, Vol. 83, September, pp. 379-398.

78. Ota, T., (1975), "An Axisymmetric Separated and Reattached Flow on a Longitudual Blunt Circular Cylinder", Trans. ASME, J. of Applied Mechanics, Vol. 42, pp. 311-315.

79. Ota, T., Motegi, H., (1980), "Turbulence Measurements in an Axisymmetric Separated and Reattached Flow over a Longitudual Blunt Circular Cylinder", J. of Applied Mechanics, Vol. 47, March, pp. 1-6.

80. Parkin, B. R., (1952), "Scale Effects in Cavitating Flow", Ph. D. Dissertation, California Institute of Technology.

81. Parkin, B. R., Holl, J. W., (1953), "Incipient Cavitation Scaling Experiments for Hemispherical and 1.5 Caliber Ogive-nosed Bodies,"

Joint CIT/Penn. State Ordnance Research Laboratory, Report NORD 7958-264.

82. Parkin, B. R., Kermeen, R. W., (1953), "Incipient Cavitation and Boundary Layer Interaction on a Streamlined Body", California Institute of Technology, Hydrodynamics Laboratory, Report No. E-35.2, December.

83. Parrent, G. B., Thompson, B. J., (1964), "On the Fraunhofer (far field) Diffraction Pattern of Opaque and Transparent Objects with Coherent Background", Opt. Acta, No. 11, pp. 183-193.

84. Peterson, F. B., (1968), "Cavitation Originating at Liquid-Solid Interfaces", Rep. 2799, Naval Ship Research and Development Center, Washington D.C., September.

85. Peterson, F. B., Daniel, F., Keller, A.P., Lecoffre, Y., (1975), "Determination of Bubbles and Particulate Spectra and Number Density in a Water Tunnel with Three Optical Techniques", 14th ITTC, Ottawa, Vol. 2, pp. 27-52.

86. Plesset, M. S., (1949), "The Dynamics of Cavitation Bubbles", Transactions ASME, J. of Applied Mechanics, Vol. 16, pp. 228-231.

87. Plesset, M. S., (1956), "Physical Effects in Cavitation and Boiling", Proceedings 1st Symposium Naval Hydrodynamics, Washington, D. C., pp. 297-323.

88. Plesset, M. S., (1969), "The Tensile Strength of Liquids", Cavitation State of Knowledge, ASME, pp. 15-25.

89. Plesset, M. S., Prosperetti, A., (1977), "Bubble Dynamics and Cavitation", Ann. Rev. Fluid Mech., Vol. 9, pp. 145-185.

90. Reed, R. L., (1969), "The Influence of Surface Characteristics and Pressure History on the Inception of Cavitation", M. S. Dissertation, Dept. of Aerospace Engineering, The Pennsylvania State University, March.

91. Ripken, J. F., Killen, J. M., (1962), "Gas Bubbles: Their Occurrence, Measurement and Influence in Cavitation Testing", Proceedings of IAHR-Symposium, Sendai, Japan, pp. 37-57.

92. Schiebe, F. R., (1969), "The Influence of Gas Nuclei Size Distribution on Transient Cavitation Near Inception", University of Minnesota, St. Anthony Falls Hydraulic Laboratory, Project Rep. No. 107, May.

93. Stahl, B., (1980), "An Investigation of Turbulent Wall-Pressure-Fluctuations in a Pipe Downstream of an Abrupt Enlargement of its Cross Sectional Area", Institute für Experimentelle Strömungsmechanik, Rep. No. DFVLR-FB80-11, Göttingen, W. Germany.

94. Stewart, G. L., Bears, J. R., (1973), Proc. Soc. Photo-Opt. Inst. Engrs., 41, pp. 183-188.

95. Taghavi, H., Wazzan, A. R., (1974), "Spatial Stability of Some Falkner-Skan Profiles with Reversed Flow", The Physics of Fluids, Vol. 17, pp. 2181-2183.

96. Thompson, B. J., Ward, J. H., (1966), "Particle Sizing-the First Direct Use of Holography", Scientific Research, Vol. 1, No. 10, pp. 37-40.

97. Thompson, B. J. Ward, J. H., Finky, W. R., (1967), "Application of Hologram Techniques for Particle Size Analysis", Applied Optics, Vol. 6, No. 3, pp. 519-526.

98. Van der Meulen, J. H. J., (1972a), "Incipient and Desinent Cavitation on Hemispherical Nosed Bodies", International Shipbuilding Progress, Vol. 19, No. 209, Jan., pp. 21-32.

99. Van der Meulen, J. H. J., (1972b), "Cavitation on Hemispherical Nosed Teflon Bodies", International Shipbuilding Progress, Vol. 19, No. 218, Oct., pp. 333-341.

100. Van der Meulen, J. H. J., (1976), "A Holographic Study of Cavitation on Axisymmetric Bodies and the Influence of Polymer Additives", Netherlands Ship Model Basin, Publication No. 509, Wageningen, The Netherlands.

101. Van der Meulen, J. H. J., (1980), "Boundary Layer and Cavitation Studies of NACA 16-012 and NACA 4412 Hydrofoils", Thirteenth Symposium on Naval Hydrodynamics, Sasakawa Hall, Tokyo, Japan, October 6-10.

102. Van der Walle, F., (1962), "On the Growth of Nuclei and the Related Scaling Factors in Cavitation Inception", Fourth Symposium on Naval Hydrodynamics, Washington D.C., ONR/ARC-92, pp.357-404.

103. Van Ingen, J. L., (1956), "A Suggested Semi-empirical Method for the Calculation of the Boundary Layer Transition Region", Report V.T.H.-74, Dept. of Aeron. Eng., University of Technology, Delft, Netherlands.

104. Van Ingen, J. L., (1975), "On the Calculation of Laminar Separation Bubbles in Two Dimensional Incompressible Flow", AGARD, Conference Proceeding on Flow Separation, Report AGARD-CP-168, No. 11, Göttingen, W. Germany.

105. Wazzan, A. R., Okamura, T. T., Smith, A. M. O., (1968), "Spatial and Temporal Stability Charts for the Falkner Skan Boundary Layer Profiles", Douglas Aircraft Company, Report No. DAC-67086, Sept. 1.

106. White, F.M., (1974), "Viscous Fluid Flow", McGraw Hill, New York.

107. Willmarth, W. W., (1975), "Pressure Fluctuations Beneath Turbulent Boundary Layers", Annual Review Fluid Mechanics, Vol. 7, pp. 13-38.

108. Willmarth, W. W., Roos, F. W., (1965), "Resolution and Structure of the Wall Pressure Field Beneath a Turbulent Boundary Layer", J. Fluid Mechanics, Vol. 22, Part 1, pp. 81-94.

109. Willmarth, W. W., Wooldridge, C. E., (1962), "Measurements of the Fluctuating Pressure at the Wall Beneath a Thick Turbulent Boundary Layer", J. Fluid Mechanics, Vol. 14, pp. 187-210.

110. Winant, C. D., Browand, F. R., (1974), Vortex Pairing the Mechanism of Turbulent Mixing Layer Growth at Moderate Reynolds Numbers", J. Fluid Mechanics, Vol. 63, pp. 237-255.

111. Saffman, P.G., Baker, G.R., (1979) "Vortex Interactions", Annual Review Fluid Mechanics, Volume 11, pp. 95-122.

Appendix III-A The Effect of Transducer Size on Pressure Fluctuation Measurements

The effect of transducer size on the pressure fluctuation measurements was discussed in several sources, especially during analysis of pressure fluctuations in turbulent boundary layers. Willmarth (1975) included a chapter which discussed the problem in a review of the work done in turbulent boundary layers pressure fluctuations. Approximated calculations of proper correction factors were made by Corcos (1963). The factors that should be applied to the power spectrum depend on the dimensionless parameter $\frac{\omega r}{u_c}$, where ω is the frequency in rad/sec, r is the radius of the transducer, and u_c is the convection velocity of a disturbance. In order to apply Corcos' calculations to the present measurements we assume that the convection velocity is half of free stream velocity. Some correction factors are presented in Table III-A.1.

f	u_∞ = 10 ft/sec	u_∞ = 20 ft/sec
10 Hz	0.97	> 0.97
50 Hz	0.83	0.91
100 Hz	0.70	0.84
200 Hz	0.47	0.7
500 Hz	0.06	0.36
1000 Hz	0.01	0.06
2000 Hz	< 0.002	0.01

Table III-A.1 Correction factors for pressure fluctuations spectrum based on Corcos technique.

Needless to say, these calculations imply that for the hemisphere measurements the high frequency peak is attenuated by at least two orders of magnitude, a result that will lead to unbelievable rms values. Willmarth and Roos (1965) reviewed Corcos' results and compared them to experimental observations using circular transducers with different diameters. They came to the conclusion that the assumed universal dimensionless parameter $\omega r/u_c$ depended on the ratio between the transducer size and the displacement thickness of the boundary layer. The condition for the failure of the universal parameter was that

$$\frac{r}{\lambda} > 0.1$$

where λ is the wavelength of fluctuations. Since in the present measurements

$$\lambda \simeq \frac{0.5\ u_\infty}{f}$$

then the critical transducer radius above which Corcos' calculations fail is

$$\frac{r}{\lambda} = \frac{fr}{0.5\ u_\infty} = 0.1$$

If we substitute for r and u_∞ we can see that the critical frequencies are 120 Hz and 240 Hz for velocities of 10 and 20 ft/sec, respectively. These results exclude the hemisphere's high frequency peaks completely from Corcos' calculations, and major portion of the peak associated with the turbulent flow in the separated zone. The blunt nose spectrum that remains within the region where Corcos' technique holds will not be changed by more than 10 percent in the peak and 20 percent in a

frequency which is three times larger. It is clear that the change in the rms values will be small.

The boundary layer corrections are based on the ratio between the transducer radius and the displacement thickness that affects the characteristic wavelength of fluctuations. The length scale in the present measurements (excluding the Tollmien Schlichting waves) is the length of the separated zone that obeys the relation

$$\frac{fL}{u_\infty} \simeq 0.56$$

or

$$\frac{L}{\lambda} \simeq 1$$

Then the present important parameter, determining the resolution of the transducer will be r/L. For the step nose measurements

$$\frac{r}{\lambda} \simeq \frac{r}{L} = 0.1 \div 0.16$$

and for the hemisphere

$$\frac{r}{\lambda} \simeq \frac{r}{L} = 0.11 \div 0.3$$

According to Willmarth and Roos, no significant attenuation can be observed in the spectrum of a turbulent boundary layer up to

$$\frac{f\delta^*}{u_\infty} = 0.32$$

If we assume, according to their results, that the convection velocity in a turbulent boundary layer is equal to $0.6\ u_\infty$ then

$$\frac{\delta^*}{\lambda} \simeq \frac{\delta^* f}{0,6\ u_\infty} = 1,67\ \frac{f\delta^*}{u_\infty} = 0,5$$

Since their biggest transducer satisfies

$$\frac{r}{\delta^*} = 0.221$$

or

$$\frac{r}{\lambda} \simeq 0,11$$

then, as long as the wavelength remains within these bounds, the attenuation in the spectrum will be small. According to Willmarth and Ross the total loss of rms in the above-mentioned transducer was around 15 percent mainly due to losses in higher frequencies. However, one can expect that a more significant attenuation will occur when the ratio between the transducer radius and the disturbance wavelength will be larger than 0.11. For example, when $r/\lambda = 0.3$ corresponding to $f\delta^*/u_\infty = 0.8$ (when $r/\delta^* = 0.221$) Willmarth and Wooldridge (1962) results show that the response of the transducer is one-third of the output of a transducer satisfying $r/\lambda = 0.08$. As a result, one can expect significant attenuations of pressure fluctuations on the surface of the hemispherical nose, when the length of the separated zone becomes shorter (higher velocities). However, the results obtained on the surface of the step nose seem to be a fairly good representation of the real pressure fluctuations on its surface.

All the above arguments apply of course to problems where the disturbance causing the fluctuations in pressure is convected by the flow. This argument does not apply to problems where the source of

disturbance is stationary, and radiates sound waves to the transducer. In this case the relation between the transducer diameter and the frequency of fluctuations is meaningless. Fricke and Stevenson (1968) provide a comparison between the response of microphones of various sizes to pressure fluctuations behind a step. Their results show that in the upstream part of the separated zone (in the region where the peak associated with the length of the separated bubble does not exist) the size of the microphone does not have an effect on the spectrum even if $r/\lambda = 0.2$. This suggests that the spectrum contains mainly radiated waves and the previous analysis does not apply. However, near the reattachment zone significant differences between microphones response can be observed in the high frequency part of the spectrum. This suggests that at least part of the fluctuations are a result of a convected disturbance. Even these significant differences occur only when $r/\lambda \geq 0.2$ (the values of λ are estimated assuming that the convection velocity is half of the free stream velocity).

The only doubts left concerning the validity of the present results are the possible attenuations of the pressure fluctuations on the surface of the hemisphere. We are concerned especially about the attenuation of the Tollmien Schlichting waves since their frequency is much higher than the turbulent generated fluctuations (see Figure 3.62). The frequencies vary from 570 to 3200 Hz when the velocity is changed from 7.7 to 23 ft/sec, corresponding to $r/\lambda = 0.62$ in the low velocity and 1.16 in the higher speed. Any convected part of these fluctuations will be largely attenuated and will have a

significant effect on the rms values. This may be the reason for the difference between the present rms values at low velocities compared to those at higher speeds. The measurements made by Huang (1975 and 1979) with a pinhole microphone (r = 0.794 mm) on a much larger hemispherical nose remain always within the unattenuated region. His rms values exceed 15 percent, three to five times larger than the present experimental results, may be a better representation of the real pressure fluctuations on the surface of the hemisphere (in spite of the fact that this is the only source that presents such high rms values of pressure fluctuations).

Before concluding this appendix, it should be noted that recent measurements of pressure fluctuations in turbulent boundary layers revealed the existence of very high frequency fluctuations (see Willmarth (1975)) that doubted the previously mentioned rms results. However, since the frequencies associated are much larger than the characteristic frequencies of separated flows, and the maximum rms change was from 0.5 to one percent, these results will not affect the present ones significantly.